McKelvey School of Engineering Theses & Dissertations

McKelvey School of Engineering

Summer 8-15-2019

Role of Submicrometer Particles in Advanced Technologies of Carbon Capture

Zhichao Li
Washington University in St. Louis

Follow this and additional works at: https://openscholarship.wustl.edu/eng_etds

Part of the Chemical Engineering Commons, and the Environmental Engineering Commons

WASHINGTON UNIVERSITY IN ST. LOUIS

McKelvey School of Engineering
Department of Energy, Environmental and Chemical Engineering

Dissertation Examination Committee:
Pratim Biswas, Chair
Richard Axelbaum
Rajan Chakrabarty
Yongqi Lu
Brent Williams

Role of Submicrometer Particles in Advanced Technologies of Carbon Capture

by
Zhichao Li

A dissertation presented to
The Graduate School
of Washington University in
partial fulfillment of the
requirements for the degree
of Doctor of Philosophy

August 2019
St. Louis, Missouri

Table of Contents

List of Figures

List of Tables

<u>Acknowledgments</u>

First, I want to sincerely thank my doctoral advisor, Dr. Pratim Biswas, for his tremendous support both on my research and career. I greatly appreciate that he was never short of ideas for my study and constantly guiding me through various problems. He was quite open-minded and inspiring when I discussed research challenges with him. He allowed me to experiment on diverse topics and led me to find out my true interest. Not only is he my respected research mentor, but he is a life-long role model for me due to his kindness and perseverance.

I also want to express my gratitude to all my committee members for their patient advisory and kind encouragement. I'm grateful to Dr. Richard Axelbaum for giving me suggestions on combustion related work. I thank Dr. Rajan Chakrabarty and Dr. Brent Williams for providing critical viewpoints on various topics ranging from particle instruments to experimental design. I appreciate all the help and support from Dr. Yongqi Lu for the field study of particles in power plant stack at University of Illinois Urbana-Champaign.

I'm thankful to Consortium for Clean Coal Utilization (CCCU) for supporting me on coal combustion and electrostatic precipitator research. And I want to appreciate specially my fellowship provider, McDonnell International Scholars Academy, for all financial support and guidance on personal growth.

I want to acknowledge my colleagues in Aerosol and Air Quality Research Laboratory (AAQRL) for kind help and collaboration throughout my doctoral study. I want to express special appreciation to Dr. He Jing for helping me in every aspect at the beginning of my research journey. I'm also greatly grateful to Dr. Yang Wang for his collaborative work on those field studies of particle measurements at power plants. I also appreciate the efforts of Zehua Wang, David Dhanraj

Dedicated to my parents, wife and family.

ABSTRACT OF THE DISSERTATION

Role of Submicrometer Particles in Advanced Technologies of Carbon Capture

by

Zhichao Li

Doctor of Philosophy in Energy, Environmental and Chemical Engineering

Washington University in St. Louis, 2019

Professor Pratim Biswas, Chair

Oxy-combustion and post-combustion carbon capture technologies are two of the most promising strategies for carbon capture and storage (CCS), which is a commonly accepted approach to address the challenge of climate change. Pressurized oxy-combustion has been actively studied due to its great potential to enhance the power plant energy efficiency by recovering latent heat from water vapor condensation without incurring additional gas compression cost. On the other hand, amine-based CO_2 scrubbers have been demonstrated to have high removal efficiency of CO_2 with the possibility to recycle amine solutions, which makes the technology a promising candidate for post-combustion carbon capture. Nonetheless, the existence of submicrometer particles (diameters $< 1\mu m$) in coal combustion exhaust can pose various challenges to both advanced technologies: (1) particle control device used widely in coal-fired power plants such as electrostatic precipitator (ESP) is only designed for normal pressure operation, while submicrometer particles are needed to be removed efficiently under high pressure in a pressurized combustion system; (2) it has been shown that submicrometer particles in flue gas can induce amine loss in scrubbers by carrying the solution out due to condensation. In light of those technological challenges, this dissertation focuses on developing an understanding of how pressure affect characteristics and electrostatic precipitation of submicrometer particles in coal combustion exhaust gas through

experimental and modeling approach, and investigates characteristics of submicrometer particles with and without pretreatment upstream amine-based CO_2 scrubbers in real coal-fired power plants.

A lab-scale pressurized ESP was constructed to investigate the effect of pressure on electrostatic collection of submicrometer particles. Current-voltage characteristics were measured using different feeding gases. Removal efficiency of the pressurized ESP was studied under various pressure conditions. A semi-empirical Deutsch-Anderson equation was developed using multivariate regression to fit the experimental removal efficiency data under high pressure with minimized error, which was thus used to design a pilot-scale pressurized ESP in a pressurized combustion system. To better understand the effect of particle properties on electrostatic precipitation, coal fly ash generated from combustion of different coal seams from China, US and India were characterized in terms of particle size distribution, charge fraction and electrostatic precipitation efficiency. How combustion pressure affects the mineralogy, morphology and chemical composition of coal fly ash was also examined for a more detailed understanding of submicrometer particles in pressurized combustion exhaust.

To investigate the characteristics of submicrometer particles upstream amine-based CO_2 scrubber, a field study on variation of particle number concentration and gas pollutants concentration under different operating scenarios in a utility-scale power plant was conducted. Five operating modes including soot blow of boilers, bypass of flue gas desulfurization (FGD) scrubber and derating of reheat burner (0%, 27% and 42%) were studied. Significant differences in mode diameter and number concentration were observed for both wet and dry aerosols across those operating modes. A photo-ionizer enhanced ESP was demonstrated with higher removal efficiency of submicrometer particles than a conventional ESP. Another field study was conducted at a utility-

scale coal-fired power plant with a pilot-scale amine-based CO_2 scrubber to investigate how different pretreatment methods affect the particle size distribution in coal combustion exhaust. Pretreatment methods including steam injection, desiccation and electrostatic precipitation were studied. Steam injection showed different effects on particle number concentration in different submicrometer size ranges. Although particles in certain small sizes showed higher concentration with ESP turned on probably due to secondary aerosol generation, ESP with an optimal voltage could remove submicrometer particles effectively, which evidenced its candidacy as a promising pretreatment technique for amine-based CO_2 scrubbing.

Chapter 1: Introduction and overview

1.1 Introduction

Worldwide economic growth and development inevitably lead to increasing energy demands. According to International Energy Agency (IEA), despite increasing sustainable and non-emitting energy, such as nuclear and solar energy, fossil fuels still contributed 82% of the global total primary energy supply in 2013 (IEA, 2015). Consequently, global carbon dioxide (CO_2) emissions have skyrocketed by nearly 90% since 1970, and close to 80% of the total greenhouse gas emissions increase during 1970–2011 was attributed to fossil fuel combustion and industrial processes (IPCC, 2014). Particularly, coal combustion, accounted for 46% of the global CO_2 emissions in 2013, was the largest carbon emission source due to its heavy carbon content per unit of energy released (IEA, 2015).

In light of global challenge of CO_2 emission, carbon capture and storage (CCS) has been widely reckoned as a viable strategy to address issues of climate change. Researches regarding CCS in the field of clean coal combustion are typically focused on two perspectives: 1) advanced energy systems capable of reducing cost of electricity generation with CCS, such as oxy-combustion and chemical looping combustion; 2) carbon capture technologies enabling high-efficiency and sustainable CO_2 mitigation in new and conventional power plants.

Pressurized oxy-combustion technology is one of the most transformational candidates for advanced energy systems. With nearly pure oxygen environment for combustion, high concentration of CO_2 can be produced with absence of nitrogen (McDonald et al., 2007), greatly simplifying the subsequent separation of CO_2 for storage. Under high pressure conditions, even more benefits can be achieved: (1) more heat from water condensation at high temperature can be utilized for high power-plant cycle efficiency (NETL, 2013); (2) combustor can be manufactured in smaller size and with lower cost due to lower gas volume (Gopan et al., 2015); (3) the cost of

compression and purification of carbon dioxide in preparation for geo-sequestration or enhanced oil recovery can be reduced.

Nevertheless, the viability of pressurized oxy-combustion systems is determined not only by its effectiveness in CCS, but also by the feasibility and performance of auxiliary pollution control technologies. Fine particle emission control has been the focus of academic studies and industrial applications especially in developing countries, such as China (Che et al., 2009; R.-J. Huang et al., 2014) and India (Mishra et al., 2015; Pachauri et al., 2013) over the past few years due to growing concerns regarding haze, a primary hazard to their atmospheric environment. Specifically, submicrometer particles and ultrafine particles with diameters less than 1.0 µm and 0.1 µm, respectively, are extensively reported to cause cardiac and pulmonary health risks (Chan et al., 2004) since they can penetrate into deep human lungs and carry large content of absorbed and toxic matters due to high number concentration and surface area (Delfino et al., 2005). Therefore, equipping the pressurized oxy-combustion system with a robust submicrometer particle control technique is essential to green upgrade of coal-fired power plants.

Electrostatic precipitators (ESPs) have been widely employed in controlling particles from various emission sources, such as conventional coal-fired power plants (McCain et al., 1975; Meij et al., 2004; Ylätalo et al., 1998), due to their high mass collection efficiency, low operation cost and capability to run under high temperature (Brown et al., 1971; Villot et al., 2012) and high pressure (Bush et al., 1979; Rinard et al., 1987) conditions. In an ESP, corona discharge can be generated around a thin wire between conductive plates using high voltage. The particles passing through the ESP are charged by the ions and electrons in the wire-to-plate space, and move towards the plate to be collected. It has been reported that corona discharge can be obtained at a pressure of up to 1.6 MPa (Bush et al., 1979) and a temperature of up to 927°C (1700°F) (Brown et al., 1971).

3

These features enable ESPs to be coupled with pressurized combustion systems for particle removal. Figure 1.1 shows a schematic diagram of a staged pressurized oxy-combustion (SPOC) system with downstream particulate filter, where a pressurized ESP can be deployed. Extensive studies have been conducted on the capture of submicrometer particles with ESPs under atmospheric pressure with both lab-scale (Bai et al., 2010; S.-H. Huang et al., 2002; Yoo et al., 1997; Zhuang et al., 2001; Zhuang et al., 2000) and industry-scale combustion systems (Li et al., 2009; McCain et al., 1975; Ylätalo et al., 1998). Yoo et al. (Yoo et al., 1997) found that the particle collection efficiency of a two-stage ESP decreased significantly as particle diameter decreased from 30 nm. Similar results obtained by Zhuang et al. (Zhuang et al., 2000) demonstrated that a continuous decrease in particle collection efficiency occurred when particle diameter was smaller than 100 nm for both one-stage and two-stage ESP and particles of different contents. Ylatalo et al. (Ylätalo et al., 1998) demonstrated existence of a penetration window of particle in diameters of 100 nm – 5μm for a normal operated ESP in a power plant. However, the capture performance for submicrometer particles in an ESP operating under high pressure and high temperature condition is not thoroughly understood. In particular, size-dependent capture efficiency data has not been reported in the submicrometer domain under varying pressure conditions. Hence, this Ph.D. work will be focused on evaluating the effects of pressure on the current-voltage characteristics and capture performance for submicrometer particles in ESPs.
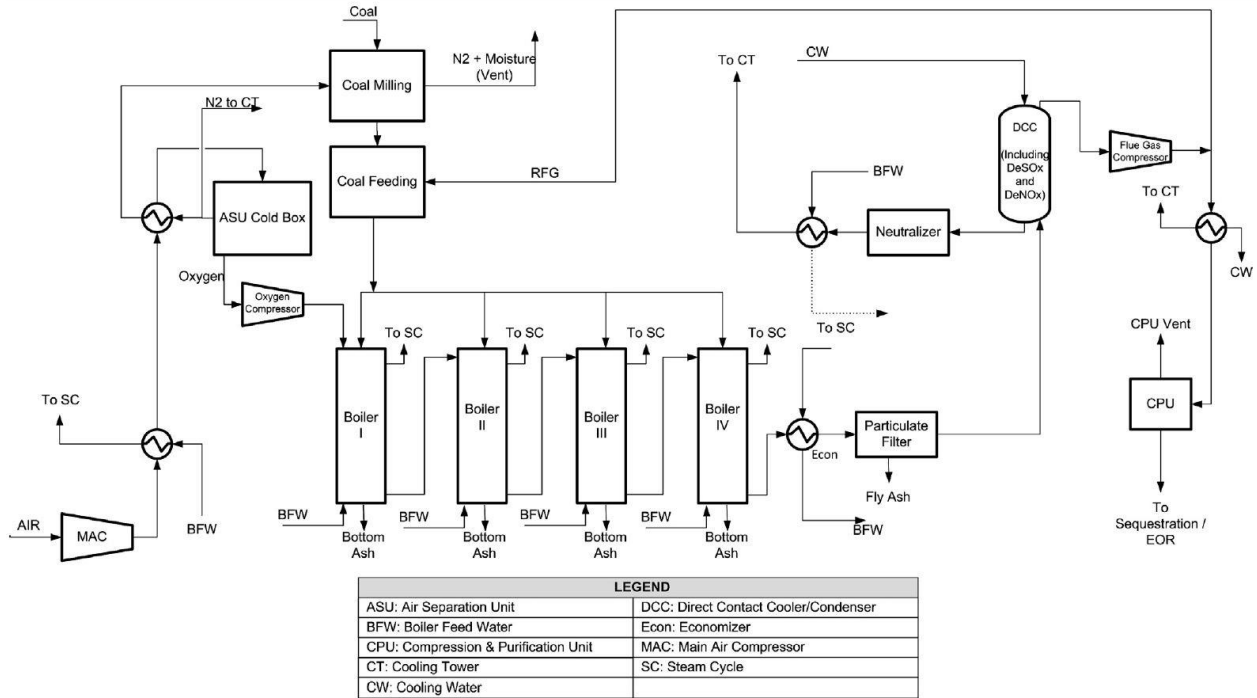
Figure 1.1 Flow diagram of a staged pressurized oxy-combustion system (Gopan et al., 2015).

Since particle charging is one of the most critical process governing the effective collection of particles in ESPs, a large number of efforts has been taken by researchers to understand the charging mechanism and efficiency of particles. Two main charging mechanisms, diffusion charging (Fuchs, 1947) and field charging (Pauthenier et al., 1932), influence the number of charges on particles in ESPs. Diffusion charging occurs when ions bombard particles and stick to them in the ESP, which is the dominant mechanism for particles less than 0.1 µm, while field charging is induced by unipolar ions driven by a strong electric field, which governs charging of particles larger than 1 µm (Hinds, 1999). As demonstrated in many studies, there is a transition regime for particle charging between 0.1–1 µm, which results in high particle penetration. Huang and Chen experimentally and theoretically confirmed that the penetration for particles below 20 and 50 nm in a single-stage and a two-stage ESP, respectively, increased remarkably due to a partial charging regime in the submicrometer size range (S.-H. Huang et al., 2002). Lin et al. obtained good agreement between numerical and experimental collection efficiencies of particles

5

less than 100 nm by incorporating a partial charging factor in a modified Deutsch-Anderson equation (Lin et al., 2012). Suriyawong et al. examined the charge fractions of particle released from a coal combustor and concluded that natural particle charging within the combustor was insufficient for effective collection in the ESP (Suriyawong et al., 2008). It can be implied that initial charges on the particle flowing into the ESP probably impact the charging effect by the diffusion and field charging processes and thus the capture performance in the ESP. Understanding the charged fraction and ash resistivity of submicrometer particles in combustion exhaust of different coal seams could provide more insight for enhancement of particle collection in ESPs.

Another approach to CCS in coal-fired power plants is to deploy carbon capture units including post-combustion and pre-combustion technologies, suitable for treating power plant flue gas (Bhown et al., 2011) and gasified coal syngas (Merkel et al., 2010), respectively. Although gasification shows advantages in clean energy production (Irfan et al., 2011), most of the current coal-fired power plants in the US and worldwide are producing electricity using conventional coal air boilers, which would be continued for the next few decades (Katzer et al., 2007). As a result, development of post-combustion CO_2 capture technologies are paid more attention globally.

Amine-based CO_2 scrubbers are the most typical and advanced candidates for post-combustion carbon capture, which have been heavily investigated over the last few decades (Dutcher et al., 2015). This technology is based on a fundamental process patented in 1930 (Rochelle, 2009), where CO_2 in the flue gas is absorbed by amine solvent in liquid phase at ambient temperature and the product is subsequently heated typically by steam to regenerate amine and release CO_2 for high pressure compression. The combination of absorption and stripping is featured with advantages in solvent recyclability and high absorption efficiency. Figure 1.2 illustrates the original design of an amine scrubbing system.
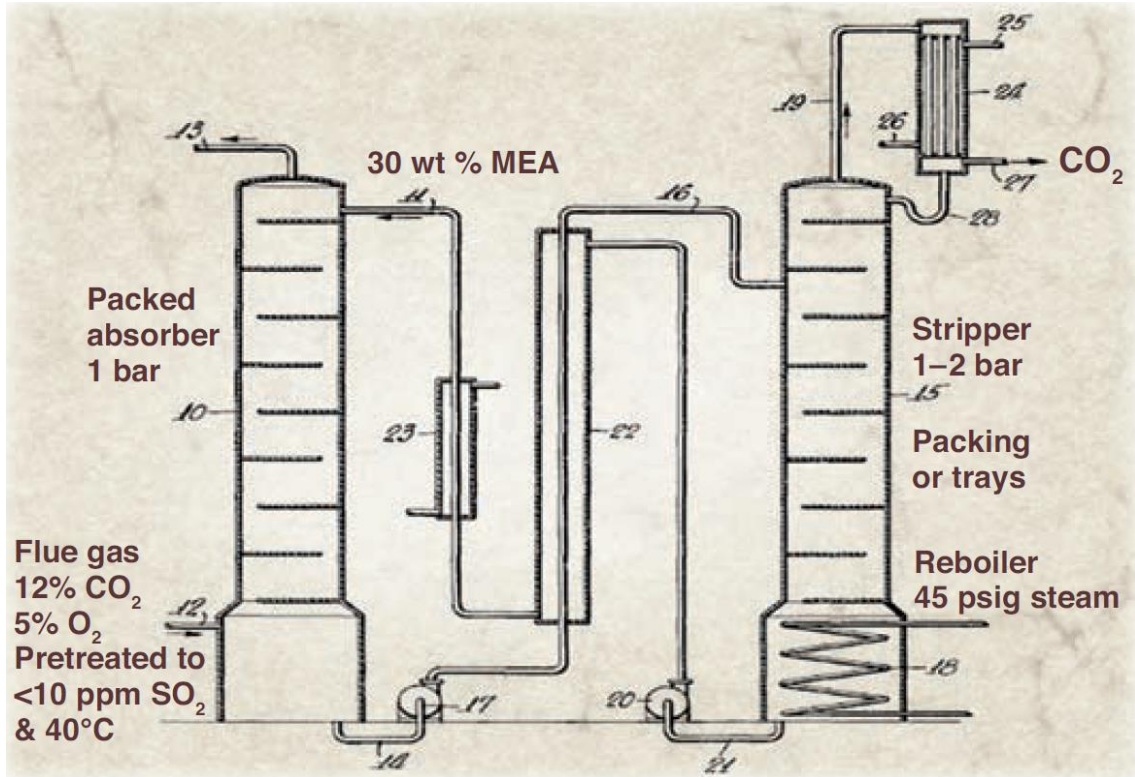
Figure 1.2 The design diagram of the amine scrubbing system patented in 1930 (Rochelle, 2009).

However, scaling up the amine scrubbing process encounters bottlenecks in terms of amine loss, toxic side product and high cost for solvent regeneration. Amine can be gradually consumed via amine degradation (Gouedard et al., 2012), evaporation (Nguyen et al., 2010) and aerosol formation and emission (Fulk et al., 2013; Khakharia et al., 2015; Mertens et al., 2014). It has been proved that amine can either be fragmented into organic acids and ammonia by oxidative pathway or be transformed into larger dimers or trimers under high temperature in stripping columns (Dutcher et al., 2015). However, recent studies have demonstrated the dominant share of aerosolized amine in total amine emission from CO_2 scrubbers. It has been reported that with the presence of soot particles in flue gas upstream a lab scale CO_2 scrubber, monoethanolamine (MEA) emissions were almost 200 mg/Nm^3, 2–4 times (Khakharia et al., 2013) higher than emissions via evaporation alone. Mertens et al. measured aerosol size distribution at the inlet and outlet of a lab-

scale CO_2 scrubber using electrical low pressure impactor (ELPI) and found that aerosols in the diameter range of 0.5–2 μm carried most of the total amine removed from the column (Mertens et al., 2014). Khakhariaa et al. evaluated the effects of lean solvent temperature, the pH of the lean solvent, the CO_2 concentration in the flue gas and type of solvent on the aerosolized amine loss.

Considering the potential negative impacts of submicrometer particles on amine consumption, it is necessary to map out the characteristics of particles in the flue gas upstream CO_2 scrubbers for better design of CO_2 scrubber and optimized operation condition of power plants. Chang et al. compared the particle size distributions at the outlet of a pilot-scale combustor using different types of fuel and under various flue gas temperature, and observed that the submicrometer particle number concentrations and peak particle size increased drastically as combustion exhaust temperature grew (Chang et al., 2004) using coal as the fuel. McElroy et al. concluded by testing particle size distributions at the outlets of six coal-fired utility boilers that peak diameter at 100 nm was a general feature for coal combustion in utility boilers (McElroy et al., 1982). Study on particle size distribution in a pilot-scale pulverized coal combustor conducted by Li et al. showed that high number concentration of ultrafine particles with the peak at around 75 nm was found in the flue gas, and an auxiliary ESP coupled with soft x-ray dramatically enhanced particle charging and collection efficiency (Li et al., 2009). A thorough review on fine particle characterizations in coal-fired power plants suggests that few researches are focused on how various operation scenarios can temporarily affect the particle size distribution in the flue gas, which then would impact the amine loss in the CO_2 scrubber. Hence, this dissertation will include field studies on particle characterization at the inlets of CO_2 scrubbers under various operation modes and pretreatment measures in utility-scale power plants.

1.2   Dissertation overview

Facing off against the global challenges of climate change, carbon capture and storage (CCS) has been widely reckoned as the most promising strategy for carbon dioxide (CO_2) emission mitigation. Oxy-combustion and post-combustion carbon capture are two of the most typical approaches to reduce CO_2 emission from coal-fired power plants, which are still the primary anthropogenic sources of greenhouse gases. Pressurized oxy-combustion systems show promising benefits over the first generation of oxy-combustion due to its capability to harness latent heat from water vapor condensation and to reduce the cost of compression and purification of CO_2.

However, a novel associated challenge for pressurized combustion systems is efficient control of emissions of submicrometer particles (diameters < 1µm), are typically featured by their hazardous effects on human cardiorespiratory health and recalcitrance in common particle removal devices. Electrostatic precipitators (ESPs) have shown extensive applications in controlling particulate matter emission from coal-fired power plants due to their high mass collection efficiency and been demonstrated to be able to operate under high temperature and high pressure conditions. Nonetheless, the collection efficiency with respect to number concentration of submicrometer particles is not clearly investigated under high pressure conditions.

Therefore, this dissertation is focused on investigating the effects of high pressure on the submicrometer particle capture performance of ESPs both in lab scale and pilot scale combustion systems. For lab scale study, the current-voltage characteristics and submicrometer particle collection efficiency of a wire-cylinder ESP under various high pressure conditions have been experimentally tested and numerically investigated. A pilot-scale pressurized ESP (PESP) was designed and constructed based on the outcome of the lab scale study, and is ready to be deployed downstream a pilot-scale staged pressurized oxy-combustor (SPOC) for study on ESP capture

9

performance in a scale-up system. Furthermore, detailed characterization of charged fractions, ash resistivity of submicrometer particles in coal combustion exhaust generated from different coal seams and its connection with electrostatic precipitation were examined. Mineralogy, morphology and chemical compositions of particles in pressurized coal combustion exhaust were also characterized for a holistic understanding.

Another popular option for CCS, post-combustion carbon capture, is typically realized by applying amine-based CO_2 scrubber based on the principle of CO_2-amine reversible reactions. However, recent studies have shown that compared with amine evaporation and degradation, aerosol formation and discharge in the scrubbers cause significant amine loss during normal operation, which could produce undesirable cost for amine makeup. Particularly, submicrometer particles are reported to be the major carriers for aerosolized amine due to condensation and coagulation. In this dissertation work, characterization of submicrometer particles in flue gas upstream CO_2 scrubbers have been done in two industrial systems. One field study on change of submicrometer particles number concentration size distributions upstream a proposed amine-based CO_2 scrubber along with various operating scenarios was performed at a utility-scale power plant. Soot blow of boilers, bypass of flue gas desulfurization (FGD) scrubber and derating of reheat burner affected total particle number concentration and size distribution in different ways. Another conducted field study indicated that impacts of steam injection on submicrometer particles are size dependent, and an ESP upstream the scrubber can be considered as a potential measure to control submicrometer particle concentration at the inlet of the scrubber.

1.3 References

Bai, M., Wang, S., Chen, Z., Leng, H., & Mao, S. (2010). The Effects of Submicrometer Dust Charging and Coagulation on ESP Efficiency by Using Alternating Electric Field. *Ieee Transactions on Plasma Science, 38*(2), 127-132. doi:10.1109/tps.2009.2037888

Bhown, A. S., & Freeman, B. C. (2011). Analysis and status of post-combustion carbon dioxide capture technologies. *Environmental Science & Technology, 45*(20), 8624-8632.

Brown, R. F., & Walker, A. B. (1971). FEASIBILITY DEMONSTRATION OF ELECTROSTATIC PRECIPITATION AT 1700 DEGREES F. *Journal of the Air Pollution Control Association, 21*(10), 617-&.

Bush, J. R., Feldman, P. L., & Robinson, M. (1979). HIGH-TEMPERATURE, HIGH-PRESSURE ELECTROSTATIC PRECIPITATION. *Journal of the Air Pollution Control Association, 29*(4), 365-371.

Chan, C.-C., Chuang, K.-J., Shiao, G.-M., & Lin, L.-Y. (2004). Personal exposure to submicrometer particles and heart rate variability in human subjects. *Environmental Health Perspectives*, 1063-1067.

Chang, M.-C. O., Chow, J. C., Watson, J. G., Hopke, P. K., Yi, S.-M., & England, G. C. (2004). Measurement of ultrafine particle size distributions from coal-, oil-, and gas-fired stationary combustion sources. *Journal of the Air & Waste Management Association, 54*(12), 1494-1505.

Che, H., Zhang, X., Li, Y., Zhou, Z., Qu, J. J., & Hao, X. (2009). Haze trends over the capital cities of 31 provinces in China, 1981-2005. *Theoretical and Applied Climatology, 97*(3-4), 235-242. doi:10.1007/s00704-008-0059-8

Delfino, R. J., Sioutas, C., & Malik, S. (2005). Potential role of ultrafine particles in associations between airborne particle mass and cardiovascular health. *Environmental Health Perspectives*, 934-946.

Dutcher, B., Fan, M., & Russell, A. G. (2015). Amine-Based $CO2$ Capture Technology Development from the Beginning of 2013 · A Review. *ACS applied materials & interfaces, 7*(4), 2137-2148.

Fuchs, N. (1947). The charges on the particles of aerocolloids. *Izv. Akad. Nauk. SSSR, Ser. Geogr. Geofiz, 11*, 341-348.

Fulk, S. M., & Rochelle, G. T. (2013). Modeling aerosols in amine-based CO_2 capture. *Energy Procedia, 37*, 1706-1719.

Gopan, A., Kumfer, B. M., & Axelbaum, R. L. (2015). Effect of operating pressure and fuel moisture on net plant efficiency of a staged, pressurized oxy-combustion power plant. *International Journal of Greenhouse Gas Control, 39*, 390-396. doi:10.1016/j.ijggc.2015.05.014

Gouedard, C., Picq, D., Launay, F., & Carrette, P.-L. (2012). Amine degradation in CO_2 capture. I. A review. *International Journal of Greenhouse Gas Control, 10*, 244-270.

Hinds, W. C. (1999). *Aerosol technology: properties, behavior, and measurement of airborne particles*: John Wiley & Sons.

Huang, R.-J., Zhang, Y., Bozzetti, C., Ho, K.-F., Cao, J.-J., Han, Y., . . . Prevot, A. S. H. (2014). High secondary aerosol contribution to particulate pollution during haze events in China. *Nature, 514*(7521), 218-222. doi:10.1038/nature13774

Huang, S.-H., & Chen, C.-C. (2002). Ultrafine aerosol penetration through electrostatic precipitators. *Environmental Science & Technology, 36*(21), 4625-4632.

IEA. (2015). CO2 emissions from fuel combustion Highlights (2015 edition). *International Energy Agency, France*.

IPCC. (2014). Mitigation of Climate Change: Contribution of Working Group III to the Fifth Assessment Report of the Intergovernmental Panel on Climate Change. *Cambridge University Press, Cambridge, UK and New York, NY*.

Irfan, M. F., Usman, M. R., & Kusakabe, K. (2011). Coal gasification in CO 2 atmosphere and its kinetics since 1948: a brief review. *Energy, 36*(1), 12-40.

Katzer, J., Ansolabehere, S., Beer, J., Deutch, J., Ellerman, A., Friedmann, S., . . . McRae, G. (2007). The future of coal: options for a carbon-constrained world. *Massachusetts Institute of Technology*, 39.

Khakharia, P., Brachert, L., Mertens, J., Anderlohr, C., Huizinga, A., Fernandez, E. S., . . . Goetheer, E. (2015). Understanding aerosol based emissions in a Post Combustion CO 2 Capture process: Parameter testing and mechanisms. *International Journal of Greenhouse Gas Control, 34*, 63-74.

Khakharia, P., Brachert, L., Mertens, J., Huizinga, A., Schallert, B., Schaber, K., . . . Goetheer, E. (2013). Investigation of aerosol based emission of MEA due to sulphuric acid aerosol and soot in a Post Combustion CO 2 Capture process. *International Journal of Greenhouse Gas Control, 19*, 138-144.

Li, Y., Suriyawong, A., Daukoru, M., Zhuang, Y., & Biswas, P. (2009). Measurement and capture of fine and ultrafine particles from a pilot-scale pulverized coal combustor with an electrostatic precipitator. *Journal of the Air & Waste Management Association, 59*(5), 553.

Lin, G.-Y., Chen, T.-M., & Tsai, C.-J. (2012). A Modified Deutsch-Anderson Equation for Predicting the Nanoparticle Collection Efficiency of Electrostatic Precipitators. *Aerosol and Air Quality Research, 12*(5), 697-706.

McCain, J. D., Gooch, J. P., & Smith, W. B. (1975). Results of field measurements of industrial particulate sources and electrostatic precipitator performance. *Journal of the Air Pollution Control Association, 25*(2), 117-121.

McDonald, D., DeVault, D., & Varagani, R. (2007). Oxy-combustion in pulverized coal power plants for carbon dioxide concentration. *Electric Power*, 1-3.

McElroy, M., Carr, R., Ensor, D., & Markowski, G. (1982). Size distribution of fine particles from coal combustion. *Science, 215*(4528), 13-19.

Meij, R., & te Winkel, B. (2004). The emissions and environmental impact of PM10 and trace elements from a modern coal-fired power plant equipped with ESP and wet FGD. *Fuel Processing Technology, 85*(6–7), 641-656. doi:http://dx.doi.org/10.1016/j.fuproc.2003.11.012

Merkel, T. C., Lin, H., Wei, X., & Baker, R. (2010). Power plant post-combustion carbon dioxide capture: an opportunity for membranes. *Journal of membrane science, 359*(1), 126-139.

Mertens, J., Brachert, L., Desagher, D., Thielens, M., Khakharia, P., Goetheer, E., & Schaber, K. (2014). ELPI+ measurements of aerosol growth in an amine absorption column. *International Journal of Greenhouse Gas Control, 23*, 44-50.

Mishra, D., Goyal, P., & Upadhyay, A. (2015). Artificial intelligence based approach to forecast PM2.5 during haze episodes: A case study of Delhi, India. *Atmospheric Environment, 102*, 239-248. doi:10.1016/j.atmosenv.2014.11.050

NETL. (2013). Advanced Combustion Systems Technology Program Plan. *US Department of Energy*.

Nguyen, T., Hilliard, M., & Rochelle, G. T. (2010). Amine volatility in CO2 capture. *International Journal of Greenhouse Gas Control, 4*(5), 707-715. doi:http://dx.doi.org/10.1016/j.ijggc.2010.06.003

Pachauri, T., Singla, V., Satsangi, A., Lakhani, A., & Kumari, K. M. (2013). Characterization of major pollution events (dust, haze, and two festival events) at Agra, India. *Environmental Science and Pollution Research, 20*(8), 5737-5752. doi:10.1007/s11356-013-1584-2

Pauthenier, M., & Moreau-Hanot, M. (1932). Charging of spherical particles in an ionizing field. *J. Phys. Radium, 3*(7), 590-613.

Rinard, G., Rugg, D. E., & Yamamoto, T. (1987). HIGH-TEMPERATURE HIGH-PRESSURE ELECTROSTATIC PRECIPITATOR ELECTRICAL CHARACTERIZATION AND COLLECTION EFFICIENCY. *Ieee Transactions on Industry Applications, 23*(1), 114-119. doi:10.1109/tia.1987.4504875

Rochelle, G. T. (2009). Amine scrubbing for CO2 capture. *Science, 325*(5948), 1652-1654.

Suriyawong, A., Hogan, C. J., Jr., Jiang, J., & Biswas, P. (2008). Charged fraction and electrostatic collection of ultrafine and submicrometer particles formed during O(2)-CO(2) coal combustion. *Fuel, 87*(6), 673-682. doi:10.1016/j.fuel.2007.07.024

Villot, A., Gonthier, Y., Gonze, E., Bernis, A., Ravel, S., Grateau, M., & Guillaudeau, J. (2012). Separation of particles from syngas at high-temperatures with an electrostatic precipitator. *Separation and Purification Technology, 92*, 181-190. doi:10.1016/j.seppur.2011.04.028

Ylätalo, S. I., & Hautanen, J. (1998). Electrostatic precipitator penetration function for pulverized coal combustion. *Aerosol Science and Technology, 29*(1), 17-30.

Yoo, K. H., Lee, J. S., & Oh, M. D. (1997). Charging and collection of submicron particles in two-stage parallel-plate electrostatic precipitators. *Aerosol Science and Technology, 27*(3), 308-323.

Zhuang, Y., & Biswas, P. (2001). Submicrometer particle formation and control in a bench-scale pulverized coal combustor. *Energy & Fuels, 15*(3), 510-516. doi:10.1021/ef000080s

Zhuang, Y., Kim, Y. J., Lee, T. G., & Biswas, P. (2000). Experimental and theoretical studies of ultra-fine particle behavior in electrostatic precipitators. *Journal of Electrostatics, 48*(3-4), 245-260. doi:10.1016/s0304-3886(99)00072-8

Chapter 2: Evaluation of submicrometer particle capture performance in a lab scale pressurized electrostatic precipitator

Abstract

This study investigated the influence of gas pressure on the submicrometer particle capture performance of an electrostatic precipitator (ESP). Current-voltage characteristics and particle capture performance of the ESP were studied in air and in simulated flue gas (SFG) under 1, 2, and 3 atm. Using negative corona and air as the feed gas, the penetration of most particles of 40–400 nm in diameter decreased from 8×10^{-4}–2×10^{-2} to 2×10^{-4}–1×10^{-2} as pressure increased from 1 atm to 3 atm at constant current; and increased from 3×10^{-5}–1×10^{-3} to 2×10^{-4}–1×10^{-2} as pressure was elevated when the voltage was held roughly constant. Similar type of disparity under different pressures were also observed for positive corona and for SFG. Experiments set up to capture fly ash in the ESP showed that with constant current, higher pressure resulted in a higher initial charge fraction of the particles from the furnace, which could facilitate the penetration of fly ash particles. A semi-empirical model was developed based on the Deutsch-Anderson (D-A) equation and experimental data under 1, 2 and 3 atm to calculate the particle penetrations under high pressure. The total charge number on a particle (n') is calculated by incorporating the effects of current (I) and pressure (P) on relative weights of the diffusion charging number (n_{diff}) and field charging number (n_{field}), i.e., $n' = B_1(I,P)n_{diff} + B_2(I,P)n_{field}$, where $B_1(I,P)$ and $B_2(I,P)$ are both empirical coefficients dependent on current and pressure. Experimental penetrations under 1.5 and 2.5 atm validated this model over the particle diameter range in 100–400 nm.

2.1 Introduction

For providing reliable and low-cost energy, advanced technologies, such as gasification (Minchener, 2005), pressurized fluidized bed combustion (Jensen et al., 1995), and pressurized oxy-combustion (Gopan et al., 2014) are considered promising alternatives to conventional coal-combustion. The application prospects of these systems are not determined just by the efficiency

of energy generation, but also by the feasibility and performance of additional pollution control measures due to growing environmental concerns. Particle control technologies have been the focus of academic studies and industrial applications especially in developing countries such as China (Che et al., 2009; R.-J. Huang et al., 2014) and India (Mishra et al., 2015; Pachauri et al., 2013) over the past few years due to growing concerns regarding haze as a major hazard to their atmospheric environment.

Electrostatic precipitators (ESPs) are widely utilized in controlling particles from various emission sources such as conventional coal-fired power plants (Meij et al., 2004; Yokoyama et al., 2000) because of their high capture efficiency, low cost of operation and ability to work in extreme environments (high temperature and high pressure) (Brown et al., 1971; Bush et al., 1979; Rinard et al., 1987; Villot et al., 2012). These qualities make them promising candidates for particle control equipment in gasification and pressurized combustion systems. It has been also reported that corona discharge, which is the main charging mechanism of ESPs, can be obtained at a pressure of up to 1.6 MPa (Bush et al., 1979) and a temperature of up to 927 °C (1700 °F) (Brown et al., 1971). However, the capture efficiency of particle in an ESP operating under high pressure condition is not well studied. In particular, no size-dependent capture efficiency data has been reported under varying pressure conditions.

Particles in the submicrometer range (particle sizes smaller than 1 μm) require special attention due to their more adverse effects on human health (Biswas et al., 2005). Extensive studies have been done on the capture of submicrometer particles with ESPs under atmospheric pressure (Bai et al., 2010; Suriyawong et al., 2008b; Zhuang et al., 2001). For example, fundamental studies have used bench-scale ESPs to study the capture efficiency of synthetic particles (S.-H. Huang et al., 2002; Jing et al., 2013; Yoo et al., 1997). Furthermore, research has been carried out on ESPs with

particles and exhaust gases from real combustion systems (McCain et al., 1975; Ylätalo et al., 1998). Nonetheless, to the best of our knowledge, the influence of pressure on the submicrometer particle capture efficiency for ESPs has not been investigated yet.

Due to its simplicity and relative accuracy, the Deutsch-Anderson (D-A) equation is extensively employed in estimating the capture efficiency of ESPs and facilitating their design (T.-M. Chen et al., 2014). However, because of certain simplifying assumptions, such as rapid mixing in the transverse direction and particles attaining the saturation charge immediately after entering the ESP, the D-A equation is limited in providing accurate particle capture efficiency estimates for certain cases. For example, it was reported that capture efficiencies predicted by the D-A equation for fine particles with diameters < 2 nm are much lower than the measured efficiencies (Riehle et al., 1993). In order to improve the accuracy, many modifications to the D-A equation have been proposed (Lin et al., 2012; J.-H. Park et al., 2002; Robinson, 1967b). Up to now, there has apparently not been any study on whether the D-A equation can be applied under elevated pressure conditions (e.g., in a pressurized ESP).

In this study, the fundamental aspects of a pressurized ESP are explored by examining the current-voltage (I-V) characteristics, and studying the performance of the pressurized ESP by measuring its capture efficiency of submicrometer particles including homogeneous NaCl particles and fly ash particles at the outlet of a pressurized drop-tube furnace. To better predict the capture efficiencies of the submicrometer particles in the ESP under high pressures, a complete calculation procedure based on the original D-A equation and experimental data fitting was established and validated.

2.2 Experimental section

2.2.1 Experimental system

The ESP used in this study was a bench-scale DC corona-based wire-cylinder ESP, which mainly

consisted of an outer PVC case, a central discharge electrode (stainless steel wire, 0.323 mm in

diameter), and a cylindrical collecting electrode (stainless steel tube, 25.4 cm in length and 4.8 cm

in diameter) enclosed by the outer case. The discharge electrode was sheathed using insulating

materials at the top and bottom. A nozzle was installed at the outlet of the ESP to reduce the

pressure from high level in the ESP to ambient pressure so that the particle size distribution

measuring instrument can be normally used downstream the pressurized ESP. The nozzle used

was actually a ball type valve, which has large-diameter, straight-through and open-position vent

so that particle losses were minimized (Komhyr, 1983; Williams et al., 2006). The ESP

configuration is shown in Figure A1.1. A Bertan power supply (Model 230-20R, Spellman,

Hauppauge, New York, USA) provided the high voltage for the ESP. The experimental system is

shown in Figure 2.1. Two types of systems generated test particles. NaCl particles were generated

by an atomizer (Model 3076, TSI Inc., Shoreview, Minnesota, USA). A Kr-85 radioactive source

(Model 3077, TSI Inc., Shoreview, Minnesota, USA) neutralized the charges on the NaCl particles

from the atomizer, and a silica gel diffusion dryer removed water vapor from the particles. It should

be noted that the particles downstream the neutralizer consist primarily of particles carrying zero

charge or very low number of charges, which can be regarded negligible compared with charge

number appeared in this study. Fly ash particles were generated in a pressurized drop-tube furnace.

The configuration and operation parameters of the furnace have been described in previous papers

(Suriyawong et al., 2006; X. Wang et al., 2015; Xiaofei Wang et al., 2013; X. Wang et al., 2013).

PRB (Powder River Basin) coal was fed at a rate of 1.5 g/hr. The drop-tube furnace was operated

at up to 3 atm in this study. Additional air, N_2, O_2, and CO_2 flows were added to the system to adjust the gas composition and the total flow rate through the ESP. The flow rates through the ESP associated with the atomizer and the furnace were kept at 15 LPM (flow velocity: 0.14 m/s) and 25 LPM (flow velocity: 0.23 m/s), respectively. The current through the ESP was measured with a microamp meter (Model 17424, Simpson Electric, Lac du Flambeau, Wisconsin, USA). A scanning mobility particle sizer (SMPS, Model 3080, TSI Inc., Shoreview, Minnesota, USA) measured the particle size distribution.
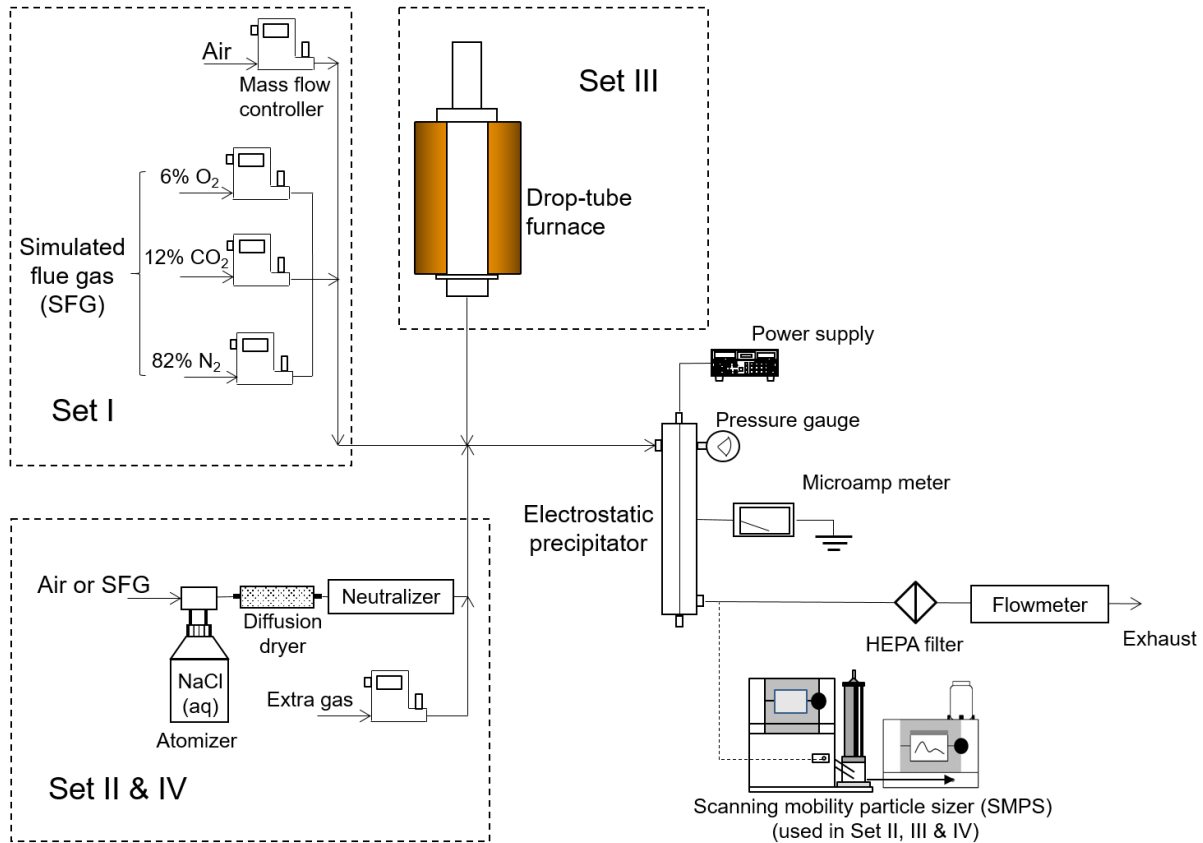
Figure 2.1 Schematic of the experimental setup.

2.2.2 Experimental plan

In this study, four sets of data were obtained. First, the operation of the pressurized ESP, i.e., its current-voltage characteristics (Set I), were established. Next, the ESP's particle capture efficiency using NaCl particles (Set II) was determined. Then, the capture of fly ash particles from a drop-

22

tube furnace in the pressurized ESP (Set III) was examined. The furnace was operated at the same

gas pressure as the ESP for each run. Finally, using the experimental data (negative ESP with air

feed) from Set II, a semi-empirical calculation procedure of capture efficiency was developed and

validated by comparing experimental capture efficiency data for NaCl particles under 1.5 and 2.5

atm (Set IV). Table 2.1 summarizes the experimental objectives and parameters.

Table 2.1 Summary of performed studies.

Set	Objective	Particles	Gas compositions	ESP operation	Gas pressure	Flow rate	Measurements
I	To investigate the I-V characteristics of the ESP	N/A	Air; simulated flue gas (6% O_2, 12% CO_2, 82% N_2)	−20 kV to +20 kV	1 atm, 2 atm, 3 atm	15 LPM	ESP current
II	To investigate the capture efficiency of NaCl particles	NaCl particles	Air; simulated flue gas (6% O_2, 12% CO_2, 82% N_2)	Current controlled (±20 µA); voltage controlled (+12.8 ~ +19.8 kV; −12.3 ~ −16.9 kV)	1 atm, 2 atm, 3 atm	15 LPM	Particle size distributions downstream of the ESP when the ESP is off and on
III	To investigate the capture efficiency of fly ash particles	Fly ash particles from drop-tube furnace	Exhaust gas from the drop-tube furnace system	−20 µA	1 atm, 2 atm, 3 atm	25 LPM	Particle size distributions downstream of the ESP when the ESP is off and on
IV	To develop a semi-empirical model	NaCl particles	Air	−20 µA	1.5 atm, 2.5 atm	15 LPM	Particle size distributions downstream of the ESP when the ESP is off and on

2.3   Results and discussion

2.3.1 Current-voltage characteristics of the pressurized ESP

The current-voltage (I-V) characteristics provide information about the corona working range, while at the same time, the current indicates the ion concentration in the ESP. Figure 2.2(a) shows the I-V characteristics of the studied ESP under three pressures (1 atm, 2 atm, and 3 atm) for air and simulated flue gas (SFG for short) composed of 6% O_2, 12% CO_2 and 82% N_2 (by mass) (Zevenhoven et al., 2001). To focus on the effect of pressure only in this study, the simulated flue gas composition was controlled at the same level with the feeding gas in normal industrial ESPs. It should be noted that pressurized oxy-combustion flue gas contains more CO_2 with an ionization potential lower than N_2 (Condon et al., 1967), which could result in lower corona onset voltage. For both positive and negative polarities, as the pressure increases, the corona onset voltage (at which point the corona began to appear) increases. In addition, at the same voltage, the ESP current is lower at higher pressure. To form the corona discharge, a certain number of ions and electrons is needed. Most of the ions and electrons are generated by impaction between gas molecules and high energy electrons. To initiate ionization, an electron must gain sufficient kinetic energy to knock a secondary electron out of a gas molecule. At higher pressure, the mean free path of the gas inside the ESP decreases. Thus, there is a higher probability that the electron will hit a gas molecule before being accelerated to achieve the critical kinetic energy necessary to ionize the gas. The ionization process is thus hindered (Robinson, 1971).
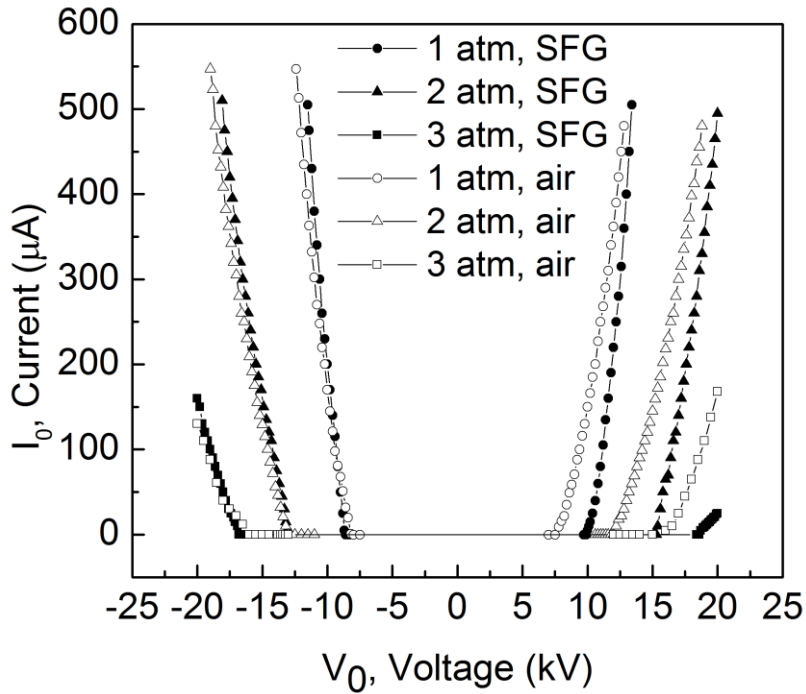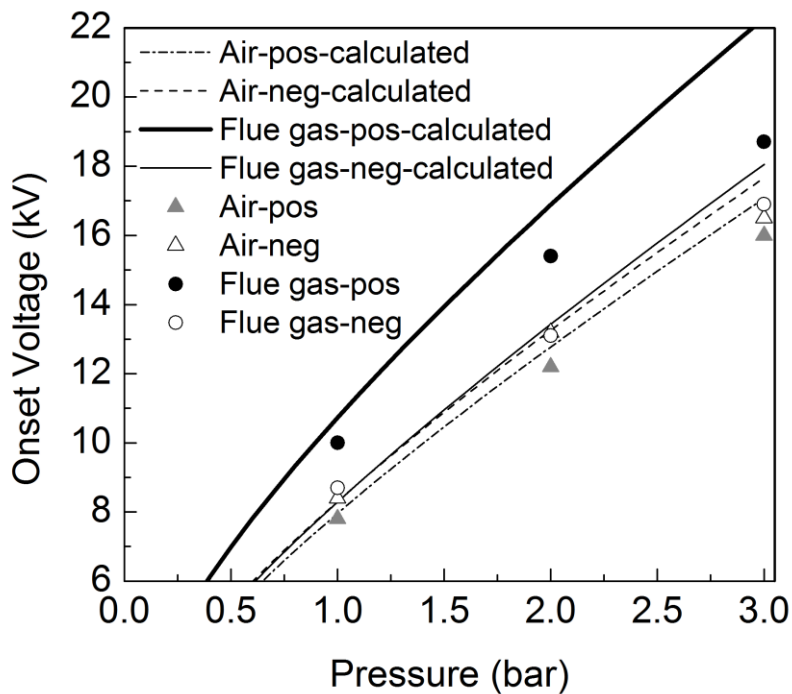
Figure 2.2 The influences of gas pressure on (a) I-V characteristics and (b) corona onset voltage with different gas compositions (air and SFG). (a) I-V curves of the ESP under three pressure conditions (1 atm, 2 atm, and 3 atm) with air and SFG as the feed gas, respectively; (b) The relationship between the corona onset voltage and gas pressure (experimental results

for air and SFG, estimation for air case based on Eq. (2), and fitting curve for SFG case; "pos": short for "positive"; "neg": short for "negative").

Figure 2.2(a) also shows that for the positive ESP polarity, the onset voltages of the ESP fed with SFG were higher than the corresponding voltages for the air feed cases. A similar phenomenon was observed by Suriyawong et al. (Suriyawong et al., 2008a). This result can be attributed to the fact that N_2 and CO_2 have higher ionization potentials than O_2 (15.6 eV, 13.8 eV, and 12.1 eV, respectively) (Condon et al., 1967). Second, CO_2 has a higher dielectric constant than O_2 and N_2 (1.6, 1.0, and 1.0, respectively), and thus a reduced effective electric field results (Lide, 2000). Furthermore, because CO_2 has negative electron affinity (Knapp et al., 1986), electron impact reactions with CO_2 usually acts as electron traps by producing oxygen radicals (O), resulting in reduced electron ionization and suppression of electric discharge (Smyth et al., 1930). Simulated flue gas (SFG) has more CO_2, slightly more N_2, and less O_2 than air; thus, the ionization is less extensive compared to air or oxygen. However, for negative ESP polarity, the I-V characteristic curves for the corresponding air and SFG case almost overlap with each other. For a negative corona to be effective, it is necessary that the gas molecules can absorb free electrons to form negative ions. The electron-absorbing tendency is determined by the electron affinity. The electron affinity of N_2, CO_2 and O_2 are -1.903 eV (Zhan et al., 2003), -1.60 eV (Linstrom et al., 2001) and -0.40 eV (Linstrom et al., 2001). It should be noted that the simulated flue gas has more N_2 and CO_2 while the air has more O_2. Therefore, there are two opposing effects on negative corona by switching the air to the simulated flue gas: (1) the higher ionization potentials of N_2 and CO_2 suppress the initial electron avalanche; (2) the higher electron-absorbing tendency of N_2 and CO_2 indicated by their electron affinities result in easier formation of negative ions by electron attachment on gas molecules. These two effects result in no significant difference between the corona onset voltages of the air and simulated flue gas. However, the positive corona is more

26

dependent on the electron avalanche, which is mainly governed by the ionization potential. The higher ionization potentials of N_2 and CO_2 leads to higher corona onset voltages of the simulated flue gas. Moreover, it has been demonstrated that negative corona discharge need to be sustained by continuous collision between electrons and neutral gas molecules and generation of "secondary electron-positive ion" pairs (J. Chen et al., 2003). On the one hand, the short-wavelength photons emitted in the corona discharge are more energetic than positive ions (mean kinetic energy: 0.01–0.1 eV) in terms of knocking out electrons. On the other hand, the stainless steel discharge electrode has a lower work function (4.4 eV for stainless steel) than the ionization energy of any gas (12.1 eV for O_2, 15.6 eV for N_2 and 13.8 eV for CO_2) used in this study. Therefore, the primary source of the secondary electrons in negative corona discharge is direct photoionization of the discharge electrode, depending rather on the material and the condition of the surface of the electrode than on the gas composition.

Because the corona onset voltage and field strength are parameters of critical importance to the ESP performance (Abdelsalam et al., 1993), the relationship between the onset field strength and the gas pressure was evaluated by using an equation (Robinson, 1967a) derived from Peek's semi-empirical equation (Peek, 1920):

$$\frac{E_C}{\delta'} = A_g + \frac{B_g}{\left(r_0 \delta'\right)^{\frac{1}{2}}} . \tag{2.1a}$$

And the relationship between the corona onset voltage and corona onset field strength at the wire surface ($r = r_0$) in a wire-cylindrical space is:

$$E_C = \frac{V_C}{r_0 \ln(r_1/r_0)}. \tag{2.1b}$$

27

By combining equations (2.1a) and (2.1b), the corona onset voltage as a function of gas pressure ($P = \delta' P_0$) is:

$$V_C = r_0 \ln\left(\frac{r_1}{r_0}\right) \cdot \left(A_g + \frac{B_g}{(r_0 \delta')^{\frac{1}{2}}}\right) \frac{P}{P_0}.$$

(2.2)

The constant A_g mainly depends on the gas type, and B_g depends on the ESP polarity. Figure 2.2(b) shows the estimated relationship between onset voltages and pressures as well as our experimental data. In the case of air, recommended values derived from the cumulative data of several investigators were used, namely 32.2×10^5 V/m for A_g and 8.46×10^4 V/m$^{1/2}$ for B_g with negative polarity (Robinson, 1967a). With these values, the estimated values match the experimental data well. Although constant values have been reported for different types of gases (Thornton, 1939), data on gas mixtures, such as the SFG used in this study, which is a mixture of N_2, O_2, and CO_2, are not reported in the literature. Thus, a weighted average method based on the mass percentage was used to estimate A_g for the SFG. A_g was estimated to be 36.0×10^5 V/m. B_g was still 8.46×10^4 V/m$^{1/2}$ for negative polarity. By fitting the estimated relationship curve with the experiment data, B_g was determined to be 10.00×10^4 V/m$^{1/2}$. With the above values, the calculated relationship matched the experimental data reasonably well. The recommended B_g value reported here can be used in estimation of the onset voltage for higher gas pressure cases and pressurized ESP design.

To better explain the experimental I-V curves and facilitate the calculation of particle penetration of the ESP, a mathematical derivation with a numerical fitting approach was used. Derived from the Poisson's equation for electric field distribution, the relationship between corona voltage and current for wire-cylinder ESPs is given (L. K. Wang et al., 2004) by

28

$$V_0 = V_C + E_C r_0 \left[(1+\phi)^{\frac{1}{2}} - 1 - \ln\left(\frac{1+(1+\phi)^{\frac{1}{2}}}{2} \right) \right], \tag{2.3}$$

Here, E_c is given by Eq. (2.1b), and ϕ is a function of current (I):

$$\phi = \left(\frac{r_1}{E_C r_0} \right)^2 \frac{I}{2\pi K_0 Z_i h}. \tag{2.4}$$

It can be implied from Eqs. (2.3) and (2.4) that when the current is zero, the corona voltage is equal to the corona onset voltage, and the corona voltage increases monotonically with the current after corona inception. As shown in Figure A1.2, the calculated corona currents based on Eqs. (2.3) and (2.4) are lower than, similar to, and higher than the experimental values with the same voltage under 1 atm, 2 atm, and 3 atm, respectively. Higher currents at 3 atm can be explained by the fact that the theoretical model above does not consider the inhibiting effect of high pressure on the ionization inside the ESP. The reason for lower calculated currents under 1 atm is that in Eq. (2.3), the space charge considered is an ionic space charge, with no consideration given to the presence of charged particles in the interelectrode space (L. K. Wang et al., 2004). In reality, such particles do contribute to the total space charge. Ignoring the contribution of the charged particles could explain the lower predicted current.

Considering the deviations between the experimental I-V curves and the calculated values based on Eq. (2.3) under different pressures, the equation was modified by adding pressure factors in the form of a_1^{P/P_0-a_2}. Numerical iterations over wide ranges of a_1 and a_2 were computed by MATLAB until reaching the minimum summation of squared deviations ($\sigma' = (N - 1)\sigma^2$) between the experimental results and calculated values. As a result, the modified equations describing the I-V relationships for negative and positive polarity voltages are

$$V_0 = \left(V_C + E_C r_0 \left[(1+\phi)^{\frac{1}{2}} - 1 - \ln\left(\frac{1+(1+\phi)^{\frac{1}{2}}}{2} \right) \right] \right) \cdot 1.135^{P/P_0 - 2.312} \text{, and} \tag{2.5}$$

$$V_0 = \left(V_C + E_C r_0 \left[(1+\phi)^{\frac{1}{2}} - 1 - \ln\left(\frac{1+(1+\phi)^{\frac{1}{2}}}{2} \right) \right] \right) \cdot 1.072^{P/P_0 - 2.025} . \tag{2.6}$$

For negative polarity, σ' decreases by 82% from 143.7 kV^2 after the modification, and for the positive voltage condition, σ' is reduced by 64% from 46.1 kV^2 to 16.8 kV^2. Figure 2.3 graphically compares the experimental and computed data based on Eqs. (2.5) and (2.6). Particularly, when the pressure is at 1 atm and the current is higher than 200 µA, the experimental values of voltages are slightly lower than the calculated voltages with the same current. Nonetheless, the other I-V curves under the three pressure conditions are well predicted by the calculations, which implies that the two semi-empirical equations for I-V characteristics are valid for deriving a capture efficiency equation for pressurized ESPs.
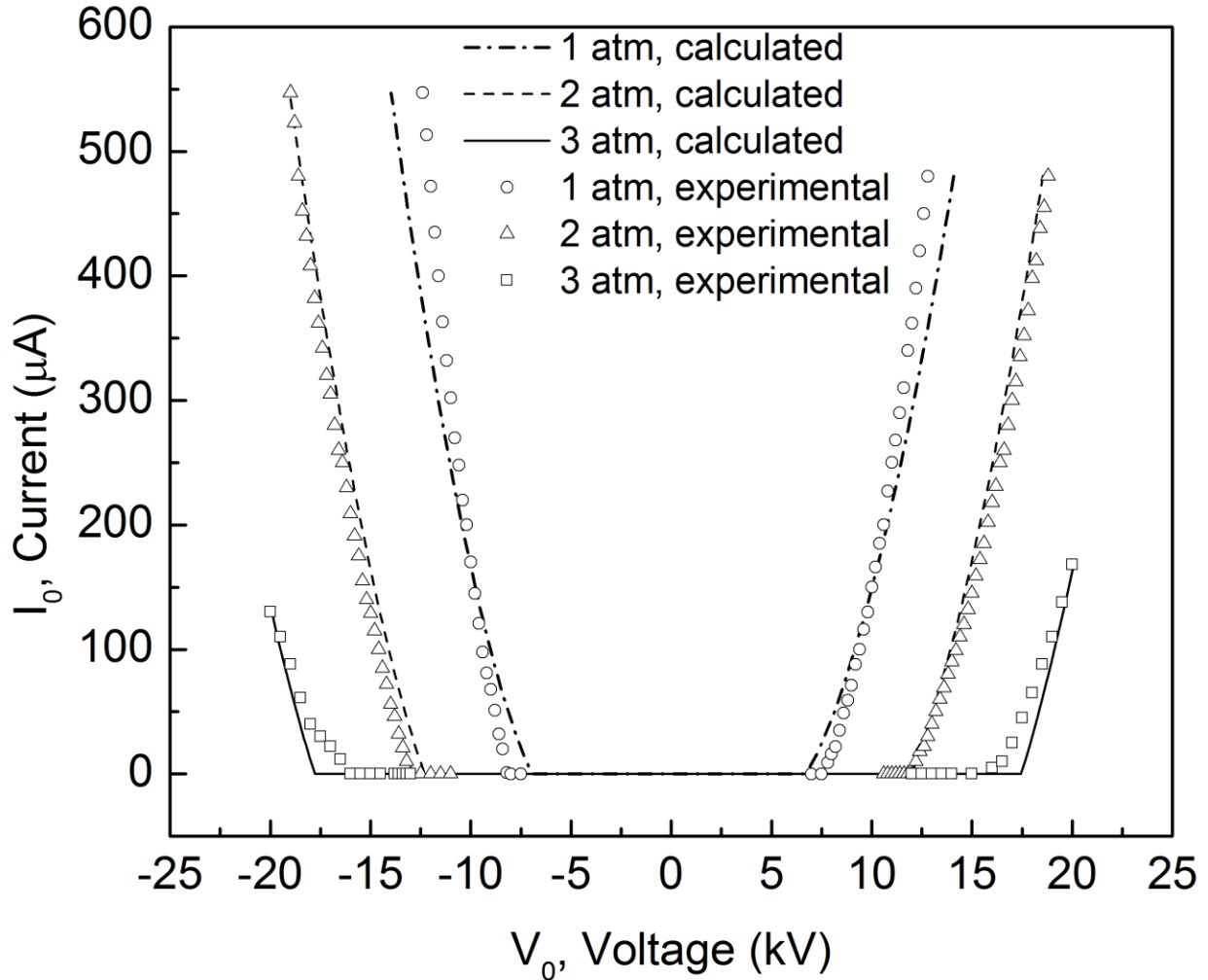
Figure 2.3 Experimental and calculated I-V curves by Eqs. (5) and (6) under different pressures.

2.3.2 Capture of NaCl particles using air as the feed gas

NaCl particles were used to evaluate the capture efficiencies of the ESP. The particles passed through a Kr-85 radioactive radiation source, which gave them an assumed Boltzmann charge distribution (Keefe et al., 1959). The size distributions of NaCl particles atomized under different gas pressures are shown in Figure A1.3. Here the particle capture is quantified using particle penetration ($p = 1 - \eta$, where η is capture efficiency), which is calculated using the following equation:

$$p = \frac{N_{on}}{N_{off}} \tag{2.7}$$

where N_{on} and N_{off} are particle number concentration downstream of the ESP when ESP is on and off, respectively.

Voltage is one of the most important ESP operation parameters. Thus, ESP performances under different gas pressures were first compared for similar ESP voltages (±16.7 kV for the 2-atm and 3-atm cases; ±12.7 kV for the 1-atm case, because the maximum current output was reached). Figures 2.4(a) and 2.4(b) show the particle penetrations through the ESP under various pressures at positive and negative potentials. High collection efficiencies over 99% for most of the particles ranging 40 nm to 400 nm in diameter was observed under all the conditions. This outcome can be attributed to low flow velocity (Lin et al., 2010) and high onset voltage required for inception of corona discharge under high pressure. More detailed discussion can be found in supplemental materials.

Figure 2.4(a) and (b) also show that the ESP behaviors under positive and negative polarities were similar: As the particle diameter increased, the particle penetration increased due to the lower electrical mobility of larger particles (Jing et al., 2013). There are similar shapes of the size dependent efficiency curve found in other studies. The experimental results in the study of Huang et al. (S.-H. Huang et al., 2002) indicate that ultrafine aerosol penetration through the single-stage ESP increases rapidly as aerosol size increases from 20 nm to 300 nm under 26.4 kV and 80 µA. Suriyawong et al. (Suriyawong et al., 2008a) found that particle penetration through a cylindrical-wire ESP also increases as particle diameter increases from 40 nm to 200 nm for different gas compositions. Interestingly, the penetration for small particles around 40–50 nm seem so low that the partial charging effects on the particle penetration might be insignificant. It has been reported

(S.-H. Huang et al., 2002) that the partial charging effects on small particles tend not to be obvious when the applied voltage is high. This is probably due to the following reasons: 1) The particle space charge density is significantly high (S. J. Park et al., 1998) due to high applied voltage, which could enhance the particle charging, and thus the collection efficiency. 2) High voltage may intensify the ionic wind (Liang et al., 1994), which could subsequently compensate for efficiency loss due to partial charging.

It can also be observed for both polarities in Figure 2.4(a) and (b) that the penetrations of most particles ranging from 40 nm to 400 nm in diameter increased approximately from $3 \times 10^{-5} - 1 \times 10^{-3}$ to $2 \times 10^{-4} - 1 \times 10^{-2}$ with higher pressure. The reason for this result is that for similar ESP voltages, the ion concentrations in the ESP decreased with higher gas pressure, which is indicated by the ESP current measurements; The lower ion concentration thus resulted in weaker particle charging (Hinds, 1999), which eventually led to higher particle penetration.
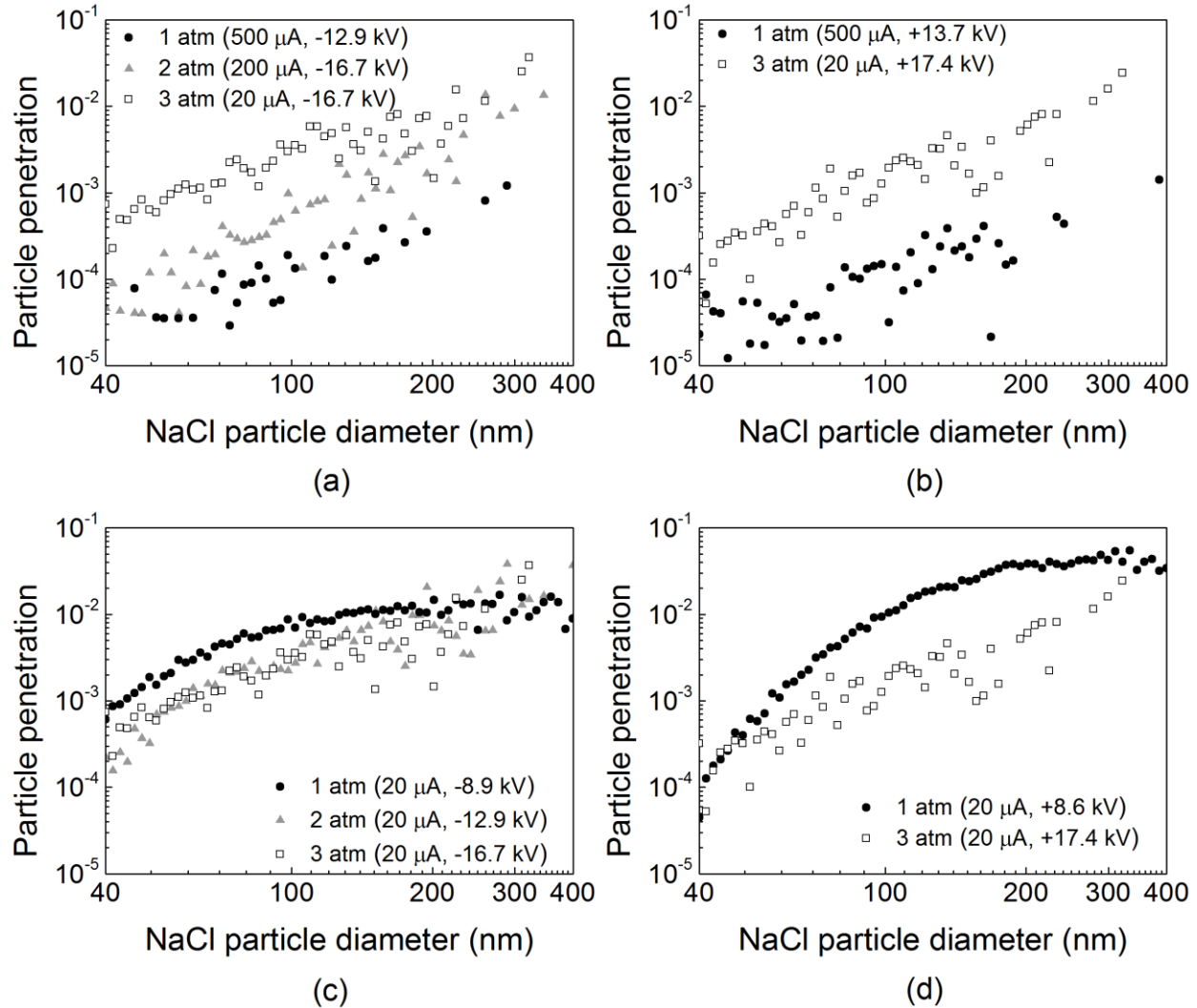
Figure 2.4 NaCl particle penetrations through the ESP using air as feed gas under different gas pressures: (a) negative ESP, voltage controlled; (b) positive ESP, voltage controlled; (c) negative ESP, current controlled; (d) positive ESP, current controlled.

To further investigate the influence of factors other than the ion concentration on the particle capture, ESP performances under different gas pressures were compared under the same current (20 µA) to maintain the same ion concentration in the ESP. Figures 2.4(c) and 2.4(d) show the particle penetrations through the ESP at three pressures (1 atm, 2 atm, and 3 atm): Similar to the results in Figure 2.4(a) and (b), for both positive and negative polarities, penetration increased with particle diameter. However, in terms of the effect of gas pressure, the penetrations of most particles ranging from 40 nm to 400 nm in diameter decreased from 8×10^{-4}–2×10^{-2} to 2×10^{-4}–1×10^{-2} as

pressure increased from 1 atm to 3 atm for negative corona; and decreased from 1×10^{-4}–5×10^{-2} to 6×10^{-5}–2×10^{-2} as pressure increased from 1 atm to 3 atm for positive corona. In this set of experiments, particle capture was mainly determined by the transport of the charged particles in the ESP, and this conclusion can be attributed to the combined effect of three factors: (1) According to ideal gas law, it can be concluded that higher pressure results in lower volumetric flow rate, and therefore, lower particle axial velocity and higher collection efficiency; (2) It is generally known that higher radial terminal electrostatic velocity v_{TE}, which is equal to $neEB$, where B is particle mechanical mobility, is conducive to particle collection. Given that voltage and electrical field strength (E) are higher under higher pressure, higher pressure is thus favorable to v_{TE} and thus collection efficiency by increasing field strength; (3) The particle mechanical mobility B can be represented by $C_c/3\mu\pi d_p$ and thus is positively proportional to the Cunningham correction factor (C_c), which is positively correlated to the mean free path (λ). Higher pressure leads to lower gas density and lower mean free path, so higher pressure could suppress radial terminal electrostatic velocity and collection efficiency by diminishing particle mechanical mobility. Factors (1) and (2) enhanced particle capture with increasing gas pressure, while factor (3) weakened particle capture by increasing gas pressure. Nonetheless, it can be inferred that higher voltage can generally enhance performance of pressurized ESP with constant current.

2.3.3 Capture of NaCl particles using SFG as the feed gas

The composition of the coal combustion exhaust is very different from ambient air; thus, the ESP under different pressures was studied with SFG to understand its performance under exhaust conditions. As illustrated in Figure 2.5, the trends for particle penetration with respect to gas pressures were similar to that of air. A particular observation where the case of SFG is different from the case using air was that for positive ESP polarity, the particle penetration did not change

35

much as the particle diameter increased. For example, the widest range of the penetration of particles ranging from 40 nm to 400 nm in diameter among the five positive corona cases was from 7×10^{-3} to 3×10^{-2} at operating condition of 1 atm, 20 µA and +10.1 kV, which spanned even less than one order of magnitude. More specifically, the penetrations for ultrafine particles with diameter below 100 nm, which is in the size range dominated by diffusion charging, were much greater (1–2 orders of magnitude) than those in the case where air was used. The reason for this phenomenon is possibly that the diffusion charging was slower because of a lower thermal ion mobility. SFG may have higher concentrations of CO_2^+ and CO^+ ions, and fewer O_2^+ ions when compared to ambient air (Smyth et al., 1930; Stueckelberg, 1929). The higher average ion mass would result in lower thermal ion mobility.
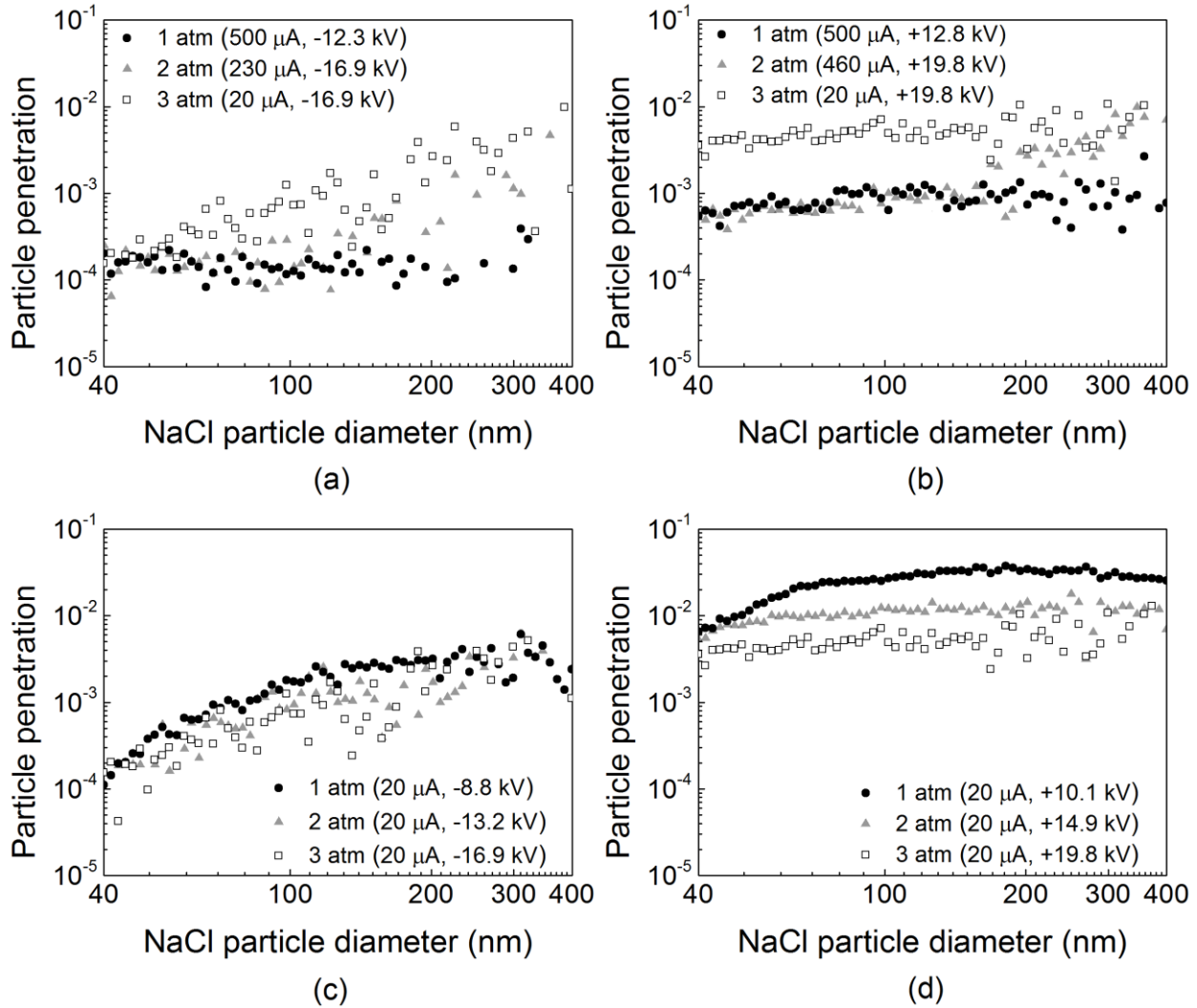
Figure 2.5 NaCl particle penetrations through the ESP using SFG as feed gas under different gas pressures: (a) negative ESP, voltage controlled; (b) positive ESP, voltage controlled; (c) negative ESP, current controlled; (d) positive ESP, current controlled.

2.3.4 Capture of fly ash particles from coal combustion in a pressurized drop-tube furnace

Fly ash particles from real combustion have different physical properties from those of NaCl particles with Boltzmann charge distributions; thus, their capture behavior in the ESP could differ from that observed in the above experiments. The effect of pressure on the capture of fly ash particles (size distributions shown in Figure A1.4) at negative ESP polarity was studied. When the negative ESP is operated at the same flow rate as the experiment Set II, namely 15 LPM, the

capture efficiencies were above 99.9% for both cases (as shown in Figure A1.5); thus, generally the capture efficiencies were higher for fly ash particles than NaCl particles with Boltzmann charge distributions. The initial charge fractions (when the particles entered the ESP) of fly ash particles were higher than that of NaCl particles (as shown in Figure A1.6), which tended to impact the capture of particles in the ESP. The high charge fraction was a result of diffusion charging and direct thermo-ionization and photoionization of the particles (Burtscher, 1992; Burtscher et al., 1986) during combustion.
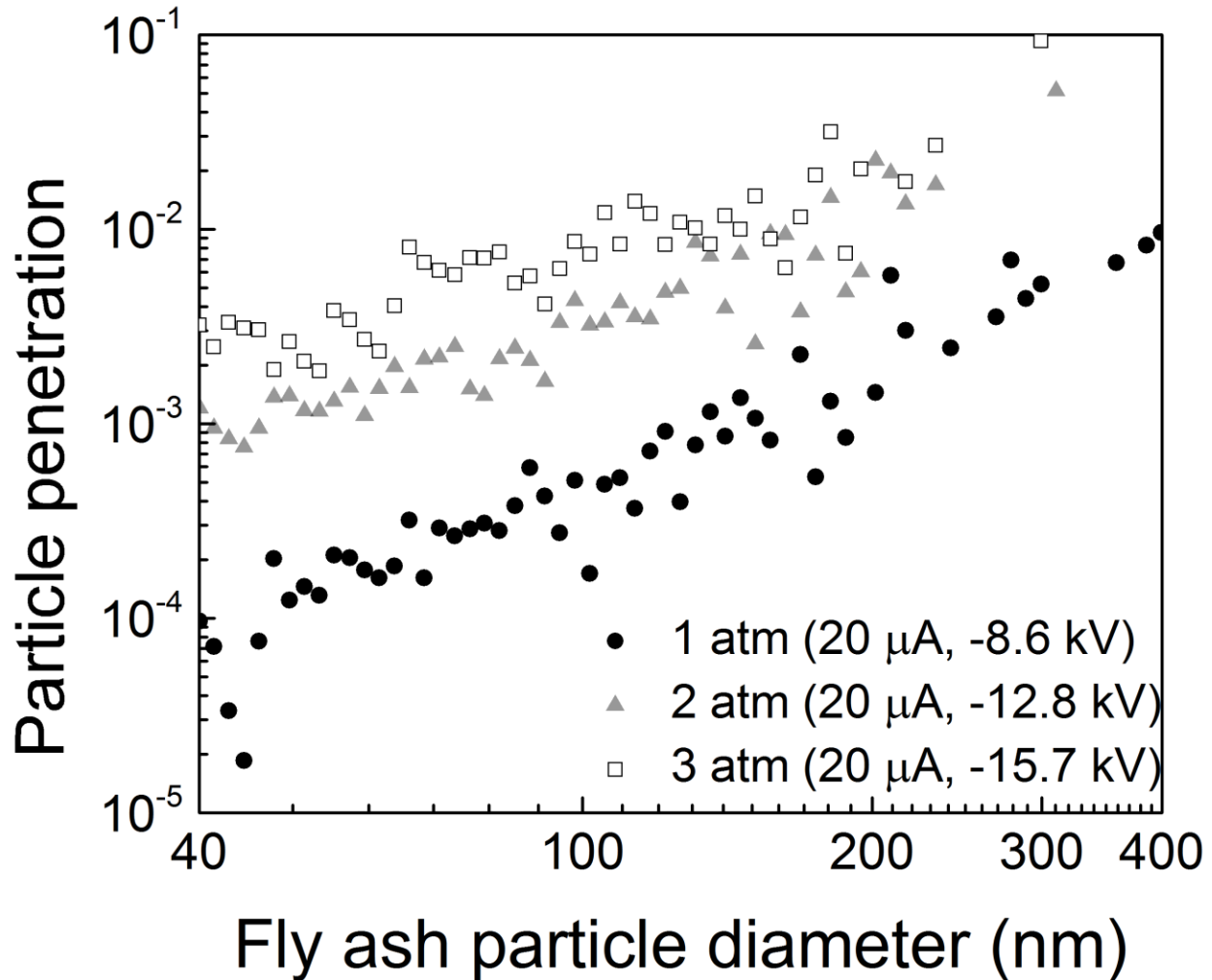
Figure 2.6 Particle penetrations through the ESP for fly ash particles of various sizes under different gas pressures.

As shown in Figure 2.6, higher penetrations of fly ash particles were obtained by increasing the flow rate to 25 LPM. The penetration increased with particle size, which was also observed in the NaCl experiments. However, the penetrations of most particles ranging from 40 nm to 400 nm in diameter increased from 8×10^{-5}–9×10^{-3} to 1×10^{-3}–2×10^{-2} as pressure increased from 1 atm to 3 atm for negative corona, which is opposite to the trend obtained in the NaCl experiment as shown in Figure 2.4(c). Although the ESP operating currents in the fly ash experiments were the same as in the NaCl experiments, the voltages were slightly different due to the differences in gas compositions, thereby affecting the I-V characteristics. This fact provides evidence that the

charging status of particles fed into the ESP plays an important role in ESP performance. In the NaCl particle tests, all the particles had a Boltzmann charge distribution; however, in the fly ash particle tests, the charge fraction varied with pressure. From the results of the charge status test (Figure A1.6), it is very probable that there was a higher percentage of multiple positively charged particles from combustion under higher gas pressure, as a result of more residence time for diffusion charging (Hinds, 1999) and direct thermionization and photoionization of particles. Those multiple positively charged particles caused an overall higher penetration in the negative ESP.

In addition, the dielectric constants of fly ash particles and NaCl particles are also different, which may influence diffusion charging in the ESP. However, because the difference is small (Table A1.1), the influence of the dielectric constant is expected to be insignificant.

2.3.5 Development of a modified D-A equation considering the effects of pressure

The D-A equation (Eq. 2.8) (Hinds, 1999) is usually used to calculate the capture efficiency of an ESP, which is given as

$$\eta = 1 - \exp\left(-\frac{A_C v_{TE}}{Q}\right). \tag{2.8}$$

This original D-A equation is based on three major assumptions: (1) Particles stick if they come into contact with the tube wall and are not reentrained. (2) The feed gas in the ESP is regarded as an ideal gas. (3) The particles are uniformly distributed across every cross section and reach an equilibrium charge distribution as soon as they enter the ESP.

In order to explore the effect of gas pressure on the capture efficiency of an ESP, parameters and variables in Eq. (2.8) were explicated termwise as follows.

According to ideal gas law, the pressure change can alter gas volume, so the volumetric flow rate in a pressurized ESP is given by

$$Q = \frac{Q_0 P_0 T}{P T_0},$$

(2.9)

indicating that higher pressure can lead to lower volumetric flow rate and thus larger residence time of the aerosol flow in the ESP.

Assuming that Stokes' law applies, the terminal electrostatic migration velocity of particles derived from the balance between the electric force and drag force can be represented by

$$v_{TE} = \frac{neEC_C}{3\pi\mu d_p},$$

(2.10)

where E is the average electric field strength that can be approximated as the field strength at the middle layer of wire-cylindrical space (i.e., at $r = \frac{r_0 + r_1}{2}$):

$$E = \frac{2r_0}{r_0 + r_1} E_0.$$

(2.11)

E_0, the field strength at $r = r_0$, is calculated from the corona voltage:

$$E_0 = \frac{V_0}{r_0 \ln(r_1 / r_0)},$$

(2.12)

where V_0 is given by Eqs. (2.5) and (2.6).

C_C considering noncontinuum effects is given by (Hinds, 1999)

$$C_C = 1 + \frac{\lambda}{d_p}\left(2.34 + 1.05\exp\left(-0.39\frac{d_p}{\lambda}\right)\right),$$ (2.13)

where λ can be related to gas pressure through the following equation (Hinds, 1999) and ideal gas law:

$$\lambda = \frac{1}{\sqrt{2}n_m\pi d_m^{\,2}} = \frac{RT}{\sqrt{2}\pi d_m^{\,2}PN_A}.$$ (2.14)

Based on two charging mechanisms, the number of elementary charges can be divided into two components:

$$n = n_{diff} + n_{field}.$$ (2.15)

Here, n_{diff} represents the number of elemental units of particle charges for diffusion charging, which is calculated by using Fuch's equation (Fuchs, 1947):

$$n_{diff} = \frac{d_p kT}{2K_E e^2}\ln\left(1 + \frac{\pi K_E d_p \bar{c}_i e^2 N_i t}{2kT}\right).$$ (2.16)

The number of elemental units of particle charges for field charging (n_{field}) is calculated by using the Pauthenier and Moreau-Hanot (Pauthenier et al., 1932) equation:

$$n_{field} = \left(\frac{3\varepsilon}{\varepsilon+2}\right)\left(\frac{Ed_p^{\,2}}{4K_E e}\right)\left(\frac{\pi K_E e Z_i N_i t}{1+\pi K_E e Z_i N_i t}\right),$$ (2.17)

where N_i is a function of current and field strength:

42

$$N_i = \frac{I}{A_C e Z_i E} \,. \tag{2.18}$$

In the whole series of equations above, the only two independent variables are corona current and gas pressure in the ESP since the dimensions of the ESP are known and other regular physical quantities are assumed constant. Thus, a complete procedure for calculating the capture efficiency of particles with diameter (d_p) by an ESP operated under particular pressure (P) and current (I) can be elaborated as follows (also shown in Figure A1.7):

1) plugging P into Eq. (2.9) to obtain the volumetric flow rate (Q), and then calculating residence time ($t = V/Q$),

2) plugging P into Eq. (2.2) to obtain the onset voltage (V_C, which can also be obtained simply by experimental measurement), calculating the onset field strength (E_C) by using Eq. (2.1b), and then plugging V_C, E_C, I and P into Eq. (2.5) (or Eq. (2.6) if polarity is positive) to estimate the applied voltage (V_0), which can be subsequently put in Eqs. (2.12) and (2.11) to get the average applied field strength (E),

3) plugging P into Eq. (2.14) and using Eq. (2.13) to obtain the Cunningham correction factor (C_C),

4) with values of I, E and t, using Eqs. (2.15)–(2.18) to calculate the number of elemental charges on a particle (n),

5) plugging n, E, and C_C into Eq. (2.10) to obtain the terminal migration velocity of the particles (v_{TE}), and

6) plugging Q and v_{TE} into Eq. (2.8) to finally obtain the capture efficiency (η).

In order to see if this calculation procedure is applicable to high pressure conditions, the measured particle penetrations (using negative ESP with air feed) from experiment Set II were compared with the corresponding calculated penetrations based on Eqs. (2.8)–(2.18). Figure A1.8 shows that the calculated particle penetrations at pressures higher than 1 atm are much lower than the corresponding experimental values, which indicates that the calculation model shown in Figure A1.7 might be a reasonable tool for calculating capture efficiency under atmospheric pressure conditions, but it is not feasible for pressurized cases.

It has been reported that the relative dominance of the diffusion charging effect compared with field charging might be dependent on applied pressure (Phelps, 1990; Romay et al., 1991) and current (Pfafflin et al., 1986) of the ESPs; moreover, Eqs. (2.16) and (2.17) are oversimplified due to some restrictive assumptions. Therefore, to obtain better simulation of particle penetrations at high pressure, the weighted influence of each of the charging mechanisms in Eq. (2.15) was modified by multiplying an empirical coefficient, which is a function of pressure and current, by each of the charge number terms:

$$n' = B_1(I,P) \cdot n_{diff} + B_2(I,P) \cdot n_{field} = \left(b_1^{\frac{\ln(I/1A)}{\ln(I_0/1A)} - \frac{P}{P_0}} \right) \cdot n_{diff} + \left(b_2^{\frac{\ln(I/1A)}{\ln(I_0/1A)} - \frac{P}{P_0}} \right) \cdot n_{field}, \qquad (2.19)$$

where b_1 and b_2 are constants to be numerically determined , and I_0 (= 20 µA) and P_0 (= 1 atm) are set as reference values since the simulated results for the experimental condition of 20 µA and 1 atm are so close to the experimental penetrations, as shown in Figure A1.8, that they are not considered to be further modified.

Using MATLAB, numerical iterations of b_1 and b_2 over wide ranges were conducted. Eventually, the minimum summation of squared deviations (σ') reached a minimum value of 0.0022 (decreased

by 46% compared with Figure A1.8) when b_1 and b_2 were 1.77 and 2.84, respectively. Thus, the

modified equation of total charge number on a particle is expressed as:

$$n' = B_1(I,P) \cdot n_{diff} + B_2(I,P) \cdot n_{field} = \left(1.77^{\frac{\ln(I/1A)}{\ln(I_0/1A)} - \frac{P}{P_0}}\right) \cdot n_{diff} + \left(2.84^{\frac{\ln(I/1A)}{\ln(I_0/1A)} - \frac{P}{P_0}}\right) \cdot n_{field} . \qquad (2.20)$$

Inputs: I (Input), P (Input) — Output: η (Output)

Note box:
* Pressure (P) and current (I) are two initial independent variables in this whole procedure. Other used parameters are given based on fixed dimensions of the ESP and regular physical conditions.
* V_C can be also obtained simply by experimental measurements.
* The meanings of all the symbols can be found in the nomenclature.
* The **modified** part is highlighted by **blue** arrow dash line.

$$Q = \frac{Q_0 P_0 T}{P T_0}$$

$$t = \frac{V}{Q}$$

$$n_{diff} = \frac{d_p kT}{2K_E e^2}\ln\left[1 + \frac{\pi K_E d_p \bar{c}_i e^2 N_i t}{2kT}\right]$$

$$N_i = \frac{I}{A_c e Z_i E}$$

$$n_{field} = \left(\frac{3\varepsilon}{\varepsilon+2}\right)\left(\frac{E d_p^2}{4K_E e}\right)\left(\frac{\pi K_E e Z_i N_i t}{1+\pi K_E e Z_i N_i t}\right)$$

$$n' = \left[1.77^{\frac{\ln(I/1A)}{\ln(I_0/1A)}\frac{P}{P_0}}\right]\cdot n_{diff} + \left[2.84^{\frac{\ln(I/1A)}{\ln(I_0/1A)}\frac{P}{P_0}}\right]\cdot n_{field}$$

$$E_C = \frac{V_C}{r_0 \ln(r_1/r_0)}$$

$$V_C = r_0 \ln\left(\frac{r_1}{r_0}\right)\left[A_g + \frac{B_g}{(r_0\delta')^{\frac{1}{2}}}\right]\frac{P}{P_0}$$

$$V_0 = \left[V_C + E_C r_0\left[(1+\phi)^{\frac{1}{2}} - 1 - \ln\left[\frac{1+(1+\phi)^{\frac{1}{2}}}{2}\right]\right]\right]\cdot 1.135^{P/P_0 - 2.312}$$

$$E_0 = \frac{V_0}{r_0 \ln(r_1/r_0)}$$

$$E = \frac{2r_0}{r_0 + r_1}E_0$$

$$v_{TE} = \frac{n'eEC_C}{3\pi\mu d_p}$$

$$\lambda = \frac{RT}{\sqrt{2}\pi d_m^2 P N_A}$$

$$C_C = 1 + \frac{\lambda}{d_p}\left[2.34 + 1.05\exp\left(-0.39\frac{d_p}{\lambda}\right)\right]$$

$$\eta = 1 - \exp\left[-\frac{A_C v_{TE}}{Q}\right]$$

Figure 2.7 Calculating procedure of capture efficiency in pressurized ESPs using Eq. (2.20) as the modified expression for the number of elementary charges of the particles.

A modified calculating procedure of capture efficiency in pressurized ESPs using Eq. (2.20) as the expression for the number of elementary charges on a particle is illustrated in Figure 2.7. Thus, a comparison between the measured particle penetrations (using negative ESP with air feed) from experiment Set II with the corresponding calculated penetrations using Eq. (2.20) is shown in Figure 2.8. The calculated curves fit the experimental penetrations reasonably well, especially in the diameter range of 70 nm to 400 nm for all five conditions, although the agreements are unfavorable for particles lower than 100 nm for the cases with high currents, i.e. 200 µA and 500 µA, which is primarily due to limitations in computational cost and algorithm. The trend of particle penetration with increasing particle size is upward as demonstrated by the experimental results, which is similar to the trend of penetration curves produced by the modified calculating procedure—all of which serves to illustrate the legitimacy of this model. This trend makes physical sense because larger particles tend to have lower electrical mobility (Jing et al., 2013) so that they are much less likely to be captured in the limited residence time inside the ESP. However, the effect of field charging would probably facilitate collection of particles larger than 200 nm by increasing particle charge number, which can be supported by the trend shown in Figure A1.9. In fact, it can be observed in Figure 2.8 that the experimental penetration dotted curves become flattened at around 200–300 nm, and the three simulated curves under pressures over 1 atm proceed through penetration peaks and even towards lower penetration in the range of 200–400 nm. These facts allow us to reasonably speculate much clearer decreasing penetration curves (increasing efficiency) as particle size increases beyond visible scale (to over 400 nm) in our study, which is due to field charging.

The experimentally speculated significance of partial charging effect on this study can be verified by the modified D-A equation and Figure A1.9. As reported by Lin et al. (Lin et al., 2012), a partial

charging effect factor ($\alpha = MIN(1, n)$) can be used in a modified D-A equation. α is equal to 1 for particle charge number greater than or equal to 1.0, and is equal to n when $n < 1.0$, or particles are partially charged. Based on calculation using the Eq. (2.20), the value of n is no less than 2.3 for particles of all concerned sizes. This fact indicates that the value of α is constantly equal to 1 and partial charging effect is negligible. In addition, as implied by Figure A1.9, the total charge number increases rapidly as particle size rises, although the portion of particles carrying few charges downstream the neutralizer also increases with larger particle size. For instance, it can be seen in Figure A1.9 that a particle in diameter of 392 nm carries around 40 charges under 1 atm, 20 μA and −8.9 kV, and it is known that particles carrying −3, −2, −1, 0, +1, +2 or +3 account for 94% (TSI, 2009) of the total particles in the same size. These two facts mean that most of the particles in diameter of 390 nm carry negligible number of charges after passing the neutralizer compared with the ultimate charge number in the ESP. Therefore, charging effect by the radioactive source should have little impact on the performance of the ESP.
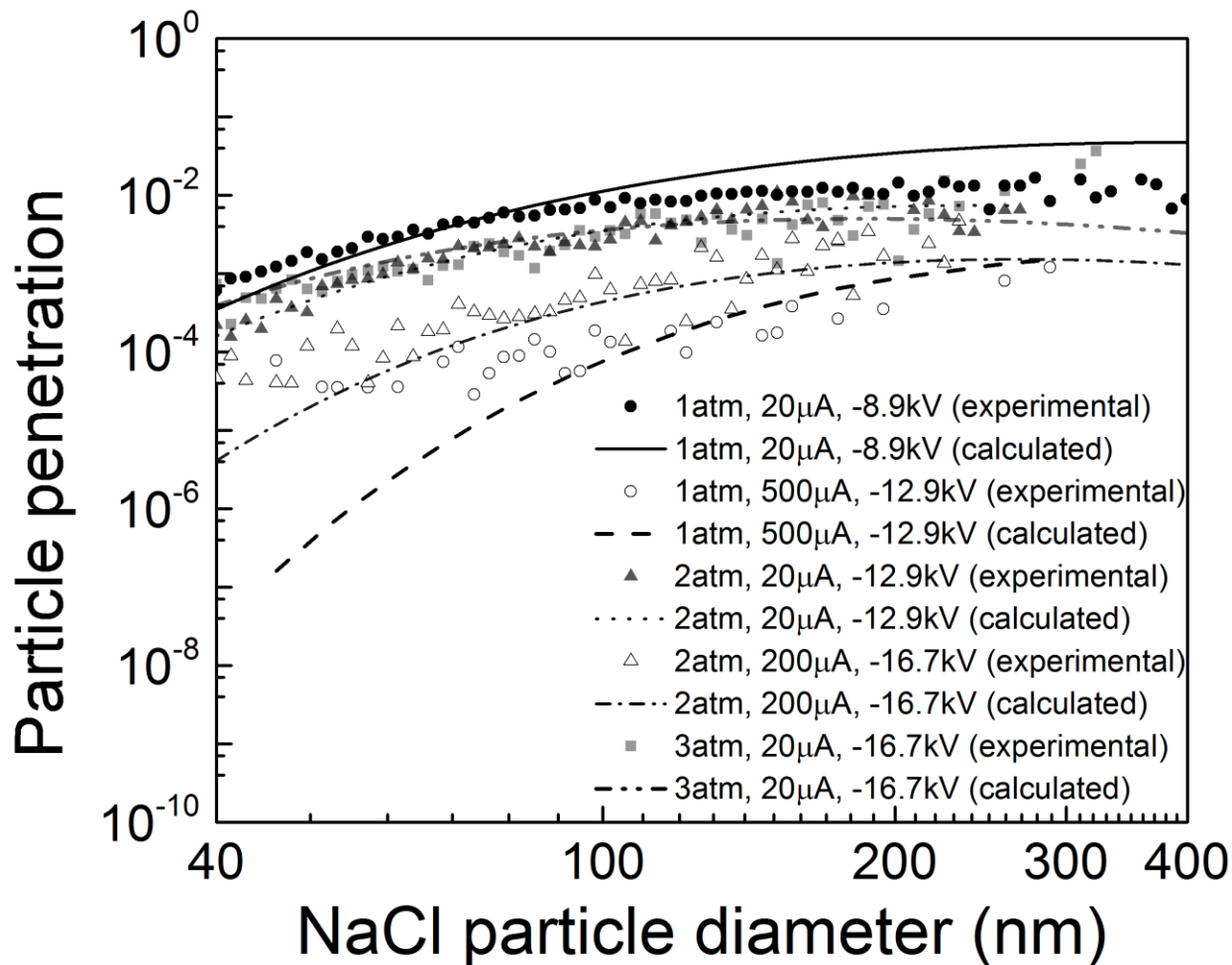
Figure 2.8 Particle penetrations for various particle sizes measured under 1, 2 and 3 atm and the corresponding calculated values using Eq. (20). (summation of squared deviations (σ') is 0.0022, which excludes the case of "1 atm and 20 μA").

In order to test the robustness of this modified model under other pressure conditions, experimental particle penetrations of NaCl particles under 1.5 atm and 2.5 atm were compared with the corresponding calculated values based on the model. It can be observed in Figure 2.9 that the calculated particle penetration for particles of each particular size was lower when pressure rose with constant current, which is the same trend as presented by the experiments at 1.5 and 2.5 atm as well as the previous experiments at 1, 2, and 3 atm. Moreover, the calculated size distribution of particle penetrations is close to the corresponding experimental dotted line especially for particles larger than 100 nm, for both the 1.5-atm and 2.5-atm cases. This outcome demonstrates

that the model using Eq. (2.20) is better able to predict the capture efficiency of particles with diameters greater than 100 nm.
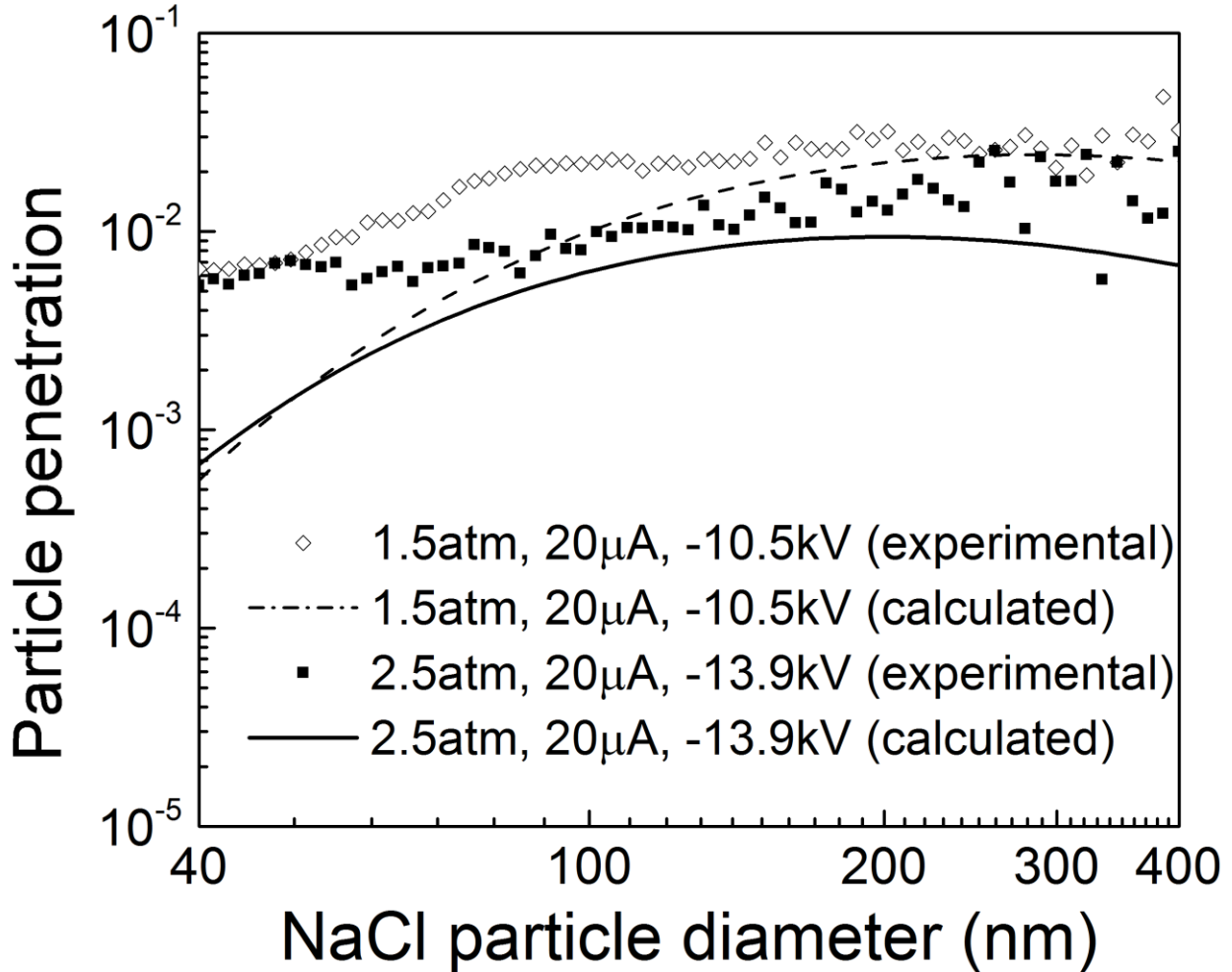
Figure 2.9 Particle penetrations for various particle sizes measured under 1.5 and 2.5 atm and the corresponding calculated values using Eq. (2.20).

2.4 Conclusion

This study examined the effect of gas pressure on the performance of an ESP. The corona onset voltage increased with the gas pressure, and under the same voltage, the ESP current was lower with higher gas pressure, because the higher gas density hindered the ionization. For positive ESP, under the same voltage, the ESP current was lower for the SFG than for the air. This phenomenon is attributed to the fact that the increase in CO_2 concentration caused a higher ionization potential,

a reduced effective electric field, and more electron traps. However, for negative voltages, the I-V characteristic curves for the cases of these two gases were similar, because the primary source of the ions for the negative corona is direct photoionization of the discharge electrode, which is independent of feed gas type.

The effect of gas pressure on the submicrometer particle capture in the ESP was studied with NaCl particles in both air and SFG. For both gas compositions, it can be concluded that: 1) at similar operating voltages, particle penetration was lower for a lower gas pressure, because the ion concentration was higher with lower gas pressure and 2) with the same current, the particle penetration was lower for a higher gas pressure, which was an outcome of the combined effects of lower particle axial velocity, lower particle radial velocity, and higher electrical field strength.

The capture of fly ash particles from a drop-tube furnace was also studied at the same three pressures. The charge status of the fly ash particles played an important role in this process. With higher pressure in the combustor, more fly ash particles might be multiple charged and gain opposite polarity to the ESP when they entered the ESP. As a result, for the same current, the particle capture efficiency became lower with higher pressure.

A semi-empirical model was established based on the theoretical D-A equation and experimental data under 1, 2 and 3 atm to calculate the particle penetrations under high pressure. Instead of simply adding up charge numbers governed by the two charging mechanisms, the total number of charges on a particle ($n' = B_1(I,P)n_{diff} + B_2(I,P)n_{field}$) was calculated by taking into account the effects of current and pressure on the relative weights of diffusion charging and field charging. Experimental penetrations under 1.5 atm and 2.5 atm validated this calculation model over the particle diameter range of 100 nm to 400 nm, which can facilitate the design of pressurized ESPs

51

for controlling submicrometer particle emissions. It is necessary to note that the implementation of this model could be limited by particular configuration and scale of ESPs and oversimplified flow and charging conditions. More detailed studies on the fundamental mechanisms of how high pressure impacts on turbulence of the flow in ESPs and on charging efficiency of ultrafine particles are needed for a better understanding of capture efficiency in pressurized ESPs.

2.5 Nomenclature

A_C = collecting area of the ESP

A_g, B_g = constants of the gas of concern in the corona onset field strength estimation equation

B_1, B_2 = coefficients to adjust relative weights of charge numbers induced by diffusion charging and field charging (functions of current and pressure)

C_C = Cunningham correction factor

$\bar{c}_i$ = rms average thermal speed of ions

d_m = collision diameter of molecules, approximately 3.7×10^{-10} m for air

d_p = particle diameter

E = average electric field strength in the wire-to-shell space

E_0 = field strength at the surface of the wire ($r = r_0$)

E_C = field strength needed to start a corona discharge

e = elementary charge, 1.6×10^{-19} (C)

h = effective length of the wire

I = current

I_0 = reference current, 20 (μA)

K_0 = permittivity of free space, 8.85×10^{-12} (F/m)

K_E = constant of proportionality, 9.0×10^9 (N·m²/C²)

k = Boltzmann constant, 1.38×10^{-23} (J/K)

m = mass of one ion

N = number of statistical values of concern

N_A = Avogadro's number, 6.02×10^{23}

N_i = ion concentration

N_{off} = particle number concentration downstream of the ESP when ESP is off

N_{on} = particle number concentration downstream of the ESP when ESP is on

n = number of elemental charges on a particle

n_m = number of molecules per cubic meter

n' = modified number of elemental charges on a particle

P = gas pressure

P_0 = atmospheric pressure, 1.01325×10^5 (Pa)

p = particle penetration

53

Q = volumetric flow rate

Q_0 = volumetric flow rate under atmospheric pressure and the reference temperature, T_0

R = idea gas law constant, 8.314 (J/mol·K)

r = horizontal distance from the center line of ESP

r_0 = radius of the discharge wire

r_1 = radius of the collection tube

T = temperature

T_0 = reference temperature, 298.15 (K).

t = residence time of particles in the ESP ($t = \dfrac{V}{Q}$)

V = volume of the ESP

V_0 = corona voltage at the surface of the central wire ($r = r_0$)

V_C = corona onset voltage

v_{TE} = terminal migration velocity of a particle

Z_i = mobility of ions, approximately 0.00015 (m²/V·s)

Greek Letters

α = partial charging effect factor

ε = relative permittivity of particles

η = capture efficiency of the ESP

λ = mean free path

μ = dynamic viscosity, 1.8×10^{-5} (Pa·s) for air

δ' = relative gas pressure compared to atmosphere pressure ($\delta' = \dfrac{P}{P_0}$)

σ' = summation of squared deviations

σ = variance

ϕ = dimensionless current

2.6 References

Abdelsalam, M., & Wiitanen, D. (1993). CALCULATION OF CORONA ONSET VOLTAGE
FOR DUCT-TYPE PRECIPITATORS. *Ieee Transactions on Industry Applications, 29*(2),
274-280. doi:10.1109/28.216532

Bai, M., Wang, S., Chen, Z., Leng, H., & Mao, S. (2010). The Effects of Submicrometer Dust
Charging and Coagulation on ESP Efficiency by Using Alternating Electric Field. *Ieee
Transactions on Plasma Science, 38*(2), 127-132. doi:10.1109/tps.2009.2037888

Biswas, P., & Wu, C.-Y. (2005). Nanoparticles and the environment. *Journal of the Air & Waste
Management Association, 55*(6), 708-746.

Brown, R. F., & Walker, A. B. (1971). FEASIBILITY DEMONSTRATION OF ELECTROSTATIC PRECIPITATION AT 1700 DEGREES F. *Journal of the Air Pollution Control Association, 21*(10), 617-&.

Burtscher, H. (1992). MEASUREMENT AND CHARACTERISTICS OF COMBUSTION AEROSOLS WITH SPECIAL CONSIDERATION OF PHOTOELECTRIC CHARGING AND CHARGING BY FLAME IONS. *Journal of aerosol science, 23*(6), 549-&. doi:10.1016/0021-8502(92)90026-r

Burtscher, H., Reis, A., & Schmidtott, A. (1986). PARTICLE CHARGE IN COMBUSTION AEROSOLS. *Journal of aerosol science, 17*(1), 47-51. doi:10.1016/0021-8502(86)90005-4

Bush, J. R., Feldman, P. L., & Robinson, M. (1979). HIGH-TEMPERATURE, HIGH-PRESSURE ELECTROSTATIC PRECIPITATION. *Journal of the Air Pollution Control Association, 29*(4), 365-371.

Che, H., Zhang, X., Li, Y., Zhou, Z., Qu, J. J., & Hao, X. (2009). Haze trends over the capital cities of 31 provinces in China, 1981-2005. *Theoretical and Applied Climatology, 97*(3-4), 235-242. doi:10.1007/s00704-008-0059-8

Chen, J., & Davidson, J. H. (2003). Model of the negative DC corona plasma: comparison to the positive DC corona plasma. *Plasma Chemistry and Plasma Processing, 23*(1), 83-102.

Chen, T.-M., Tsai, C.-J., Yan, S.-Y., & Li, S.-N. (2014). An efficient wet electrostatic precipitator for removing nanoparticles, submicron and micron-sized particles. *Separation and Purification Technology, 136*, 27-35.

Condon, E. U., & Odishaw, H. (1967). *Handbook of Physics*. New York: McGraw-Hill.

Fuchs, N. (1947). The charges on the particles of aerocolloids. *Izv. Akad. Nauk. SSSR, Ser. Geogr. Geofiz, 11*, 341-348.

Gopan, A., Kumfer, B. M., Phillips, J., Thimsen, D., Smith, R., & Axelbaum, R. L. (2014). Process design and performance analysis of a Staged, Pressurized Oxy-Combustion (SPOC) power plant for carbon capture. *Applied Energy, 125*, 179-188.

Hinds, W. C. (1999). *Aerosol technology: properties, behavior, and measurement of airborne particles*: John Wiley & Sons.

Huang, R.-J., Zhang, Y., Bozzetti, C., Ho, K.-F., Cao, J.-J., Han, Y., . . . Prevot, A. S. H. (2014). High secondary aerosol contribution to particulate pollution during haze events in China. *Nature, 514*(7521), 218-222. doi:10.1038/nature13774

Huang, S.-H., & Chen, C.-C. (2002). Ultrafine aerosol penetration through electrostatic precipitators. *Environmental Science & Technology, 36*(21), 4625-4632.

Jensen, A., Johnsson, J. E., Andries, J., Laughlin, K., Read, G., Mayer, M., . . . Bonn, B. (1995). Formation and reduction of NOx in pressurized fluidized bed combustion of coal. *Fuel, 74*(11), 1555-1569. doi:http://dx.doi.org/10.1016/0016-2361(95)00155-X

Jing, H., He, S., Ou, Q., Hsiao, T.-C., & Chen, D.-R. (2013). Development of a Compact Electrostatic Nanoparticle Sampler for Offline Aerosol Characterization. *Mapan, 28*(3), 217-226.

Keefe, D., Nolan, P. J., & Rich, T. A. (1959). Charge equilibrium in aerosols according to the Boltzmann law. *Proceedings of the Royal Irish Academy, Section A (Mathematical, Astronomical and Physical Science), 60*(4), 27-45.

Knapp, M., Echt, O., Kreisle, D., Märk, T. D., & Recknagel, E. (1986). Formation of long-lived CO_2^-, N_2O^-, and their dimer anions, by electron attachment to van der waals clusters.

Chemical Physics Letters, 126(3–4), 225-231. doi:http://dx.doi.org/10.1016/S0009-2614(86)80074-4

Komhyr, W. (1983). An aerosol and gas sampling apparatus for remote observatory use. *Journal of Geophysical Research: Oceans, 88*(C6), 3913-3918.

Liang, W.-J., & Lin, T. (1994). The characteristics of ionic wind and its effect on electrostatic precipitators. *Aerosol Science and Technology, 20*(4), 330-344.

Lide, D. (2000). CRC Handbook of Chemistry and Physics 1999–2000: A Ready-Reference Book of Chemical and Physical Data, 81: CRC Press, Boca Raton, FL.

Lin, G.-Y., Chen, T.-M., & Tsai, C.-J. (2012). A Modified Deutsch-Anderson Equation for Predicting the Nanoparticle Collection Efficiency of Electrostatic Precipitators. *Aerosol and Air Quality Research, 12*(5), 697-706. doi:10.4209/aaqr.2012.04.0085

Lin, G.-Y., Tsai, C.-J., Chen, S.-C., Chen, T.-M., & Li, S.-N. (2010). An efficient single-stage wet electrostatic precipitator for fine and nanosized particle control. *Aerosol Science and Technology, 44*(1), 38-45.

Linstrom, P. J., & Mallard, W. (2001). NIST Chemistry webbook; NIST standard reference database No. 69.

McCain, J. D., Gooch, J. P., & Smith, W. B. (1975). Results of field measurements of industrial particulate sources and electrostatic precipitator performance. *Journal of the Air Pollution Control Association, 25*(2), 117-121.

Meij, R., & te Winkel, B. (2004). The emissions and environmental impact of PM10 and trace elements from a modern coal-fired power plant equipped with ESP and wet FGD. *Fuel Processing Technology, 85*(6–7), 641-656. doi:http://dx.doi.org/10.1016/j.fuproc.2003.11.012

Minchener, A. J. (2005). Coal gasification for advanced power generation. *Fuel, 84*(17), 2222-2235.

Mishra, D., Goyal, P., & Upadhyay, A. (2015). Artificial intelligence based approach to forecast PM2.5 during haze episodes: A case study of Delhi, India. *Atmospheric Environment, 102*, 239-248. doi:10.1016/j.atmosenv.2014.11.050

Pachauri, T., Singla, V., Satsangi, A., Lakhani, A., & Kumari, K. M. (2013). Characterization of major pollution events (dust, haze, and two festival events) at Agra, India. *Environmental Science and Pollution Research, 20*(8), 5737-5752. doi:10.1007/s11356-013-1584-2

Park, J.-H., & Chun, C.-H. (2002). An improved modelling for prediction of grade efficiency of electrostatic precipitators with negative corona. *Journal of aerosol science, 33*(4), 673-694.

Park, S. J., & Kim, S. S. (1998). Effects of particle space charge and turbulent diffusion on performance of plate–plate electrostatic precipitators. *Journal of Electrostatics, 45*(2), 121-137.

Pauthenier, M., & Moreau-Hanot, M. (1932). Charging of spherical particles in an ionizing field. *J. Phys. Radium, 3*(7), 590-613.

Peek, F. W. (1920). *Dielectric phenomena in high voltage engineering*: McGraw-Hill Book Company, Incorporated.

Pfafflin, J. R., & Ziegler, E. N. (1986). *Advances in environmental science and engineering*: CRC Press.

Phelps, A. V. (1990). THE DIFFUSION OF CHARGED-PARTICLES IN COLLISIONAL PLASMAS - FREE AND AMBIPOLAR DIFFUSION AT LOW AND MODERATE PRESSURES. *Journal of Research of the National Institute of Standards and Technology, 95*(4), 407-431. doi:10.6028/jres.095.035

Riehle, C., & Löffler, F. (1993). Reflections on similarity laws concerning particle transport in electrical precipitators. *Powder technology, 77*(2), 201-208.

Rinard, G., Rugg, D. E., & Yamamoto, T. (1987). HIGH-TEMPERATURE HIGH-PRESSURE ELECTROSTATIC PRECIPITATOR ELECTRICAL CHARACTERIZATION AND COLLECTION EFFICIENCY. *Ieee Transactions on Industry Applications, 23*(1), 114-119. doi:10.1109/tia.1987.4504875

Robinson, M. (1967a). The corona threshold for coaxial cylinders in air at high pressures. *Power Apparatus and Systems, IEEE Transactions on*(2), 185-189.

Robinson, M. (1967b). A modified Deutsch efficiency equation for electrostatic precipitation. *Atmospheric Environment (1967), 1*(3), 193-204.

Robinson, M. (1971). Electrostatic precipitation. *Air pollution control, 1*, 227-335.

Romay, F. J., Pui, D. Y. H., & Adachi, M. (1991). UNIPOLAR DIFFUSION CHARGING OF AEROSOL-PARTICLES AT LOW-PRESSURE. *Aerosol Science and Technology, 15*(1), 60-68. doi:10.1080/02786829108959513

Smyth, H. D., & Stueckelberg, E. C. G. (1930). The ionization of carbon dioxide by electron impact. *Physical Review, 36*(3), 0472-0477. doi:10.1103/PhysRev.36.472

Stueckelberg, E. C. G. (1929). Simultaneous ionization and dissociation of oxygen and intensities of the ultra-violet O-2(+) bands. *Physical Review, 34*(1), 65-67. doi:10.1103/PhysRev.34.65

Suriyawong, A., Gamble, M., Lee, M.-H., Axelbaum, R., & Biswas, P. (2006). Submicrometer particle formation and mercury speciation under O-2-CO2 coal combustion. *Energy & Fuels, 20*(6), 2357-2363. doi:10.1021/ef060178s

Suriyawong, A., Hogan, C. J., Jiang, J., & Biswas, P. (2008a). Charged fraction and electrostatic collection of ultrafine and submicrometer particles formed during O 2–CO 2 coal combustion. *Fuel, 87*(6), 673-682.

Suriyawong, A., Hogan, C. J., Jr., Jiang, J., & Biswas, P. (2008b). Charged fraction and electrostatic collection of ultrafine and submicrometer particles formed during O(2)-CO(2) coal combustion. *Fuel, 87*(6), 673-682. doi:10.1016/j.fuel.2007.07.024

Thornton, W. (1939). LXVIII. The electric strength of gases, measured by corona discharge. *The London, Edinburgh, and Dublin Philosophical Magazine and Journal of Science, 28*(191), 666-678.

TSI. (2009). *Model 3080 SMPS Operation and Service Manual*. St Paul, MN: TSI Inc.

Villot, A., Gonthier, Y., Gonze, E., Bernis, A., Ravel, S., Grateau, M., & Guillaudeau, J. (2012). Separation of particles from syngas at high-temperatures with an electrostatic precipitator. *Separation and Purification Technology, 92*, 181-190. doi:10.1016/j.seppur.2011.04.028

Wang, L. K., Pereira, N. C., & Hung, Y.-T. (2004). *Air pollution control engineering* (Vol. 1): Springer.

Wang, X., Cotter, E., Iyer, K. N., Fang, J., Williams, B. J., & Biswas, P. (2015). Relationship between pyrolysis products and organic aerosols formed during coal combustion. *Proceedings of the Combustion Institute, 35*, 2347-2354. doi:10.1016/j.proci.2014.07.073

Wang, X., Daukoru, S. M., Torkamani, S., Wang, W.-N., & Biswas, P. (2013). Role of exhaust gas recycle on submicrometer particle formation during oxy-coal combustion. *Proceedings of the Combustion Institute, 34*, 3479-3487. doi:10.1016/j.proci.2012.07.049

Wang, X., Williams, B. J., Wang, X., Tang, Y., Huang, Y., Kong, L., . . . Biswas, P. (2013). Characterization of organic aerosol produced during pulverized coal combustion in a drop

tube furnace. *Atmospheric Chemistry and Physics, 13*(21), 10919-10932. doi:10.5194/acp-13-10919-2013

Williams, B. J., Goldstein, A. H., Kreisberg, N. M., & Hering, S. V. (2006). An In-Situ Instrument for Speciated Organic Composition of Atmospheric Aerosols: T hermal Desorption A erosol GC/MS-FID (TAG). *Aerosol Science and Technology, 40*(8), 627-638.

Ylätalo, S. I., & Hautanen, J. (1998). Electrostatic precipitator penetration function for pulverized coal combustion. *Aerosol Science and Technology, 29*(1), 17-30.

Yokoyama, T., Asakura, K., Matsuda, H., Ito, S., & Noda, N. (2000). Mercury emissions from a coal-fired power plant in Japan. *Science of the Total Environment, 259*(1–3), 97-103. doi:http://dx.doi.org/10.1016/S0048-9697(00)00552-0

Yoo, K. H., Lee, J. S., & Oh, M. D. (1997). Charging and collection of submicron particles in two-stage parallel-plate electrostatic precipitators. *Aerosol Science and Technology, 27*(3), 308-323.

Zevenhoven, R., & Kilpinen, P. (2001). *Control of pollutants in flue gases and fuel gases*: Helsinki University of Technology Espoo, Finland.

Zhan, C.-G., Nichols, J. A., & Dixon, D. A. (2003). Ionization potential, electron affinity, electronegativity, hardness, and electron excitation energy: molecular properties from density functional theory orbital energies. *The Journal of Physical Chemistry A, 107*(20), 4184-4195.

Zhuang, Y., & Biswas, P. (2001). Submicrometer particle formation and control in a bench-scale pulverized coal combustor. *Energy & Fuels, 15*(3), 510-516. doi:10.1021/ef000080s

Chapter 3: Comparison of size distribution, charge fraction and electrostatic precipitation of fly ash from combustion of India, US and China coal

Abstract

India, US and China are the top three countries in coal consumption. This study focused on investigating characteristics of coal fly ashes generated from combustion of representative coal seams from those three countries. The size distributions of particle number concentration were measured by a scanning mobility particle sizer (SMPS) and an aerodynamic particle sizer (APS). The fly ashes of low-rank US and India coals had higher concentration and geometric mean size than the China coal fly ash. The US coal shows the highest number and mass concentration fine/coarse ratios, which are 1.34×10^4 and 1.08, respectively. Charged particle fraction was examined by using a charged particle remover (CPR). The results showed that charged particle fraction increased with growing particle size for submicrometer fly ashes produced by combustion of India and US coals, which was probably governed by thermo-ionization charging. Smaller China coal fly ash had higher charged particle fraction possibly due to diffusion charging. Besides, the ash resistivity tests showed that India and China coal fly ashes had higher ash resistivity than the US coal fly ash. The electrostatic precipitation tests evidenced that smaller particles for high resistivity coal fly ashes might suffer more significantly from back corona. Notably, back corona effect was reduced by increasing the applied voltage of the electrostatic precipitator (ESP). These findings are crucial to tailoring electrostatic precipitation technology for controlling coal fly ashes commonly discharged by coal-fired power plants from India, US and China.

3.1 Introduction

Particulate matter has been scientifically demonstrated to be one of the most detrimental environmental threat since it can causes reduced visibility (Cao et al., 2012) and human respiratory health issues (Gilmour et al., 2004). Fine (diameter <2.5 µm) and ultrafine (diameter <0.1 µm) particles are notoriously featured with various types of emission sources, such as vehicle exhaust,

64

residential biomass burning and industrial process, and complex formation pathways (Hu et al., 2015) including direct emission and secondary aerosol formation. Particularly, fly ash in coal combustion exhaust gas is a major source of fine particulate matter in atmosphere in India (Chowdhury et al., 2007; Gummeneni et al., 2011), US (Kim et al., 2016; Laden et al., 2000) and China (R.-J. Huang et al., 2014; Zhang et al., 2015). This fact is partially attributed to the vast coal consumption in the three countries, accounting for more than 70% of world coal use (EIA, 2016) and consequent enormous particles emission. In addition, fine particles have much higher tendency to escape common particle control equipment and discharge into atmosphere. To better understand fine particle formation in coal combustion and more effectively control particle emission, it is imperative to explore the characteristics of fly ash from combustion of coal seams widely used in different countries and how the particle controlling process could be impacted.

Particle number concentration size distribution has been widely studied using different coal seams. However, there are few researches reporting the comparison of fly ash size distribution from in combustion exhaust gas using different coal types under well-controlled experimental conditions. Using a laboratory scale single-particle combustion furnace and testing the particle size distributions burning different coal seams under identical condition could provide insight for emission characteristics of different coals.

Electrostatic precipitator (ESP) is regarded as one of the most popular industrial particle emission control technology due to its high mass collection efficiency, capability to collect particles with diverse composition and long-term reliability. Extensive studies have been conducted on the capture of submicrometer particles using ESPs with both lab scale (Bai et al., 2010; S.-H. Huang et al., 2002; Yoo et al., 1997; Zhuang et al., 2001; Zhuang et al., 2000) and industrial scale combustion systems (Y. Li et al., 2009; McCain et al., 1975; Ylätalo et al., 1998). Yoo et al. (Yoo

et al., 1997) found that the particle collection efficiency of a two-stage ESP decreases significantly as particle diameter decreases from 30 nm. Similar results obtained by Zhuang et al. (Zhuang et al., 2000) demonstrated that a continuous decrease in particle collection efficiency occurred when particle diameter was smaller than 100 nm for both one-stage and two-stage ESP and particles of different contents. Ylatalo et al. (Ylätalo et al., 1998) demonstrated existence of a penetration window of particle in diameters of 100 nm – 5μm for a normal operated ESP in a power plant. It needs to be noted that fly ash particles in combustion exhaust gas have been reported catching significant amount charges, which might influence the particle charging process in the ESP and its capture performance. Maricq (Maricq, 2004) concluded that a remarkable fraction of the soot particles are charged mainly with a single charge during the combustion, and the numbers of positive and negative particles are equal. Suriyawong et al. examined the charge fraction of submicrometer particles from oxy-combustion and electrostatic collection performance, and suggested that there were more positive ions present in the combustor than negative ions (Suriyawong et al., 2008). ESP performance under various pressure conditions studied by Li et al. (Z. Li et al., 2016) indicated that existing charges on the fly ash particles could counteract particle capture in the ESP. The results above lead to the fact that knowing charging status of fly ash is informative for better design and control of ESPs. To the best of our knowledge, no study has been conducted to compare the charging status of fly ash from combustion of different coal seams.

This study examined the size distribution and charged fraction of fly ash from combustion of coal from India, US and China. All the experiments are conducted using a lab scale drop-tube combustor. The results are presented in four perspectives: (1) particle size distribution downstream the combustor; (2) charged fraction of fly ash; (3) size-dependent penetration of ultrafine particles in a lab scale cylindrical ESP.

3.2 Experimental section

3.2.1 Experimental system

A lab scale drop-tube furnace system was used as the fly ash source as shown in Figure 3.1. Coal was fed by a coal feeder at a rate of 1.5 g/hr. The flow rate through the furnace was 3 lpm. The dilution flow rate downstream furnace was 5 lpm, resulting in a total flow rate of 8 lpm. The furnace temperature was controlled at 1100 °C. The particle size distribution in the range of less than 420 nm was measured by a scanning mobility particle sizer (SMPS, Model 3080, TSI Inc., Shoreview, MN, USA), whose sheath flow and inlet aerosol flow were fixed at 6 lpm and 0.3 lpm, respectively, for India and US coal. For china coal, however, the sheath flow and inlet aerosol flow were 10 lpm and 0.3 lpm, respectively, since the corresponding fly ash dominated at lower size range. The particle size distribution in the range of larger than 500 nm was measured by an Aerodynamic Particle Sizer (APS, Model 3321, TSI Inc.). In the charged fraction study, a charged particle remover (CPR) was installed to remove all the charged particles in the flue gas. The CPR can remove nearly 100% of charged particles at ± 2 kV, ± 3 kV and ± 4 kV, so the voltage is controlled at -2 kV for all measurements of charged fraction. A dilution tube was placed upstream the ESP to maintain high flow rate (56 lpm with dilution ratio of 7) and low residence time (0.49 s with a face velocity of 0.52 m/s) in the ESP, which is close to industrial operating condition. The configuration of ESP is described previously (Z. Li et al., 2016). The fly ash was collected by a Quartz filter and its resistivity was tested by a powder resistivity test cell (Model 828M, Electro-Tech Systems, Inc.).
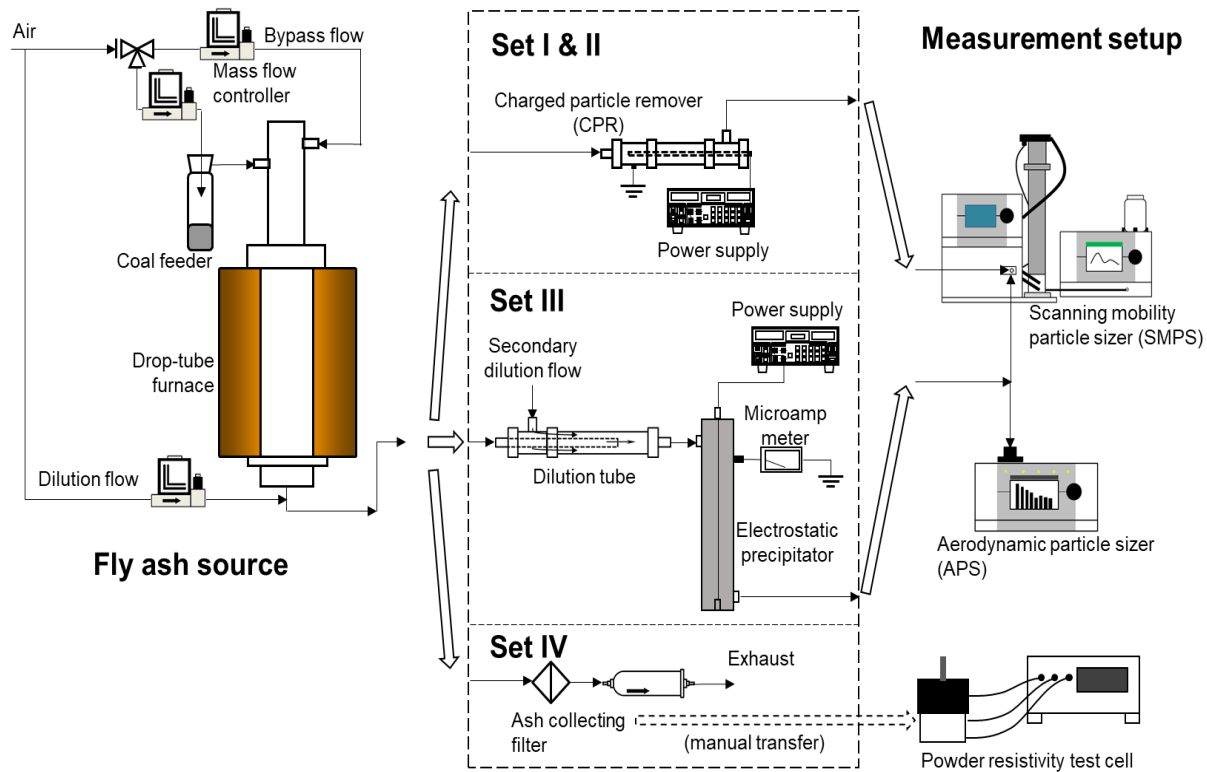
Figure 3.1 Schematic of the experimental setup.

3.2.2 Experimental plan

Three types of coal, Chandrapur coal from India, Shaanxi coal from China, and Powder River Basin coal from the US were studied. Their proximate and ultimate analyses are shown in Table 3.1 and Figure 3.2. The sizes of coal particles were between 25 μm and 45 μm. The rank of coal is typically determined by fixed carbon, moisture, volatile matter and heating value. A high-rank coal usually has high fixed carbon and heating value (Schweinfurth, 2009). It can be observed from Figure 3.2 that China coal has considerably high fixed carbon, while US coal has the highest heating value. Therefore, China and US coals are considered as coals with higher rank than India coal, which has higher ash content.

Table 3.1 Proximate and ultimate analyses of experimented coals.

Coal type	Proximate Analysis (wt %)				Ultimate Analysis (wt %)					$Q_{net,d}$ (MJ/kg)
	Moisture	Ash	VM[1]	FC[2]	C	H	O	S	N	
India[3] Chandrapur *(Lignite)*	5.00	47.00	20.50	27.50	37.69	2.66	5.78	0.80	1.07	15.28
US[4] PRB *(Sub-bituminous)*	20.70	8.00	28.40	42.90	67.30	4.58	19.92	0.57	0.96	28.04
China[4] Shaanxi *(Sub-bituminous)*	0.71	26.43	16.06	57.51	62.60	3.23	4.59	2.30	0.85	24.67

Note: 1: volatile matter; 2: fixed carbon; 3: Ohio Supercomputer Center, "Anthropogenic Emissions from energy activities in India: Generation and Source Characterization", https://www.osc.edu/research/archive/pcrm/emissions/coal; 4: Analyses supplied by Ameren UE.

(a)   (b)
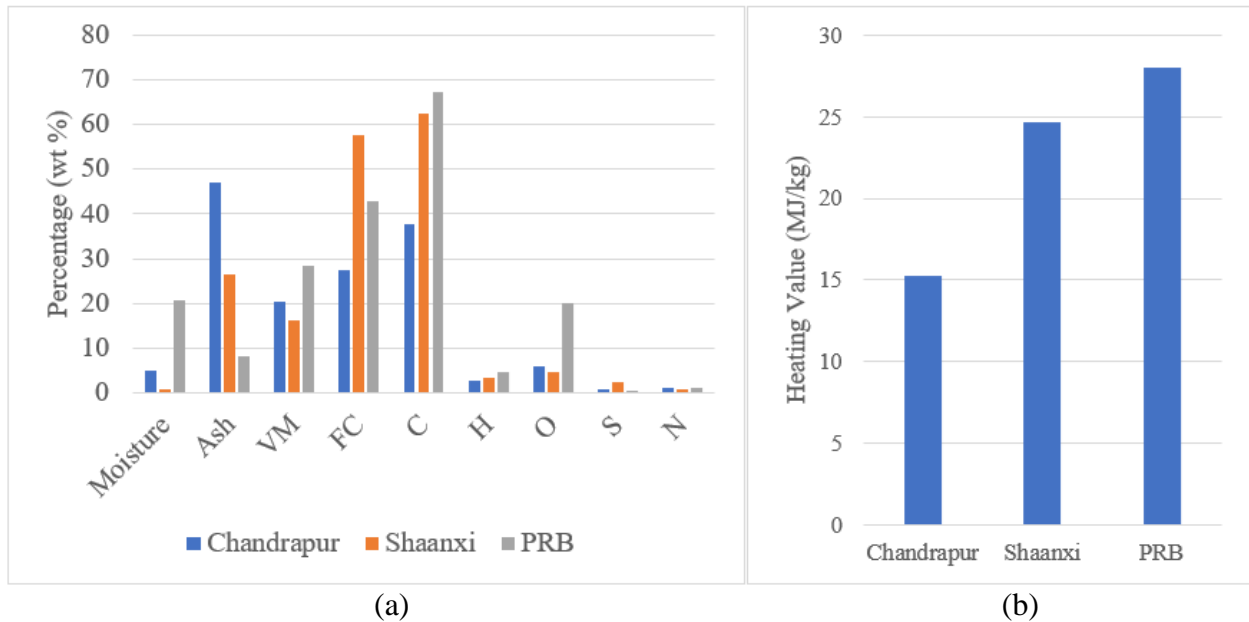
Figure 3.2 Comparison of (a) compositions and (b) heating value for three coal seams.

In experiment set I and II, the total particle concentration and uncharged particle concentration as functions of particle diameter were measured when the CPR was off and on, respectively. Thus, the charged particle fraction can be calculated for each size by using Eq. (3.1a). For set III, particle number concentration at downstream the ESP with various voltages were tested and thus the

particle collection efficiency can be calculated using Eq. (3.1b). In set IV, the fly ash generated from combustion of three types of coal is collected and tested by the resistivity test system separately. The experimental design is shown in Table 3.2.

$$f(d_p) = 1 - \frac{n(d_p)_{CPR\_on}}{n(d_p)} \tag{3.1a}$$

$$\eta(d_p) = 1 - \frac{n(d_p)_{ESP\_on}}{n(d_p)} \tag{3.1b}$$

Table 3.2 Summary of performed experiments.

Set	Coal	CPR	ESP	Instrument	Objective
I	India Chandrapur coal; China Shaanxi coal; US PRB coal (respectively)	off	N/A	SMPS	Total particle number concentration; size distribution
II		-2 kV	N/A	SMPS	Uncharged particle concentration; charged fraction
III		N/A	±8 kV; off (for blank)	SMPS, APS	ESP collection efficiency size distribution
IV		N/A	N/A	Ash resistivity test cell	Fly ash resistivity

3.3   Results and discussion

3.3.1 Particle size distributions

Figure 3.3(a) and 3.3(b) show the size distributions of particles with diameters between 10 nm to 20 μm for coal fly ash generated from combustions of three coals measured by SMPS and APS, respectively. The CPR was turned off when these measurements were performed. The geometric mean sizes for the fly ashes of US, India and China coals were 43.5 nm, 29.6 nm and 13.3 nm, respectively. For the SMPS measurements, the US coal fly ash showed the largest geometric mean

size with higher total concentration. Because US and India coal were low-rank, they tended to have more porosity and higher reactivity, which resulted in more rapid burning. Therefore, the particle size distributions evolved more quickly and displayed much larger geometric mean sizes for both US and India coals. In addition, low-rank coals contained more incombustible minerals, so those incombustible ash particles could be wrapped with organic compounds after char oxidation to form larger particles eventually (Dunn-Rankin et al., 1987). On the other hand, China coal was a higher-rank coal with lower ash content, and it had more fixed carbon. Smaller soot particles might form after char oxidation, which resulted in a smaller particle size distribution for China coal.
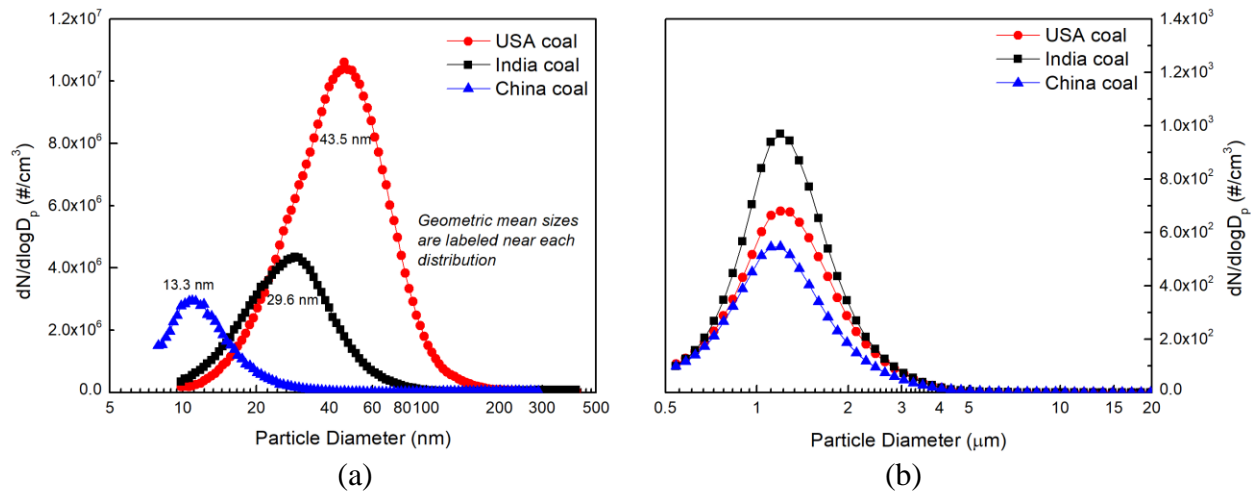
Figure 3.3 Size distributions of particles with diameters between 10 nm to 20 µm for coal fly ash generated from combustions of three coals: (a) SMPS and (b) APS.

Table 3.3 summarizes the total number concentration and mass concentrations for fly ash of different coal combustion. And number and mass concentration ratios of fine to coarse particles are showed in Figure 3.4. The US coal shows the highest number and mass concentration fine/coarse ratios, and its mass ratio is reasonably close to the value (0.97) reported by Suriyawong (Suriyawong et al., 2006). The US coal had more volatile matter content, which could facilitate the dominant mechanism of submicrometer particle formation including vaporization, nucleation,

71

condensation and coagulation (Damle et al., 1981). This fact can explain why it shows the highest

fine-to-coarse ratios.

Table 3.3 Total number and mass concentrations for fly ash of different coal combustion.

Coal	Total number concentration ($\#/cm^3$) (<500 nm)	Total number concentration ($\#/cm^3$) (>500 nm)	Number Ratio (fine/coarse)	Total mass concentration (ug/m^3) (<500 nm)	Total mass concentration (ug/m^3) (>500 nm)	Mass Ratio (fine/coarse)
India	1.96×10^6	526	3.73×10^3	568.0	1377.6	0.41
US	5.12×10^6	382	1.34×10^4	780.4	721.6	1.08
China	9.22×10^6	304	3.03×10^3	198.8	465.6	0.43
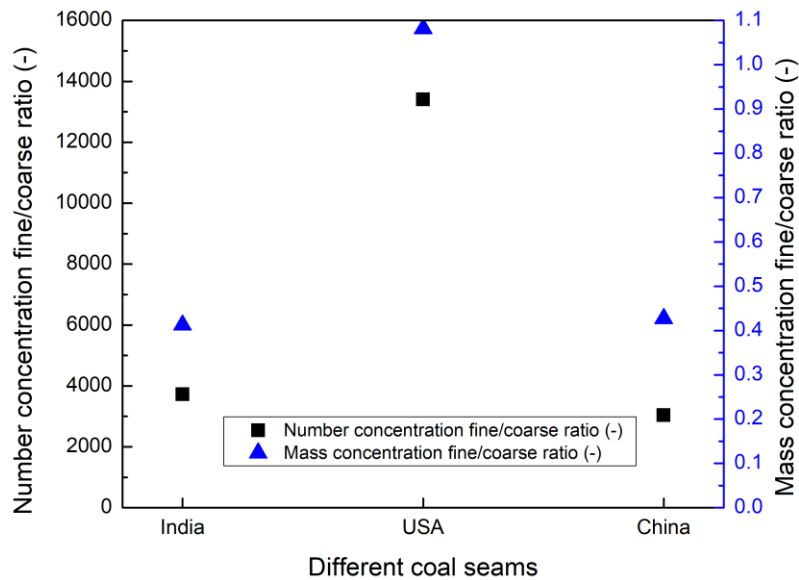
Figure 3.4 Number and mass concentration ratios of fine (<500 nm) to coarse (>500 nm) particles.

3.3.2 Charge particle fractions

Figure 3.5(a) shows the particle size distributions of both total particles and uncharged particles,

and Figure 3.5(b) shows the charged particle fractions of fly ash with diameter less than 100 nm

from different coal combustion. The total charged fraction by number of fly ash particles is 54%,

44% and 53% for India, USA and China coal, respectively. Although India coal combustion

72

generated less particles as indicated by Figure 3.5(a), but a larger portion of charged particles was observed. For both India and US coals, uncharged particles show lower geometric mean sizes than total particles. As shown in Figure 3.5(b), charged particle fraction increased from 30% at 20 nm to 80% at 100 nm for India coal fly ash. Similar trend was observed for US coal fly ash particles. However, the fractions of charged particles in US coal fly ash were lower than those for India coal fly ash. The rising charged particle fraction along with increasing particle diameter can be attributed to the fact that larger particles have more surface area available for ions and electrons attachment. This result is consistent with other studies (Sahu et al., 2012). Jiang reported that the charge attachment coefficient of particles is positively proportional to particle diameter (Jiang et al., 2007). Moreover, it can be speculated that charged fractions of larger India and US fly ash were governed by thermo-ionization charging. The equation of thermo-ionization yield coefficient is reported by Richardson and Dushman (Dushman, 1923):

$$\gamma^+(v,q) = AT^2 \exp\left(-\frac{\pi(v,q)}{k_B T}\right)\frac{4\pi a^2}{e} \tag{3.2}$$

where $\pi(v,q)$ is the work function of particle material, T is temperature, A is a constant dependent on material and a is particle radius. India coal fly ash had significantly more ash content than fixed carbon, and metal typically has lower work function than carbon. Based on the Eq. (3.2), it is reasonable that India coal fly ash had higher thermo-ionization yield coefficient and thus higher charged particle fraction. On the other hand, China coal fly ash had higher charged fraction over the entire concerned size range probably due to the dominance of diffusion charging mechanism in smaller size range.
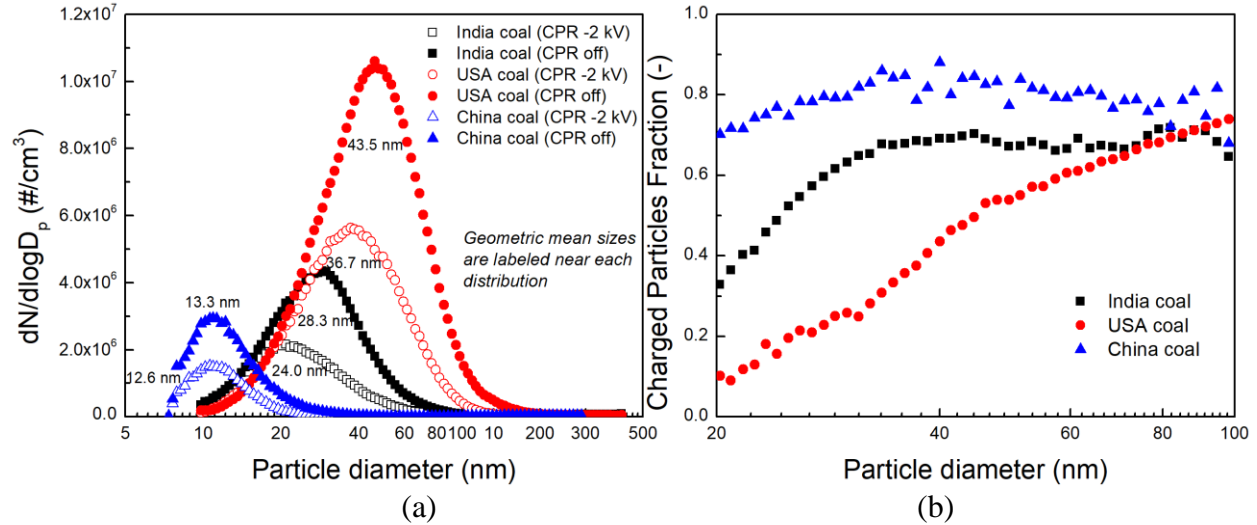
Figure 3.5 (a) Particle size distributions of total and uncharged particles with diameter less than 500 nm; (b) Charged particle fraction of fly ash with diameter less than 100 nm from different coal combustion.

3.3.3 Fly ash resistivity

The reason why fly ash resistivity was examined was that effective ESP operation greatly depends on the particle resistivity. If high volume of particles with high resistivity are deposited on the collecting electrode, an electric field across the duct layer can form and even ionize the gas in local pores. Those ions and electrons generated in dust layer can neutralize charged particles and thus suppress the migration of particles towards the collecting electrode, leading to lower removal efficiency. This phenomenon was widely reckoned as back corona. For appropriate ESP operation, the resistivity of fly ash was commonly considered between 10^7 and 10^{11} $\Omega \cdot$cm under various temperature conditions (Zheng et al., 2017).

Figure 3.6(a) and 3.6(b) show the correlations of resistivity with carbon and ash content in three coals, respectively. It is observed that India coal fly ash has the highest resistivity, while China and US coal fly ashes have relatively lower resistivity. It is interestingly illustrated by Figure 3.6(a) that the carbon percentage correlates with the ash resistivity quite well. It was reported by Zheng that high-carbon fly ash particles are typical particles with low resistivity (Zheng et al., 2017), so

it might be implied that US coal fly ash contained more carbon, which came from generated organic compounds during combustion. For India coal fly ash, Chandra (Chandra, 2009) also studied several types of India coals and found that the fly ash resistivity of common India coals was in the range between 10^{11} and 10^{13} $\Omega\cdot$cm, which is consistence with the measured value in this study. Based on the values of resistivity for three coal fly ashes, it could be indicated that India coal fly ash is most difficult to be effectively removed by ESP, while US coal fly ash might suffer less from potential back corona effect.
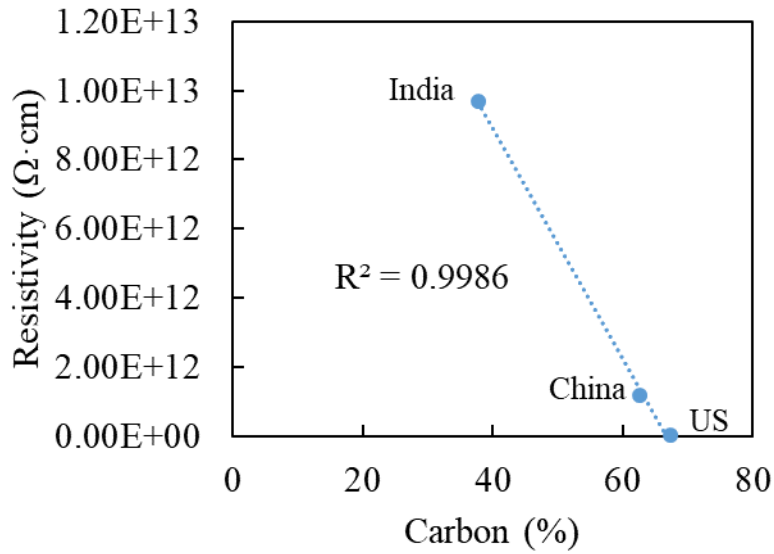
(a)
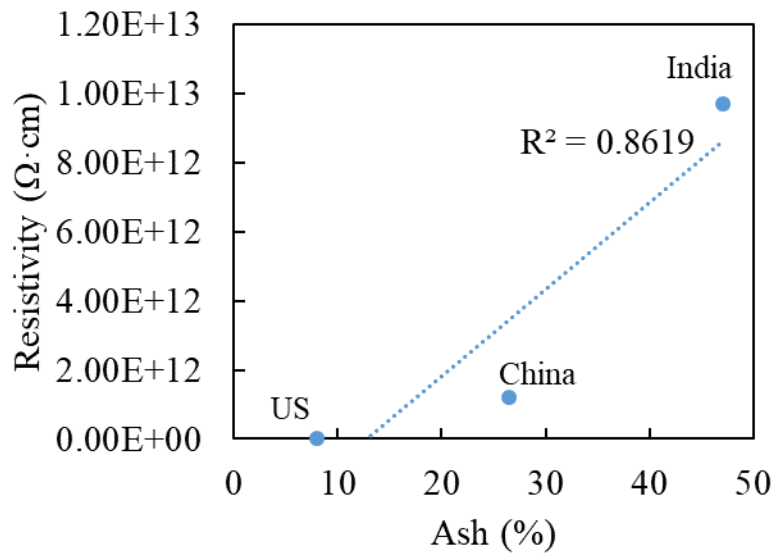
(b)

Figure 3.6 Correlations of resistivity with (a) carbon and (b) ash content in three coals.

3.3.4 ESP collection efficiency

Figure 3.7 shows the ESP collection efficiency of fly ash from combustion of India, US and China

coals in different size ranges. For submicrometer size range as shown in Figure 3.7(a), the ESP

operated at -8 kV and 5 µA could collect most of the fly ash whose diameter were less than 500

nm of US coal and India coal, while China coal displayed significantly lower collection efficiency

around 100 nm. There is a penetration window at 20-40 nm for US PRB coal, which is on the left side of the peak diameter (48 nm) of its submicrometer particle size distribution. However, the penetration window for India Chandrapur coal is from 30 to 150 nm, much wider than that of US coal. Moreover, the penetration window resides on the right side of the peak diameter (22 nm) of its submicrometer particle size distribution. The center diameter of penetration window for China Shaanxi coal is much larger than those of other two coals. This observation might indicate possible back corona occurrence, because China coal fly ash had high resistivity, which could reduce effective voltage and particle migration velocity. Particularly, the fly ash with diameter between 100 and 200 nm displays significantly low collection efficiency. These observations illustrate the remarkable distinction in electrostatic collection between the fly ashes from combustion of three coals.

As illustrated by Figure 3.7(a), (b) and (c), increase in voltage and current raised the collection efficiency remarkably for all three coal fly ashes. In addition, the collection efficiency increased as the particle diameter increased, which means that large particles tended to be collected more easily. Notably, there are flat areas in the size range from 500 nm to 1 µm with low collection efficiency for both India and China coal fly ashes when the ESP voltage was -8.1 kV, which might be caused by back corona effect. As particle size increased, the collection efficiency eventually broke out of the flat regions and increased further. This observation indicates that larger particles probably with more charges were more resistant to back corona, while small particles with few charges can be easily neutralized due to the backward electric field in dust layer. Nonetheless, the back corona problem was less prominent as the ESP voltage increased since the dust-layer electric field was overwhelmed by the applied external electric field.
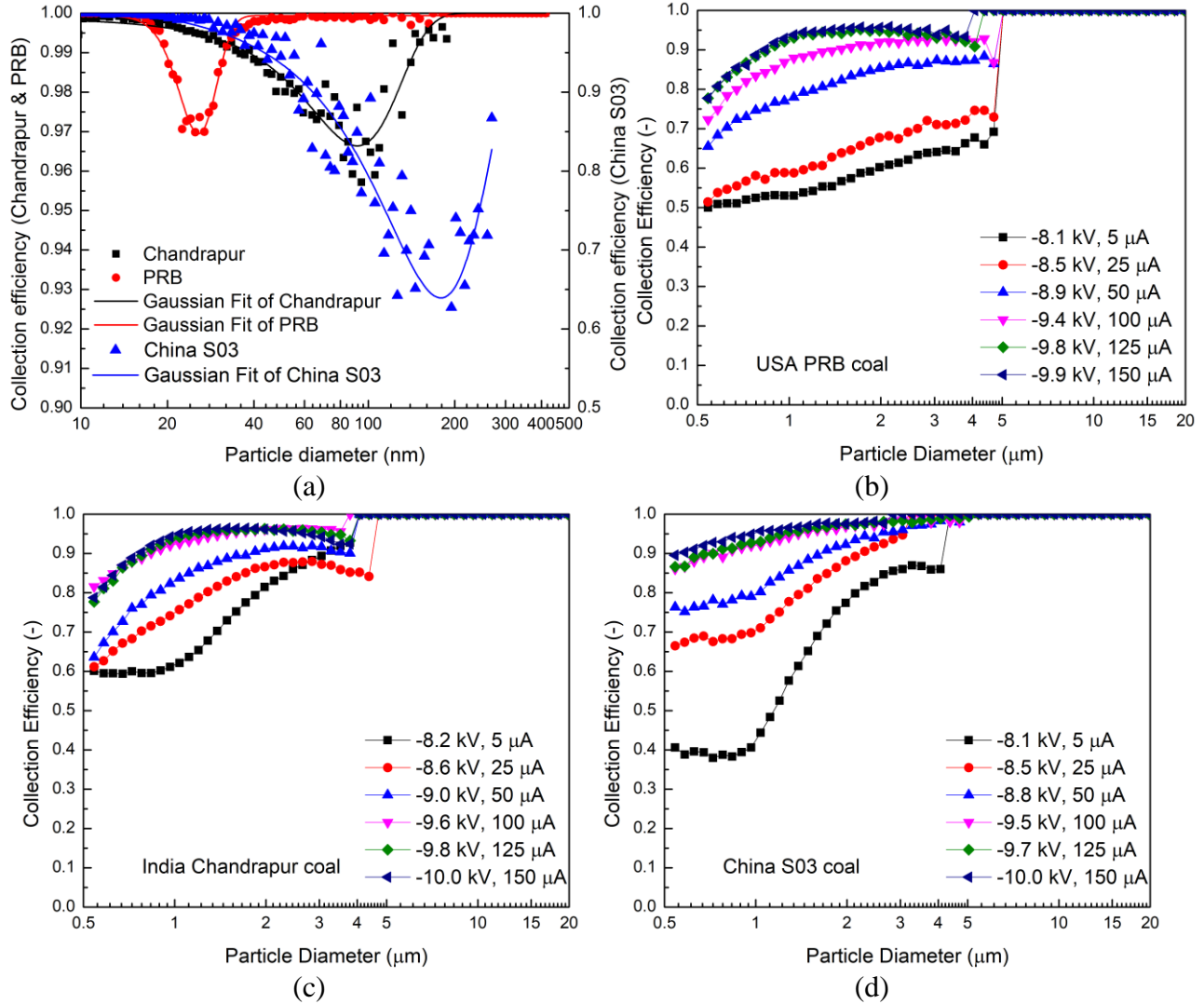
Figure 3.7 Comparison of ESP collection efficiency of fly ash from combustion of India, US and China coal. (a) in the diameter range of 10 – 420 nm, ESP -8.2 kV and 5 µA; (b), (c) and (d) are in the diameter range of 0.5 – 20 µm for US, India and China coal, respectively.

3.4 Conclusion

The size distributions of particle number concentration, charged fraction, ash resistivity and electrostatic collection efficiency were investigated for three coals from India, US and China. The fly ashes of low-rank US and India coals had higher concentration and geometric mean size than the China coal fly ash. The US coal shows the highest number and mass concentration fine/coarse ratios, which are 1.34×10^4 and 1.08, respectively.

The total charged fraction by number of fly ash particles is 54%, 44% and 53% for India, USA and China coal, respectively. Charged particle fraction increased with growing particle size for submicrometer fly ashes produced by combustion of India and US coals, which was probably governed by thermo-ionization charging. Smaller China coal fly ash had higher charged particle fraction possibly due to diffusion charging.

Besides, India and China coal fly ashes had higher ash resistivity than the US coal fly ash, so they were more prone to the back corona effect. The ESP collection tests evidenced that smaller particles with diameter less than 1 µm for high resistivity coal fly ashes suffered more significantly from back corona. Notably, back corona effect was shadowed by higher ESP voltage. The results in this study can provide valuable insights for establishment of particle control technology for combustion of different coal seams.

3.5 References

Bai, M., Wang, S., Chen, Z., Leng, H., & Mao, S. (2010). The Effects of Submicrometer Dust Charging and Coagulation on ESP Efficiency by Using Alternating Electric Field. *Ieee Transactions on Plasma Science, 38*(2), 127-132. doi:10.1109/tps.2009.2037888

Cao, J.-j., Wang, Q.-y., Chow, J. C., Watson, J. G., Tie, X.-x., Shen, Z.-x., . . . An, Z.-s. (2012). Impacts of aerosol compositions on visibility impairment in Xi'an, China. *Atmospheric Environment, 59*, 559-566. doi:https://doi.org/10.1016/j.atmosenv.2012.05.036

Chandra, A. (2009). Some investigations on fly ash resistivity generated in Indian power plants *Electrostatic Precipitation* (pp. 399-405): Springer.

Chowdhury, Z., Zheng, M., Schauer, J. J., Sheesley, R. J., Salmon, L. G., Cass, G. R., & Russell, A. G. (2007). Speciation of ambient fine organic carbon particles and source apportionment of PM2. 5 in Indian cities. *Journal of Geophysical Research: Atmospheres, 112*(D15).

Damle, A., Ensor, D., & Ranade, M. (1981). Coal combustion aerosol formation mechanisms: a review. *Aerosol Science and Technology, 1*(1), 119-133.

Dunn-Rankin, D., Hoornstra, J., Gruelich, F., & Holve, D. (1987). Combustion of coal—water slurries: Evolution of particle size distribution for coals of different rank. *Fuel, 66*(8), 1139-1145.

Dushman, S. (1923). Electron emission from metals as a function of temperature. *Physical Review, 21*(6), 623.

EIA, U. E. I. A. (2016). International energy outlook 2016.

Gilmour, M. I., O'Connor, S., Dick, C. A., Miller, C. A., & Linak, W. P. (2004). Differential pulmonary inflammation and in vitro cytotoxicity of size-fractionated fly ash particles from pulverized coal combustion. *Journal of the Air & Waste Management Association, 54*(3), 286-295.

Gummeneni, S., Yusup, Y. B., Chavali, M., & Samadi, S. (2011). Source apportionment of particulate matter in the ambient air of Hyderabad city, India. *Atmospheric Research, 101*(3), 752-764.

Hu, J., Wu, L., Zheng, B., Zhang, Q., He, K., Chang, Q., . . . Zhang, H. (2015). Source contributions and regional transport of primary particulate matter in China. *Environmental Pollution, 207*, 31-42.

Huang, R.-J., Zhang, Y., Bozzetti, C., Ho, K.-F., Cao, J.-J., Han, Y., . . . Canonaco, F. (2014). High secondary aerosol contribution to particulate pollution during haze events in China. *Nature, 514*(7521), 218.

Huang, S.-H., & Chen, C.-C. (2002). Ultrafine aerosol penetration through electrostatic precipitators. *Environmental Science & Technology, 36*(21), 4625-4632.

Jiang, J., Lee, M.-H., & Biswas, P. (2007). Model for nanoparticle charging by diffusion, direct photoionization, and thermionization mechanisms. *Journal of Electrostatics, 65*(4), 209-220. doi:10.1016/j.elstat.2006.07.017

Kim, Y. H., Krantz, Q. T., McGee, J., Kovalcik, K. D., Duvall, R. M., Willis, R. D., . . . Gilmour, M. I. (2016). Chemical composition and source apportionment of size fractionated particulate matter in Cleveland, Ohio, USA. *Environmental Pollution, 218*, 1180-1190.

Laden, F., Neas, L. M., Dockery, D. W., & Schwartz, J. (2000). Association of fine particulate matter from different sources with daily mortality in six US cities. *Environmental Health Perspectives, 108*(10), 941.

Li, Y., Suriyawong, A., Daukoru, M., Zhuang, Y., & Biswas, P. (2009). Measurement and capture of fine and ultrafine particles from a pilot-scale pulverized coal combustor with an electrostatic precipitator. *Journal of the Air & Waste Management Association, 59*(5), 553.

Li, Z., Jing, H., & Biswas, P. (2016). Capture of submicrometer particles in a pressurized electrostatic precipitator. *Aerosol Science and Technology, 50*(10), 1115-1129.

Maricq, M. (2004). Size and charge of soot particles in rich premixed ethylene flames. *Combustion and flame, 137*(3), 340-350.

McCain, J. D., Gooch, J. P., & Smith, W. B. (1975). Results of field measurements of industrial particulate sources and electrostatic precipitator performance. *Journal of the Air Pollution Control Association, 25*(2), 117-121.

Sahu, M., Park, J., & Biswas, P. (2012). In Situ Charge Characterization of TiO2 and Cu–TiO2 Nanoparticles in a Flame Aerosol Reactor. *Journal of Nanoparticle Research, 14*(2), 1-11.

Schweinfurth, S. P. (2009). An introduction to coal quality. *The National Coal Resource Assessment Overview: US Geological Survey Professional Paper*.

Suriyawong, A., Gamble, M., Lee, M.-H., Axelbaum, R., & Biswas, P. (2006). Submicrometer particle formation and mercury speciation under O-2-CO2 coal combustion. *Energy & Fuels, 20*(6), 2357-2363. doi:10.1021/ef060178s

Suriyawong, A., Hogan, C. J., Jr., Jiang, J., & Biswas, P. (2008). Charged fraction and electrostatic collection of ultrafine and submicrometer particles formed during O(2)-CO(2) coal combustion. *Fuel, 87*(6), 673-682. doi:10.1016/j.fuel.2007.07.024

Ylätalo, S. I., & Hautanen, J. (1998). Electrostatic precipitator penetration function for pulverized coal combustion. *Aerosol Science and Technology, 29*(1), 17-30.

Yoo, K. H., Lee, J. S., & Oh, M. D. (1997). Charging and collection of submicron particles in two-stage parallel-plate electrostatic precipitators. *Aerosol Science and Technology, 27*(3), 308-323.

Zhang, Y.-L., & Cao, F. (2015). Fine particulate matter (PM2. 5) in China at a city level. *Scientific Reports, 5*.

Zheng, C., Shen, Z., Chang, Q., Su, Q., Zhu, X., & Gao, X. (2017). Experimental study on electrostatic precipitation of low-resistivity high-carbon fly ash at high temperature. *Energy & Fuels, 31*(6), 6266-6273.

Zhuang, Y., & Biswas, P. (2001). Submicrometer particle formation and control in a bench-scale pulverized coal combustor. *Energy & Fuels, 15*(3), 510-516. doi:10.1021/ef000080s

Zhuang, Y., Kim, Y. J., Lee, T. G., & Biswas, P. (2000). Experimental and theoretical studies of ultra-fine particle behavior in electrostatic precipitators. *Journal of Electrostatics, 48*(3-4), 245-260. doi:10.1016/s0304-3886(99)00072-8

Chapter 4: Effects of pressure on mineralogy, morphology and chemical composition of coal fly ashes

The results of this chapter will be compiled as a paper for submission to Aerosol and Air Quality Research (Wang Z., Li, Z., Ma, S., Zheng, S., & Biswas, P. Effects of pressure and coal type on characteristics of coal fly ash and submicrometer particle size distribution).

Abstract

Pressurized oxy-coal combustion has been studied as a promising technology in the context of carbon capture and storage because it can enhance plant energy efficiency without additional gas compression cost. Characterization of submicrometer particles in high pressure coal combustion exhaust can provide crucial information for efficiency particle control in the system. This study was to investigate the effects of combustion pressure and coal seams from India, US and China on submicrometer particle size distribution in coal combustion exhaust gas and properties of coal fly ash and. The size distribution of submicrometer particles in coal combustion exhaust gas for US Powder River Basin (PRB) sub-bituminous coal was observed with a larger peak size and higher number concentration than those for India Chandrapur lignite and China S02 lignite, while the submicrometer particle size distribution for China S02 lignite had the smallest peak size and the lowest number concentration. As pressure was elevated, the total number concentration of submicrometer particles was reduced and the peak size increased for all three coals. Chemical composition analysis showed that US PRB coal fly ash was mainly composed of Si, Ca, Al, and Fe, with a higher Ca content and lower Al content than India Chandrapur and China S02 coal fly ashes. India Chandrapur coal fly ash had the highest Si content, while China S02 coal fly ash is the richest in Al. For all three coals, more volatile species (Na, Mg, Fe, and Ca) were enriched in the submicrometer particles generated from pressurized combustion.

4.1 Introduction

Although various renewable energy sources such as wind, solar and nuclear energy have emerged over the past few decades, coal combustion is still a dominant source for electricity around the globe. Coal combustion accounted for 33%, 72%, and 77% of the electricity generation in the US, China, and India, respectively (EIA, 2017a, 2017b). In addition, China, India and the US are the

top three countries in coal consumption worldwide. China, the US, and India respectively accounted for 50.2%, 11.7%, and 8% of global coal consumption in 2012 (Yao et al., 2015). The large usage of coal generates huge amount of fly ash in the exhaust gas of coal boilers. There were approximately 580, 160, and 130 million tons of coal fly ash produced in China, India, and the US in 2015, respectively, which pose great challenges for appropriate disposal and re-utilization (Ding et al., 2017; Yao et al., 2015). Notably, the mineralogy, morphology, and chemical composition of coal fly ash are crucial information in designing processes for its re-utilization (Ding et al., 2017; Luo et al., 2016; Z. Wang et al., 2016; Yao et al., 2015). Moreover, many toxic metals (Biswas et al., 1998; Suriyawong et al., 2009; Lei Zhang et al., 2013), organic constituents (Xiaofei Wang et al., 2015; X Wang et al., 2013), and hazardous submicrometer particles (Li et al., 2009; Linak et al., 2007; Lei Zhang et al., 2013; Zhuang et al., 2001) are released into the ambient air after coal combustion, which seriously compromises environmental safety and sustainability. In particular, submicrometer particles are typically generated in high concentrations and often enriched in toxic metallic species, and they can penetrate deeply into the bronchioles and alveoli of the human lung, causing serious public health concerns (Zhuang et al., 2001). Therefore, it is imperative to advance our understanding of the physical and chemical characteristics of submicrometer particles in the exhaust gas of coal combustion.

Characterization of mineralogy, chemical composition, and morphology of coal fly ash from different coal fired power plants have been extensively reported (Chancey et al., 2010; Furuya et al., 1987; Gutiérrez et al., 1993; Levandowski et al., 2009; McCarthy et al., 1984; Medina et al., 2010; Moreno et al., 2005; Nathan et al., 1999; Norton et al., 1986; Qi et al., 2011; Vempati et al., 1994). Although those studied coal fly ashes were sampled from plants in different countries, there is no comparative investigation that we are aware of on coal fly ashes from the US, India, and

China. Examination of coal fly ashes from those three countries can provide valuable information for cost-effective particle emission control over the regions with significant coal consumption.

Notably, pressurized oxy-combustion, which was demonstrated to be capable of increasing combustion energy efficiency without incurring additional cost for carbon capture and sequestration, is considered as a promising alternative to conventional coal combustion (Gopan et al., 2014; Hong et al., 2009). To better understand how the particles can be removed in high pressure combustion system, the chapter 2 of this dissertation investigated the influence of gas pressure on the submicrometer particle capture performance of an electrostatic precipitator (ESP). However, the pressurized ESP performance depends greatly upon particle properties under various pressure and temperature, which is not well understood. There are a few studies on effects of coal combustion conditions on particle size distributions in coal combustion exhaust gas. Zhang (Lei Zhang et al., 2013) investigated the effects of different Chinese coal seams, coal feeding rate, and size of coal powders on submicrometer particle size distribution. Zhuang (Zhuang et al., 2001) studied the effects of temperature and residence time on submicrometer particle size distribution. Jia (Jia et al., 2012) examined the effects of temperature, coal type, and gas phase conditions on particle formation. Wu (H. Wu et al., 2000) studied the effect of pressure in the coal combustor on micrometer particle size distribution, and they found that as the pressure increased, the ash particles became finer due to higher proportions of porous char particles which fragment into fine ash particles. However, to the best of our knowledge, the effects of pressure on submicrometer particle size distribution and on the characteristics of coal fly ash have not been well studied.

This study focuses on investigating the effects of pressure and coal type on various characteristics of coal fly ash and the submicrometer particle size distribution. Fly ash samples were produced by combustion of coals from the US, India, and China in a laboratory-scale drop-tube furnace under

different pressures. The submicrometer particle size distribution, mineralogy, morphology, and chemical composition of the generated fly ashes were examined. This study of the characteristics of submicrometer particles and coal fly ash generated from pressurized combustion systems, can provide insights for more effective capture of submicrometer particles in pressurized particle collection devices and re-utilization of coal fly ashes generated from pressurized combustion of coal from the US, India, and China.

4.2 Experimental section

4.2.1 Experimental system

As shown in Figure 4.1, the experimental setup consists of a fluidized bed coal feeder, a drop tube furnace (Lindberg Blue M, Model HTF55342C, ThermoElectron Co.) containing an alumina tube with an inner diameter of 5.72 cm and a length of 121.92 cm, a cascade impactor (Mark III, Pollution Control System Co.), a scanning mobility particle sizer (SMPS, TSI Inc.), and a filter (A polycarbonate membrane with 0.2 μm pore size and 47 mm diameter, Isopore). Three different kinds of coals were selected: US Powder River Basin (PRB) sub-bituminous coal, China S02 lignite coal, and India Chandrapur lignite coal. The coals were pulverized and coal samples with particle sizes ranging from 0–45 μm were prepared using American standard sieves. 3 g coal samples dried at 105 $^{\circ}$C were loaded in the tube of fluidized bed coal feeder. The feed rates of coals were fixed at 1 g/h. 1 lpm of particle–free air stream controlled by a mass flow controller was introduced into the tube of fluidized bed coal feeder to carry the coal particles into the drop tube furnace, and another 2 lpm of particle–free air stream controlled by a mass flow controller was introduced at the inlet of the drop tube furnace directly; therefore, a total of 3 lpm of carrier gas passed through the heated alumina tube to achieve complete char burnout. The temperature in the heated drop tube furnace was held constant at 1100 $^{\circ}$C. At the exit of the furnace, 5 lpm of

87

particle–free dilution air controlled by a mass flow controller was added to quench the aerosol dynamics. To create high experimental pressures, an orifice was placed downstream of the furnace outlet and the dilution flow was adjusted to obtain different pressures. The valve of the flow line with impactor was initially turned off. After the system turned stable, the flow rate of another flow line was measured so that the flow rate was equal to the flow rate of the total diluted exhaust gas. As shown in Table 4.1, the flow rate of the total diluted exhaust gas was respectively 8.2, 9.5, 14.0, and 19.3 lpm under pressures of 1, 2, 3, and 4 atm. Then, the valve of the flow line with impactor was turned on, one flow of the diluted exhaust gas passed through a six-stage cascade impactor to remove particles with diameters larger than 0.5 μm, all the remaining particles in the exhaust gas were then measured by SMPS under atmospheric pressure. All the number concentrations under various conditions were normalized by the corresponding dilution ratios. Meanwhile, a filter holder containing a circular polycarbonate membrane filter was connected to another flow line of the diluted exhaust gas, therefore, another flow of the diluted exhaust gas passed through a polycarbonate membrane filter to collect the coal fly ash particles for further characterization, the collection time for each sample was 3 h. The collected coal fly ash samples are referred to as N–P (where N is the name of the coal, and P is the pressure) in the rest of this report.
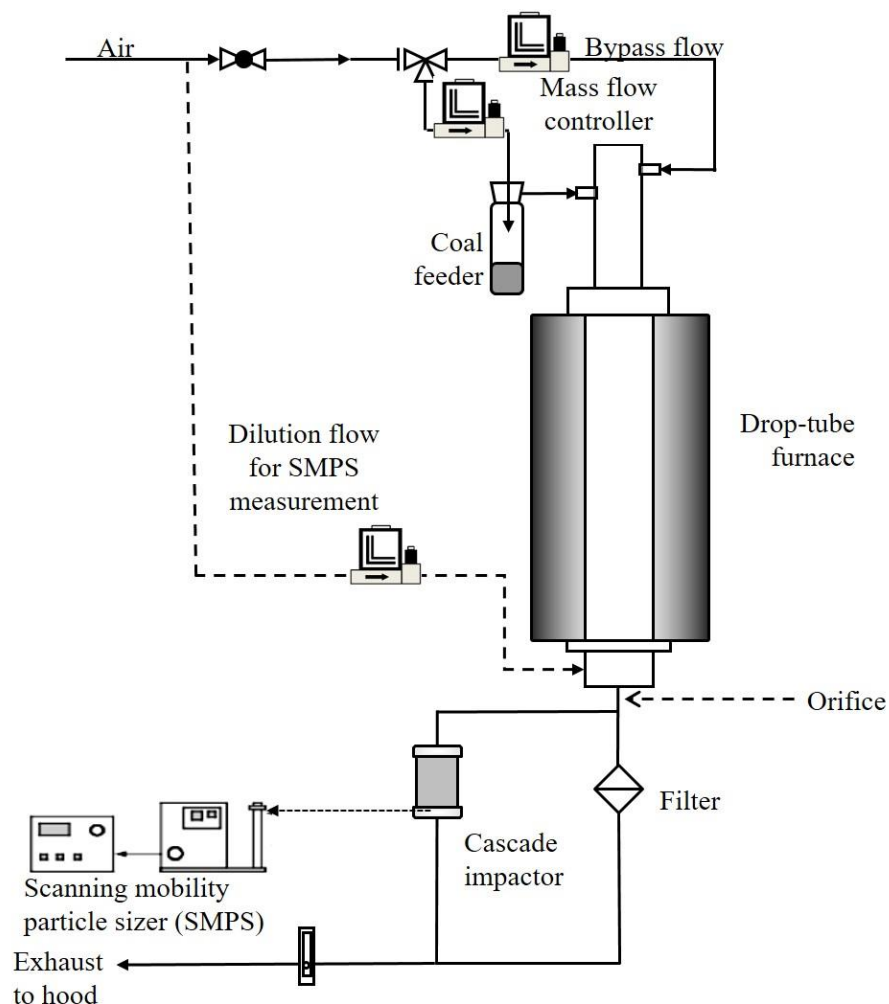
Figure 4.1 Schematic diagram of the experimental setup for coal combustion.

Downstream of the impactor, the submicrometer particles were measured by a SMPS in real time to obtain the particle size distribution in the range of 9–425 nm. The coal fly ash particles collected from the filter were characterized by X–ray diffraction (XRD, Bruker d8) to identify the mineralogy. The morphology and chemical composition were examined using a scanning electron microscope with an energy dispersive X-ray spectroscope (SEM-EDS, FEI Nova 230).

4.2.2 Experimental plan

The test plan is summarized in Table 4.1. The objective of Experimental Set I was to investigate the effect of pressure on the submicrometer particle size distribution and the characteristics of coal fly ash from the combustion of US PRB sub-bituminous coal. Experimental Set II sought to establish the effect of pressure on the submicrometer particle size distribution and characteristics of coal fly ash from the combustion of India Chandrapur lignite coal. Experimental Set III was to determine the effect of pressure on the submicrometer particle size distribution and the characteristics of coal fly ash from the combustion of China S02 lignite coal.

Table 4.1 Summary of experiments performed.

Set	Coal type	Pressure (atm)	Flow rate of exhaust gas (lpm)	Objective	Measurements
I	US PRB	1	8.2	To investigate the effect of pressure on the combustion of US PRB coal	Submicrometer particle size distribution, mineralogy, morphology & composition
		2	9.5		
		3	14.0		
		4	19.3		
II	India Chandrapur	1	8.2	To investigate the effect of pressure on the combustion of India Chandrapur coal	Submicrometer particle size distribution, mineralogy, morphology & composition
		2	9.5		
		3	14.0		
		4	19.3		
III	China S02	1	8.2	To investigate the effect of pressure on the combustion of China S02 coal	Submicrometer particle size distribution, mineralogy, morphology & composition
		2	9.5		
		3	14.0		
		4	19.3		

The analysis results of the above three different kinds of coals are listed in Table 4.2. The US PRB sub-bituminous coal has a higher fixed carbon content and higher heating value than those of China S02 lignite coal and India Chandrapur lignite coal. The XRD patterns of the three different coals are shown in Figure 4.2. They imply that quartz (SiO_2) was the main mineral in US PRB sub-bituminous coal, accompanied by some kaolinite ($Al_2O_3 \cdot 2SiO_2 \cdot 2H_2O$). India Chandrapur lignite coal was mainly composed of quartz, kaolinite, and calcite ($CaCO_3$). However, kaolinite and boehmite ($AlO(OH)$) were the dominant minerals in China S02 lignite coal. Thus, Si was the dominant mineral element in both US PRB sub-bituminous and India Chandrapur lignite, and Al was the dominant mineral element in China S02 lignite.

Table 4.2 Proximate and ultimate analyses of experimented coals.

Coal type	Proximate Analysis (wt %)				Ultimate Analysis (wt %)					$Q_{net,d}$ (MJ/kg)
	Moisture	Ash	VM[1]	FC[2]	C	H	O	S	N	
US[4] PRB *(Sub-bituminous)*	20.70	8.00	28.40	42.90	67.30	4.58	19.92	0.57	0.96	28.04
China[4] S02 *(Lignite)*	17.8	33.27	27.03	39.70	49.16	2.76	13.32	0.60	0.89	17.43
India[3] Chandrapur *(Lignite)*	5.00	47.00	20.50	27.50	37.69	2.66	5.78	0.80	1.07	15.28

Note: 1: volatile matter; 2: fixed carbon; 3: Ohio Supercomputer Center, "Anthropogenic Emissions from energy activities in India: Generation and Source Characterization", https://www.osc.edu/research/archive/pcrm/emissions/coal; 4: Analyses supplied by Ameren UE.
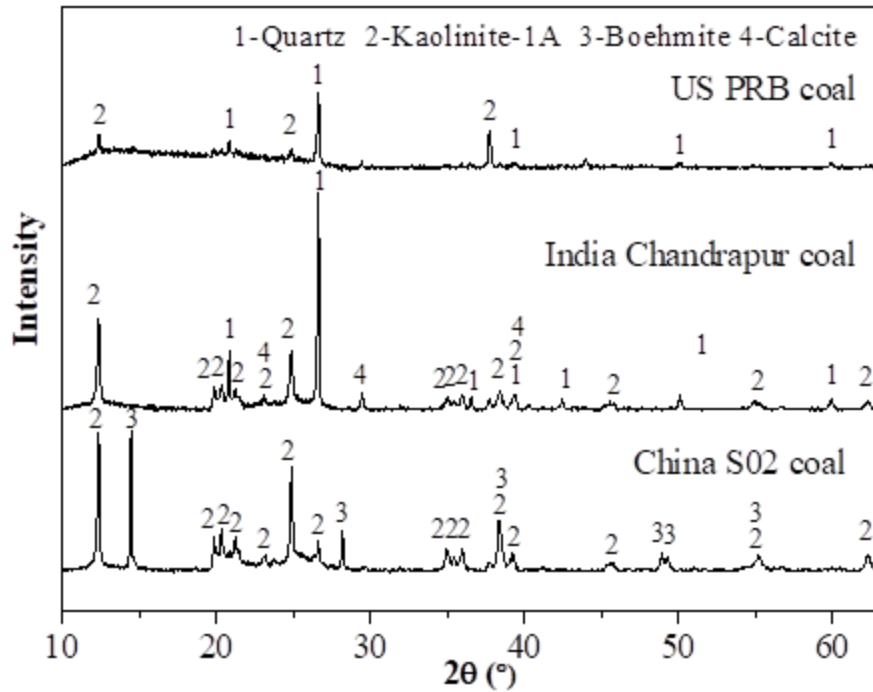
Figure 4.2 XRD patterns of different coals.

4.3 Results and discussion

4.3.1 Particle size distributions

Submicrometer particles are formed primarily through mechanisms of vaporization, nucleation, condensation, and coagulation (Linak et al., 1984; Suriyawong et al., 2006; Zhuang et al., 2001). There are two paths for vaporization: direct vaporization for volatile matter (e.g. Na, K, S, P), and chemical transformation via reduction reaction for refractory species (e.g. Mg, Ca, Fe, Si, Al) to form suboxide (SiO) or metal (Ca, Mg) vapor (Linak et al., 1984; Neville et al., 1981; Quann et al., 1982; Suriyawong et al., 2006; Zhuang et al., 2001). Therefore, the characteristics of coal samples, such as their ASTM rank (according to the fixed carbon content, volatile matter content, etc.) and their mineral composition, play important roles in the formation of submicrometer particles.

92

Figure 4.3 shows the submicrometer particle size distributions in exhaust gases produced by combustion of the three different coals under different pressures. Under the same pressure, US PRB sub-bituminous coal generated submicrometer particles with a larger peak size and higher number concentration than India Chandrapur lignite coal and China S02 lignite coal. It has been reported that the combustion rate decreases rapidly as the rank of coal increases (Haykiri-Açma et al., 2002). Also, fast chemical reactions may lead to initiation of nucleation and the formation of very small particles, whereas slower reactions and the dominance of condensation can favor the formation of larger particles (Biswas et al., 1998). Therefore, US PRB sub-bituminous coal was likely to be combusted more slowly, resulting in higher condensation and larger submicrometer particles, compared with India Chandrapur lignite coal and China S02 lignite coal. The analysis results show that US PRB sub-bituminous coal contained more volatile matter, and its dominant mineral component was SiO_2. It has been reported that during coal combustion, refractory SiO_2 can be reduced by CO to form more volatile SiO, which discharges from the burning particles and is then re-oxidized, resulting in nucleation of SiO_2 submicrometer particles (Neville et al., 1981; Quann et al., 1982; Suriyawong et al., 2006). Here, we found that combustion of US PRB sub-bituminous coal generated submicrometer particles with a high number concentration. In addition, submicrometer particles generated from combustion of China S02 lignite coal had a smaller peak size and a lower number concentration than those from the combustion of India Chandrapur lignite coal. Because Al and Si were the dominant mineral elements of China S02 lignite coal and India Chandrapur lignite coal, respectively, and nuclei with larger sizes, generated from SiO rather than from Al, might shorten the time of nucleation and coagulation, resulting in larger submicrometer particle sizes (Lei Zhang et al., 2013). Moreover, it has been reported that the vaporization rate of Si is larger than that of Al, which would contribute to the higher number concentration of

submicrometer particles from the combustion of India Chandrapur lignite coal, because SiO_2 was the dominant mineral in Chandrapur lignite (Liu et al., 2007).
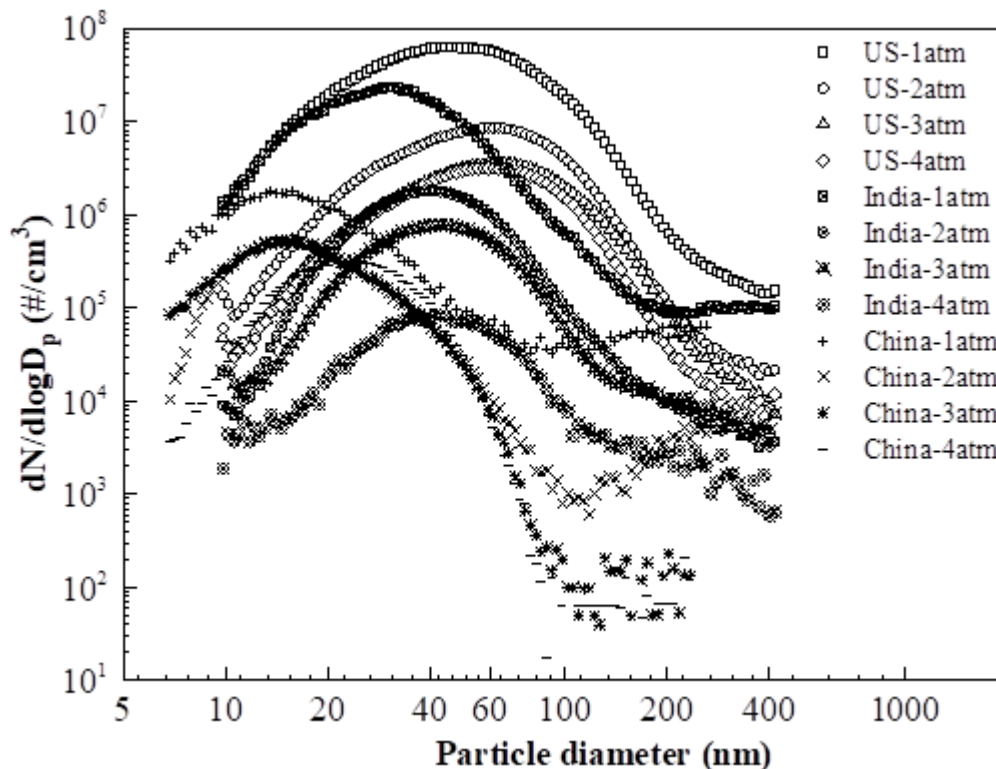
Figure 4.3 Submicrometer particle size distributions in exhaust gases generated by combustion of three coals under different pressures.

Figure 4.3 also shows the effect of pressure on the formation of submicrometer particles. With an increase in pressure, the peak sizes of the submicrometer particles in exhaust gases generated by combustions of different coals increase, as shown in Figure 4.4(a), because higher pressure led to less vaporization and condensation growth was the dominant mechanism in a limited vapor system, resulting in the formation of more large particles (C.-Y. Wu et al., 1998; Zhuang et al., 2001). Moreover, the number concentrations of submicrometer particles generated by combustion of all three different coals decrease as the pressure increases, as shown in Figure 4.4(b). In detail, the number concentrations of submicrometer particles in peak sizes generated by combustion of US PRB sub-bituminous, India Chandrapur lignite, and China S02 lignite were reduced from 6.29×10^7

94

#/cm^3, 4.12×10^7 #/cm^3, and 1.78×10^6 #/cm^3 to 3.19×10^6 #/cm^3, 8.59×10^4 #/cm^3, and 3.16×10^5 #/cm^3, respectively, when the pressure increased from 1 atm to 4 atm. These observations can be attributed to the facts that higher pressure led to less vaporization, and that condensation was the dominant growth mechanism in a limited vapor system. In addition, higher condensation could suppress nucleation, decreasing the formation of submicrometer particles by nucleation and growth (Niksa et al., 2003; Seebauer et al., 1997; Tomeczek et al., 2003; Wall et al., 2002; C.-Y. Wu et al., 1998).
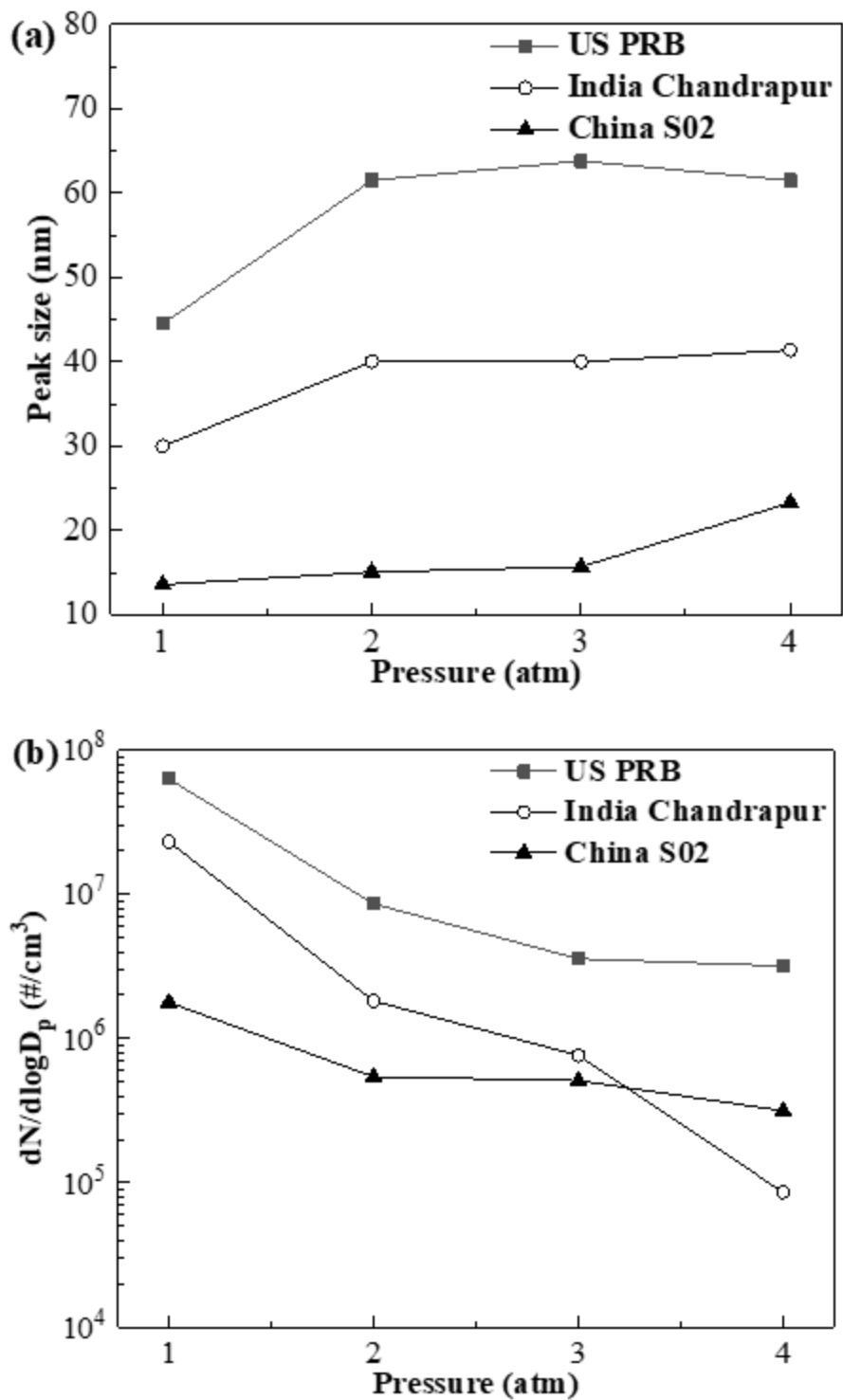
Figure 4.4 (a) Peak sizes and (b) their corresponding number concentrations for submicrometer particles in exhaust gases generated by combustion of different coals under different pressures.

4.3.2 Mineralogy

XRD patterns of coal fly ashes generated by combustion of different coals are shown in Figure 4.5. US PRB coal fly ash was mainly composed of quartz (SiO_2), anhydrite ($CaSO_4$), lime (CaO), and hematite (Fe_2O_3), while both India Chandrapur coal fly ash and China S02 coal fly ash were mainly composed of quartz and mullite ($3Al_2O_3 \cdot 2SiO_2$). The formation of mullite is attributed to the decomposition of kaolinite ($Al_2O_3 \cdot 2SiO_2 \cdot 2H_2O$), which could be further decomposed to form mullite and quartz when the temperature was higher than 1050 °C, as shown in Eq. (4.1) (Gualtieri et al., 1995; Ptáček et al., 2011).

$$3(Al_2O_3 \cdot 2SiO_2 \cdot 2H_2O) \xrightarrow{1100°C} 3Al_2O_3 \cdot 2SiO_2 + 4SiO_2 + 6H_2O \tag{4.1}$$
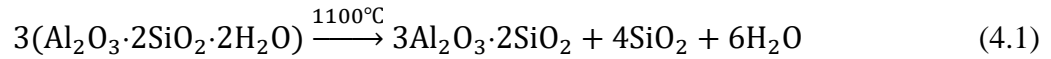
The mullite formed in China S02 coal fly ash might also result from the reaction of Al_2O_3, obtained from the decomposition of boehmite ($AlO(OH)$) in China S02 lignite coal, with SiO_2. However, mullite did not appear in the US PRB coal fly ash, which might due to the low content of kaolinite in US PRB sub-bituminous coal. This finding is consistent with the XRD results shown in Figure 4.2. In addition, Figure 4.5 implies that quartz was the main mineral in all of the three coal fly ashes, and India Chandrapur coal fly ash showed a high diffraction intensity of quartz, probably due to a high content of quartz in the original coal and a high content of kaolinite, which was decomposed to form quartz. Although China S02 lignite coal did not contain quartz, quartz was observed in the China S02 coal fly ash, this might be attributed to the decomposition of kaolinite, which was the dominant mineral in China S02 coal.
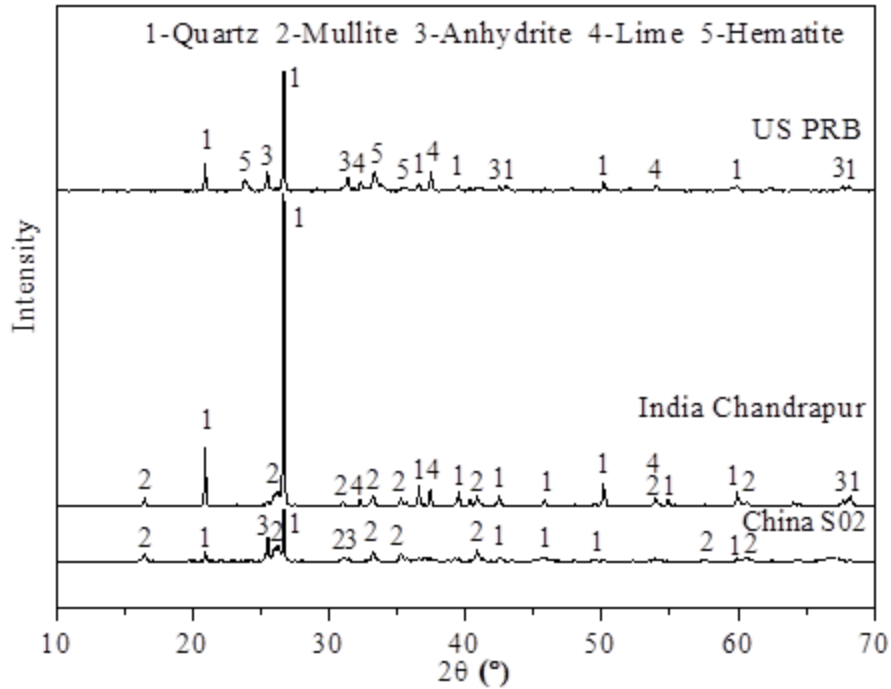
Figure 4.5 XRD patterns of coal fly ashes generated by combustion of different coals.

4.3.3 Morphology and chemical composition

Figure 4.6 shows the SEM images and EDS analysis of coal fly ashes generated by combustion of US PRB sub-bituminous coal under different pressures. The SEM images indicate that US PRB coal fly ash particles are mainly spherical, with diameters ranging from a few nanometers to several micrometers. All submicrometer particles generated under different pressures were nearly spherical, implying that the primary mechanisms for formation and growth of submicrometer particles were nucleation and condensation, respectively (Chen et al., 2005; Suriyawong et al., 2006). With an increase in pressure, the super-micrometer particles tended to be larger, which might due to the increased residence time for condensation growth in a limited vapor system under high pressure (C.-Y. Wu et al., 1998; Zhuang et al., 2001).

98
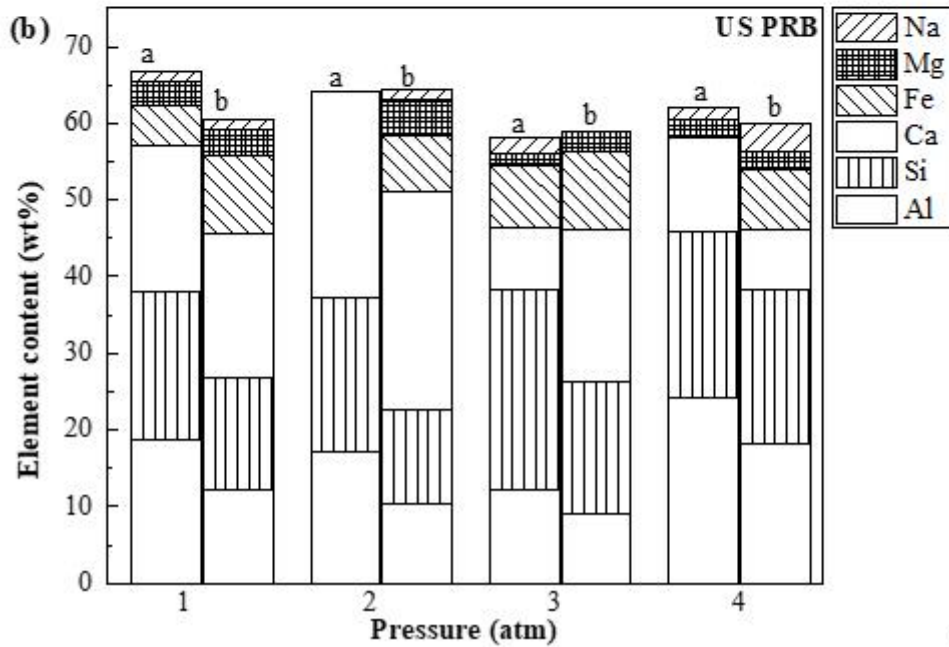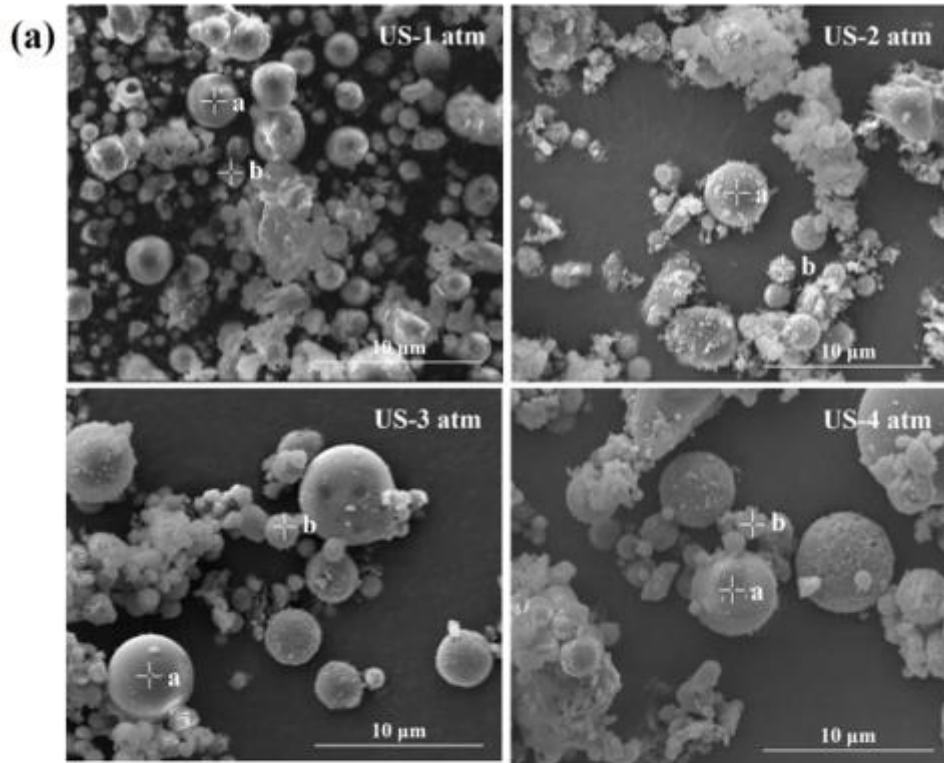
Figure 4.6 (a) SEM images and (b) EDS analysis of coal fly ashes generated by combustion of US PRB coal under different pressures (Note: a, super-micrometer particle; b, submicrometer particle).

The EDS analysis indicates that US PRB coal fly ashes generated under different pressures were mainly composed of Si, Ca, Al, and Fe, with a higher Ca content and lower Al content than those of India Chandrapur and China S02 coal fly ashes. This finding is consistent with the XRD results shown in Figure 4.5, in which the main minerals in US PRB coal fly ash are quartz (SiO_2), anhydrite ($CaSO_4$), lime (CaO), and hematite (Fe_2O_3). An interesting phenomenon is that mullite ($3Al_2O_3 \cdot 2SiO_2$) did not form in the US PRB coal fly ashes, but it formed in the India Chandrapur coal fly ashes and China S02 coal fly ashes, which is probably due to less Al content in US PRB sub-bituminous coal than in India Chandrapur lignite coal and China S02 lignite coal. During combustion, Al in US PRB coal might form amorphous calcium aluminosilicate glasses, along with O, Si, and Ca (Chancey et al., 2010; Chen et al., 2004; Moreno et al., 2005; Nathan et al., 1999). Besides calcium aluminosilicate, organically bound calcium might also be vaporized and nucleated as CaO, or reacted with SO_2 to form $CaSO_4$ (Liu et al., 2007). Trace FeS_2 in US PRB coal might be reduced by CO to form Fe vapor, released from char particles and re-oxidized to nucleate or condense on the surface of particles (Huffman et al., 1990). As shown in Figure 4.6, Na and Mg also appeared in the submicrometer particles formed by the combustion of US PRB coal, which is ascribed to the vaporization of volatile sodium species and organically bound magnesium (Lind et al., 1996; Lian Zhang et al., 2007). As shown in Table 4.2, both super-micrometer particles and submicrometer particles of US PRB coal fly ashes contained Ca, Fe, Mg, and Na, as well as Al and Si, due to high content of volatile matters in US PRB coal. Nevertheless, the super-micrometer particles had higher contents of refractory Al and Si than the submicrometer particles, but the submicrometer particles contained more volatile Na, Mg, Fe, and Ca, because the vaporization rate of each individual element decreased in the order: Na > K >Mg > Ca > Fe > Si > Al (Liu et al., 2007). With an increase in pressure, the reduction reactions of refractory oxides

were suppressed, vaporization was less, and condensation was the dominant growth mechanism in the limited vapor system (Niksa et al., 2003; Seebauer et al., 1997; Tomeczek et al., 2003; Wall et al., 2002; C.-Y. Wu et al., 1998). Moreover, molecules prefer to condense on the surface of smaller submicrometer particles, because the condensation rate is proportional to the reciprocal of particle size, and submicrometer particles have a larger specific surface area (C.-Y. Wu et al., 1998). Therefore, under higher pressure, the submicrometer particles contained higher content of Na, Mg, and Fe than those of the larger super-micrometer particles. However, Ca in US PRB coal did not behave like Na, Mg, and Fe during combustion, due to its high content and formation of amorphous calcium aluminosilicate glasses.

The SEM images and EDS analysis of coal fly ashes generated by combustions of India Chandrapur lignite coal under different pressures are shown in Figure 4.7. The SEM images show that the India Chandrapur coal fly ash particles are mainly spherical, with some irregular particles, and their morphology did not change significantly as the pressure increased.
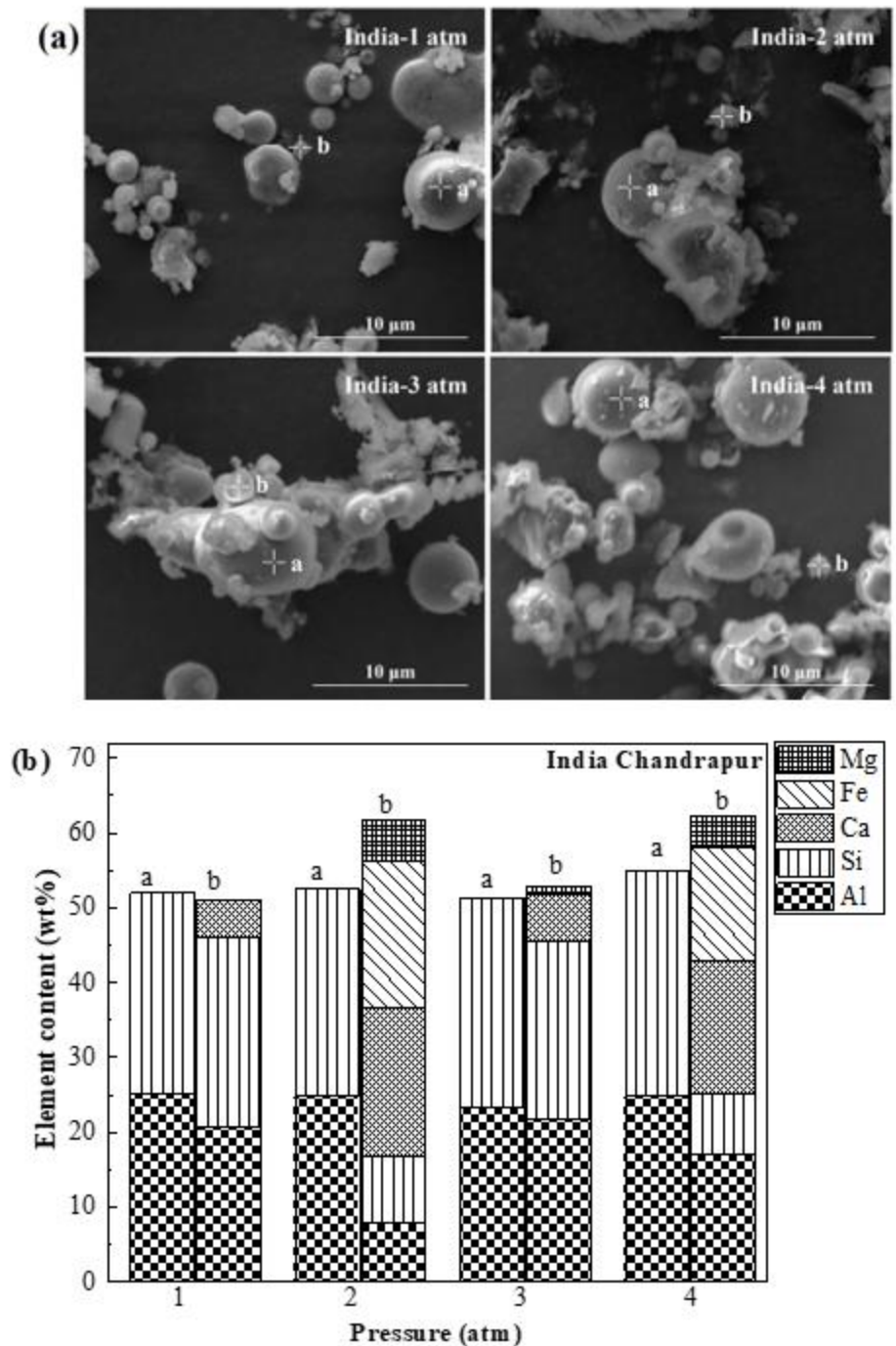
Figure 4.7 (a) SEM images and (b) EDS analysis of coal fly ashes generated by combustion of India Chandrapur coal under different pressures (Note: a, super-micrometer particle; b, submicrometer particle).

The EDS analysis indicates that all coal fly ashes from the combustion of India Chandrapur lignite

coal under different pressures were mainly composed of Al and Si, with more Si than Al and a

mass ratio of Al/Si smaller than 1.0. This finding is consistent with the XRD results for the India Chandrapur coal fly ash, which indicated that it was mainly composed of quartz and mullite. This composition is ascribed to the fact that the main minerals in India Chandrapur lignite coal were quartz and kaolinite. It has been reported that the vaporization rate of each individual element decreases in the order: Na > K > Ca > Fe > Si > Al (Liu et al., 2007). However, refractory Si and Al also appeared in the submicrometer particles, due to reduction reactions forming more volatile suboxides and to re-oxidation leading to nucleation (Linak et al., 1984; Neville et al., 1981; Quann et al., 1982; Suriyawong et al., 2006; Zhuang et al., 2001). Compared with the US PRB coal fly ashes, an obvious difference is that India Chandrapur coal fly ashes did not contain Na. Another interesting observation is that the submicrometer particles contained Ca, Mg, and Fe, in addition to Al and Si, while the super-micrometer particles contained only Al and Si under any pressure, which is probably due to low content of volatile matter in India Chandrapur lignite, as shown in Table 4.2. This finding reveals that India Chandrapur lignite coal contained only a small quantity of organically bound magnesium and calcium, which was released from coal particles to the gas phase during combustion and formed submicrometer particles by nucleation (Lind et al., 1996; Lian Zhang et al., 2007). With an increase in pressure, higher pressure led to less vaporization, condensation growth was the dominant mechanism in a limited vapor system, and because molecules preferred to condense on the surface of smaller submicrometer particles, more Mg, Fe, and Ca were concentrated in submicrometer particles (C.-Y. Wu et al., 1998; Zhuang et al., 2001).

Figure 4.8 shows SEM images and EDS analysis of coal fly ashes generated by combustion of China S02 lignite coal under different pressures. The SEM images indicate that the morphology of China S02 coal fly ash particles is mainly irregular, and more spherical particles appeared as the pressure increased.
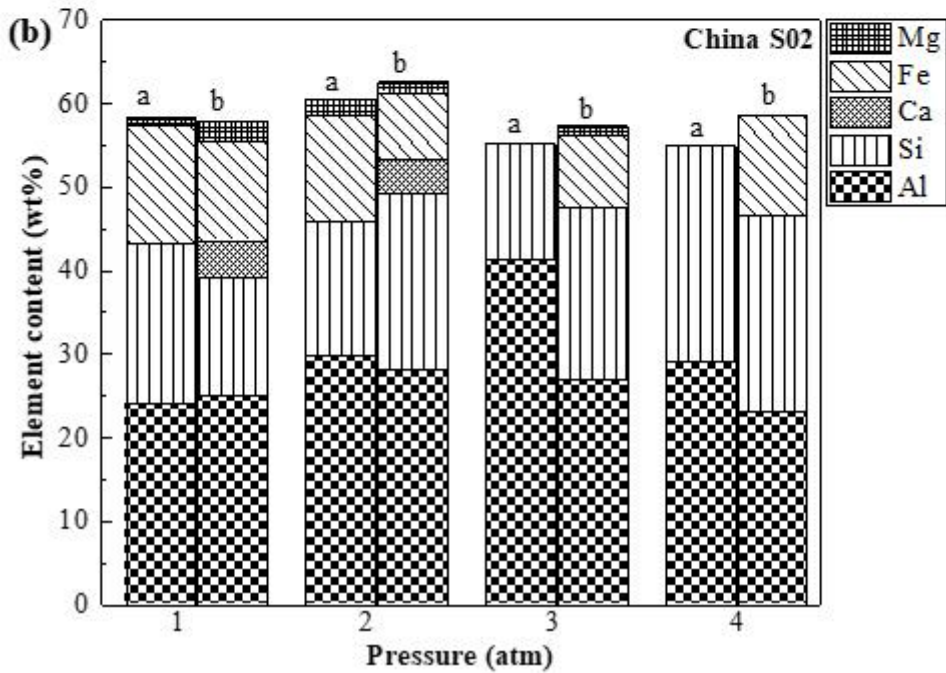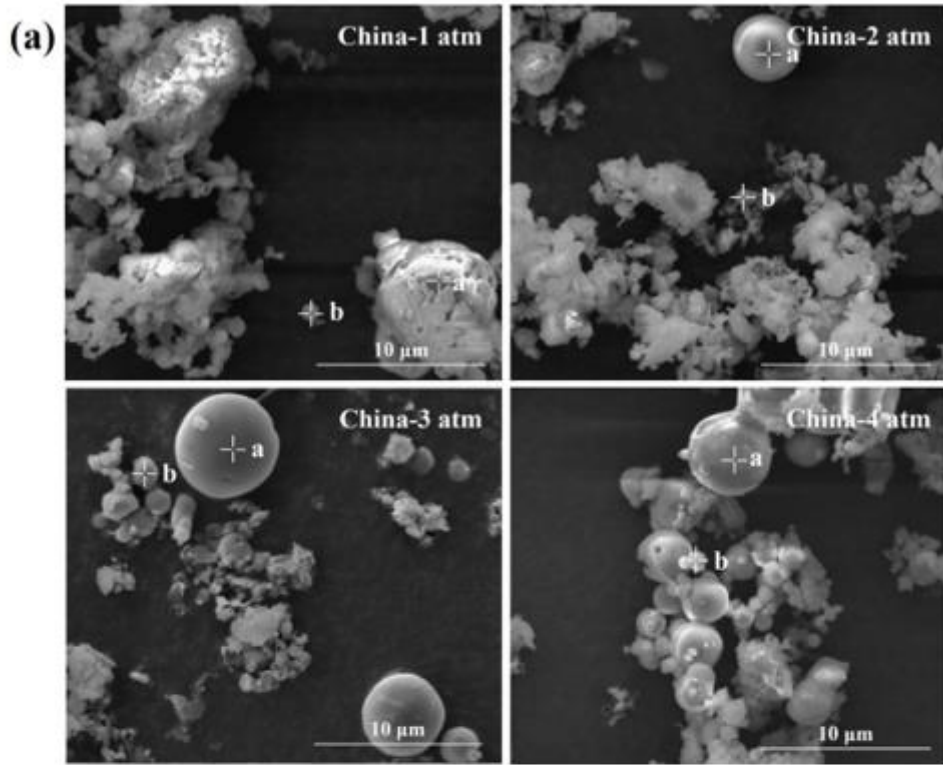
Figure 4.8 (a) SEM images and (b) EDS analysis of coal fly ashes generated by combustion of China S02 coal under different pressures (Note: a, super-micrometer particle; b-submicrometer particle).

The EDS analysis indicates that all the coal fly ashes generated by combustion of China S02 lignite coal under different pressures were mainly composed of Al and Si, with a mass ratio of Al/Si larger than 1.0, because the main minerals in China S02 lignite coal were kaolinite and boehmite. This finding is also consistent with the XRD results for the China S02 coal fly ash indicating that it was mainly composed of quartz and mullite. Under low pressure, Fe and Mg were uniformly distributed in the super-micrometer and submicrometer particles. As the pressure increased, Fe and Mg were enriched in the submicrometer particles, because higher pressure led to less vaporization. The vaporization rate of each individual element decreased in the order: Mg > Fe > Si > Al (Liu et al., 2007), and vaporized molecules preferred to condense on the surface of smaller submicrometer particles (C.-Y. Wu et al., 1998).

4.4   Conclusion

We investigated the effects of pressure, from 1 atm to 4 atm, and coal type on the characteristics of the coal fly ash and submicrometer particle size distribution. Under the same pressure, US PRB sub-bituminous coal generated submicrometer particles with a larger peak size and higher number concentration than India Chandrapur lignite and China S02 lignite, while the submicrometer particles generated by combustion of China S02 lignite coal had the smallest peak size and the lowest number concentration. With an increase in pressure, the number concentrations and peak particle sizes of submicrometer particles generated by combustion of all three different coals decreased and increased, respectively, because higher pressure led to less vaporization and condensation growth was the dominant mechanism in a limited vapor system under high pressure.

US PRB coal fly ash was mainly composed of quartz (SiO_2), anhydrite ($CaSO_4$), lime (CaO), and hematite (Fe_2O_3), while both India Chandrapur coal fly ash and China S02 coal fly ash mainly contained quartz and mullite ($3Al_2O_3 \cdot 2SiO_2$). Moreover, US PRB coal fly ashes generated under

different pressures were mainly composed of Si, Ca, Al, and Fe, with a higher Ca content and lower Al content than those of the India Chandrapur and China S02 coal fly ashes. Both India Chandrapur and China S02 coal fly ashes generated under different pressures were mainly composed of Al and Si. Nevertheless, India Chandrapur coal fly ashes had the highest Si content, while China S02 coal fly ashes had the highest Al content. As the pressure increased, the more volatile species (Na, Mg, Fe, and Ca) were enriched in the submicrometer particles. Vaporization was reduced under higher pressure, condensation was the dominant growth mechanism in the limited vapor system, and molecules preferred to condense on the surface of smaller submicrometer particles. This study of the effect of pressure and coal type on thes characteristics of submicrometer particles and coal fly ash, can provide insights for more effective capture of submicrometer particles in pressurized particle collection devices and application of coal fly ashes generated from pressurized coal combustion.

4.5 References

Biswas, P., & Wu, C. Y. (1998). Control of toxic metal emissions from combustors using sorbents: a review. *Journal of the Air & Waste Management Association, 48*(2), 113-127.

Chancey, R. T., Stutzman, P., Juenger, M. C., & Fowler, D. W. (2010). Comprehensive phase characterization of crystalline and amorphous phases of a Class F fly ash. *Cement and Concrete research, 40*(1), 146-156.

Chen, Y., Shah, N., Huggins, F. E., & Huffman, G. P. (2005). Transmission electron microscopy investigation of ultrafine coal fly ash particles. *Environmental science & technology, 39*(4), 1144-1151.

Chen, Y., Shah, N., Huggins, F. E., Huffman, G. P., Linak, W. P., & Miller, C. A. (2004). Investigation of primary fine particulate matter from coal combustion by computer-controlled scanning electron microscopy. *Fuel Processing Technology, 85*(6-7), 743-761.

Ding, J., Ma, S., Shen, S., Xie, Z., Zheng, S., & Zhang, Y. (2017). Research and industrialization progress of recovering alumina from fly ash: A concise review. *Waste Management, 60*, 375-387.

EIA, U. (2017a). *Annual energy outlook 2017*. Washington, DC: US Engery Information Administration.

EIA, U. (2017b). *International energy outlook 2017*. Washington, DC: US Energy Information Administration.

Furuya, K., Miyajima, Y., Chiba, T., & Kikuchi, T. (1987). Elemental characterization of particle size-density separated coal fly ash by spectrophotometry, ICP (inductively coupled plasma emission spectrometry), and scanning electron microscopy-energy dispersive x-ray analysis. *Environmental science & technology, 21*(9), 898-903.

Gopan, A., Kumfer, B. M., Phillips, J., Thimsen, D., Smith, R., & Axelbaum, R. L. (2014). Process design and performance analysis of a Staged, Pressurized Oxy-Combustion (SPOC) power plant for carbon capture. *Applied Energy, 125*, 179-188.

Gualtieri, A., Bellotto, M., Artioli, G., & Clark, S. (1995). Kinetic study of the kaolinite-mullite reaction sequence. Part II: mullite formation. *Physics and chemistry of minerals, 22*(4), 215-222.

Gutiérrez, B., Pazos, C., & Coca, J. (1993). Characterization and leaching of coal fly ash. *Waste management & research, 11*(4), 279-286.

Haykiri-Açma, H., Ersoy-Meriçboyu, A., & Küçükbayrak, S. (2002). Combustion reactivity of different rank coals. *Energy conversion and management, 43*(4), 459-465.

Hong, J., Chaudhry, G., Brisson, J., Field, R., Gazzino, M., & Ghoniem, A. F. (2009). Analysis of oxy-fuel combustion power cycle utilizing a pressurized coal combustor. *Energy, 34*(9), 1332-1340.

Huffman, G., Huggins, F., Shah, N., & Shah, A. (1990). Behavior of basic elements during coal combustion. *Progress in energy and combustion science, 16*(4), 243-251.

Jia, Y., & Lighty, J. S. (2012). Ash particulate formation from pulverized coal under oxy-fuel combustion conditions. *Environmental science & technology, 46*(9), 5214-5221.

Levandowski, J., & Kalkreuth, W. (2009). Chemical and petrographical characterization of feed coal, fly ash and bottom ash from the Figueira Power Plant, Paraná, Brazil. *International Journal of Coal Geology, 77*(3), 269-281.

Li, Y., Suriyawong, A., Daukoru, M., Zhuang, Y., & Biswas, P. (2009). Measurement and capture of fine and ultrafine particles from a pilot-scale pulverized coal combustor with an electrostatic precipitator. *Journal of the Air & Waste Management Association, 59*(5), 553.

Linak, W. P., & Peterson, T. W. (1984). Effect of coal type and residence time on the submicron aerosol distribution from pulverized coal combustion. *Aerosol Science and Technology, 3*(1), 77-96.

Linak, W. P., Yoo, J.-I., Wasson, S. J., Zhu, W., Wendt, J. O., Huggins, F. E., . . . Gilmour, M. I. (2007). Ultrafine ash aerosols from coal combustion: Characterization and health effects. *Proceedings of the Combustion Institute, 31*(2), 1929-1937.

Lind, T., Kauppinen, E. I., Maenhaut, W., Shah, A., & Huggins, F. (1996). Ash vaporization in circulating fluidized bed coal combustion. *Aerosol Science and Technology, 24*(3), 135-150.

Liu, X., Xu, M., Yao, H., Yu, D., Gao, X., Cao, Q., & Cai, Y. (2007). Effect of combustion parameters on the emission and chemical composition of particulate matter during coal combustion. *Energy & Fuels, 21*(1), 157-162.

Luo, Y., Ma, S., Liu, C., Zhao, Z., Zheng, S., & Wang, X. (2016). Effect of particle size and alkali activation on coal fly ash and their role in sintered ceramic tiles. *Journal of the European Ceramic Society*.

McCarthy, G. J., Swanson, K. D., Keller, L. P., & Blatter, W. C. (1984). Mineralogy of western fly ash. *Cement and Concrete research, 14*(4), 471-478.

Medina, A., Gamero, P., Querol, X., Moreno, N., De León, B., Almanza, M., . . . Font, O. (2010). Fly ash from a Mexican mineral coal I: Mineralogical and chemical characterization. *Journal of hazardous materials, 181*(1), 82-90.

Moreno, N., Querol, X., Andrés, J., Stanton, K., Towler, M., Nugteren, H., . . . Jones, R. (2005). Physico-chemical characteristics of European pulverized coal combustion fly ashes. *Fuel, 84*(11), 1351-1363.

Nathan, Y., Dvorachek, M., Pelly, I., & Mimran, U. (1999). Characterization of coal fly ash from Israel. *Fuel, 78*(2), 205-213.

Neville, M., Quann, R., Haynes, B., & Sarofim, A. (1981). *Vaporization and condensation of mineral matter during pulverized coal combustion.* Paper presented at the Symposium (international) on combustion.

Niksa, S., Liu, G.-s., & Hurt, R. H. (2003). Coal conversion submodels for design applications at elevated pressures. Part I. devolatilization and char oxidation. *Progress in energy and combustion science, 29*(5), 425-477.

Norton, G. A., Markuszewski, R., & Shanks, H. R. (1986). Morphological and chemical characterization of iron-rich fly ash fractions. *Environmental science & technology, 20*(4), 409-413.

Ptáček, P., Šoukal, F., Opravil, T., Havlica, J., & Brandštetr, J. (2011). The kinetic analysis of the thermal decomposition of kaolinite by DTG technique. *Powder Technology, 208*(1), 20-25.

Qi, L., & Yuan, Y. (2011). Characteristics and the behavior in electrostatic precipitators of high-alumina coal fly ash from the Jungar power plant, Inner Mongolia, China. *Journal of hazardous materials, 192*(1), 222-225.

Quann, R., & Sarofim, A. (1982). *Vaporization of refractory oxides during pulverized coal combustion.* Paper presented at the Symposium (international) on combustion.

Seebauer, V., Petek, J., & Staudinger, G. (1997). Effects of particle size, heating rate and pressure on measurement of pyrolysis kinetics by thermogravimetric analysis. *Fuel, 76*(13), 1277-1282.

Suriyawong, A., Gamble, M., Lee, M.-H., Axelbaum, R., & Biswas, P. (2006). Submicrometer particle formation and mercury speciation under O_2-CO_2 coal combustion. *Energy & Fuels, 20*(6), 2357-2363.

Suriyawong, A., Smallwood, M., Li, Y., Zhuang, Y., & Biswas, P. (2009). Mercury capture by nano-structured titanium dioxide sorbent during coal combustion: lab-scale to pilot-scale studies. *Aerosol Air Qual Res, 9*, 394-403.

Tomeczek, J., & Gil, S. (2003). Volatiles release and porosity evolution during high pressure coal pyrolysis. *Fuel, 82*(3), 285-292.

Vempati, R., Rao, A., Hess, T., Cocke, D., & Lauer, H. (1994). Fractionation and characterization of Texas lignite class 'F' fly ash by XRD, TGA, FTIR, and SFM. *Cement and Concrete research, 24*(6), 1153-1164.

Wall, T. F., Liu, G.-s., Wu, H.-w., Roberts, D. G., Benfell, K. E., Gupta, S., . . . Harris, D. J. (2002). The effects of pressure on coal reactions during pulverised coal combustion and gasification. *Progress in energy and combustion science, 28*(5), 405-433.

Wang, X., Cotter, E., Iyer, K. N., Fang, J., Williams, B. J., & Biswas, P. (2015). Relationship between pyrolysis products and organic aerosols formed during coal combustion. *Proceedings of the Combustion Institute, 35*(2), 2347-2354.

Wang, X., Williams, B., Wang, X., Tang, Y., Huang, Y., Kong, L., . . . Biswas, P. (2013). Characterization of organic aerosol produced during pulverized coal combustion in a drop tube furnace. *Atmos. Chem. Phys, 13*(21), 3345-3377.

Wang, Z., Ma, S., Tang, Z., Wang, X., & Zheng, S. (2016). Effects of particle size and coating on decomposition of alumina-extracted residue from high-alumina fly ash. *Journal of hazardous materials, 308*, 253-263.

Wu, C.-Y., & Biswas, P. (1998). Particle growth by condensation in a system with limited vapor. *Aerosol Science and Technology, 28*(1), 1-20.

Wu, H., Bryant, G., & Wall, T. (2000). The effect of pressure on ash formation during pulverized coal combustion. *Energy & Fuels, 14*(4), 745-750.

Yao, Z., Ji, X., Sarker, P., Tang, J., Ge, L., Xia, M., & Xi, Y. (2015). A comprehensive review on the applications of coal fly ash. *Earth-Science Reviews, 141*, 105-121.

Zhang, L., Daukoru, M., Torkamani, S., Wang, S., Hao, J., & Biswas, P. (2013). Measurements of mercury speciation and fine particle size distribution on combustion of China coal seams. *Fuel, 104*, 732-738.

Zhang, L., Wang, Q., Sato, A., Ninomiya, Y., & Yamashita, T. (2007). Interactions among inherent minerals during coal combustion and their impacts on the emission of PM10. 2. Emission of submicrometer-sized particles. *Energy & Fuels, 21*(2), 766-777.

Zhuang, Y., & Biswas, P. (2001). Submicrometer particle formation and control in a bench-scale pulverized coal combustor. *Energy & Fuels, 15*(3), 510-516.

Chapter 5: Investigation of aerosol and gas emissions from a coal-fired power plant under various operating conditions

Abstract

The concentrations of fine particles and selected gas pollutants in the flue gas entering the stack were measured under several common operation modes in an operating coal power plant producing electricity. Particle size distributions in a diameter range from 10 nm to 20 µm were measured by a scanning mobility particle sizer (SMPS), and the flue gas temperature and concentrations of CO_2 and SO_2 were monitored by a continuous emission monitoring system (CEMS). During the test campaign, five plant operating modes were studied: soot blowing, bypass of flue-gas desulfurization (FGD), reheat burner operating at 0% (turned off), 27%, and 42% (normal condition) of its full capacity. For wet and dry aerosols, the measured mode sizes were both around 40 nm, but remarkable differences were observed in the number concentrations (#/cm^3, count per square centimeter). A prototype photo-ionizer enhanced electrostatic precipitator (ESP) showed improved removal efficiency of wet particles at voltages above +11.0 kV. Soot blowing and FGD bypass both increased the total particle number concentration in the flue gas. The temperature was slightly increased by the FGD bypass mode and varied significantly as the rating of reheat burner changed. The variations of CO_2 and SO_2 emissions showed correlations with the trend of total particle number concentration possibly due to the transitions between gas and particle phases. The results are useful in developing coal-fired power plant operation strategies to control fine particle emissions and developing amine-based CO_2 capture technologies without operating and environmental concerns associated with volatile amine emissions.

5.1 Introduction

Coal-fired power plants have been regarded as primary contributors to particulate matter (PM) (Guttikunda et al., 2014; Xiong et al., 2016; Xu et al., 2017; Zhang et al., 2013), acidic gas (SO_2, NO_x) (Guttikunda et al., 2014; Xiong et al., 2016; Xu et al., 2017) and greenhouse gas (CO_2) (Dang

114

et al., 2015; Liu et al., 2015; Tola et al., 2016) emissions. A source apportionment study showed that the contributions of sulfate and nitrate to $PM_{2.5}$ from coal-fired power plants around the Yangtze River Delta region in China ranged between 37.3–72.7% and 45.0–73.8%, respectively (L. Li et al., 2015). For the same region in China, it was also reported that about 97 % and 86 % of the total SO_2 and NO_x emissions could be attributed to coal-fired power plants and other industrial facilities (C. Huang et al., 2011). Other researchers used continuous emission monitoring system (CEMS) data to conclude that U.S. coal-fired power plants were responsible for the largest annual CO_2 emissions of all sources of combustion in the U.S. over the last decade (De Gouw et al., 2014). To address the issues of all these types of pollutants, various pollution control technologies are applied in electricity generation units (EGUs). Particle control devices, such as electrostatic precipitators (ESPs) (S.-H. Huang et al., 2002; Meij et al., 2004; Strand et al., 2002; Ylätalo et al., 1998; Zhuang et al., 2000) and bag-house filters (Yi et al., 2008) have been widely applied downstream of industrial coal boilers in power plants due to their high efficiency in removing fine particles. Huang et al. found that a lab-scale single-stage ESP could achieve >99% collection efficiency of particles with a diameter less than 20 nm (S.-H. Huang et al., 2002). And it has been demonstrated that a bag-house in a 220 MW coal-fired power plant could collect 99.57% PM_{10} (Yi et al., 2008). Flue gas desulfurization (FGD) (Meij et al., 2004; Zhao et al., 2008) technology has proven similarly effective in removing SO_2. Meanwhile, the amine-based CO_2 scrubbers are widely-studied and well-established technologies for CO_2 capture because they have great potential to be energy-efficient with process and solvent improvements (Rochelle, 2009).

Nevertheless, the introduction of an amine scrubber for CO_2 capture raises another potential issue: The treated flue gas from a power plant may contain a large number of fine particles, which can carry a large amount of amine in aerosol phase out of the CO_2 scrubber, resulting in increased

amine losses and causing environmental concerns. A recent assessment of the NO_x control selective catalytic reduction (SCR) (Z. Li et al., 2015) indicated that the SCR treatment tremendously increased both the number and mass concentration of $PM_{2.5}$ emitted by a coal-fired power plant. The presence of fine particles in the flue gas could be attributed to a "penetration window", which is the size range of particles that pass through the ESP, around 100 nm for traditional ESPs (Strand et al., 2002; Ylätalo et al., 1998; Zhuang et al., 2000). Consequently, a large number of fine particles provide seed nuclei onto which volatile amine species condense causing significant amine emissions from CO_2 scrubbers (Kamijo et al., 2013; Khakharia et al., 2015; Khakharia et al., 2013; Mertens et al., 2014; Mertens et al., 2012; Mertens et al., 2013). A laboratory study on CO_2 capture found that when soot particles, which contain mostly carbon and result from incomplete coal combustion, were present in the flue gas, the amine emission loss 2-4 times higher than that without fine particles present in the inlet gas (Khakharia et al., 2013). Mertens (Mertens et al., 2014) reported that particles with diameters below 100 nm were more likely to create amine mist emissions downstream of the CO_2 scrubber. To reduce the negative effect of fine particles on amine emissions and CO_2 capture operation at a full-scale power plant, it is important to know the quantity, size distribution, and composition of fine particle as well as gas impurities in the plant's flue gas. A common approach to obtaining such information is to perform real-time flue gas measurements in a power plant under its actual operating conditions.

Numerous studies have focused on measuring the concentration of fine particles before or after a particle control unit, such as an ESP or a bag-house filter, because it is typically the principal unit that causes the most significant variation in particle concentration in the exhaust. Li et al. (2009) used a scanning mobility particle sizer (SMPS) and an electrical low-pressure impactor (ELPI) to measure the particle size distribution in the flue gas upstream and downstream of a pilot-scale ESP,

and found that adding photoionizers (such as a soft X-ray (SXR)) could enhance the particle removal efficiency in the submicrometer range. Strand et al. (Strand et al., 2002) studied the effect of an ESP and condenser on the particle concentrations from 10 nm to 10 µm in the exhaust gas from a 6 MW biomass combustor. They concluded that the exhaust gas condenser affected the particle mass concentration more significantly than the number concentration, while the ESP exhibited an opposite effect due to the re-entrainment of coarse particles caused by ESP rapping, which is a process of releasing the particles deposited on ESP electrodes by vibration. The removal efficiency of particles from 30 nm to 10 µm for a bag-house filter installed at a 220 MW anthracite coal-fired power plant was studied using an ELPI (Yi et al., 2008), and bimodal number concentration size distributions were observed before and after the bag-house filter. These studies indicate that the particle size distribution in the flue gas varies remarkably after different processing stages, and also varies when distinct types of fuel, combustor or particle control device are employed. However, the operating parameters of the boiler and flue gas treatment devices were kept constant and thus were not comprehensive to power plant operation in those studies. There are no investigations of which we are aware about how varying operating conditions of the major units in a dynamic power generation plant could affect the particle size and concentration and gas composition in the flue gas. This scientific gap needs to be bridged in terms of developing multi-pollutant emission mitigation.

In this study, the size distribution and mass concentration of particles and the concentrations of SO_2 and CO_2 in the flue gas were measured at a bituminous coal-fired power plant. The sampling point was downstream of a FGD scrubber and a reheat burner, and before the inlet of the stack. The aerosol and gas properties were investigated at five operating modes of the power plant: soot blowing in the boiler (releasing soot deposited on boiler wall), flue gas bypass of the FGD, reheat

117

burner operating at 0% (off), 27%, and 42% (normal steady state condition) of its full capacity. The effects of these different conditions on the aerosol and gas characteristics are discussed. Besides, the particle collection efficiency of a lab-scale ESP with SXR and without SXR were examined to demonstrate the potential improvement of using SXR. Notably, this study was conducted at a nameplate 35 MWe coal-fired power plant which is under a feasibility study to install a novel amine-based CO_2 capture unit. Since the aerosol and gas concentrations in the flue gas might have significant influences on the potential amine loss and CO_2 capture performance, the research outcome could provide insights for the design of the aerosol pretreatment and CO_2 scrubbing devices.

5.2 Experimental section

5.2.1 Sampling location
The primary flue gas treatment units within the coal-fired power plant are shown in Figure 5.1. Two boilers, Boilers 5 and 7, both of which are of a chain-grate Stoker design, were in operation during the test campaign. The two boilers combined are capable of producing up to 350,000 lb/hr of steam, equivalent to 35 MWe electricity. An Illinois 6# high sulfur coal was burned in the power plant. As shown in the figure, after heat exchange in the economizer and air preheater, the flue gas produced by each boiler travels through the ESP, where most of the combustion-generated fly ash and soot particles are captured. However, particles with diameters between 100 nm and 1 μm tend to penetrate the ESP (S.-H. Huang et al., 2002; Strand et al., 2002; Ylätalo et al., 1998; Zhuang et al., 2000). The flue gases from both ESPs are mixed together and then passes through a wet jet bubbling FGD scrubber to remove SO_x species. To meet the discharge emission standard for opacity, the exhaust flue gas is generally reheated by a natural gas burner to inhibit condensation of water vapor or formation of droplets before the gases are emitted from the stack. The reheat

burner can be operated at different ratings, and a higher reheating percentage is typically used during wintertime. A CEMS measures the concentration of SO_2 and CO_2 in the flue gas between the reheat burner and the stack. In this study, the aerosol sampling was conducted close to the CEMS sampling port, so that we could study the correlation between the properties of aerosols and exhaust gas species.
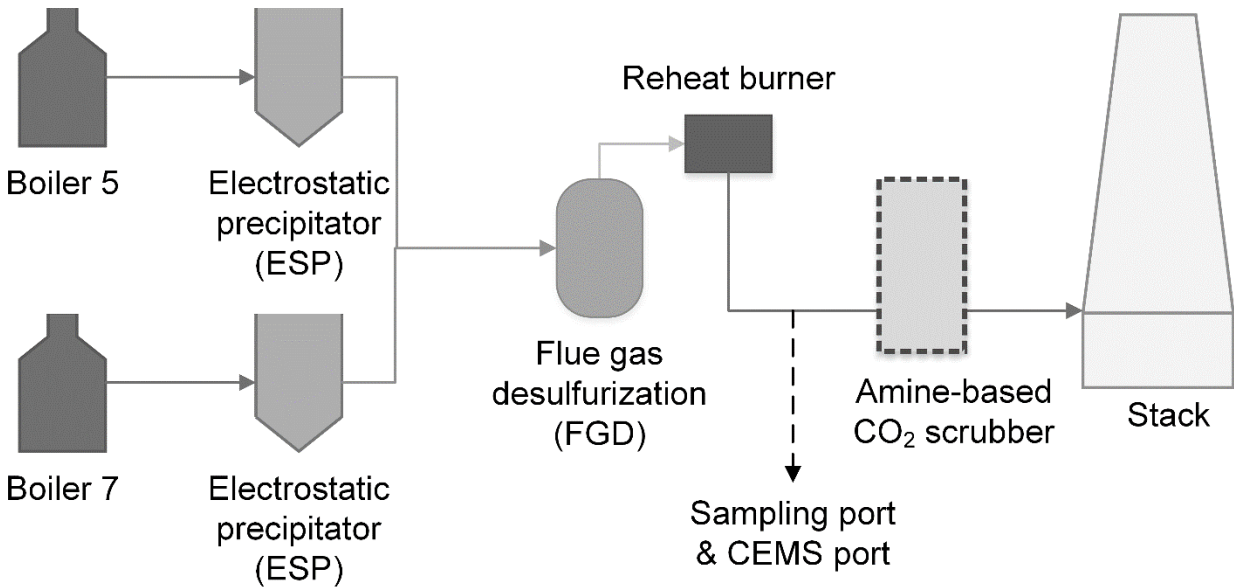
Figure 5.1 Process flow diagram of the coal-fired power plant (sampling port location is marked).

5.2.2 Experimental system

A schematic diagram of the experimental setup for measuring the particle concentration and size distributions is shown in Figure 5.2. A stainless-steel tube with an outer diameter (OD) of 0.5 inch and a length of 5 feet was used to take samples from the flue gas duct. The sampling tube was made long enough so that it drew particles from the center of the flue gas duct. The end of the tube in the flue gas duct was also bent at a right angle to achieve isokinetic sampling for a range of particle sizes in the submicrometer and micrometer regimes. The section of the sampling tube outside the flue gas duct was covered with a heating tape to suppress condensation of water vapor. A stream of particle-free air (18 lpm) from a compressed air tank was mixed with the sampled flue

gas (1.5 lpm) at the outlet of the sampling tube to dilute the aerosols and reduce water vapor concentration. Before entering the measurement system, the diluted gas sample was split into two streams, one (13 lpm) of which passed to a vacuum pump and the other (6.5 lpm) to a silica gel diffusion dryer to remove the water content. The desiccated gas stream was further split into two streams going to a scanning mobility particle sizer (SMPS, Model 3076, TSI Inc., Shoreview, MN, USA) and an aerodynamic particle sizer (APS, Model 3321, TSI Inc., Shoreview, MN, USA) separately. The size distributions of particles from 10 nm to 450 nm were measured continuously in real time with the SMPS. The SMPS uses a differential mobility analyzer (DMA) to classify particles as a function of electrical mobility size, and a condensation particle counter (CPC) to measure particle concentrations. The APS operated by the time-of-flight theory measures the aerodynamic size distributions of particles ranging from 0.5 to 20 μm. In certain tests to determine the influence of water content on particle size distributions and number concentrations, the diffusion dryer was bypassed. In addition, a SidePak^{TM} AM510 (TSI Inc., Shoreview, MN, USA) was used to determine the total mass concentration of the particles below 2.5 μm ($PM_{2.5}$) in the flue gas. During the mass concentration measurement, the compressed air tank and vacuum pump were turned off, and a diffusion dryer and the SidePak were placed at the outlet of the sampling tube directly (shown in the dashed box in Figure 5.2), because the internal pump in the SidePak cannot withstand a pressure difference generated by the vacuum pump. Flow rate controllers, SMPS, APS and SidePak were calibrated in laboratory environment before the measurement campaign, and to ensure normal working environment of all instruments, the instruments were placed on the back seat of a vehicle and their surrounding temperature was maintained in appropriate range using vehicle air-conditioner. The entire sampling line was ensured with no leakage both in laboratory and field.
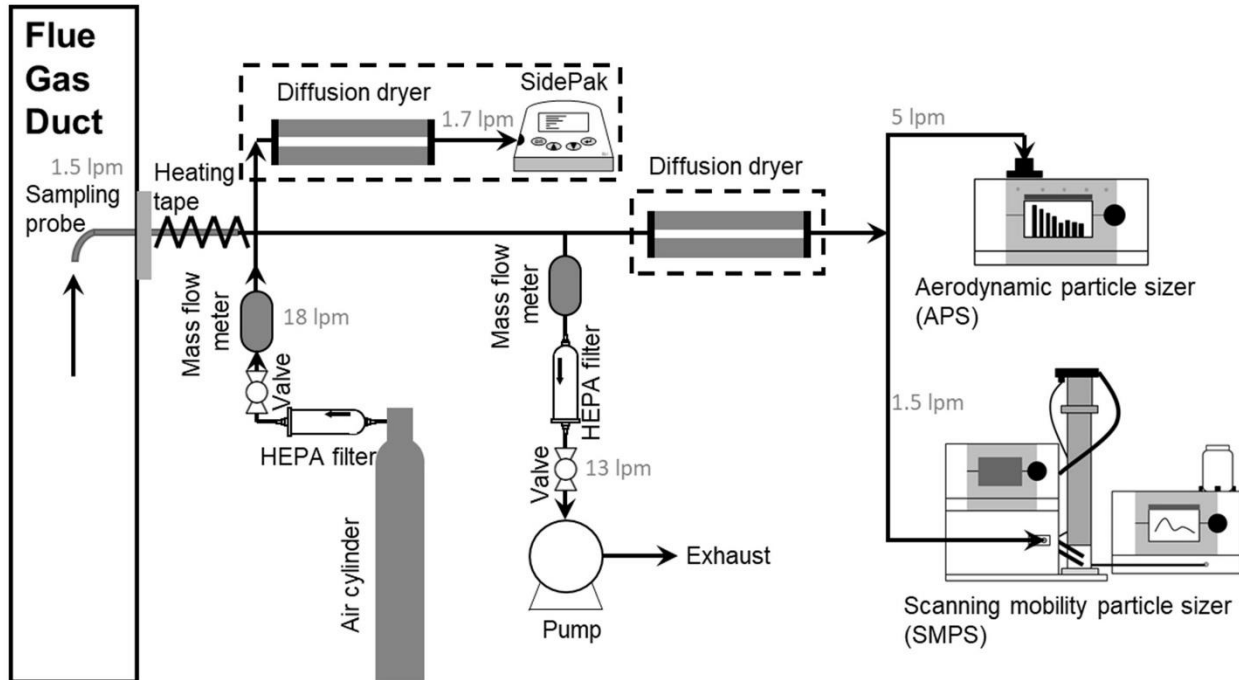
Figure 5.2 Schematic diagram of the experimental setup.

5.2.3 Experimental plan

Aerosol size distributions and concentrations were measured at five different operating modes of

the power plant. During the test campaign, the two boilers were operated with a total coal feed rate

of 10,614 kg/hr, generating a total flue gas flow rate of 204,116 kg/hr, equivalent to an actual scale

of approximately 20 MWe. Table 1 provides a brief summary of the experiments conducted in

chronological order. In the results and discussion section, we present the test results in the order

of reheat burner operating at 42% of its full capacity (normal steady state condition), reheat burner

operating at 0% and 27% of its full capacity, flue gas bypass of the FGD (FGD bypass), and soot

blowing in the boilers. The reported particle size distribution corresponding to a certain condition

is the averaged result of at least 3 sampling runs in the stable phase of that condition. For each

condition, the temperature and gas concentrations are time-averaged values over the whole stable

phase of that condition.

Table 5.1 Summary of performed experiments

Test No.	Test condition		Dryer	ESP	Soft X-ray	Instruments used
1	Soot blowing	Boiler 5 soot blowing	on	N/A	N/A	SMPS, APS
		Boiler 7 soot blowing	on	N/A	N/A	SMPS, APS
2	FGD bypass		on	N/A	N/A	SMPS, APS
3	Reheat burner off (0%)		on	N/A	N/A	SMPS, APS, SidePak
			off	N/A	N/A	SMPS, APS
4	Reheat burner (27% of full capacity)		on	N/A	N/A	SMPS, APS, SidePak
5	Reheat burner (42% of full capacity, normal operation)		on	N/A	N/A	SMPS, APS
			off	N/A	N/A	SMPS, APS
			off	+8.0, +11.0, +13.5 kV	off	SMPS
			off	+8.0, +11.0, +13.5 kV	on	SMPS

5.3 Results and discussion

This section first presents the particle characteristics during the normal steady state operation of the reheat burner. The effects of adding a diffusion dryer and a photo-ionizer (SXR) enhanced ESP on the steady state particle size distributions are elaborated. The following part of this section focuses on understanding how the modes of derated reheat burner, FGD bypass and soot blowing affect the particle size distributions. The last section discusses variation of the temperature, CO_2 and SO_2 concentrations along with the changing operating modes during the measurement.

5.3.1 Reheat burner operated at 42% of full capacity (normal steady state condition)

Figure 5.3(a) and (b) show the size distributions of aerosols downstream of the reheat burner during the normal operation of the power plant measured by SMPS and APS, respectively. The size distributions measured with and without diffusion dryers are both presented. A diffusion dryer ensured that only desiccated particles were measured. The standard deviation of the measurement was negligible, indicating a relatively constant aerosol property at the sampling location. For the results measured with a dryer (represented by white connected symbols), the particles had a mode diameter of 37.2 nm, a value similar to those found in previous studies on particle measurement in flue gas (Li et al., 2009; Ylätalo et al., 1998). The concentration of particles at 37.2 nm was 3.3×10^8 #/cm^3. The total particle number concentration (over the size range of 15.7 to 399.5 nm throughout this report) was calculated by integrating the size distribution, yielding a value of 9.0×10^9 #/cm^3. It should be noted that the scales of the vertical axes in the SMPS and APS figures are different. Hence, it can be concluded that very few particles were larger than 0.5 μm, and most particles were in the range of 10 to 100 nm, consistent with the "penetration window" through a conventional ESP (Li et al., 2009; Ylätalo et al., 1998; Zhuang et al., 2000). Ylatulo et al. found that the size of the particles with the highest number concentration at the outlet of an ESP was approximately 70 nm (Ylätalo et al., 1998), which was higher than the observed peak size in Figure 5.3(a). This slight distinction may be attributed to evaporation of volatile contents induced by the reheat burner. The penetration of fine particles could result in aerosol growth in the proposed amine-based CO_2 scrubber downstream of the reheat burner, and eventually could cause amine loss, primarily due to a large total surface area of submicrometer particles available for volatile amine condensational growth (Schaber, 1995).
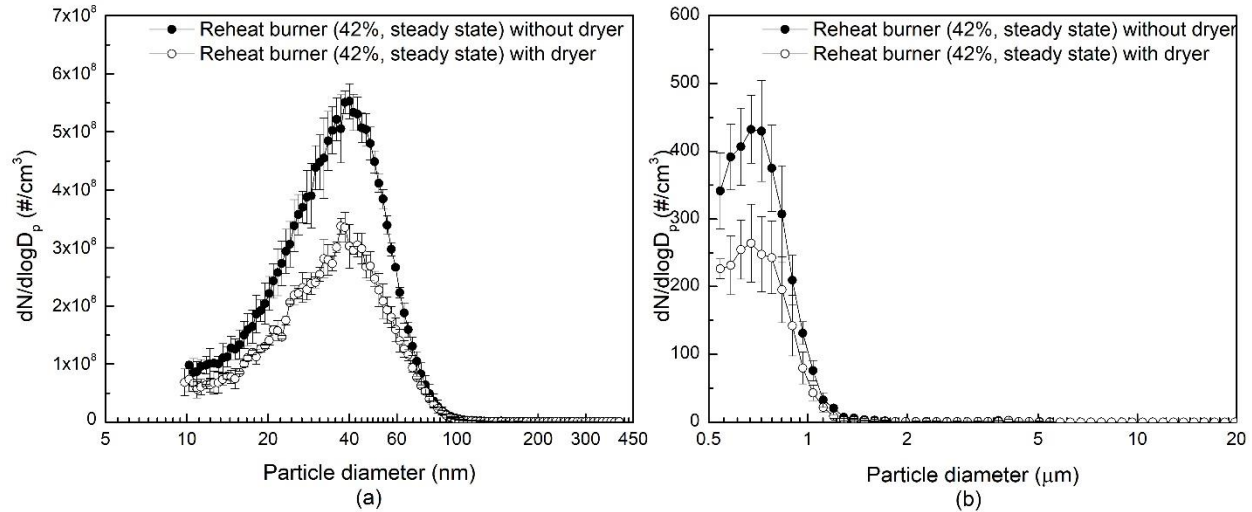
Figure 5.3 Size distributions of particles with diameters between 10 nm to 20 µm when the reheat burner rating was 42% of full capacity (normal steady state condition) (both with and without dryer): (a) SMPS and (b) APS.

The black connected symbols in Figure 5.3(a) and (b) display the size distributions of particles from the reheat burner without desiccation by a diffusion dryer. The highest number concentration was reached at around 40 nm, which was similar to the result for dry particles. However, the total number concentration of wet particles was around 1.50×10^{10} #/cm^3, which was significantly higher than that of dry particles. The highest concentration was around 5.5×10^8 #/cm^3, nearly double the result obtained when a diffusion dryer was used, which emphasizes the effect of water droplets in the original flue gas. Given the fact that the test campaign was conducted during wintertime and the flue gas duct was exposed to ambient air, the observed water vapor condensation could have occurred due to reduced temperature during transport in the duct. By implication, the reheat burner should operate at a higher rating when the outdoor temperature is remarkably low.

It has been demonstrated that SXR enhanced ESP can boost the capture efficiency for ultra-fine particles because SXR can increase ion concentrations by enhancing photoionization at both electrode surface and gas molecules (Hogan et al., 2004; Kulkarni et al., 2002). Kulkarni et al. found that the capture efficiency for particles ranging in diameter from 20 to 600 nm could increase

remarkably when SXR was used with the ESP, and the SXR enhancement was augmented as the applied voltage was elevated from 5 kV to 10 kV (Kulkarni et al., 2002). However, there is no study on applying SXR to capture fine particles in coal-fired power plants. In our work, the capture efficiency of a lab-scale SXR-enhanced ESP, whose configuration details can be found in Figure A3.1 in the supplemental information and in previous studies (Jing et al., 2015), was tested with the undesiccated wet flue gas. Figure A3.2 shows the current-voltage (I-V) characteristics of the ESP with SXR. For both positive and negative polarity, the onset voltage of the ESP with SXR turned on was slightly lower than the ESP without SXR, which is consistent with the results obtained by Hogan et al. (Hogan et al., 2004). Besides, for both positive and negative polarity, the current was higher with SXR at low voltages. Interestingly, with voltages higher than 12 kV, the currents were similar regardless of the presence of SXR, which was not reported in previous studies (Hogan et al., 2004; Jing et al., 2015; Kulkarni et al., 2002).

Figure 5.4(a), (b) and (c) show the particle penetration size distributions with SXR off and on using ESP voltages of 8.0 kV, 11.0 kV and 13.5 kV, respectively. It is observed that particles in diameter of 50 nm have the highest collection efficiency compared with particles in diameter of 20 or 100 nm. This result can be attributed to the fact that the particle migration in the radial direction is governed by the balance between drag force and electric force. As the particle diameter decreases from 50 nm to 20 nm, the diffusion charging mechanism becomes invalid since calculated number of charges on particles can be less than unity, which means that only a portion of such small particles obtain one charge (Friedlander, 1977). Study by Pui et al. showed that the charging efficiency by a corona was reduced from nearly 100% for 50-nm particles to 5-15% for 5-nm particles (Pui et al., 1988). Zhuang et al. demonstrated that charging rate for 50-nm particles was much faster than that of 20-nm particles and the decrease in collection efficiency for particles

below 60 nm was attributed to partial charging for smaller particles (Zhuang et al., 2000). Similar

results were also reported by Kulkarni et al. The collection efficiency decreased from 31% at 50

nm to 11% at 20 nm (Kulkarni et al., 2002). It has been reported that ultrafine particles have low

saturation charge and are also difficult to charge due to low ion attachment coefficients (Adachi et

al., 1985). Therefore, smaller particles carry much fewer charges resulting in the dominance of

drag force over electric force and thus they tend to escape from ESP. As the particle diameter

increases from 50 nm to 100 nm, although particles can be sufficiently charged by diffusion

charging, the larger particles suffer more from the increasing drag force based on the form of

Cunningham correction factor. Increased drag force reduced the collection of particles in diameter

close to 100 nm. As illustrated, at each ESP voltage, the penetrations of most of the particles with

diameters between 20 nm and 100 nm were lower with SXR turned on. As the voltage increased,

the particle penetration was reduced for all the particles in that size range. It should be noted that

the particle penetration ($p(d_p)$) and capture efficiency ($\eta(d_p)$) of particles with a given diameter

were calculated using Eq. (5.1):

$$p(d_p) = 1 - \eta(d_p) = \frac{N_{on}(d_p)}{N_{off}(d_p)}, \qquad (5.1)$$

where $N_{on}(d_p)$ and $N_{off}(d_p)$ are the particle number concentrations at the outlet of the ESP when

ESP is turned on and off, respectively. Figure 5.4(c) shows that ESP with SXR on still achieved

higher capture efficiency than a bare ESP, although the current was not increased at the same

voltage. It was reported by Kulkarni et al. (Kulkarni et al., 2002) that the SXR affected the ESP

performance in two primary ways: ion concentration enhancement due to bipolar ions created by

photoionization, and photoionization of particles. It can be speculated that when the applied

voltage is high, the ion concentration increase is dominantly contributed by electron-molecule

bombardment driven by the high electric field, while the ions yielded by photoionization due to SXR could be negligible. Therefore, the current might be governed by the voltage magnitude when the voltage is over a certain threshold, which is indicated by the I-V characteristics in Figure A3.2. Nonetheless, when particles are present, the presence of SXR could still facilitate particle charging by direct particle photoionization, which is probably the mechanism behind the increasing capture efficiency illustrated in Figure 5.4(c). It also needs to be emphasized that this study used a positive corona, which allows more effective particles charging when coupled with SXR than a negative corona (Kulkarni et al., 2002). Based on the SXR experimental results and an approximate estimate of energy requirement of applying SXR as shown in the supplemental material, it is advised for air quality management professionals in coal-fired power plants that SXR can be utilized with ESP with careful design and operation strategy. The tradeoff between energy investment and emission control efficiency should be addressed appropriately during special operation periods such as peak electricity consumption season with high emissions.
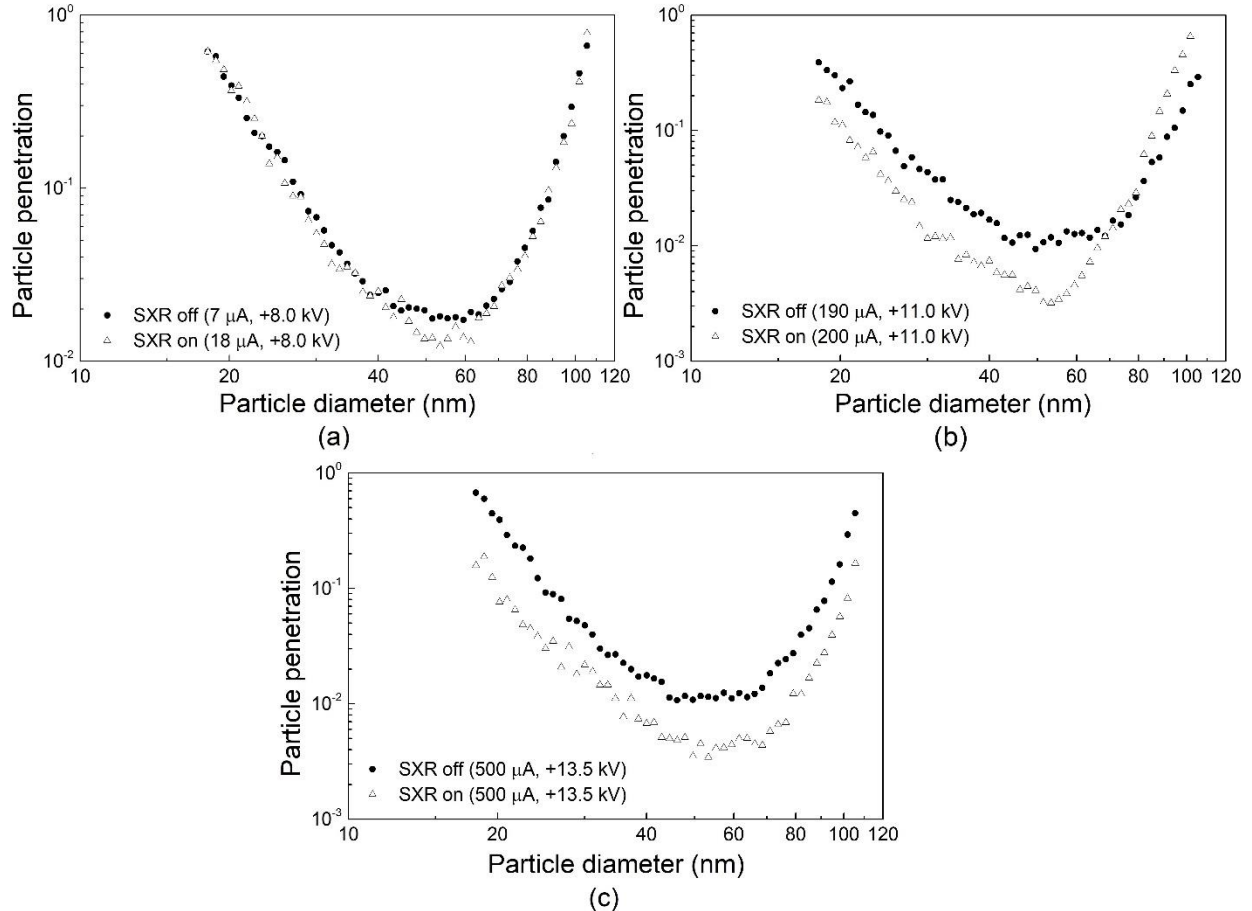
Figure 5.4 Particle penetration in the ESP with SXR (on and off) at different voltages: (a) +8.0 kV; (b) +11.0 kV; (c) +13.5 kV.

5.3.2 Effect of derating reheat burner on the aerosol size distribution

Flue gas processed by FGD scrubbing is typically cooled and saturated with water vapor and commonly needs to be reheated by a gas burner to avoid duct corrosion by suppressing condensation of water or other vapors and improve plume buoyancy from the stack (Rubin et al., 1978; Sijbesma et al., 2008). As a side benefit, the number concentration of fine particles can be also reduced at an elevated temperature. Therefore, the operation of the reheat burner is crucial to controlling of particles in the flue gas. The effect of flue gas reheating was investigated when the reheat burner was operated at two lower ratings, i.e., 0% (shutoff) and 27% of its full capacity. Figure 5.7 compares the particle size distributions when the ratings of the reheat burner were maintained at 0% and 42% (steady state condition described before). For each rating, the size

128

distributions measured with and without the diffusion dryer are also shown. Figure A3.3 in the supplemental information shows the size distributions when the rating of reheat burner was 27%. When the reheat burner was in steady state, the mode diameters of the size distributions with and without the dryer were 38.5 and 40.0 nm, respectively, as shown in Figure 5.5(a). However, when the reheat burner was turned off, the mode diameters of the size distributions with and without the dryer were both greater than the values obtained under the normal condition. These observations indicate that reducing the reheat burner rating might allow new particles to form and grow by condensation of more water vapor. In addition, the number concentrations of particles in most sizes shown in Figure 5.5(a) and (b) were significantly higher when the reheat burner was turned off, which can be attributed to the possibility that more droplets were formed at lower temperature and carried over by the flue gas. A field study at a 450 MW coal-fired power plant (Sijbesma et al., 2008) showed that the flue gas after passing through a scrubber and before entering a reheat burner contained 11.2 vol.% H_2O, 150–300 vppm NO_x and 50–100 vppm SO_2. It has been reported that if the temperature of flue gas is lower than the sulfuric acid dew point, H_2SO_4 aerosols can be generated and corrode the reheat burner tubes (Rubin et al., 1978). Therefore, to extend the service life of the reheat burner and control the particle emissions, it is essential to maintain an elevated temperature in the burner to inhibit water vapor and SO_2 condensation. A comparison of the size distributions of dry aerosols suggests that a higher reheat burner rating could even lead to a lower number concentration of dry aerosols and a lower mode diameter. This result also implies that there might be some volatile components in dry aerosols than can be released by the reheating.
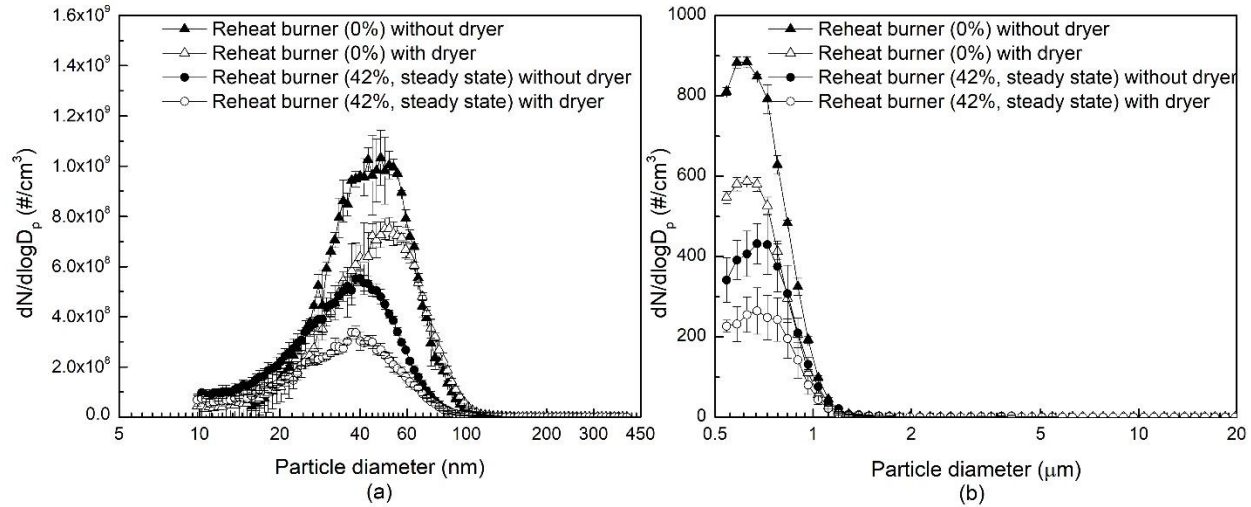
Figure 5.5 Size distributions at different operating ratings of the reheat burner (both with and without dryer): (a) SMPS, and (b) APS.

Table 5.2 lists the total number concentrations of dry aerosols in different size ranges and mass concentrations of $PM_{2.5}$ obtained by the SidePak downstream of the diffusion dryer when the reheat burner was operated at 0% and 27% ratings. The total number concentration in the range of 15.7–399.5 nm when the reheat burner was turned off was 2.5 times as high as the value when the reheat burner rating was 27%. This conclusion is consistent with a comparison of results between the 0% and 42% ratings. Nonetheless, the mass concentrations of $PM_{2.5}$ were similar for both ratings. Meanwhile, the total number concentration in the range of 0.54–19.81 µm, as measured by the APS, for the 0% rating was close to that for the 27% rating as well. It appears that the mass concentration was governed by the number concentration of larger particles, because mass is proportional to the cube of particle size. Comparing the size distributions of dry aerosols for the 27% rating and 42% rating in Figure A3.3 and Figure 5.3, it is interesting to find that the 27% rating can achieve size distributions of submicrometer particles as low as the 42% rating, although the 42% rating results in a much lower size distribution of particles larger than 500 nm. It can be implied that the rating increase from 27% to 42% might not be necessary to suppress

submicrometer dry aerosols. Nonetheless, the chemical compositions of dry aerosols collected at

different ratings of reheat burner are important for further studies.

Table 5.2 Comparison of number and mass concentrations of dry aerosols at different operating conditions of reheat burner

Derating mode	Total number concentration by SMPS (15.7–399.5 nm) (#/cm^3)	Total number concentration by APS (0.54–19.81 µm) (#/cm^3)	PM$_{2.5}$ (mg/m^3)
Reheat burner (0%, dryer on)	2×10^{10}	4.0×10^3	1.65 ± 0.12
Reheat burner (27%, dryer on)	8×10^9	4.2×10^3	1.55 ± 0.05

5.3.3 Effect of FGD bypass on the size distribution of dry aerosols

FGD bypass is an operating mode that may temporarily occur when the boiler is in the starting

phase, when FGD is malfunctioning, or when the flue gas flowing into the FGD exceeds the

desulfurization capacity. Partially bypassing the FGD as long as the SO$_2$ emission standard is

achieved can minimize the FGD energy requirement (Rubin et al., 1978). Nevertheless, while FGD

removes the SO$_x$ species in the flue gas, particles may also be collected by the scrubbing liquid. It

has been reported that wet FGD can remove more than 50% of fly ash particles with sizes larger

than 2.5 µm (Meij et al., 2004). Hence, it is reasonable to expect a greater particle number

concentration in the flue gas bypassing the FGD than that treated with the FGD. Figure 5.6 shows

the comparison of particle size distributions from 10 nm to 20 µm between FGD bypass mode and

steady state operation mode, both of which were measured with the diffusion dryer installed in the

sampling line. Compared with the steady state result, the number concentrations of particles in

diameter of from 10 nm to 120 nm and from 500 nm to 1 µm were higher when the FGD was

bypassed. For the results measured by the SMPS as shown in Figure 5.6(a), the mean diameter of

size distribution shifted from 40.9 nm to 55.3 nm when the mode changed from steady state operation into FGD bypass (explicit values of mean diameters are summarized in Table S1 in the supplemental material). The total number concentration of particle in diameter of from 15.7 to 399.5 nm was 1.96×10^{10} #/cm^3 in FGD bypass mode, 2.2 times as high as that of steady state operation mode. The highest concentration in FGD bypass mode measured by the APS shown in Figure 5.6(b) was 2.5 times as high as that of steady state operation mode. All the findings imply that many dry particles were captured in the FGD scrubber. Furthermore, more than 50% of the particles in the size range from 50nm to 100 nm and from 500 nm to 700 nm are trapped in the FGD during steady state operation as indicated by Figure 5.6(a) and 5.6(b), respectively. Two studies (Wang et al., 2008; Yang et al., 2010) showed that the particle removal efficiency of wet FGD was enhanced as particle size grew, which is consistent with the observations in Figure 5.6. Therefore, it can be inferred that much more fine particles could exist in the flue gas when the FGD bypass is implemented, requiring careful design of targeted particle control strategy.
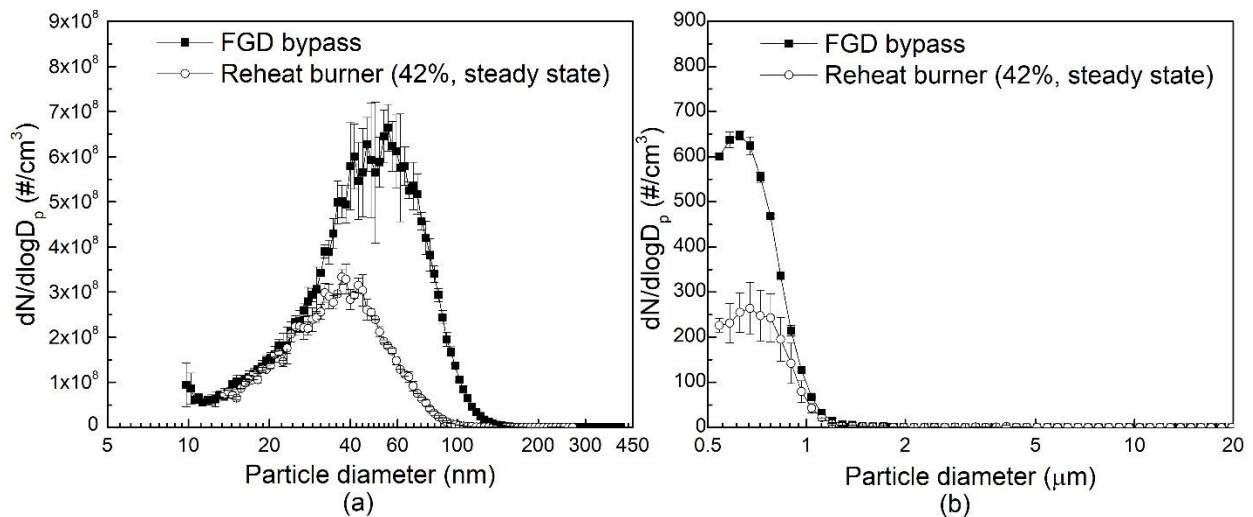
Figure 5.6 Effect of FGD bypass on particle size distribution: (a) SMPS, and (b) APS.

5.3.4 Effect of soot blowing on the size distribution of dry aerosols

Soot-blowing is widely employed by coal-fired power plants to avoid deterioration of thermal efficiency due to soot accumulation in the coal boiler (Shi et al., 2015). Soot blowers using compressed air or steam are triggered periodically to blow away the ash attached on boiler tubes, which inevitably increases the amount of fly ash leaving the boiler. Figure 5.7 shows the size distributions measured by the SMPS and APS during soot blowing in boilers 5 and 7 compared with those obtained under the normal operating condition. During soot blowing in either boiler 5 or 7, the measured size distributions showed no significant difference. Like the result of FGD bypass mode, most of submicrometer particles displayed higher number concentrations at soot blowing mode. The total particle number concentrations reached 1.95×10^{10} and 1.88×10^{10} #/cm^3 when conducting soot blowing in boiler 5 and boiler 7, respectively. These observations verified that soot blowing could increase the particle number concentration in the flue gas even though the gas passed through the ESP and FGD. Valmari et al. demonstrated in a field study that around 70% by weight of the total generated fly ash could be deposited on the surface of a heat exchanger between two consecutive soot blowing operations, and significant emissions would be expected during soot blowing (Valmari et al., 1999). This statement is consistent with the results shown in Figure 5.7. Their study also showed that nearly all particles with diameters larger than 10 µm were deposited, but only a small portion of particles smaller than 3 µm was deposited. Nonetheless, our study indicates that the smaller particles re-entrained in the flue gas by soot blowing could double the particle load emitted to the atmosphere. On the contrary, the large particles generated by soot blowing can probably be re-captured by the ESP and FGD, which both have high removal efficiency for larger particles (Li et al., 2009; Wang et al., 2008; Yang et al., 2010; Zhuang et al., 2000).
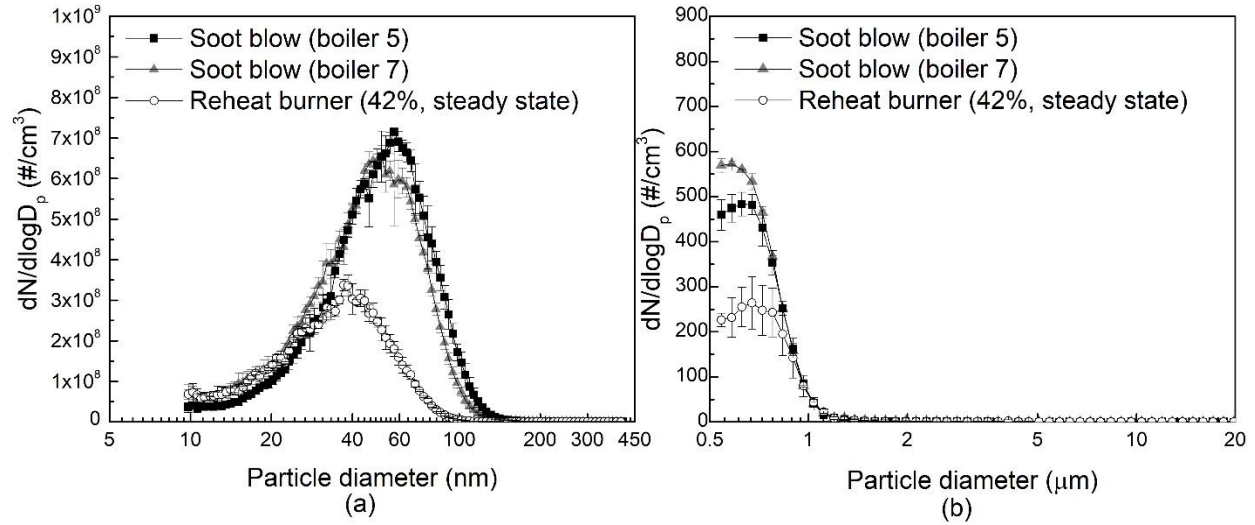
Figure 5.7 Effect of soot blowing on particle size distribution: (a) SMPS, and (b) APS.

5.3.5 Variations of temperature, total particle number concentration and gas concentrations

The temperature of the flue gas duct at the sampling location was monitored by an electronic thermometer as aerosol measurements were conducted. The normalized temperatures and total number concentrations (from 15.7 to 399.5 nm) measured in every test scenario were plotted in Figure 5.8(a). As shown, after transitioning from SootBlow7 to FGDbypass mode, the temperature increased because the FGD typically reduces the flue gas temperature from 150 °C to 50 °C (Rubin et al., 1978; Sijbesma et al., 2008) due to possible condensation of sulfuric acid on passing aerosols, and the total particle number concentration increased slightly, indicating the capability of FGD to remove submicrometer particles to some small extent. When the reheat burner was turned off, the total particle number concentration remained nearly the same, but the flue gas temperature began to decline. Nonetheless, the total particle number concentration grew after the dryer was offline. The same phenomenon was also observed when comparing Reheat42 and Reheat42_NoDryer mode. These observations imply that derating the reheat burner barely affected the quantity of dry aerosols, but had a strong influence on wet particles, probably due to the enhancement of particle nucleation and condensation at lower temperature. Furthermore, as the reheat burner rating was

134

increased to 27% of full capacity, the temperature increased as expected, but the total number concentration of dry aerosols plummeted, and stayed low after the reheat burner operated at 42% of full capacity. This variation implies that there were dry aerosols composed of highly volatile matters which probably vaporized at elevated temperature. It is proposed that the chemical composition of those volatile dry aerosols would be of great interest for further study of fly ash behavior in coal-fired power plants.

(a)

(b)
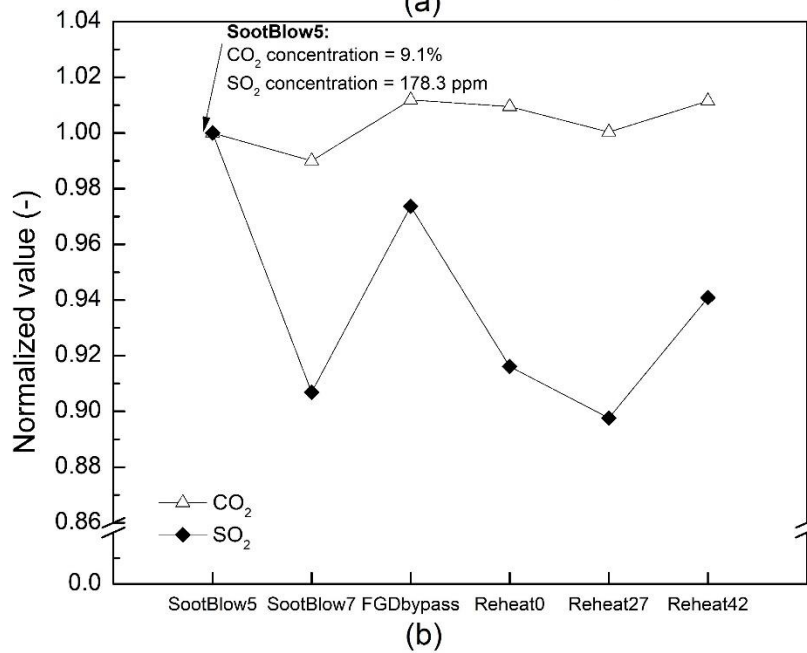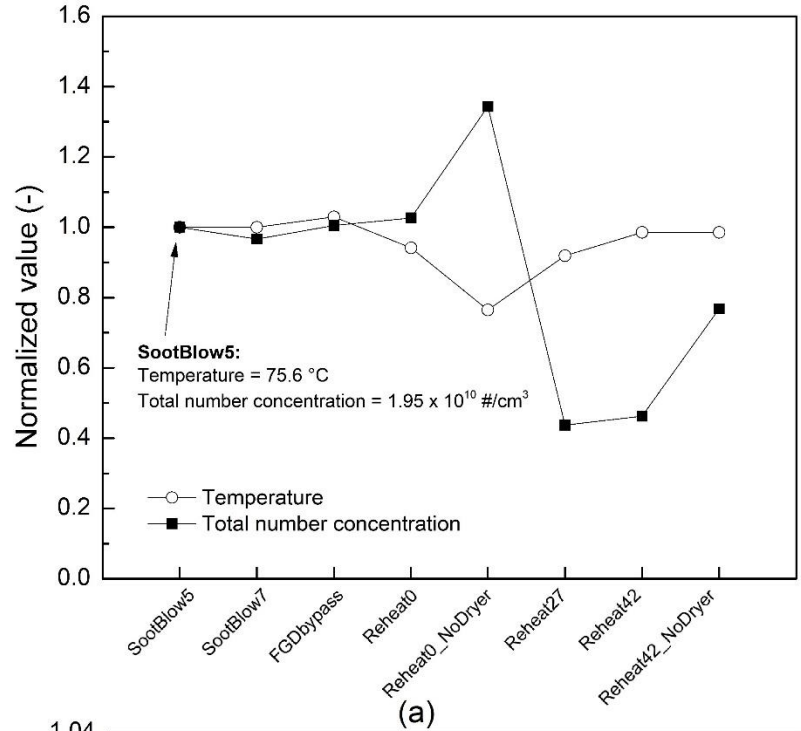
Figure 5.8 (a) Temperature and total number concentration for different scenarios in the order tested (normalized by the value of SootBlow5). (b) CO_2 and SO_2 average concentration obtained from CEMS measurements for different operating modes (normalized by the value of SootBlow5). (Annotations: • SootBlow5: Soot blowing of boiler 5 (with dryer); • SootBlow7: Soot blowing of boiler 7 (with dryer); • FGDbypass: bypass of FGD (with dryer); • Reheat_0: Reheat burner 0% (with dryer); • Reheat_0_NoDryer: Reheat burner 0% (without dryer); • Reheat_27: Reheat burner 27% (with dryer); • Reheat_42: Normal

136

operation (Reheat burner 42%; with dryer); • Reheat_42_NoDryer: Normal operation (Reheat burner 42%; without dryer).).

As illustrated in Figure 5.8(b), between SootBlow7 and FGDbypass mode, the concentrations of both CO_2 and SO_2 grew considerably. The SO_2 concentration increase is intuitively attributed to the bypass of the FGD, but it seems more interesting that the FGD could also capture much CO_2. It has been found that suspensions of lime (Juvekar et al., 1973; Ryu et al., 2006) can absorb CO_2 efficiently through carbonation. Thereafter, when the FGD bypass mode was disabled and the reheat burner was turned off, the concentrations of CO_2 and SO_2 both decreased, which can be attributed to the FGD capture effect and possibly to gas-to-particle conversion via nucleation and condensation, at lower temperature due to the derated reheat burner. The total particle number concentration increase from FGDbypass to Reheat0 can be observed in Figure 5.8(a). Thereafter, as the reheat burner returned to its normal operating condition, the CO_2 and SO_2 concentrations increased, possibly due to particle-to-gas conversion caused by desorption and vaporization of volatile aerosols. This speculation can also be evidenced by the decrease in total number concentration after transitioning from Reheat0 to Reheat42 as shown in Figure 5.8(a).

5.4   Conclusion

The size distribution of particles from 10 nm to 20 µm in the flue gas before entering the stack was investigated under various operating modes at a 35 MW full-scale coal-fired power plant. Particles with diameters of around 40 nm showed the highest number concentration at a normal steady state operating condition. A substantial fraction of particles was found as wet droplets. SXR was demonstrated to allow the ESP to capture more particles, and the removal efficiency increased as the applied voltage was elevated. Derating the reheat burner and bypassing the FGD resulted in more wet droplets and more larger particles, respectively. Soot blowing increased the number of submicrometer particles significantly, even after partial capture in the ESP and FGD. The flue gas

temperature was slightly increased by the FGD bypass mode, which could be attributed to the absence of condensation of sulfuric acid in the FGD, and varied significantly as the rating of reheat burner changed. The variations of CO_2 and SO_2 emissions showed correlations with the trend of total particle number concentration possibly due to the transitions between gas and particle phases.

This study focused on examining the effect of several common operating modes incurred in the power plant on the fine particle size distribution and main gases in flue gas. The outcomes provided robust evidence of the presence of a large number of fine particles in the flue gas. It is suggested for air quality control management professionals in coal-fired power plants that appropriate operation changes such as increasing the operation voltage of ESP, install SXR photoionizer on the ESP or suppress the inlet flow rate to amine CO_2 scrubber need to be implemented during soot blowing and FGD bypass modes. The characteristic information of aerosols and main gas pollutants in the flue gas is extremely important for developing and deploying CO_2 scrubbers, whose amine emissions and operating effectiveness depends greatly on the upstream concentrations of fine particles, SO_2, etc. from the power plant. Further investigations on chemical compositions of wet and dry aerosols before entering the scrubber are highly proposed.

5.5 References

Adachi, M., Kousaka, Y., & Okuyama, K. (1985). Unipolar and bipolar diffusion charging of ultrafine aerosol particles. *Journal of aerosol science, 16*(2), 109-123.

Dang, Q., Mba Wright, M., & Brown, R. C. (2015). Ultra-Low Carbon Emissions from Coal-Fired Power Plants through Bio-Oil Co-Firing and Biochar Sequestration. *Environmental Science & Technology, 49*(24), 14688-14695. doi:10.1021/acs.est.5b03548

De Gouw, J., Parrish, D., Frost, G., & Trainer, M. (2014). Reduced emissions of CO2, NOx, and SO2 from US power plants owing to switch from coal to natural gas with combined cycle technology. *Earth's Future, 2*(2), 75-82. doi:10.1002/2013EF000196

Friedlander, S. K. (1977). Smoke, dust and haze: Fundamentals of aerosol behavior. *New York, Wiley-Interscience, 1977. 333 p.*

Guttikunda, S. K., & Jawahar, P. (2014). Atmospheric emissions and pollution from the coal-fired thermal power plants in India. *Atmospheric Environment, 92*, 449-460. doi:10.1016/j.atmosenv.2014.04.057

Hogan, C. J., Lee, M.-H., & Biswas, P. (2004). Capture of viral particles in soft X-ray–enhanced corona systems: charge distribution and transport characteristics. *Aerosol Science and Technology, 38*(5), 475-486. doi:10.1080/02786820490462183

Huang, C., Chen, C., Li, L., Cheng, Z., Wang, H., Huang, H., . . . Chen, Y. (2011). Emission inventory of anthropogenic air pollutants and VOC species in the Yangtze River Delta region, China. *Atmospheric Chemistry and Physics, 11*(9), 4105-4120. doi:10.5194/acp-11-4105-2011

Huang, S.-H., & Chen, C.-C. (2002). Ultrafine aerosol penetration through electrostatic precipitators. *Environmental Science & Technology, 36*(21), 4625-4632. doi:10.1021/es011157+

Jing, H., Wang, X., Wang, W.-N., & Biswas, P. (2015). Elemental mercury oxidation in an electrostatic precipitator enhanced with in situ soft X-ray irradiation. *Journal of the Air & Waste Management Association, 65*(4), 455-465. doi:10.1080/10962247.2014.998352

Juvekar, V., & Sharma, M. (1973). Absorption of CO2 in a suspension of lime. *Chemical Engineering Science, 28*(3), 825-837.

Kamijo, T., Kajiya, Y., Endo, T., Nagayasu, H., Tanaka, H., Hirata, T., . . . Tsujiuchi, T. (2013). SO 3 impact on amine emission and emission reduction technology. *Energy Procedia, 37*, 1793-1796. doi:10.1016/j.egypro.2013.06.056

Khakharia, P., Brachert, L., Mertens, J., Anderlohr, C., Huizinga, A., Fernandez, E. S., . . . Goetheer, E. (2015). Understanding aerosol based emissions in a Post Combustion CO 2 Capture process: Parameter testing and mechanisms. *International Journal of Greenhouse Gas Control, 34*, 63-74. doi:10.1016/j.ijggc.2015.01.001

Khakharia, P., Brachert, L., Mertens, J., Huizinga, A., Schallert, B., Schaber, K., . . . Goetheer, E. (2013). Investigation of aerosol based emission of MEA due to sulphuric acid aerosol and soot in a post combustion CO 2 capture process. *International Journal of Greenhouse Gas Control, 19*, 138-144. doi:10.1016/j.ijggc.2013.08.014

Kulkarni, P., Namiki, N., Otani, Y., & Biswas, P. (2002). Charging of particles in unipolar coronas irradiated by in-situ soft X-rays: enhancement of capture efficiency of ultrafine particles. *Journal of aerosol science, 33*(9), 1279-1296. doi:10.1016/S0021-8502(02)00067-8

Li, L., An, J., Zhou, M., Yan, R., Huang, C., Lu, Q., . . . Qiao, L. (2015). Source apportionment of fine particles and its chemical components over the Yangtze River Delta, China during a heavy haze pollution episode. *Atmospheric Environment, 123*, 415-429. doi:10.1016/j.atmosenv.2015.06.051

Li, Y., Suriyawong, A., Daukoru, M., Zhuang, Y., & Biswas, P. (2009). Measurement and capture of fine and ultrafine particles from a pilot-scale pulverized coal combustor with an electrostatic precipitator. *Journal of the Air & Waste Management Association, 59*(5), 553. doi:10.3155/1047-3289.59.5.553

Li, Z., Jiang, J., Ma, Z., Wang, S., & Duan, L. (2015). Effect of selective catalytic reduction (SCR) on fine particle emission from two coal-fired power plants in China. *Atmospheric Environment, 120*, 227-233. doi:10.1016/j.atmosenv.2015.08.046

Liu, F., Zhang, Q., Tong, D., Zheng, B., Li, M., Huo, H., & He, K. (2015). High-resolution inventory of technologies, activities, and emissions of coal-fired power plants in China from 1990 to 2010. *Atmospheric Chemistry and Physics, 15*(23), 13299-13317. doi:10.5194/acp-15-13299-2015

Meij, R., & Te Winkel, B. (2004). The emissions and environmental impact of PM 10 and trace elements from a modern coal-fired power plant equipped with ESP and wet FGD. *Fuel Processing Technology, 85*(6), 641-656. doi:10.1016/j.fuproc.2003.11.012

Mertens, J., Brachert, L., Desagher, D., Thielens, M., Khakharia, P., Goetheer, E., & Schaber, K. (2014). ELPI+ measurements of aerosol growth in an amine absorption column. *International Journal of Greenhouse Gas Control, 23*, 44-50. doi:10.1016/j.ijggc.2014.02.002

Mertens, J., Knudsen, J., Thielens, M.-L., & Andersen, J. (2012). On-line monitoring and controlling emissions in amine post combustion carbon capture: a field test. *International Journal of Greenhouse Gas Control, 6*, 2-11. doi:10.1016/j.ijggc.2011.11.015

Mertens, J., Lepaumier, H., Desagher, D., & Thielens, M.-L. (2013). Understanding ethanolamine (MEA) and ammonia emissions from amine based post combustion carbon capture: Lessons learned from field tests. *International Journal of Greenhouse Gas Control, 13*, 72-77. doi:10.1016/j.ijggc.2012.12.013

Pui, D., Fruin, S., & McMurry, P. (1988). Unipolar diffusion charging of ultrafine aerosols. *Aerosol Science and Technology, 8*(2), 173-187.

Rochelle, G. T. (2009). Amine scrubbing for CO2 capture. *Science, 325*(5948), 1652-1654. doi:10.1126/science.1176731

Rubin, E. S., & Nguyen, D. G. (1978). Energy requirements of a limestone FGD system. *Journal of the Air Pollution Control Association, 28*(12), 1207-1212. doi:10.1080/00022470.1978.10470728

Ryu, H.-J., Grace, J. R., & Lim, C. J. (2006). Simultaneous CO2/SO2 capture characteristics of three limestones in a fluidized-bed reactor. *Energy & Fuels, 20*(4), 1621-1628.

Schaber, K. (1995). Aerosol formation in absorption processes. *Chemical Engineering Science, 50*(8), 1347-1360. doi:10.1016/0009-2509(95)98846-7

Shi, Y., Wang, J., & Liu, Z. (2015). On-line monitoring of ash fouling and soot-blowing optimization for convective heat exchanger in coal-fired power plant boiler. *Applied Thermal Engineering, 78*, 39-50. doi:10.1016/j.applthermaleng.2014.12.002

Sijbesma, H., Nymeijer, K., van Marwijk, R., Heijboer, R., Potreck, J., & Wessling, M. (2008). Flue gas dehydration using polymer membranes. *Journal of membrane science, 313*(1), 263-276.

Strand, M., Pagels, J., Szpila, A., Gudmundsson, A., Swietlicki, E., Bohgard, M., & Sanati, M. (2002). Fly ash penetration through electrostatic precipitator and flue gas condenser in a 6 MW biomass fired boiler. *Energy & Fuels, 16*(6), 1499-1506. doi:10.1021/ef020076b

Tola, V., Cau, G., Ferrara, F., & Pettinau, A. (2016). CO2 emissions reduction from coal-fired power generation: a techno-economic comparison. *Journal of Energy Resources Technology, 138*(6), 061602. doi:10.1115/1.4034547

142

Valmari, T., Lind, T., Kauppinen, E., Sfiris, G., Nilsson, K., & Maenhaut, W. (1999). Field study on ash behavior during circulating fluidized-bed combustion of biomass. 2. Ash deposition and alkali vapor condensation. *Energy & Fuels, 13*(2), 390-395.

Wang, H., Song, Q., Yao, Q., & CHEN, C.-h. (2008). Experimental study on removal effect of wet flue gas desulfurization system on fine particles from a coal-fired power plant. *Proceedings-Chinese Society of electrical engineering, 28*(5), 1.

Xiong, T., Jiang, W., & Gao, W. (2016). Current status and prediction of major atmospheric emissions from coal-fired power plants in Shandong Province, China. *Atmospheric Environment, 124*(Part A), 46-52. doi:10.1016/j.atmosenv.2015.11.002

Xu, Y., Hu, J., Ying, Q., Hao, H., Wang, D., & Zhang, H. (2017). Current and future emissions of primary pollutants from coal-fired power plants in Shaanxi, China. *Science of the Total Environment, 595*, 505-514. doi:10.1016/j.scitotenv.2017.03.267

Yang, L., Bao, J., Yan, J., Liu, J., Song, S., & Fan, F. (2010). Removal of fine particles in wet flue gas desulfurization system by heterogeneous condensation. *Chemical Engineering Journal, 156*(1), 25-32.

Yi, H., Hao, J., Duan, L., Tang, X., Ning, P., & Li, X. (2008). Fine particle and trace element emissions from an anthracite coal-fired power plant equipped with a bag-house in China. *Fuel, 87*(10), 2050-2057. doi:10.1016/j.fuel.2007.10.009

Ylätalo, S. I., & Hautanen, J. (1998). Electrostatic precipitator penetration function for pulverized coal combustion. *Aerosol Science and Technology, 29*(1), 17-30. doi:10.1080/02786829808965547

Zhang, R., Jing, J., Tao, J., Hsu, S.-C., Wang, G., Cao, J., . . . Zhao, Y. (2013). Chemical characterization and source apportionment of PM 2.5 in Beijing: seasonal perspective. *Atmospheric Chemistry and Physics, 13*(14), 7053-7074. doi:10.5194/acp-13-7053-2013

Zhao, Y., Wang, S., Duan, L., Lei, Y., Cao, P., & Hao, J. (2008). Primary air pollutant emissions of coal-fired power plants in China: Current status and future prediction. *Atmospheric Environment, 42*(36), 8442-8452. doi:10.1016/j.atmosenv.2008.08.021

Zhuang, Y., Kim, Y. J., Lee, T. G., & Biswas, P. (2000). Experimental and theoretical studies of ultra-fine particle behavior in electrostatic precipitators. *Journal of Electrostatics, 48*(3-4), 245-260. doi:10.1016/s0304-3886(99)00072-8

Chapter 6: Understanding the effects of flue gas aerosol pretreatments upstream amine-based CO$_2$ scrubber

Abstract

Amine-based CO_2 scrubbers are widely considered a promising technology for post-combustion CO_2 capture. However, the main challenge for this technology has been reported as the amine loss caused by influent particles in coal-fired power plant flue gas. To ensure cost-effective operation of amine scrubbers, several particle pretreatment measures were explored in this study. The particles were sampled from the flue gas upstream a pilot-scale amine scrubber in a utility-scale coal-fired power plant. The effects of steam injection, water desiccation and electrostatic precipitation were investigated. Steam injection caused a decrease of particle concentration in the range of 20 nm to 40 nm, and an increase of particle concentration in the range of 40 nm to 60 nm. Higher steam flow rate could increase the peak size of the particle size distribution. Whether the diffusion dryer was installed before the particle instruments showed on significant effect on particle size distributions. Electrostatic precipitator (ESP) could reduce the number concentrations of particles in most sizes by >2 orders of magnitude. Almost 99.9% of the particles ranging from 25 nm to 80 nm in diameter were removed by the ESP with a voltage of 18.1 kV. Evidence showed that secondary aerosol like H_2O-H_2SO_4 could be generated from SO_2 in flue gas inside the ESP.

6.1   Introduction

Amine-based CO_2 scrubbers are extensively considered as promising technologies for CO_2 capture because they have great potential to be energy-efficient with process and solvent improvements (Rochelle, 2009). Linde and BASF have been developing a post-combustion carbon capture technology based on BASF OASE® Blue technology (Stoffregen et al., 2014). The technology uses a novel solvent that are quite stable in coal-fired power plant flue gas environment, which can help reducing solvent regeneration energy requirements. However, amine-based CO_2 scrubbing technologies were typically suffering from the amine loss issue caused by fine particles in flue gas.

146

Particularly, fine particles in flue gas can act as nuclei for amine vapor in the scrubbers and thus a remarkable amount of amine can be carried out of the device by flue gas flow (Kamijo et al., 2013; Khakharia et al., 2015; Khakharia et al., 2013; Mertens, Brachert, et al., 2014; Mertens et al., 2012; Mertens et al., 2013). Moreover, it has been widely reported that aerosol number concentration and size distributions upstream amine-based CO_2 scrubber are crucial to the capture efficiency of CO_2 and amine loss in the scrubber (Khakharia et al., 2013; Mertens et al., 2012; Mertens et al., 2013). Khakharia found that flue gas with carbon-enriched soot particles generated from incomplete coal combustion could cause amine emission loss 2-4 times higher than inlet gas without fine particles (Khakharia et al., 2013). It has been reported by Mertens (Mertens, Brachert, et al., 2014) that particles with diameters less than 100 nm tended to create more amine mist emissions downstream of the CO_2 scrubber. And Mertens also demonstrated that amine mist formation significantly depended on the flue gas composition upstream the CO_2 capture facility and on the plant's engineering design and operating conditions (Mertens et al., 2013). Due to the diversity of phases, chemical composition, physical sizes of the particles in flue gas, it is quite challenging to effectively reduce amine loss with appropriate particle control technologies.

Therefore, to eliminate the undesirable impact of fine particles on amine emissions and CO_2 capture at a full-scale power plant, it is crucial to explore countermeasures that leverage different working mechanisms to treat particles in the flue gas upstream the scrubbers. Mertens has studied the effectiveness of wet electrostatic precipitator (WESP) to control amine mist formation and concluded that it was necessary to remove SO_2 from the flue gas using an alkaline scrubber for the WESP to be effective on amine mist formation control because of formation of H_2SO_4 aerosol (Mertens, Anderlohr, et al., 2014). Another study on applying an acid wash scrubber using sulfuric

147

acid for amine emission control showed that ammonia emissions can be reduced from 15-20 mg/Nm^3 to below 5 mg/Nm^3 at a pH of 6 (Khakharia et al., 2014).

This study was focused on investigating particle size distributions in coal-fired power plant flue gas upstream a pilot-scale amine-based CO_2 scrubber based on BASF OASE[®] Blue technology and effects of different pretreatment measures on particle size distributions. In this study, state of the art research grade instrumentation was deployed beside the real facility to measure the real-time particle size distributions in flue gas. Then, the aerosol properties were also measured with different flow rates of steam injection as well as without steam injection. The effects of water content in aerosols were investigated by using a diffusion dryer. Besides, performance of a bench scale electrostatic precipitator (ESP) was evaluated with steam injection on in terms of collection efficiency of particles in the flue gas. Detailed particle characterization under various pretreatment scenarios produced by this study can be valuable for development of novel technologies for amine emission control.

6.2   Experimental section

6.2.1   Sampling location
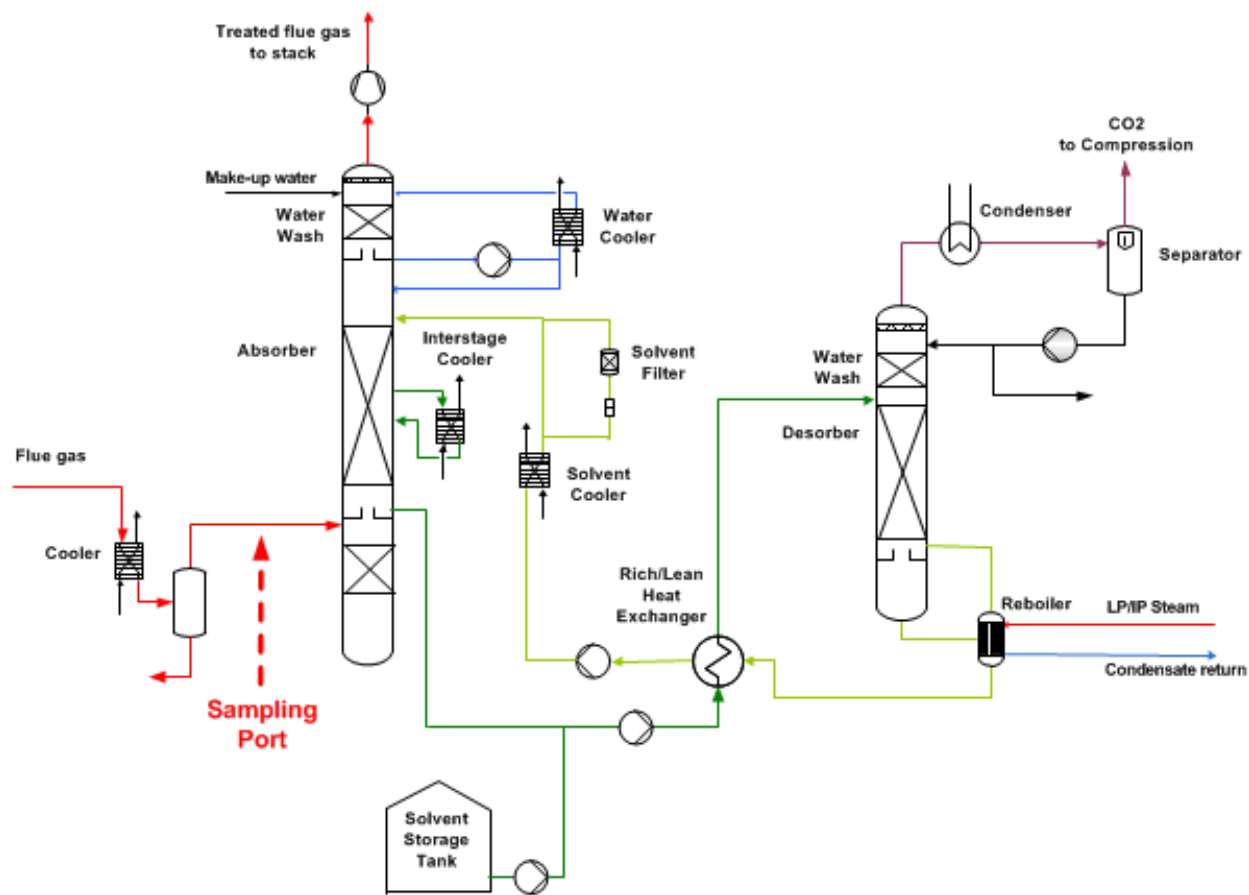
Figure 6.1 Layout of the post carbon capture facility and sampling location.

Funded by US Department of Energy, Linde and BASF have built a 1-1.5 MW$_{el}$ scale post-combustion carbon capture pilot plant at the National Carbon Capture Center (NCCC) in Wilsonville, Alabama. The pilot plant receives a slipstream of the flue gas from a coal fired power plant (Illinois #6 coal) as feed gas to be processed. The layout of the pilot plant is shown in Figure 6.1. The sampling port is located right before the inlet of the amine-based scrubber based on BASF OASE® Blue technology.

6.2.2 Experimental system

The schematic diagram of the experimental setup for measuring the particle concentration and size distributions is shown in Figure 6.2. A stainless-steel tube with an OD of 3/8" and a length of 5 feet was used to take samples from the flue gas duct. The sampling tube was cut to the length so

that it can draw particles from the center, inner wall and outer wall of the flue gas duct. The tube was also bend at the end to achieve isokinetic sampling (designed for a range of particle sizes in the submicrometer and micrometer regimes). A stream of particle-free air mixed with the sample at the end of the sampling tube to dilute the aerosol and reduce the water vapor concentration. Before entering the instruments, the diluted aerosol sample was split to two streams, one passed to a vacuum pump and the other to a diffusion dryer to remove the water content. The dried aerosols were drawn by the instruments: a scanning mobility particle sizer (SMPS, TSI Inc.) and an aerodynamic particle sizer (APS, TSI Inc.). In several of the tests, the diffusion dryer was unused to examine the influence of water content on particle size distributions and number concentrations. The internal pumps in the instruments pulled aerosols at a flow rate of 6.5 lpm, while the flow rates of the dilution air from the compressed air tank and the slip stream going to the pump were both maintained at 10 lpm. The resultant dilution ratio was 2.54.

In this study, the size distributions of particles from 10 nm to 200 nm were measured continuously in real time with the SMPS. High resolution particle size distributions were obtained through the measurement at 64 different sizes (channels). The SMPS uses a differential mobility analyzer (DMA) to classify particles as a function of electrical mobility size, and a condensation particle counter (CPC) to measure particle concentrations. The continuous particle size distribution function is obtained through data inversion, which relates particle concentration to the charging efficiency of the neutralizer, the detection efficiency of the CPC, and the transfer function of the DMA (Stolzenburg et al., 2008).

Operated by the time-of-flight theory, the APS measures the aerodynamic size distributions of particles ranging from 0.5 to 20 μm. In the APS, the sampled particles flow along the centerline of an accelerating flow created by the sheath air. As they pass through two broadly focused laser

beams, each particle scattered light twice, which is collected by the photodetector in the APS. The

aerodynamic particle size is then calculated based on the time interval between the pulses of the

scattered light.
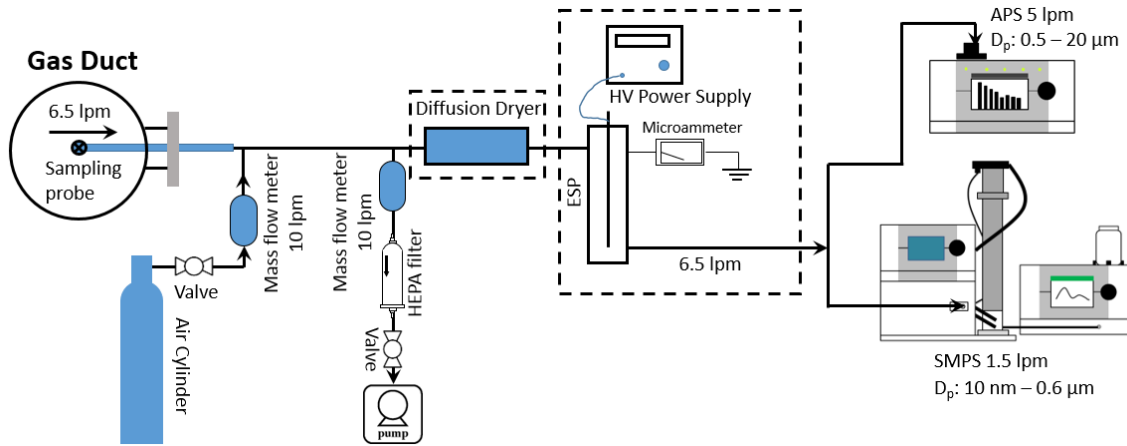
Figure 6.2 Schematic diagram of the experimental setup.

6.2.3 Experimental plan

Aerosol size distributions and concentrations were measured at five point along radial direction on

the plane of cross section, which is illustrated in Figure 6.3. Table 6.1 provides a brief summary

of the experimental plan in chronological order. In the results and discussion section, we present

the test results in the order of measurement system characterization, effects of steam injection and

diffusion dryer, and effect of ESP on the flue gas at the inlet of the scrubber.
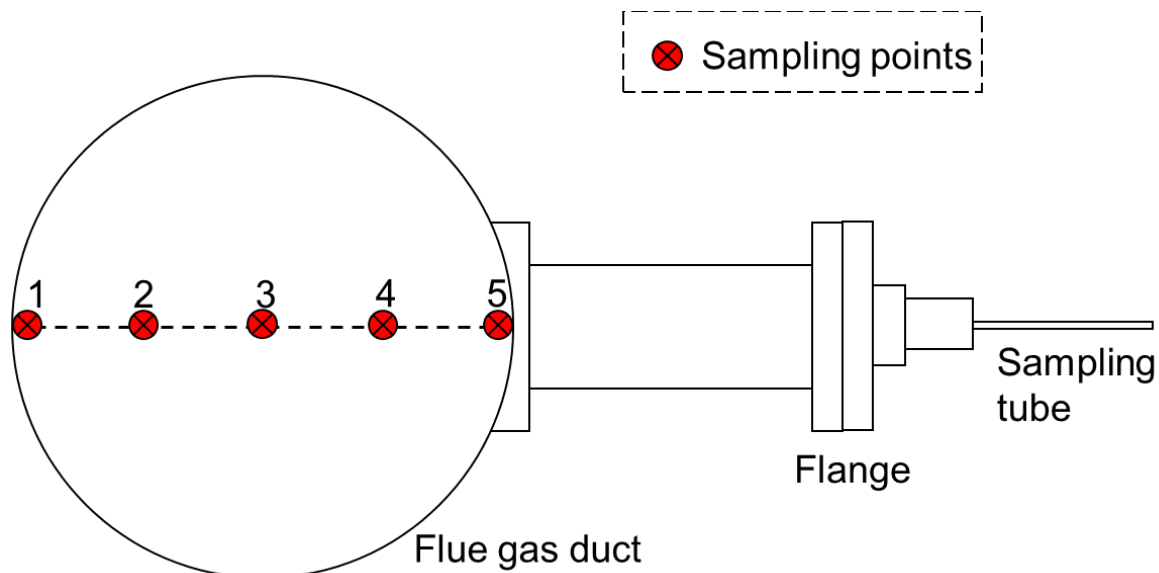
Figure 6.3 Sampling points (#1–5) in radial direction on the cross section plane inside the 10-inch flue gas duct (Supposing the point #3 is at origin, then #1–5 are at −5 in, −2.5 in, 0 in, 2.5 in, and 5 in, respectively).

Table 6.1 Summary of performed tests.

Test #	Sampling point in radial direction	Steam injection	ESP	Diffusion dryer	Instruments
1	1	off	off	√	
2	2	off	off	√	
3	3	off	off	√ ✕	
4	4	off	off	√	
5	5	off	off	√	SMPS, APS
6	1	on	off	√	
7	2	on	off	√	
8	3	on	off on	√ ✕	
9	4	on	off	√	
10	5	on	off	√	

6.3 Results and discussion

6.3.1 Aerosol characterization

Figure 6.4 shows a representative size distribution of particles in flue gas measured by the SMPS

and APS at the center of the flue gas duct. Steam injection was turned off and a diffusion dryer

was used before the size measuring instruments. According to Figure 6.4, concentration of

particles above 400 nm is minimal compared to that of particles below 100 nm, suggesting that most of the particles were in the submicron range. Similar shapes of particle size distribution were also observed in our previous measurement in the Abbott Power Plant, IL and in some other studies (Ylätalo et al., 1998). The measured particles have a mode size of 37.2 nm, and the particle concentration at 37.2 nm is 4.5×10^6 #/cm^3. Compared to the measurement results in the Abbott Power Plant (mode size: 40 nm; concentration at 40 nm: 3.0×10^8 #/cm^3), the mode particle size is similar, while the concentration at mode size is significantly lower. It needs be noted that the flue gas pulled from the Gaston plant in the this study was a slipstream of water-saturated flue gas downstream a baghouse filter and a flue gas desulfurization (FGD) unit, typically at atmospheric pressure and a temperature of 50-60 °C. However, for the Abbott plant study, the particle filtration device used was an ESP, which could be less efficient in particle collection than the baghouse used in this study. Another cause for the difference in particle size distribution could be the fact that the sampling location in this study was downstream a SO_2 polishing scrubber using NaOH, which was designed for cooling down the flue gas to a temperature suitable for efficient CO_2 absorption and minimizing solvent degradation due to SO_2-amine complex formation (Stoffregen et al., 2014). The additional removal of SO_2 besides the upstream FGD could result in lower H_2SO_4 aerosol concentration in this study. The total particle concentration can be calculated by integrating the particle size distribution, yielding a value of 1.2×10^6 #/cm^3 (8.9×10^9 #/cm^3 at Abbott Power Plant). The lower particle concentration is beneficial in controlling amine loss in the absorber.
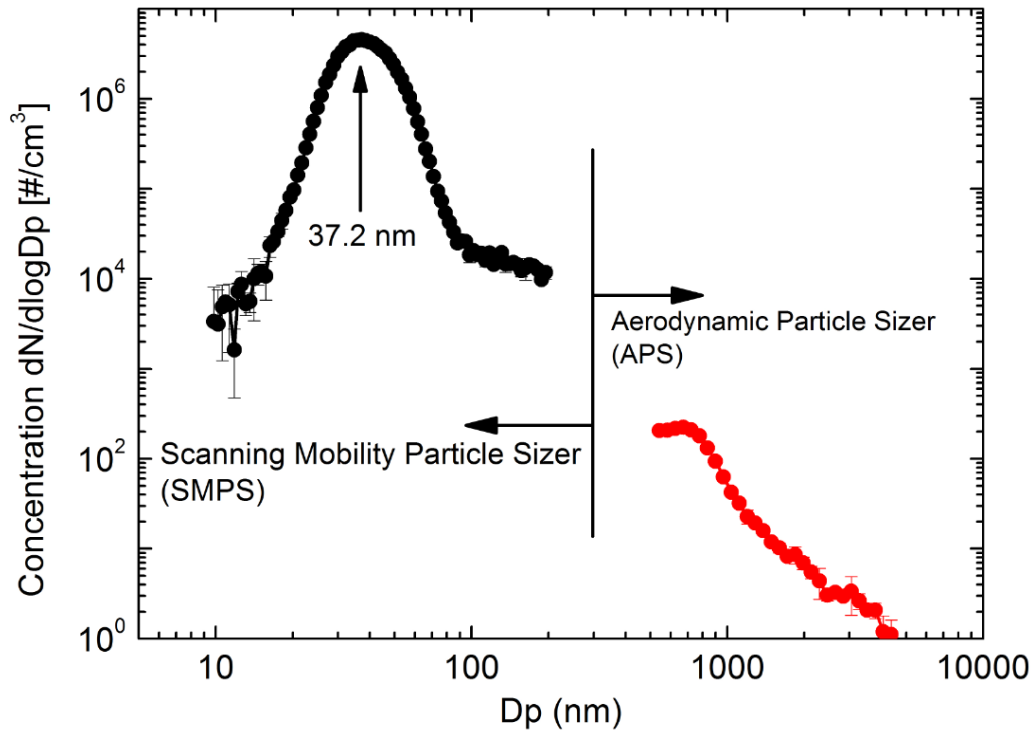
Figure 6.4 A representative particle size distribution measured with SMPS and APS (Test #3 with diffusion dryer).

Figure 6.5 is a contour plot of particle size distributions measured at different radial locations of the 10-inch flue gas pipe (x-axis represents radial location, y-axis represents particle size, and color mapping represents particle concentration). Radial location of the sampling probe indeed had an influence on particle size distribution measurement. At all tested locations, the mode particle size is around 37 nm, while the concentrations at walls of the pipe are lower due to wall loss. The difference in the particle concentration is within 35%.
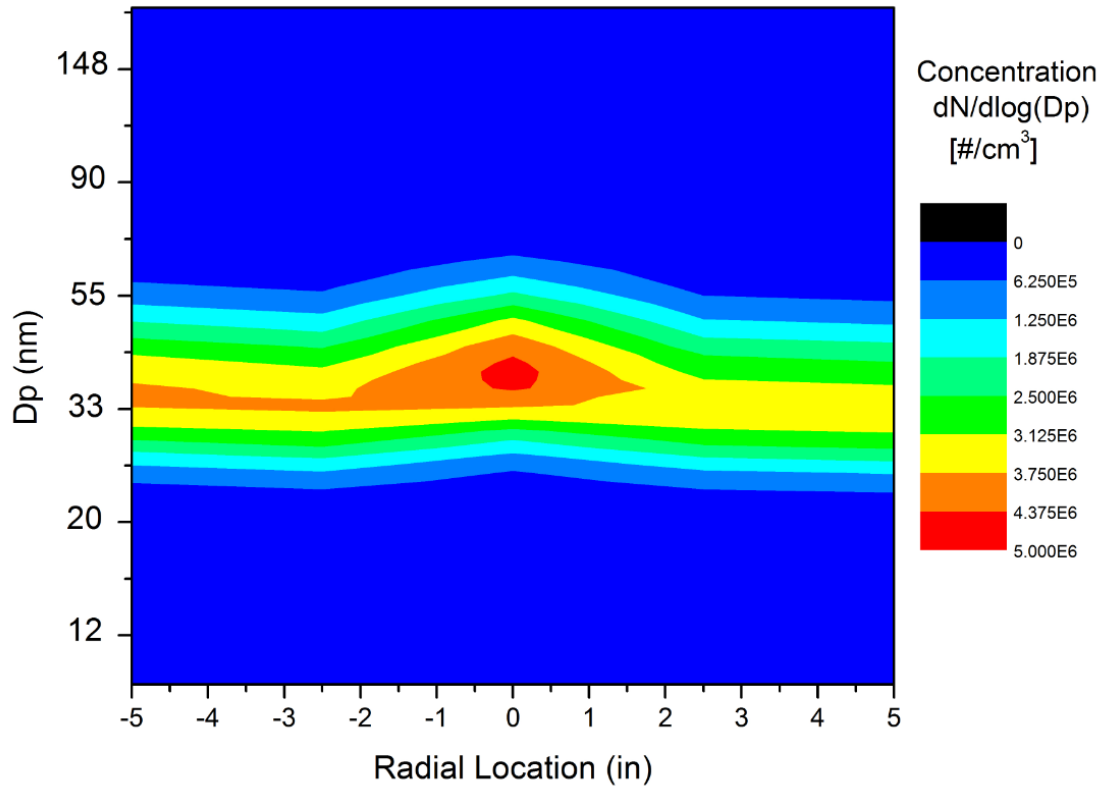
Figure 6.5 Radial distribution of particle size distribution in the size range below 160 nm. Measurements were conducted in a 10-inch flue gas pipe at radial locations of −5 in, −2.5 in, 0 in, 2.5 in, and 5 in.

6.3.2 Effect of steam injection on aerosol size distribution

The effect of steam injection on particle removal was examined by measuring particle size distributions under different steam flow rates. To avoid the fluctuation of aerosol properties over a long period of time of power plant operation, the measurement was conducted intensively during 6-8 pm on July 22nd. The line plot in Figure 6.6 shows the particle size distribution when steam injection was turned off. Particles mainly distributed in the size range of 20 to 60 nm. The line-symbol plots represent the relative magnitude of particle size distributions compared to the size distribution when the steam injection was off. Hence, a relative magnitude lower than 1 signifies the removal of particles, and a relative magnitude higher than 1 indicates the generation of particles. Figure 6.6 shows that in the size range of 20 to 60 nm where the particles mostly

155

concentrated, steam injection caused a decrease of particle concentration in the range of 20 nm to 40 nm, and an increase of particle concentration in the range of 40 nm to 60 nm. This effect was enhanced when a higher steam flow rate was used. This phenomenon may be a result of water vapor condensation on the existing particles in the flue gas, which shifted the particle size distributions to larger sizes. For example, particles with the mode size of 37 nm may grow to 50 nm, causing an increase of relative magnitude of particle size distributions at 50 nm. In the size range outside 20 to 60 nm, the relative magnitude values fluctuated around 0.8, indicating an overall effect of particle removal through steam injection. However, since particles are mostly distributed in the size range between 20 and 60 nm, this removal effect is relatively insignificant. Integrating the particle size distributions measured at different steam injection flow rates, we obtained that the total particle number concentration at steam flow rates of 0, 150, 400, and 600 lb/hr were 1.47×10^6, 1.46×10^6, 1.39×10^6, and 1.35×10^6 #/cm^3.
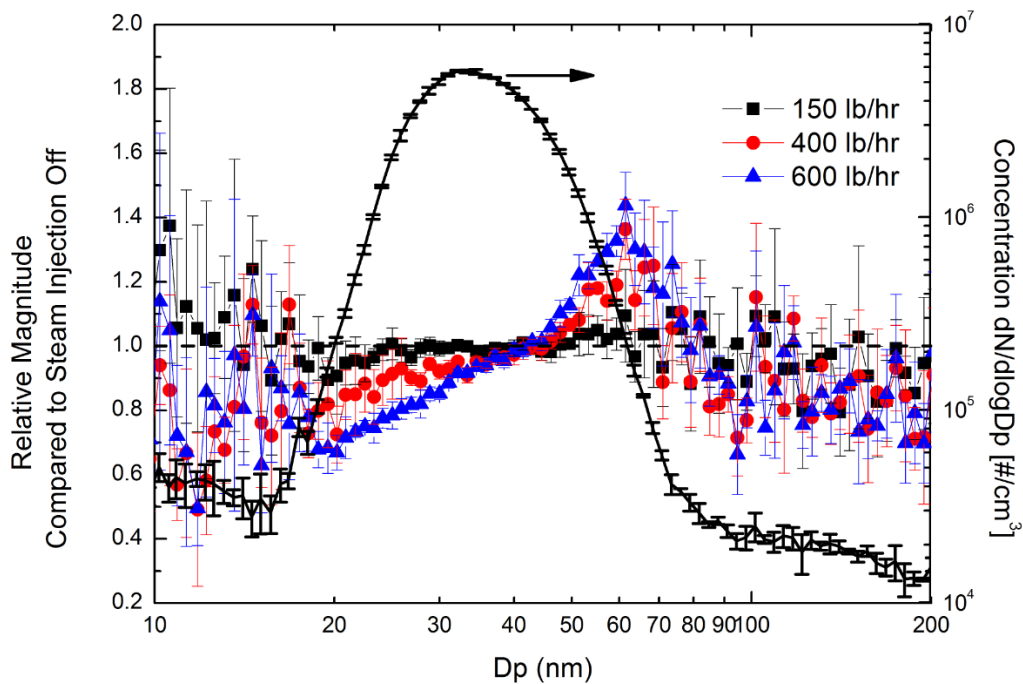
Figure 6.6 Influence of steam injection on particle size distribution (Value of 1 on the left axis implies no change on steam injection.)

156

6.3.3 Effect of diffusion dryer on aerosol size distribution

Figure 6.7 shows the effect of adding a diffusion dryer before the instruments on particle size measurement. The particle concentrations measured with 150 lb/hr steam injection was higher than those of steam injection turned off, which is probably caused by the fluctuation of aerosol properties during the power plant operation, since these experiments were conducted in two separate days (July 21st 3-4 pm and July 22nd 6-8 pm). Adding a diffusion dryer before the instruments did not significantly shrink the particle size, indicating that the water content in particles were low. We can recall that the effect of adding a diffusion dryer on particle concentration measurement was relatively significant at the Abbott Power Plant measurement (~40% difference with and without a diffusion dryer). One explanation can be that the flue gas temperature in this study (~103 deg F) was lower than the other study (~170 deg F). At the same time, the ambient temperature (~100 deg F) and humidity in this study were also higher. This means that less water vapor can be condensed on the particles in the flue gas pipe, and the condensed water vapor is more difficult to be removed by the diffusion dryer.
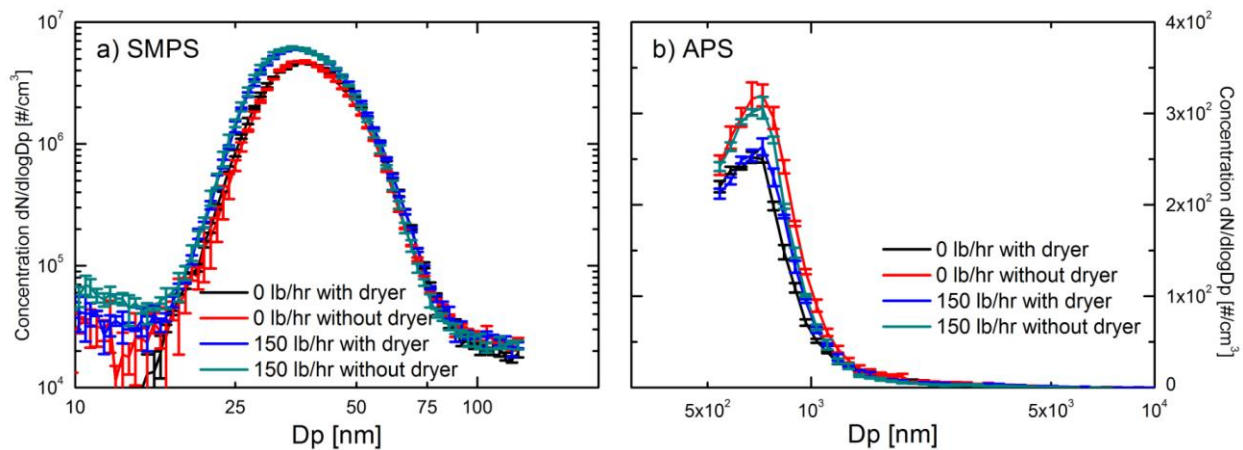
Figure 6.7 Effect of adding a diffusion dryer before size measurement. (with and without steam injection).

6.3.4 Particle removal by electrostatic precipitator (ESP)

Figure 6.8(a) and (b) show the effect of applying an ESP to treating the wet flue gas after steam injection in terms of results of SMPS and APS, respectively. The onset voltage for the ESP was 12.0 kV. Figure 6.8(a) shows that even with very small current of 20 µA at 12.3 kV, the number concentrations of most of the particles decrease by nearly 2 orders of magnitude. When the voltage was enhanced to 18.1 kV, almost 99.9% of the particles ranging from 25 nm to 80 nm in diameter were removed by the ESP. In fact, higher particle capture efficiency with higher voltage of ESP was extensively reported (Li et al., 2009; Suriyawong et al., 2008; Zhuang et al., 2000). Interestingly, when the voltage kept increasing to 18.4 kV and then to 19.2 kV, particles with diameter of 10 nm to 100 nm showed higher number concentration compared with the case under 18.1 kV. Especially, the number concentration of particles smaller than 25 nm when the voltage is 19.2 kV was significantly higher than that when the ESP is off. Similar increase of number concentration of particles along with increasing voltage of ESP was also observed by other researchers both in lab scale and pilot combustor studies (Jing, 2016; Li et al., 2009). Jing found that newly generated secondary aerosols had a unimodal size distribution with a peak size of 20 nm, and the total number concentration of secondary aerosols increased as the applied voltage of ESP rose from −8 kV to −10 kV. These findings are well consistent with the results shown in Figure 6.8(a). Therefore, it is reasonable to infer that this phenomenon can be probably attributed to secondary aerosol generation inside the ESP since SO_2 in the flue gas can be oxidized by radicals in the ESP and react with water to form some H_2O-H_2SO_4 aerosols (Jing, 2016). Figure 6.8(b) shows significant decrease in number concentrations of particles larger than 500 nm in diameter under all tested voltages, which implies that no large particles were obviously generated.
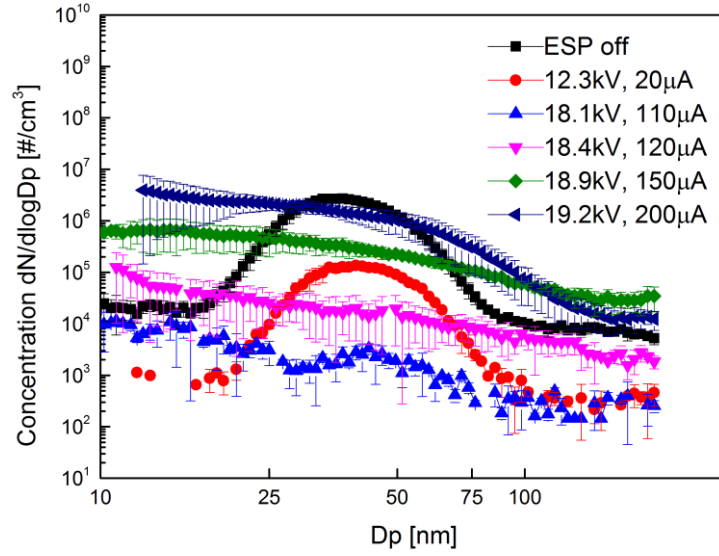
(a)
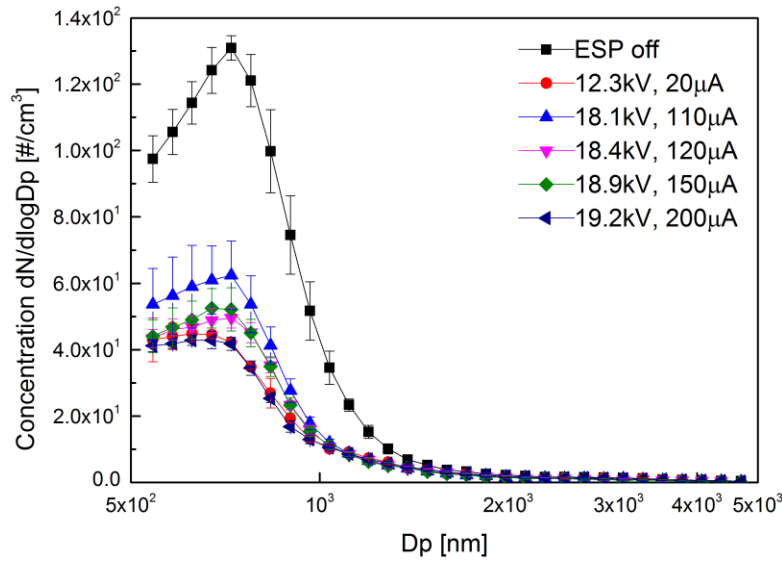
(b)

Figure 6.8 Particle size distribution measured with different ESP voltages: (a) SMPS; (b) APS.

6.4 Conclusion

The particles in the flue gas were mostly in the size range of 20 to 60 nm. Steam injection caused a decrease of particle concentration in the range of 20 nm to 40 nm, and an increase of particle concentration in the range of 40 nm to 60 nm. This effect was enhanced when a higher steam flow rate was used. Tests with diffusion dryer before the instruments indicate that the water content in the particles in the flue gas were low. Small particles in the range of 10 to 100 nm in diameter were

generated inside the ESP probably due to high content of SO_2 and water in the flue gas. Nonetheless, a light-weight ESP can be still considered to be installed upstream the scrubber and operated under appropriate voltages to reduce the number concentration of ultrafine particles flowing into the scrubber to ultimately avoid amine loss issues.

6.5 References

Jing, H. (2016). Novel Applications of Electrostatic Precipitators in Coal-Biomass Combustion Systems.

Kamijo, T., Kajiya, Y., Endo, T., Nagayasu, H., Tanaka, H., Hirata, T., . . . Tsujiuchi, T. (2013). SO 3 impact on amine emission and emission reduction technology. *Energy Procedia, 37*, 1793-1796. doi:10.1016/j.egypro.2013.06.056

Khakharia, P., Brachert, L., Mertens, J., Anderlohr, C., Huizinga, A., Fernandez, E. S., . . . Goetheer, E. (2015). Understanding aerosol based emissions in a Post Combustion CO 2 Capture process: Parameter testing and mechanisms. *International Journal of Greenhouse Gas Control, 34*, 63-74. doi:10.1016/j.ijggc.2015.01.001

Khakharia, P., Brachert, L., Mertens, J., Huizinga, A., Schallert, B., Schaber, K., . . . Goetheer, E. (2013). Investigation of aerosol based emission of MEA due to sulphuric acid aerosol and soot in a post combustion CO 2 capture process. *International Journal of Greenhouse Gas Control, 19*, 138-144. doi:10.1016/j.ijggc.2013.08.014

Khakharia, P., Huizinga, A., Jurado Lopez, C., Sanchez Sanchez, C., de Miguel Mercader, F., Vlugt, T. J. H., & Goetheer, E. (2014). Acid Wash Scrubbing as a Countermeasure for Ammonia Emissions from a Postcombustion CO2 Capture Plant. *Industrial & Engineering Chemistry Research, 53*(33), 13195-13204. doi:10.1021/ie502045c

Li, Y., Suriyawong, A., Daukoru, M., Zhuang, Y., & Biswas, P. (2009). Measurement and capture of fine and ultrafine particles from a pilot-scale pulverized coal combustor with an electrostatic precipitator. *Journal of the Air & Waste Management Association, 59*(5), 553.

Mertens, J., Anderlohr, C., Rogiers, P., Brachert, L., Khakharia, P., Goetheer, E., & Schaber, K. (2014). A wet electrostatic precipitator (WESP) as countermeasure to mist formation in amine based carbon capture. *International Journal of Greenhouse Gas Control, 31*, 175-181. doi:https://doi.org/10.1016/j.ijggc.2014.10.012

Mertens, J., Brachert, L., Desagher, D., Thielens, M., Khakharia, P., Goetheer, E., & Schaber, K. (2014). ELPI+ measurements of aerosol growth in an amine absorption column. *International Journal of Greenhouse Gas Control, 23*, 44-50. doi:10.1016/j.ijggc.2014.02.002

Mertens, J., Knudsen, J., Thielens, M.-L., & Andersen, J. (2012). On-line monitoring and controlling emissions in amine post combustion carbon capture: a field test. *International Journal of Greenhouse Gas Control, 6*, 2-11. doi:10.1016/j.ijggc.2011.11.015

Mertens, J., Lepaumier, H., Desagher, D., & Thielens, M.-L. (2013). Understanding ethanolamine (MEA) and ammonia emissions from amine based post combustion carbon capture: Lessons learned from field tests. *International Journal of Greenhouse Gas Control, 13*, 72-77. doi:10.1016/j.ijggc.2012.12.013

Rochelle, G. T. (2009). Amine scrubbing for CO2 capture. *Science, 325*(5948), 1652-1654. doi:10.1126/science.1176731

Stoffregen, T., Rigby, S., Jovanovic, S., & Krishnamurthy, K. R. (2014). Pilot-scale demonstration of an advanced aqueous amine-based post-combustion capture technology for CO2 capture from power plant flue gases. *Energy Procedia, 63*, 1456-1469.

Stolzenburg, M. R., & McMurry, P. H. (2008). Equations governing single and tandem DMA configurations and a new lognormal approximation to the transfer function. *Aerosol Science and Technology, 42*(6), 421-432.

Suriyawong, A., Hogan, C. J., Jr., Jiang, J., & Biswas, P. (2008). Charged fraction and electrostatic collection of ultrafine and submicrometer particles formed during $O(2)$-$CO(2)$ coal combustion. *Fuel, 87*(6), 673-682. doi:10.1016/j.fuel.2007.07.024

Ylätalo, S. I., & Hautanen, J. (1998). Electrostatic precipitator penetration function for pulverized coal combustion. *Aerosol Science and Technology, 29*(1), 17-30.

Zhuang, Y., Kim, Y. J., Lee, T. G., & Biswas, P. (2000). Experimental and theoretical studies of ultra-fine particle behavior in electrostatic precipitators. *Journal of Electrostatics, 48*(3-4), 245-260. doi:10.1016/s0304-3886(99)00072-8

Chapter 7: Pilot-scale pressurized electrostatic precipitator (PESP) design, simulation and demonstration

Abstract

A pressurized ESP (PESP) was designed and constructed for particle removal in pressurized oxy-combustion system. The collection efficiencies for particles in different sizes were predicted by the previously developed semi-empirical ESP performance model. Hazard and operability study (HAZOP) was conducted to ensure safety of mechanical and electrical operation. Current-voltage characteristics showed that the highest current achievable under 15 bar was 30 µA with 50.2 kV. Sparkover occurred at high voltage and limited the maximum obtainable current of the P-ESP. 2D axis-symmetrical simulation of gas flow field and electrical field inside the P-ESP was performed using COMSOL, which can provide crucial information for particle tracing study and performance modeling in the future. Experiments on particle size distributions in exhaust gas from pressurized oxy-combustor and particle capture performance of PESP under different flow conditions need to be performed in next steps.

7.1 Introduction

Pressurized oxy-combustion has been recently studied as a promising advanced combustion technology for carbon capture because it can reduce the energy requirement (Gopan et al., 2015; Gopan et al., 2014; Xia et al., 2016; Zheng et al., 2010). The primary advantage of the pressurized oxy-combustion technology is that the water vapor in the combustor can condense more easily under high pressure and thus more latent heat of water can be recovered to improve the overall energy efficiency. A novel approach to pressurized oxy-combustion, staged pressurized oxy-combustion (SPOC), has been developed at Washington University in St. Louis. By staging the delivery of fuel, the energy cost of recycling large amount of flue gas for temperature control was effectively reduced (Gopan et al., 2014).

However, one of the main challenges of pressurized combustion system is that particles in the flue gas need to be removed under high pressure. Conventional electrostatic precipitators (ESPs) are widely used in coal-fired power plants due to its high removal efficiency and easy operation, but there is little understanding of how ESP performs under high pressure. A pressurized ESP (PESP) is needed for particle control in a pressurized oxy-combustion system.

Previous study has been focused on investigating the pressure effect on particle penetration using a lab-scale PESP and developing a semi-empirical Deutsch-Anderson equation for estimating particle collection efficiency (Li et al., 2016). This chapter will cover the engineering design, current-voltage characteristics and basic computational fluid dynamics simulation of a newly-designed pilot-scale PESP, which is counted as a preliminary contribution for pilot-scale PESP demonstration.

7.2 Experiment setup

7.2.1 Engineering design

| (a) | (b) |
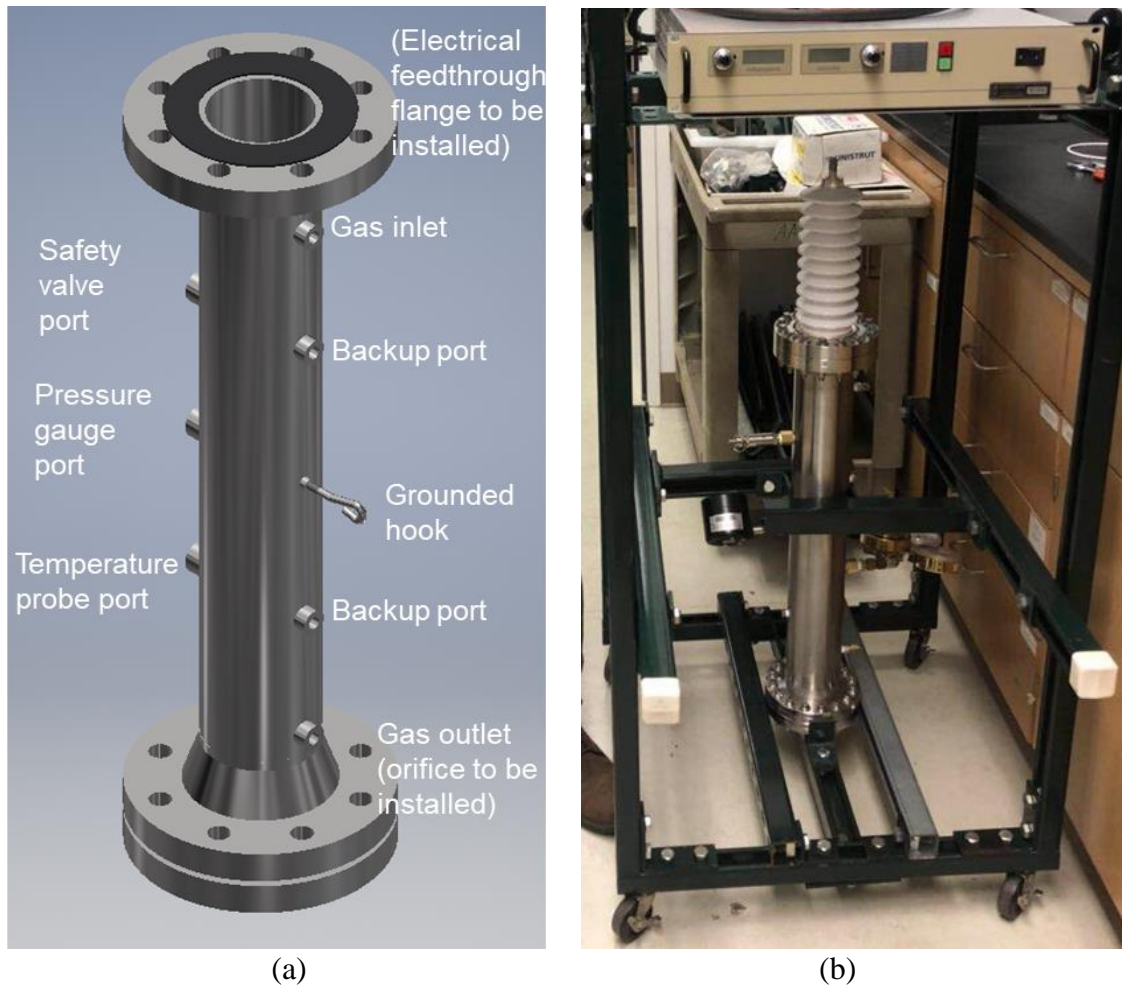
Figure 7.1 (a) Engineering drawing of the PESP in 3D; (b) PESP photo.

A pilot-scale PESP was designed using Autodesk Inventor with the configuration shown in Table 7.1. The semi-empirical Deutsch-Anderson equation was used to evaluate the predicted performance of the PESP, and the computer code in MATLAB is attached in Appendix V. The predicted particle collection efficiency when the flow rate is 15 SLPM is showed in Table 7.2.

Table 7.1 Summary of specification of the PESP.

Parameters	Value
Body material	ASME/ANSI B36.10/19 Pipe Size 3 inch SS304/L Schedule 160
Height	24 inch
Outer diameter	3.5 inch
Wall	0.438 inch
Inner diameter	2.624 inch
Wire diameter	0.007 inch

Table 7.2 Particle collection efficiency predicted by the semi-empirical Deutsch-Anderson equation when the flow rate is 15 SLPM.

Diameter	5 nm	10 nm	100 nm	300 nm	1 μm	10 μm	20 μm
Collection efficiency (10 bar, 54 kV)	98%	95%	81%	80%	80%	83%	84%
Collection efficiency (15 bar, 59 kV)	63%	53%	38%	38%	38%	40%	40%

7.2.2 Hazard and operability study (HAZOP)

To ensure safe operation during P-ESP experiments with SPOC facility, a thorough HAZOP review was conducted under the guidance of professional electrical engineers and laboratory safety manager. Risk scenarios related to high pressure, high voltage and mechanical failure are listed in the following Table 7.3. Certain consequences corresponding risk scenarios are summarized, and

mitigation strategies are created based on electrical and high-pressure safety principles and operating manuals. Recommended actions have been performed for risk prevention.

Table 7.3 HAZOP summary.

Risk scenarios	Consequences	Mitigation	Recommended actions
CeramTec high-voltage high-pressure electrical flange feedthrough breaks.	Large volume of combustion exhaust gas will be released into room.	Information from vendor confirms that the part cannot break under 750 psi (51 bar), and it can only have small leakage.	Leakage checking will be done every time before starting experiment.
Pressure inside the P-ESP cannot reach 15 bar due to leakage somewhere in the setup.	A small volume of combustion exhaust gas will be released into the room.	Close the valve at the inlet of the P-ESP; open slowly the regulator to release the high-pressure gas inside the P-ESP.	
Ionized gas is generated over the top of the electrical feedthrough.	It is dangerous for the operator to touch the power supply and metal frame.		Install an electrical insulation layer between the top of the feedthrough and the bottom of the power supply.
Arc occurs frequently under high voltage and high pressure.	Current jumps up and down unstably, and sharp sound occurs.	Information from vendor confirms that it is perfectly safe to turn down the voltage or current dial on the front panel of the power supply. Arc Trip option can be configured as if one arc occurs the unit will shut down with an ARC fault.	Enhance grounding safety: (1) scratch paint off the metal frame so that metal frame is electrically connected with the power supply and thus is grounded perfectly. (2) green wire for earth grounding needs to be extended from the receptacle and
Central discharge wire fails.	Wire touches inner wall of P-ESP, and short circuit occurs.	The power supply unit can automatically detect short	

Too much water is condensed inside the P-ESP.	Short circuit occurs and the current is off the limit of the power supply.	circuit and shut down according to its manual.	connected with the grounding wire of the power supply. (3) receptacle needs to be moved to a dedicated 208V circuit. (4) stand on an insulation mat or put on electrical protection shoes while operating.
Sonic nozzle is clogged.	The pressure inside ESP ramps up.	Close the valve at the inlet of the P-ESP; open slowly the regulator to release the high-pressure gas inside the P-ESP.	(1) Replace the existing inlet and outlet valves with high temperature plug valves;
Valve fails or malfunctions	The gas flow from SPOC cannot be stopped.	Multiple shut-off valves connected to ESP	(2) increase the drip leg capacity.
SPOC pressure suddenly ramps up.	The P-ESP current will suddenly drop, and pressure will ramp up.	Safety relief valve on ESP will open at 300 psi (20 bar) to reduce the pressure. Or close the valve at the inlet of the P-ESP; open slowly the regulator to release the high-pressure gas inside the P-ESP.	
Water in the drip leg overflows into the gas tube.	The water blocks sonic nozzle, and tube downstream of the nozzle will have water droplet; Or the water flows into the P-ESP leading to short circuit.	Close the valve-2 and then the valve-1; slowly open the valve-3 to release some water and close it; open regulator to release gas; open the valve-3 to release all water in the drip leg.	

7.2.3 Particle and flue gas sampling setup

The particle sampling setup was designed and completely assembled as shown in Figure 7.2. Heating tape wrapped around the inflow tube was used to maintain the inflow gas temperature greater than 100 °C to prevent water condensation. The temperature at the bottom of the ESP was also monitored. A drip leg was installed at the outlet of the ESP to collect condensed water. A sonic nozzle with diameter of 0.78 mm and upstream pressure of 15 bar allows flow rate of 72 SLPM downstream.
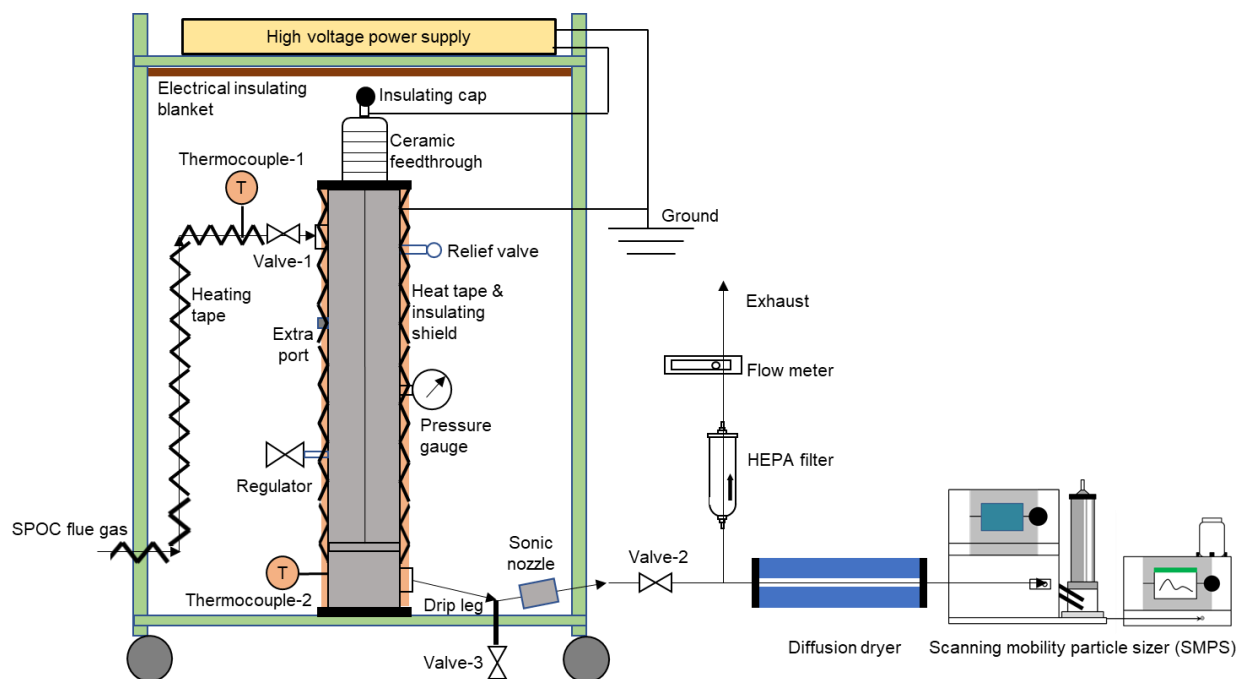
Figure 7.2 Schematic diagram of PESP sampling setup.

7.3 Results and discussion

7.3.1 Current-voltage characteristics

Current-voltage (I-V) characteristics of the P-ESP using positive voltage was measured under 3, 5, 7, 11 and 15 bar. A 0.78 mm nozzle was installed at the gas outlet of the P-ESP for maintaining high pressure inside the vessel. Flow rate of air varied under different pressure conditions. As shown in Figure 7.3, the corona onset voltages under 3, 5, 7, 11 and 15 bar are 13.0, 19.9, 23.3,

29.7 and 32.0 kV, respectively. The onset voltage increased as the pressure increased. It is interesting to observe that spark breakdown (sparkover) occurred under all pressure conditions as long as the voltage was high enough. The breakdown voltages under 3, 5, 7, 11 and 15 bar are 36.8, 42.3, 46.9, 49.2 and 50.2 kV, respectively. When spark started, current suddenly increased and decreased to zero due to arc protection mode of the power supply was activated. The sparkover phenomenon can limit the maximum obtainable current of the P-ESP and thus the removal efficiency. The highest current achievable under 15 bar is 30 µA with 50.2 kV. The current increasing gradient is extremely low when the pressure is 15 bar.
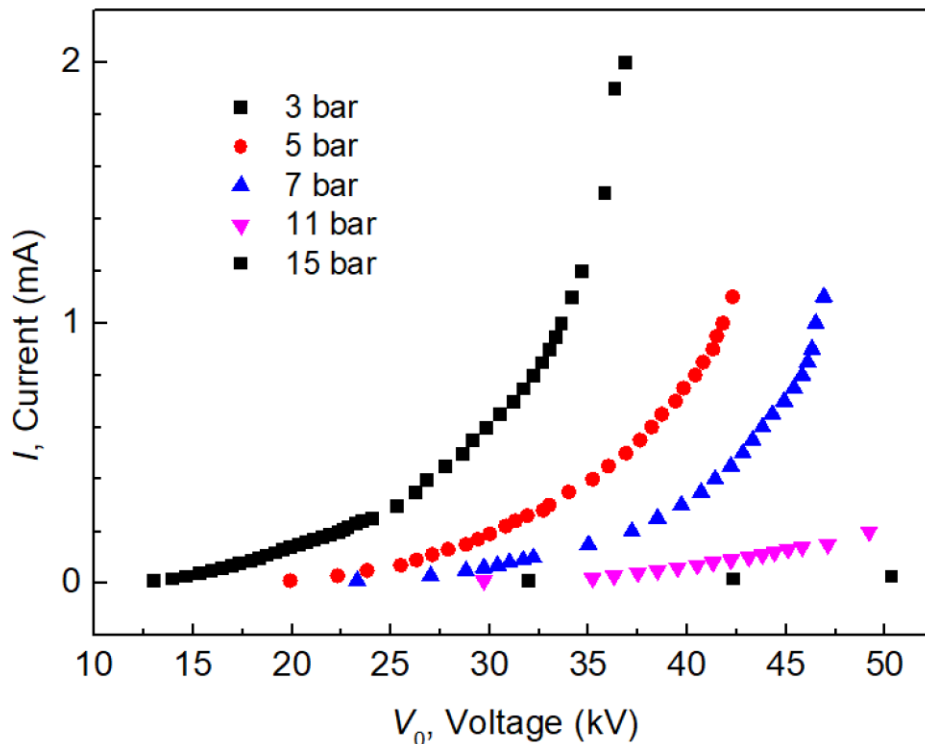
Figure 7.3 Current-voltage (I-V) characteristics of the P-ESP under 3, 5, 7, 11 and 15 bar.

7.3.2 Computer fluid dynamics (CFD) simulation

The flow field and electric field are simulated with COMSOL CFD software as shown in Figure 7.4. The simulated pressure and temperature are 15 bar and 300 °C, which are the practical conditions of SPOC combustion exhaust gas. The inlet flow rate is 62 SLPM, while the applied

171

voltage is 30 kV. These two simulated results can be used in particle tracing study, which helps understand particle removal efficiency of PESP under different conditions. Although the flow velocity is high at the inlet and outlet, the flow is slow inside the PESP body, which provides enough residence time for particles to be collected. It is observed that swirl flow exists close to the inlet of the PESP. That flow turns turbulent and small particles are thus transported by turbulent and Brownian diffusion to the collecting electrode. In a highly turbulent region, molecular diffusion is negligible compared with transport by the turbulent eddies. The general expression for the diffusion flux in a turbulent flow is $\bar{J} = -(D + \epsilon)\frac{\partial \bar{n}}{\partial y}$, where D is diffusion coefficient, ϵ is eddy diffusion coefficient that increases with kinematic viscosity ν. For particle diffusion, $\nu \gg D$. Hence, particle can penetrate closer to the collecting electrode by turbulent diffusion before Brownian diffusion can take significant effect. Therefore, particle collection can be enhanced by the swirl flow at the entrance (Friedlander, 1977). On the other hand, the swirl flow could result in severe nonuniformity, which can cause erosion and excessive re-entrainment of the collected particles from the collecting electrode as well as lead to variable gas treatment times in the ESP. These multiple effects can reduce the collection efficiency (Oglesby et al., 1978). Simulation of gas flow and electrical field inside the P-ESP is crucial to following particle tracing study and performance modeling.
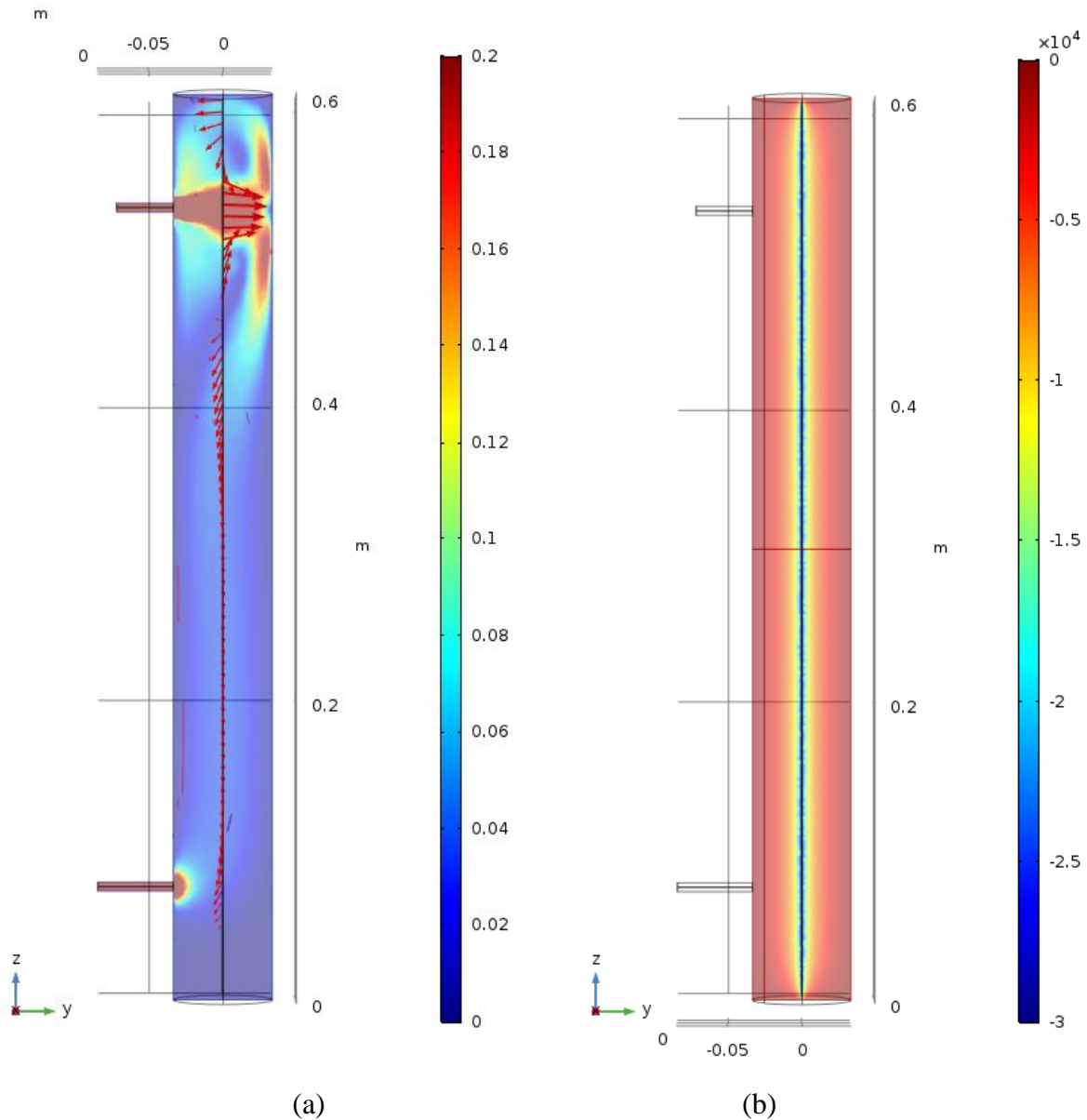
Figure 7.4 (a) Flow field and (b) electrical field simulated results using COMSOL.

7.4 Conclusion

A pressurized ESP (PESP) was designed and constructed for particle removal in pressurized oxy-combustion system. The collection efficiencies for particles in different sizes were predicted by the previously developed semi-empirical ESP performance model. Hazard and operability study (HAZOP) was conducted to ensure safety of mechanical and electrical operation. Current-voltage characteristics showed that onset voltage for 15 bar was 32 kV and the highest current achievable

173

under 15 bar was 30 μA with 50.2 kV. Sparkover voltage differed under various pressures and it could limit the maximum obtainable current of the P-ESP. 2D axis-symmetrical simulation of gas flow field and electrical field inside the P-ESP was performed using COMSOL, which can provide crucial information for particle tracing study and performance modeling in the future. Experiments on particle size distributions in exhaust gas from pressurized oxy-combustor and particle capture performance of PESP under different flow conditions need to be performed in next steps.

7.5 References

Friedlander, S. K. (1977). Smoke, dust and haze: Fundamentals of aerosol behavior. *New York, Wiley-Interscience, 1977. 333 p.*

Gopan, A., Kumfer, B. M., & Axelbaum, R. L. (2015). Effect of operating pressure and fuel moisture on net plant efficiency of a staged, pressurized oxy-combustion power plant. *International Journal of Greenhouse Gas Control, 39*, 390-396. doi:https://doi.org/10.1016/j.ijggc.2015.05.014

Gopan, A., Kumfer, B. M., Phillips, J., Thimsen, D., Smith, R., & Axelbaum, R. L. (2014). Process design and performance analysis of a Staged, Pressurized Oxy-Combustion (SPOC) power plant for carbon capture. *Applied Energy, 125*, 179-188.

Li, Z., Jing, H., & Biswas, P. (2016). Capture of submicrometer particles in a pressurized electrostatic precipitator. *Aerosol Science and Technology, 50*(10), 1115-1129.

Oglesby, S., & Nichols, G. B. (1978). *Electrostatic precipitation* (Vol. 21): Marcel Dekker Incorporated.

Xia, F., Yang, Z., Adeosun, A., Gopan, A., Kumfer, B. M., & Axelbaum, R. L. (2016). Pressurized oxy-combustion with low flue gas recycle: Computational fluid dynamic simulations of radiant boilers. *Fuel, 181*, 1170-1178.

Zheng, L., Pomalis, R., Clements, B., & Herage, T. (2010). *Optimization of a high pressure oxy-fuel combustion process for power generation and CO2 capture.* Paper presented at the The 35th international technical conference on clean coal & fuel systems. Clearwater, FL.

Chapter 8: Summary and recommendations for future work

8.1 Summary

Pressurized oxy-combustion and amine-based CO_2 scrubbers are two types of advanced technologies in the context of carbon capture and storage. Meanwhile, submicrometer particles are a remarkable contributor to air pollution. Because it is imperative to create innovative approach to address the nexus of climate change and air pollution, this dissertation explored the critical role and control strategies of submicrometer particles in the path of addressing the challenges against those two promising technologies.

To develop a robust solution for particle removal in pressurized combustion system, the effects of high pressure on the submicrometer particle capture performance of ESPs in lab-scale combustion systems were investigated. Current-voltage characteristics and particle capture performance of the ESP were studied in air and in simulated flue gas (SFG) under various pressure conditions. Using negative corona and air as the feed gas, the penetration of most particles of 40–400 nm in diameter decreased from 8×10^{-4}–2×10^{-2} to 2×10^{-4}–1×10^{-2} as pressure increased from 1 atm to 3 atm at constant current; and increased from 3×10^{-5}–1×10^{-3} to 2×10^{-4}–1×10^{-2} as pressure was elevated when the voltage was held roughly constant. Particle capture experiments showed that with constant current, higher pressure resulted in a higher initial charge fraction of the particles from the furnace, which could facilitate the penetration of fly ash particles. A semi-empirical model was developed based on the Deutsch-Anderson (D-A) equation and experimental data under 1, 2 and 3 atm to calculate the particle penetrations under high pressure. The model has been used to design and construct a pilot-scale pressurized ESP for particle removal in staged pressurized oxy-combustion (SPOC) system.

To better understand the particle charging status in flue gas and its potential effect on electrostatic precipitation, a study on particle charged fraction, ash resistivity and ESP capture performance was performed using different coal seams from India, US and China. The fly ashes of low-rank US and India coals had higher concentration and geometric mean size than the China coal fly ash. The US coal shows the highest number and mass concentration fine/coarse ratios, which are $1.34{\times}10^4$ and 1.08, respectively. Charged particle fraction was examined by using a charged particle remover (CPR). The results showed that charged particle fraction increased with growing particle size for submicrometer fly ashes produced by combustion of India and US coals, which was probably governed by thermo-ionization charging. Smaller China coal fly ash had higher charged particle fraction possibly due to diffusion charging. Besides, the ash resistivity tests showed that India and China coal fly ashes had higher ash resistivity than the US coal fly ash. The electrostatic precipitation tests evidenced that smaller particles for high resistivity coal fly ashes might suffer more significantly from back corona. Notably, back corona effect was reduced by increasing the applied voltage of the ESP. These findings are crucial to tailoring electrostatic precipitation technology for controlling coal fly ashes commonly discharged by coal-fired power plants from India, US and China.

Mineralogy, morphology and chemical compositions of particles in pressurized coal combustion exhaust were also characterized because pressurized ESP capture performance is also dependent on particle compositions. As pressure was elevated, the total number concentration of submicrometer particles decreased and the peak size increased for all three coals. Furthermore, chemical composition analysis showed that coal fly ashes of US PRB, India Chandrapur and China S02 were mainly enriched in Ca, Si and Al, respectively. For all three coals, more volatile species (Na, Mg, Fe, and Ca) were accumulated in the submicrometer particles when pressure was higher.

To investigate the flue gas properties upstream amine-based CO_2 scrubbers, the concentrations of fine particles and selected gas pollutants in the flue gas entering the stack were measured under several common operation modes in an operating coal power plant producing electricity. For wet and dry aerosols, the measured mode sizes were both around 40 nm, but remarkable differences were observed in the number concentrations (#/cm^3, count per square centimeter). A prototype photo-ionizer enhanced electrostatic precipitator (ESP) showed improved removal efficiency of wet particles at voltages above +11.0 kV. Soot blowing and FGD bypass both increased the total particle number concentration in the flue gas. The temperature was slightly increased by the FGD bypass mode and varied significantly as the rating of reheat burner changed. The variations of CO_2 and SO_2 emissions showed correlations with the trend of total particle number concentration possibly due to the transitions between gas and particle phases. The results are useful in developing coal-fired power plant operation strategies to control fine particle emissions and developing amine-based CO_2 capture technologies without operating and environmental concerns associated with volatile amine emissions.

To ensure cost-effective operation of amine scrubbers, several particle pretreatment measures were explored in this dissertation. The particles were sampled from the flue gas upstream a pilot-scale amine scrubber in a utility-scale coal-fired power plant. The effects of steam injection, water desiccation and electrostatic precipitation were investigated. Steam injection caused a decrease of particle concentration in the range of 20 nm to 40 nm, and an increase of particle concentration in the range of 40 nm to 60 nm. Higher steam flow rate could increase the peak size of the particle size distribution. Whether the diffusion dryer was installed before the particle instruments showed on significant effect on particle size distributions. Electrostatic precipitator (ESP) could reduce the number concentrations of particles in most sizes by >2 orders of magnitude. Almost 99.9% of the

particles ranging from 25 nm to 80 nm in diameter were removed by the ESP with a voltage of 18.1 kV. Evidence showed that secondary aerosol like H_2O-H_2SO_4 could be generated from SO_2 in flue gas inside the ESP. Nonetheless, a light-weight ESP can be still considered to be installed upstream the scrubber and operated under appropriate voltages to reduce the number concentration of ultrafine particles flowing into the scrubber to ultimately avoid amine loss issues.

8.2   Recommendations for future work

For modelling ESP particle capture performance under high pressure, there are two promising directions to be explored. One direction is to address the multiple assumptions of the original Deutsch-Anderson equation by using more sophisticated physical and transport principles. A robust model needs to be suitable for different configurations of ESP with fewer constraints of physical conditions like high pressure, high temperature or high turbulence. A computational fluid dynamics approach might require more attention because it can effectively couple multiple physics together to simulate real particles interacting with flow and electric field. The other direction is to leverage more power of data-driven approach such as machine learning to generate accurate statistical model based on experimental data, whose amount needs to be large enough though. The collection efficiency data collection needs to be fast enough to satisfy the need of a machine learning algorithm, which requires advancements in instrumentation and experimental design.

Detailed characterization of charge fractions of submicrometer particles from pressurized drop-tube combustor and its impacts on particle charging in pressurized ESP can be further examined using tandem differential mobility analyzer (TDMA) and condensation particle counter (CPC). Initial particles charging status is critical to charging and particle migration processes inside ESPs. It would be valuable to understand how many charges each particle carries and the interactions between charged particles and free ions or electron.

To better control amine loss, particles need to be effectively removed upstream amine scrubbers. Different variants of ESP technologies such as wet ESPs can be explored due to their high removal efficiency. Besides, development of aerosol dynamics models can help understand how the aerosols in the scrubbers absorb amine and what the fates of aerosols and amine vapor and droplets are. Chemical reactions need to be incorporated in the aerosol model to take into account amine degradation.

Appendix I: Supplemental information for Chapter 2
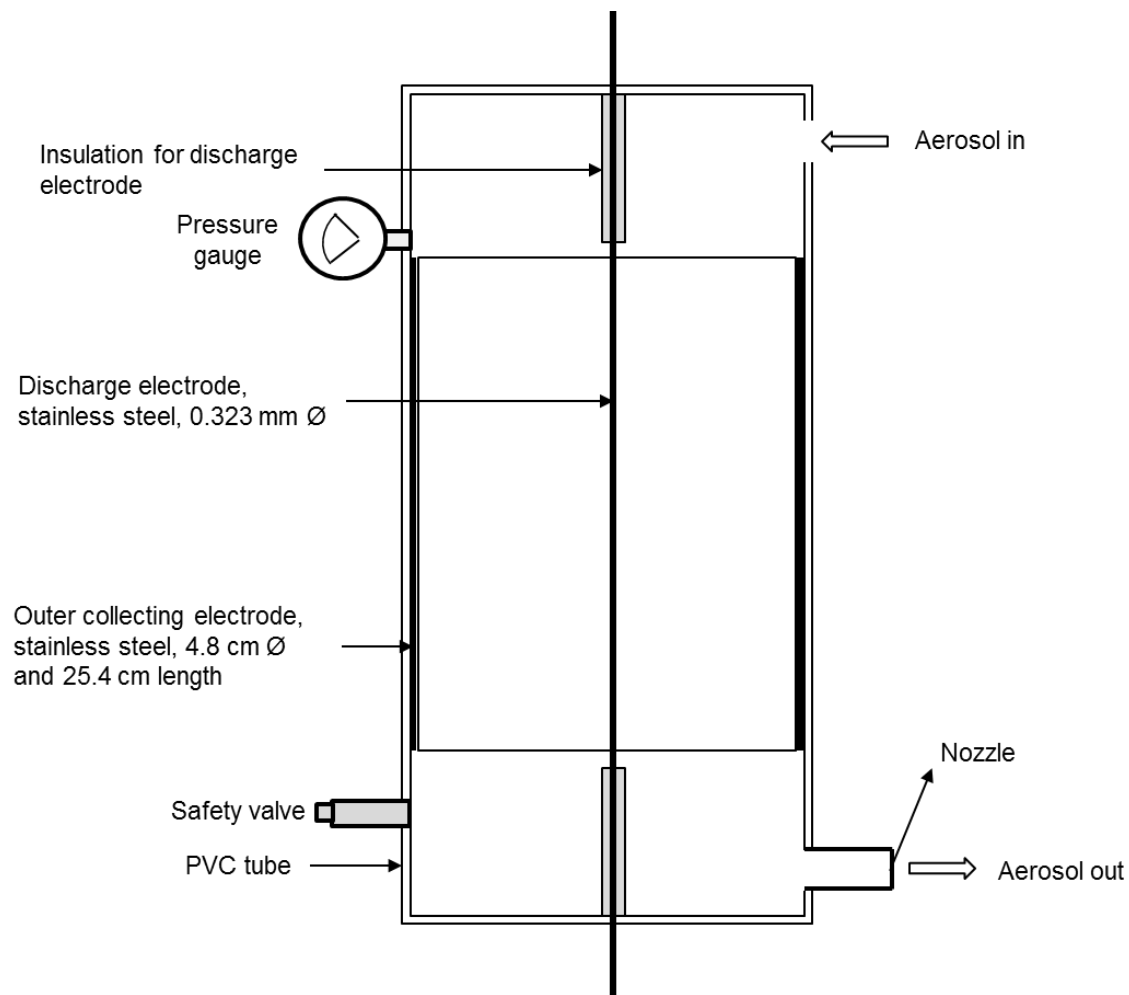
Figure A1.1 Configuration of the studied ESP.

2.2 Experimental Section

2.2.1 Experimental System

It should be noted that according to the calculated fractions of particles carrying different number of charges after passing the neutralizer (TSI, 2009), for particles in diameter of 39 nm, the particles carrying −1, 0 or +1 charge account for 99%, and for particles in diameter of 392 nm, the particles carrying −3, −2, −1, 0, +1, +2 or +3 account for 94%. These facts indicate that the particles upstream the ESP consist primarily of particles carrying very low charge number, which is about to be proved negligible compared with charge number appeared in this study.
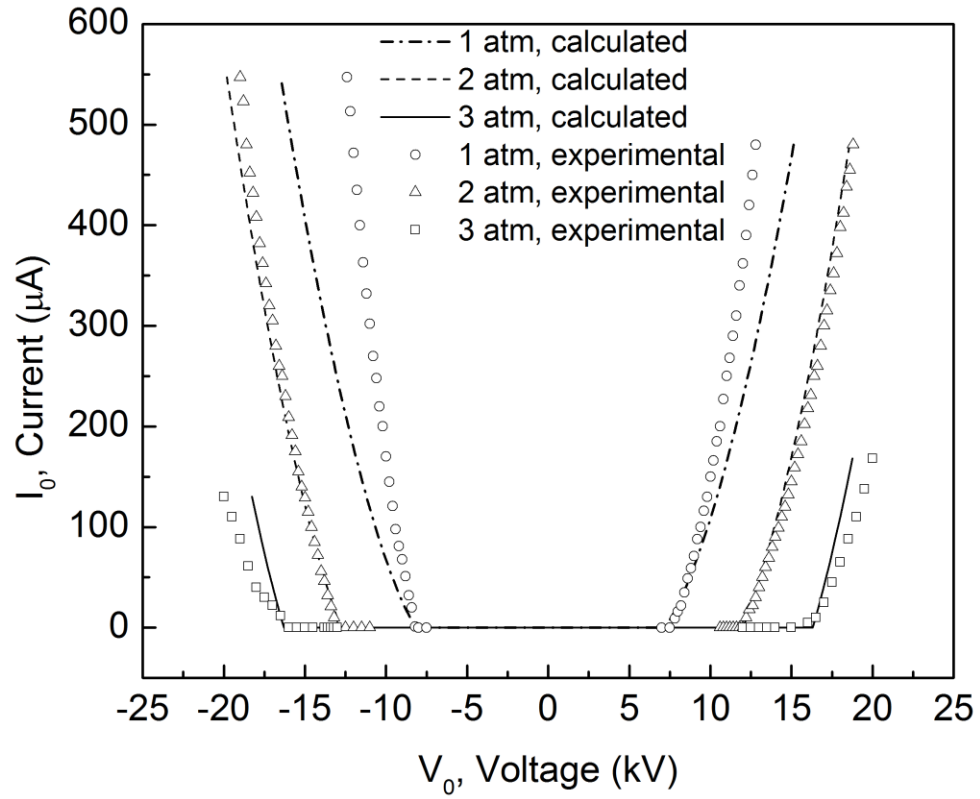
Figure A1.2 Experimental and calculated I-V curves by Eq. (2.3) under different pressures.
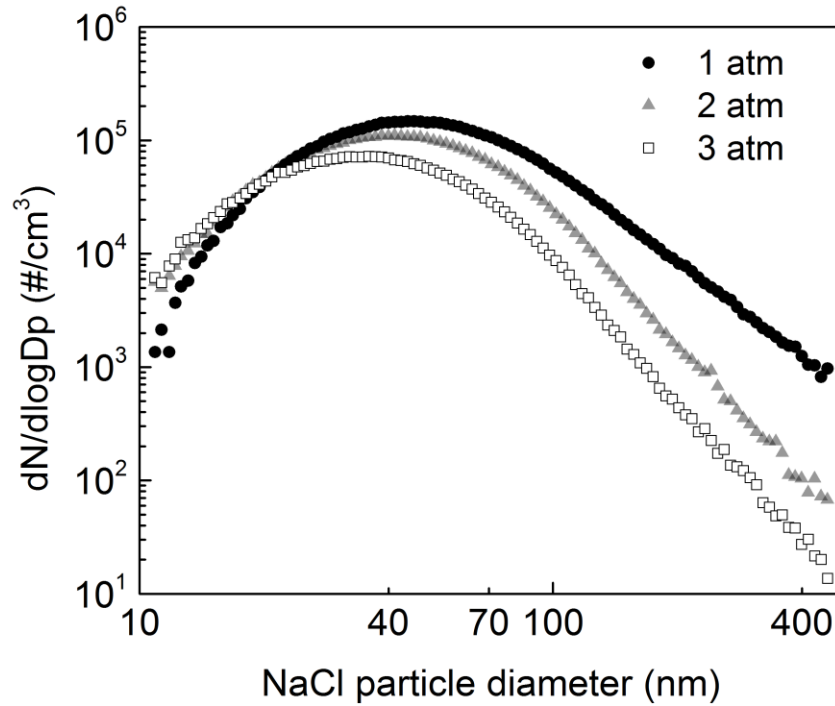
Figure A1.3 Size distributions of the NaCl particles atomized under various pressures.

Although the size distributions with different pressures were different, it should be noted that this studied aerosol system was so dilute in particle concentration that the difference in size distribution would have negligible impact on ESP performance in terms of electric field, ion concentration and particle-particle interactions.

2.3 Results and discussion

2.3.2 Capture of NaCl particles using air as the feed gas

High collection efficiencies over 99% for most of the particles ranging 40 nm to 400 nm in diameter was observed under all the conditions. First, this outcome can be attributed to the flow velocity (0.1m/s) lower than the mean gas velocity in ESPs (0.2–2.0 m/s) usually reported in literature. Some researchers found that the minimum collection efficiency for particles from 16.8 to 615 nm in electrical mobility diameter could be increased from 84.1% to 96.9% when the flow velocity was reduced by half (Lin et al., 2010). It has been reported that when the flow velocity is below 0.6 m/s, the ionic wind may have a significant influence on the flow field (Liang et al., 1994). Ionic wind is known as a secondary ion flow induced by the ions flowing from the discharge electrode to the collecting electrode. On the one hand, a strong ionic flow may force ultrafine particles to move towards the collecting surface and be ultimately collected (Huang et al., 2002). Besides, although some circulation cells generated in the ionic wind may reduce the collection efficiency, the charging time and the charge number increase, and thus compensate the collection efficiency loss due to the circulation cells (Liang et al., 1994). As a result, the collecting efficiency grows high when the flow velocity is low. Second, it should be noted that high onset voltage was required for inception of corona discharge under 3 atm, and in order to investigate the effect of current on the ESP collection efficiency, the voltage under lower pressure (1 and 2 atm) need to be set approximately at the same level as the 3 atm case. Therefore, for many experimental sets in this study, high voltage was applied, which tended to increase the electrical mobility of the particles and resulted in high collection efficiency, especially as the current was high at the same time for 1 and 2 atm cases.
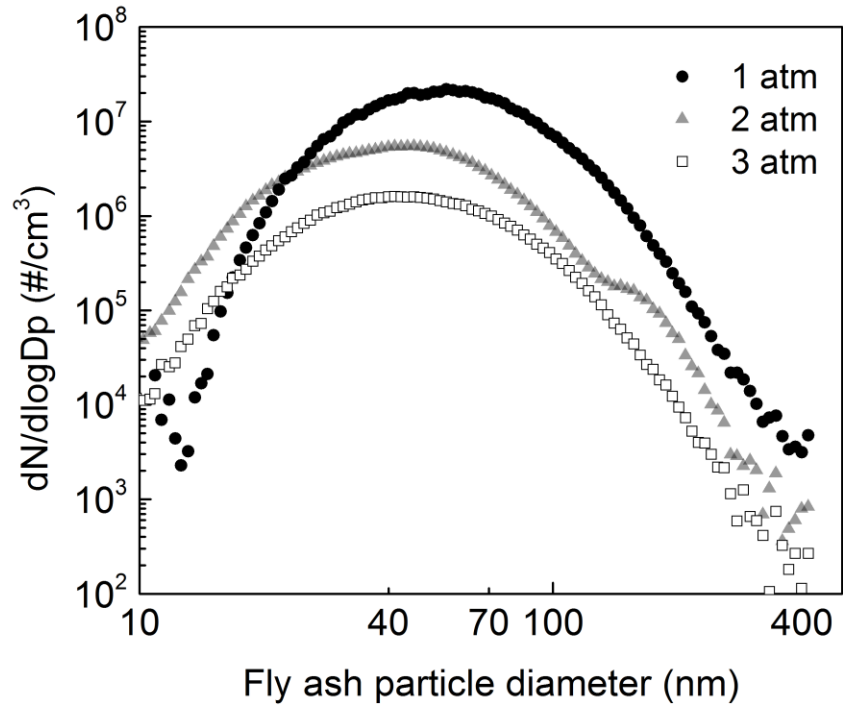
Figure A1.4 Size distributions of the fly ash particles at the outlet of the drop-tube furnace under various pressures.
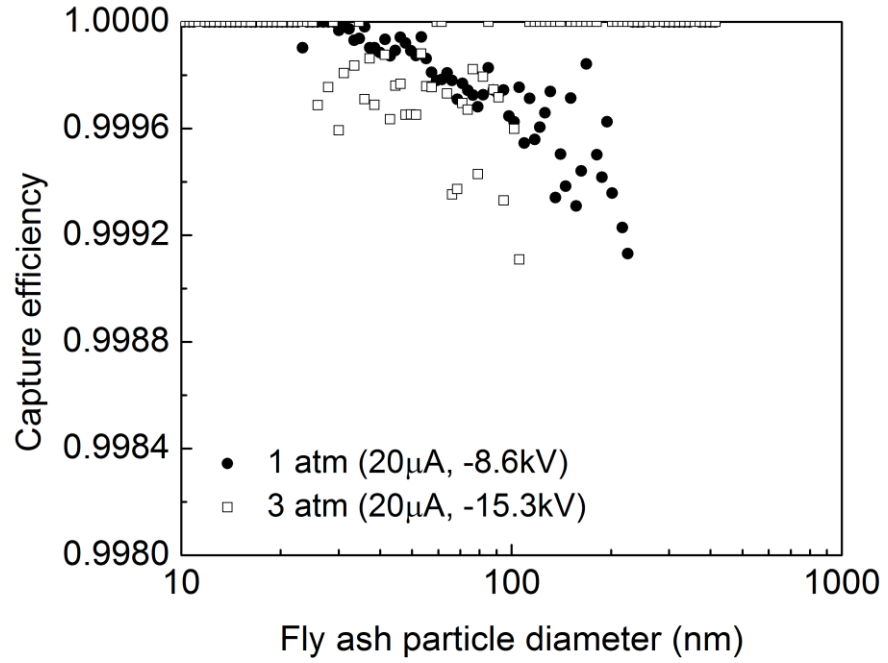
Figure A1.5 ESP capture efficiencies for fly ash particles of various sizes under different gas pressures.

To explain the behavior of fly ash particles in the ESP, we studied the charge status of fly ash particles before they entered the ESP. A method adapted from Suriyawong et al. (Suriyawong et al., 2008) was applied. The particles were either directly introduced into the DMA (differential mobility analyser) of the SMPS or first passed through a Po-210 radioactive source to give the particles a known charge distribution and then introduced into the DMA. The concentrations of particles penetrating through the DMA were measured with the CPC (condensation particle counter) of the SMPS. The DMA was operated under both negative and positive applied voltages to determine the charges of particles with positive and negative charges, respectively. From the concentration measurements, we calculated the charge index, using the following equation to indicate the charge status of the particles:

$$I_C = \frac{N_C}{N_{Ceq}} Cf_{eq1},$$

where I_C is the charge index, N_C is the number concentration of charged particles of diameter d_p, N_{Ceq} is the number concentration of charged particles of diameter d_p measured after charge neutralization, and Cf_{eq1} is the equilibrium charge fraction for particles of diameter d_p with one unit charge, calculated as described by Wiedensohler (Wiedensohler, 1988). The physical meaning of the charge index is the charged fraction of particles, with the assumption that all the particles are singly charged (with +1 or −1 unit charge). However, it should be noted that multiple charged particles with the same electrical mobility as the singly charged particles of the concerned size also contribute to this index.

The charge indices of the particles with diameters of 20 nm, 30 nm, 40 nm, 60 nm, 100 nm, 200 nm for the 1, 2 and 3 atm conditions are shown in Figure A1.6. The indices of the smaller particle

diameters (20 nm, 30 nm) under 3 atm (positive) are higher than 1, which is a strong evidence that some of the fly ash particles were multiple positively charged in the 3 atm combustion. The main charging mechanisms of the particles inside the drop-tube furnace is diffusion charging (Burtscher, 1992; Burtscher et al., 1986), which increases the probability of multiple charging at 3 atm.

Based on the above discussion, it is hypothesized that with a higher gas pressure in the coal combustor, the charge fraction and number of average charges on the particles are both larger for the particles of each size exiting the combustor. This hypothesis is correct theoretically. With a higher gas pressure, the residence time of the submicrometer particles in the drop-tube furnace is higher, which results in both a larger charge fraction and a larger number of the average charges based on the theory of diffusion charging (Hinds, 1999). A longer residence time also enhances the direct thermionization and photo-ionization of particles, which contributes to increasing the charge fraction and number of charges as well, although their effects are secondary to diffusion charging (Burtscher, 1992). At the same time, with a higher gas pressure, the charge indices for smaller particles (20 nm, 30 nm, and 40 nm) are larger, and those for larger particles (60 nm, 100 nm, 200 nm) are smaller (Figure A1.6). These findings also support the hypothesis that with higher gas pressure in the combustor, the particles exiting the combustor have a larger chance to be multiple charged.
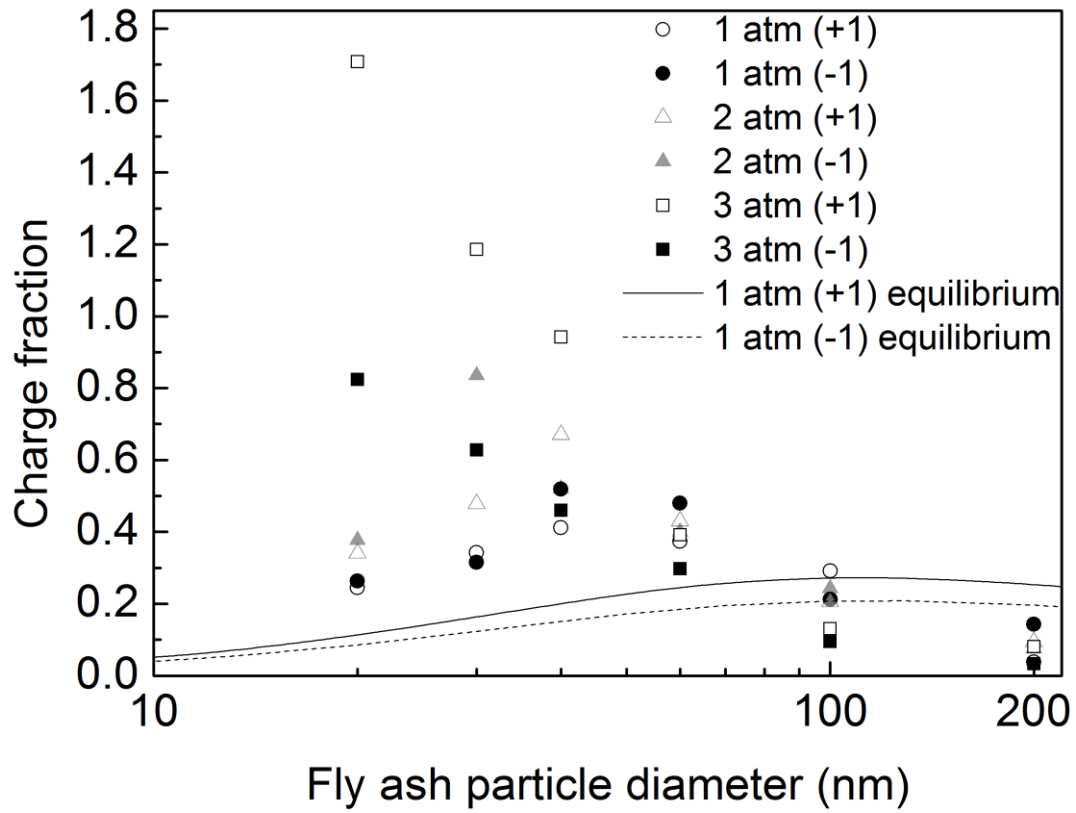
Figure A1.6 Charge indices of particles of various sizes under 1, 2 and 3 atm.

Table A1.1 Relative permittivity of several types of substances in the particles.

Compound	Relative Permittivity
Sodium Chloride (NaCl)	5.9
Silicon Dioxide (SiO$_2$)	4.5
Iron Oxide (Fe$_2$O$_3$)	14.2
Aluminum Oxide (Al$_2$O$_3$)	4.5
Calcium Oxide (CaO)	11.8

Source: http://www.clippercontrols.com/pages/Dielectric-Constant-Values.html

$$Q = \frac{Q_0 P_0 T}{P T_0}$$

$$t = \frac{V}{Q}$$

$$n_{diff} = \frac{d_p kT}{2K_E e^2} \ln\left(1 + \frac{\pi K_E d_p \bar{c}_i e^2 N_i t}{2kT}\right)$$

$$N_i = \frac{I}{A_c e Z_i E}$$

$$n_{field} = \left(\frac{3\varepsilon}{\varepsilon+2}\right)\left(\frac{Ed_p^2}{4K_E e}\right)\left(\frac{\pi K_E e Z_i N_i t}{1+\pi K_E e Z_i N_i t}\right)$$

$$n = n_{diff} + n_{field}$$

I (Input)

$$E_C = \frac{V_C}{r_0 \ln(r_1/r_0)}$$

P (Input)

$$V_c = r_0 \ln\left(\frac{r_1}{r_0}\right)\left[A_g + \frac{B_g}{(r_0 \delta')^{\frac{1}{2}}}\right]\frac{P}{P_0}$$

$$V_0 = \left\{V_C + E_C r_0\left[(1+\phi)^{\frac{1}{2}} - 1 - \ln\left(\frac{1+(1+\phi)^{\frac{1}{2}}}{2}\right)\right]\right\} \cdot 1.135^{P/P_0 - 2.312}$$

$$E_0 = \frac{V_0}{r_0 \ln(r_1/r_0)}$$

$$E = \frac{2r_0}{r_0 + r_1} E_0$$

$$v_{TE} = \frac{neEC_C}{3\pi\mu d_p}$$

$$\eta = 1 - \exp\left(-\frac{A_C v_{TE}}{Q}\right)$$

η (Output)

$$\lambda = \frac{RT}{\sqrt{2}\pi d_m^2 PN_A}$$

$$C_C = 1 + \frac{\lambda}{d_p}\left(2.34 + 1.05\exp\left(-0.39\frac{d_p}{\lambda}\right)\right)$$
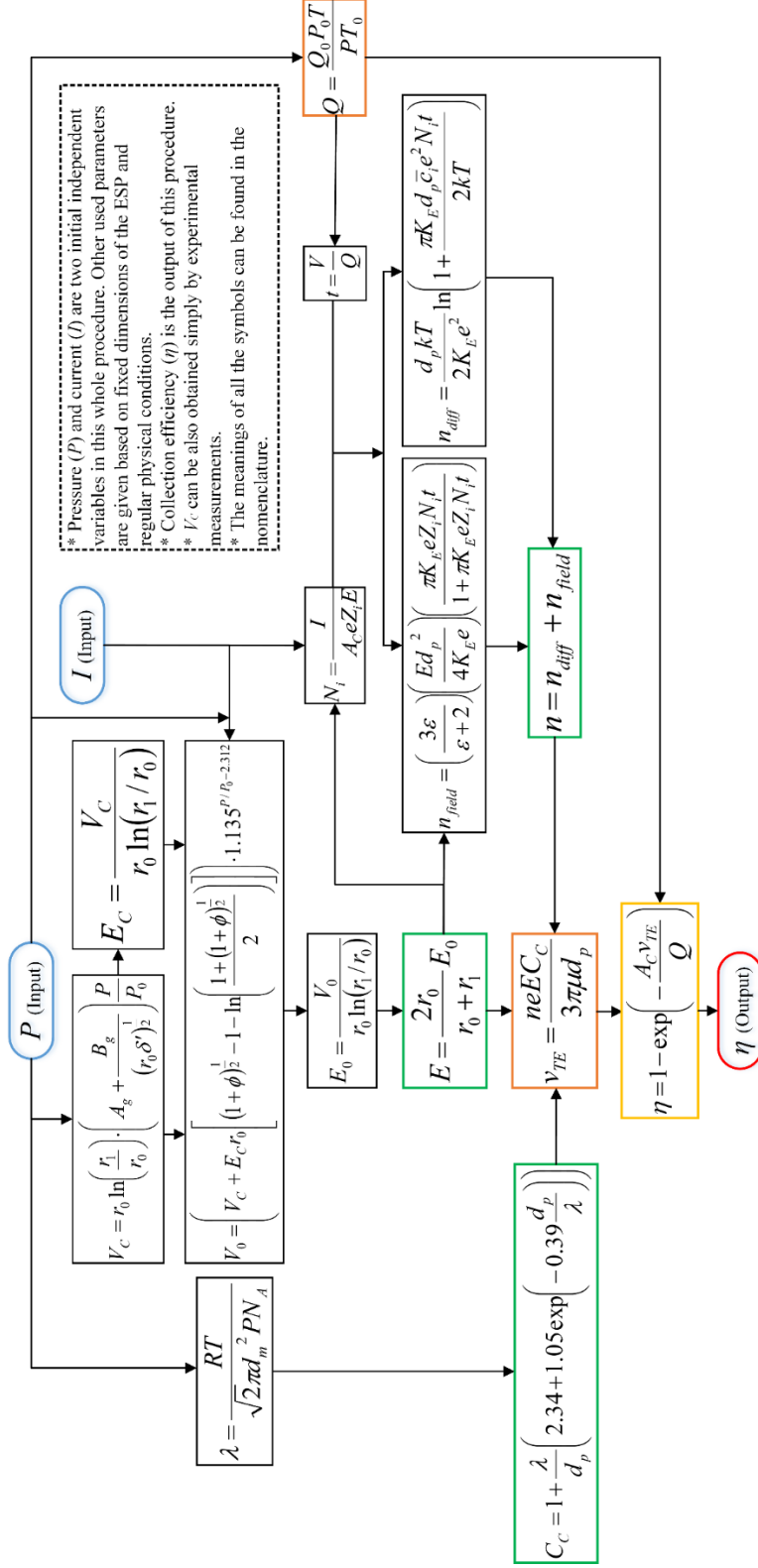
Figure A1.7 Calculating procedure of capture efficiency in pressurized ESPs using Eq. (2.15) as the expression for the number of elementary charges of the particles.
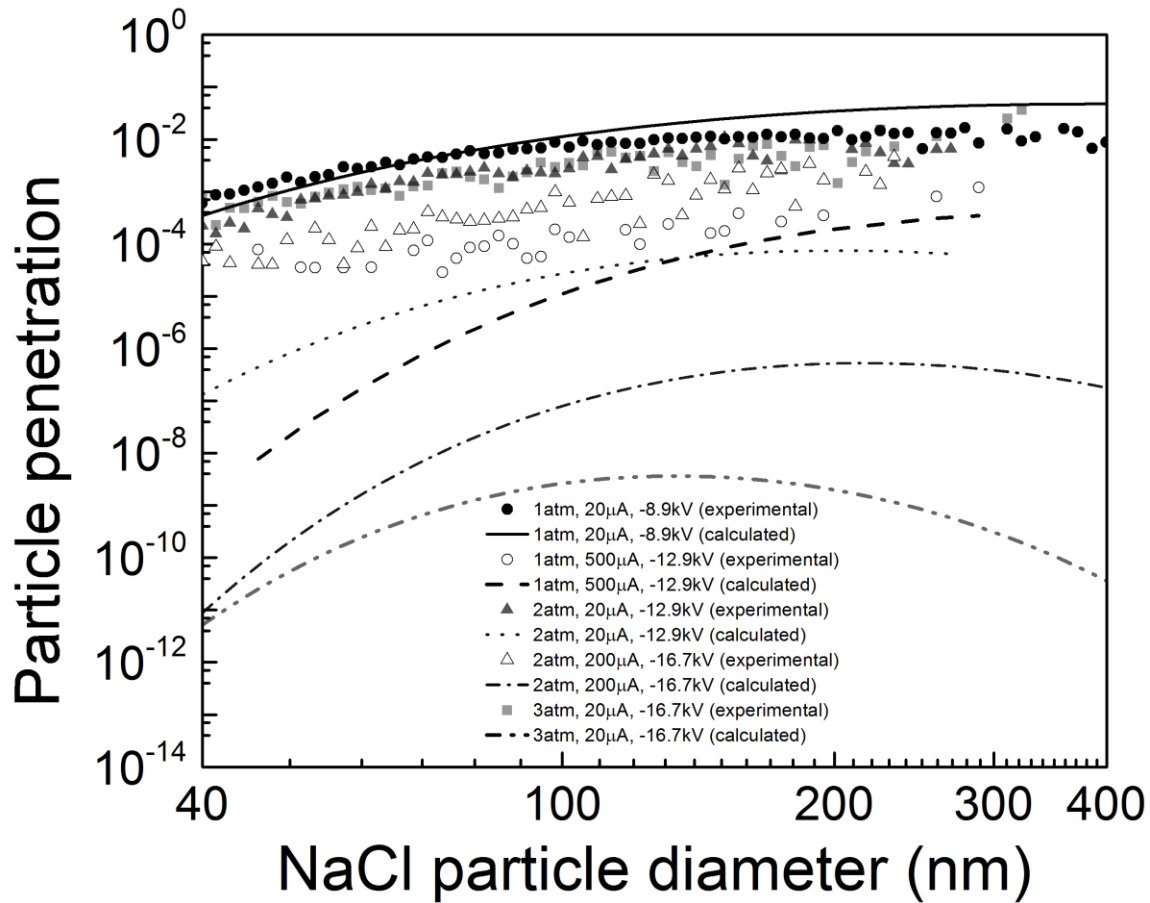
Figure A1.8 Particle penetrations for various particle sizes measured under 1, 2 and 3 atm and the corresponding calculated values using Eq. (2.15). (summation of squared deviations (σ') is 0.0041, which excludes the case of "1 atm and 20 µA").
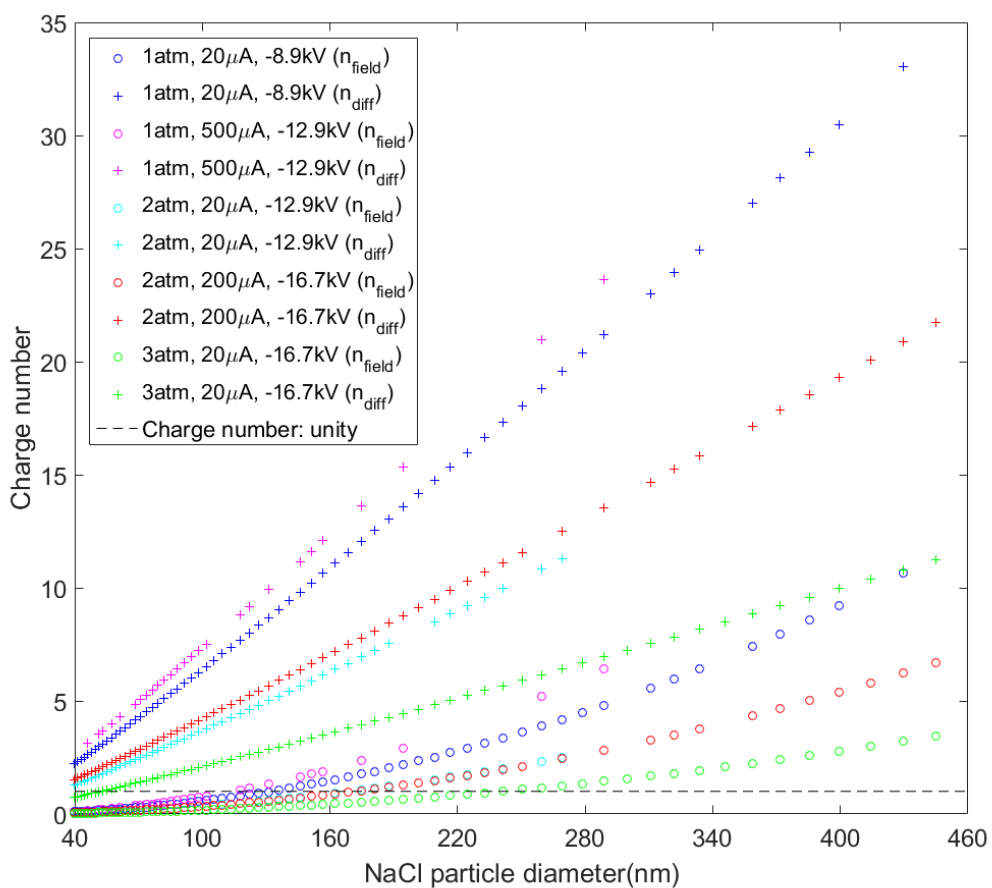
Figure A1.9 Calculated charge numbers induced by diffusion charging and field charging as functions of particle diameter based on the modified D-A equation.
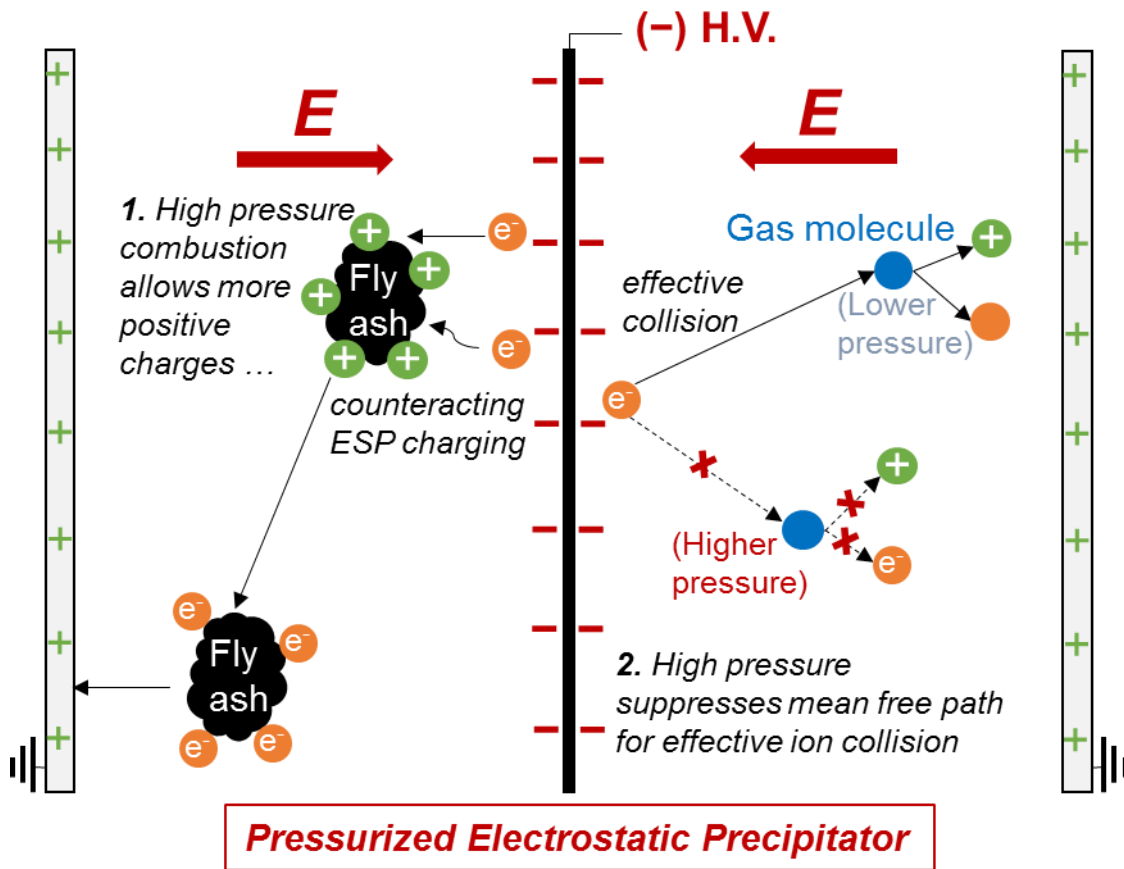
Figure A1.10 Two primary mechanisms of high pressure affecting ESP capture performance.

References

Burtscher, H. (1992). MEASUREMENT AND CHARACTERISTICS OF COMBUSTION AEROSOLS WITH SPECIAL CONSIDERATION OF PHOTOELECTRIC CHARGING AND CHARGING BY FLAME IONS. *Journal of aerosol science, 23*(6), 549-&. doi:10.1016/0021-8502(92)90026-r

Burtscher, H., Reis, A., & Schmidtott, A. (1986). PARTICLE CHARGE IN COMBUSTION AEROSOLS. *Journal of aerosol science, 17*(1), 47-51. doi:10.1016/0021-8502(86)90005-4

Hinds, W. C. (1999). *Aerosol technology: properties, behavior, and measurement of airborne particles*: John Wiley & Sons.

Huang, S.-H., & Chen, C.-C. (2002). Ultrafine aerosol penetration through electrostatic precipitators. *Environmental Science & Technology, 36*(21), 4625-4632.

Liang, W.-J., & Lin, T. (1994). The characteristics of ionic wind and its effect on electrostatic precipitators. *Aerosol Science and Technology, 20*(4), 330-344.

Lin, G.-Y., Tsai, C.-J., Chen, S.-C., Chen, T.-M., & Li, S.-N. (2010). An efficient single-stage wet electrostatic precipitator for fine and nanosized particle control. *Aerosol Science and Technology, 44*(1), 38-45.

Suriyawong, A., Hogan, C. J., Jiang, J., & Biswas, P. (2008). Charged fraction and electrostatic collection of ultrafine and submicrometer particles formed during O 2–CO 2 coal combustion. *Fuel, 87*(6), 673-682.

TSI. (2009). *Model 3080 SMPS Operation and Service Manual*. St Paul, MN: TSI Inc.

Wiedensohler, A. (1988). An approximation of the bipolar charge distribution for particles in the submicron size range. *Journal of aerosol science, 19*(3), 387-389.

Appendix II: Supplemental information for Chapter 3
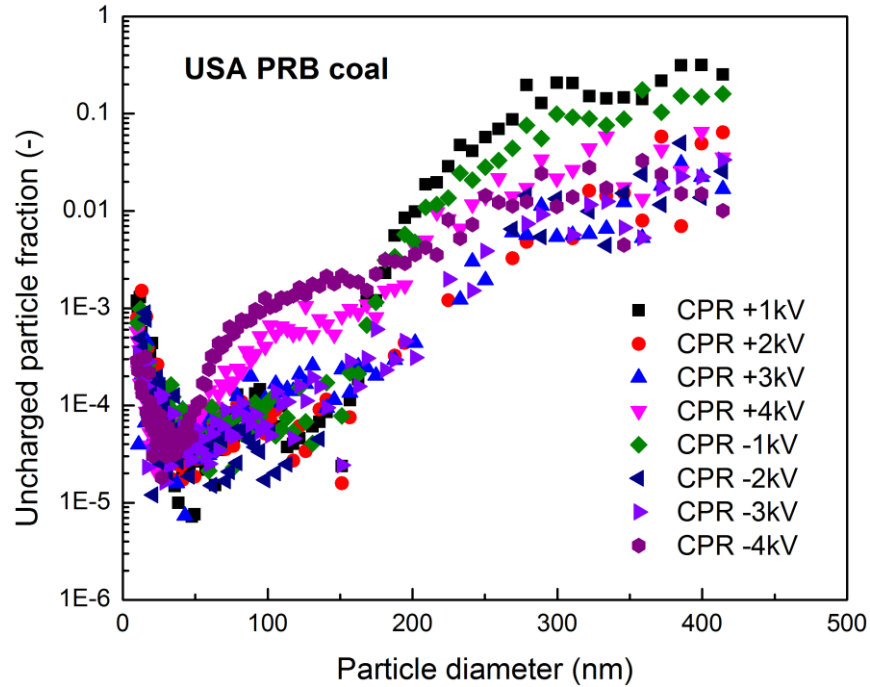
Figure A2.1 Uncharged particle fraction of the flue gas from combustion using US PRB coal and using various CPR voltages.

The uncharged particle fraction is shown in the Figure A2.1 with different voltage applied to CPR.

Three conclusions can be observed: 1) Most of the particles in the combustion exhaust gas are

charged, which would inevitably influence the performance of an ESP. 2) The capture performance

of CPR is nearly independent of the polarity of the voltage applied to the CPR. 3) Uncharged

particle fractions are slightly lower when using 2 or 3kV than those when using 1 or 4 kV. It can

be implied that further increase in voltage might not enhance capture performance of CPR.

Therefore, -2kV will be fixed for subsequent experiments. This result is consistent with what is

reported by Sahu (Sahu et al., 2012).
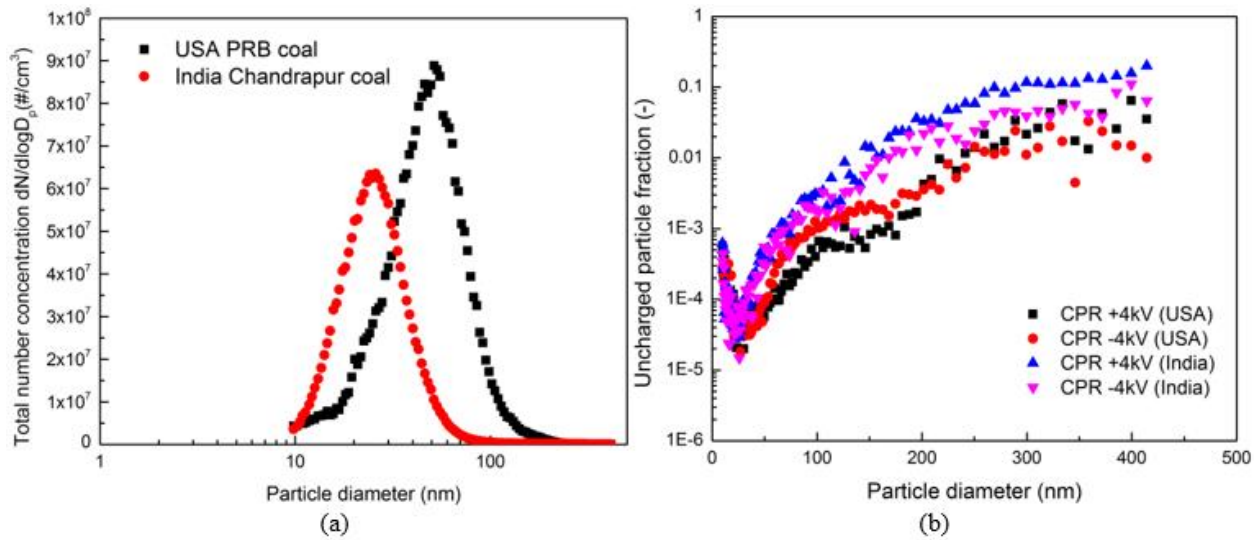
Figure A2.2 (a) Total number concentrations in flue gas from combustion of USA PRB coal and India Chandrapur coal; (b) Uncharged particle fraction for different coal combustion flue gas measured using voltages of 4 kV applied to CPR.

Comparison of charged particle fractions between US coal and India coal is shown in Figure A2.2. The particles in the flue gas display smaller peak size and lower total number concentration for India coal combustion. It can be observed in Figure A2.2(b) that although US coal combustion flue gas shows slightly lower uncharged particle fraction for particles larger than 50 nm, it might be attributed to fewer total number concentration in the corresponding size range, which is shown by Figure A2.2(a). It can be speculated that the CPR capture effect is independent of coal type.

Reference

Sahu, M., Park, J., & Biswas, P. (2012). In Situ Charge Characterization of TiO2 and Cu-TiO2

Nanoparticles in a Flame Aerosol Reactor. *Journal of Nanoparticle Research, 14*(2).

doi:10.1007/s11051-011-0678-3

Appendix III: Supplemental information for Chapter 5

Insulation on the DE to
prevent corona formation

Discharge electrode (DE)
Stainless steel, 0.323 mm
diameter

Collecting electrode
Stainless steel: 4.8 cm
diameter and 25.4 cm length

PVC tube for shielding
the soft X-ray

Aerosol In

Kapton 30HN polyamide film

X-ray
Photoionizer

Aerosol Out
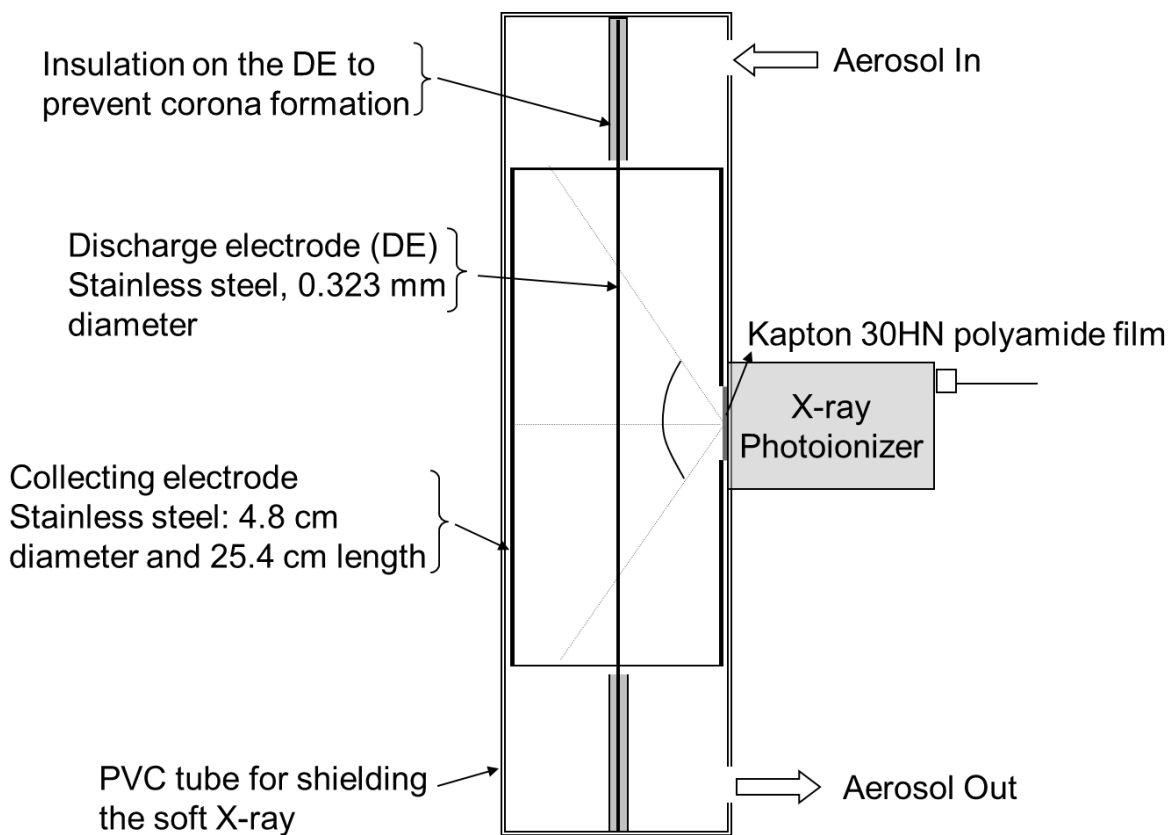
Figure A3.1 Configuration of the soft X-ray (SXR)-enhanced ESP used in the experiment. (The soft X-rays emitted by the photoionizer entered the ESP body through a circular hole (1.7 cm in diameter). A thin polyamide film (Kapton® 30HN, DuPont Corp., 30 µm thick) was used to seal the ESP. The penetrability of soft X-rays through the polyamide film was estimated to be around 90%.)
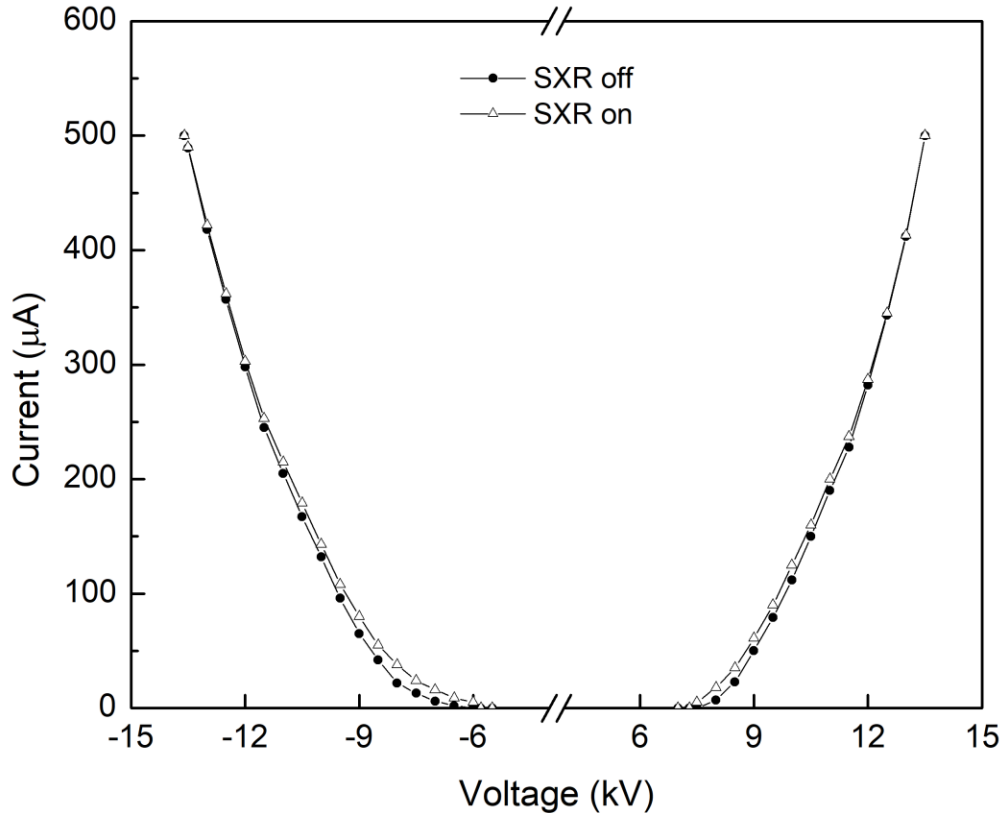
Figure A3.2 Current-voltage characteristics of the ESP with soft X-ray (SXR).

SXR energy requirement estimation

Assume a typical industrial ESP has a plate area of 10000 ft^2 (929 m^2) (Turner, et al., 1988). The

plate area of the ESP used in this study is 0.0383 m^2. Therefore, approximately 929/0.0383=24256

ESPs used in this study are needed for industry-scale application. The maximum distance that the

SXR can cover is 30 cm according to its manual, while the ESP diameter is only 5 cm. Therefore,

it is assumed that the SXR can be associated with 30/5=6 ESPs in our study. Thus 24256/6=4043

SXRs used in this study are needed for the same industry-scale application. The maximum power

of the SXR photoionizer is 4 W. Suppose there are 8760 hrs operation of both ESP and associated

SXR in one year. Then the energy cost of industrial ESP for one year is calculated by the following

equation (Turner et al., 1988):

$$OP_{ESP} = 1.94 \times 10^{-3} A\theta = 1.94 \times 10^{-3} \times 10000 \times 8760 = 170 \times 10^3 (kWh/yr)$$

$$= 170 (MWhs/yr)$$

where OP_{ESP} is annual ESP operating power (kWh/yr), A is ESP collecting area (ft^2) and θ is annual operating time (hr/yr).

The energy cost of the associated SXR for one year is:

$$4043 \times 4 \ (W) \times 8760 \ (hr/yr) = 142 \ (MWhs/yr)$$

The energy requirement for SXR can be even lower if its operation duration can be cut off when the requirement of particle removal is less strict, for example while the amine scrubber is offline.

Operational challenges of SXR include: (1) the SXR emitter needs to be installed in an X-ray shielded cabinet to avoid human X-ray exposure; (2) leakage monitoring procedure is needed to check the X-ray leakage around the emitter.

Table A3.1 Summary on the total number concentration (15.7–399.5 nm), PM$_{2.5}$ mass concentration and mean particle size for the tested conditions.

Test #	Test condition		Diffusion dryer	Total Num. Conc. (#/cm^3)	PM$_{2.5}$ Mass Conc. (mg/m^3)	Mean size (nm)
1	Soot blow	Boiler 5 soot blow	installed	1.95×10^{10}	N/A	57.2
		Boiler 7 soot blow	installed	1.88×10^{10}	N/A	50.9
2	FGD bypass		installed	1.96×10^{10}	N/A	55.3
3	Reheat burner off (0%)		installed	2.00×10^{10}	1.65	50.3
			N/A	2.62×10^{10}	N/A	45.5
4	Reheat burner (27% of full capacity)		installed	0.85×10^{10}	1.55	48.1
5	Reheat burner (42% of full capacity, normal operation)		installed	0.90×10^{10}	N/A	40.9
			N/A	1.50×10^{10}	N/A	42.1
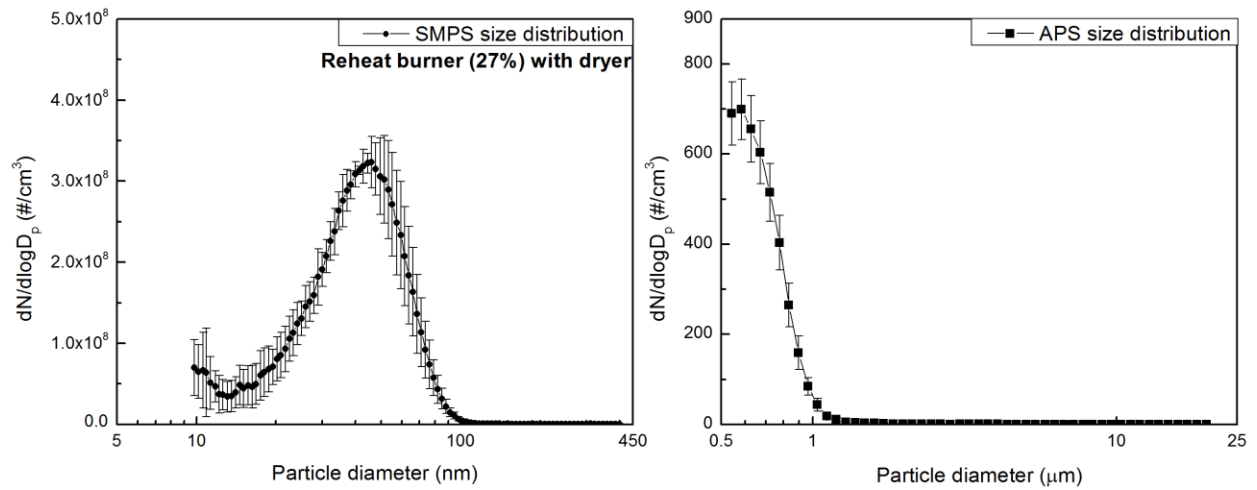
Figure A3.3 Size distribution of particles with size between 10 nm to 20 µm when the reheat burner rating is 27%: (a) SMPS and (b) APS. (A diffusion dryer was used before the instruments.)

References

Turner, J. H., Lawless, P. A., Yamamoto, T., Coy, D. W., Greiner, G. P., McKenna, J. D., & Vatavuk, W. M. (1988). Sizing and Costing of Electrostatic Precipitators: Part I. Sizing Considerations. *Japca, 38*(4), 458-471.

Appendix IV: Supplemental information for pressurized electrostatic precipitator (PESP) design

1. Electrical feedthrough flange

Due to the stringent requirement of high operating voltage under high pressure, the ESP needs to be equipped with a robust electrical feedthrough flange, which lets high voltage wire pass and maintains perfect sealing. This kind of flange with ratings of 20 bar and 100 kV is rarely commercially available and could cost much budget and time if it'd be customized. Fortunately, the CeramTec North America provides an electrical flange similar to what is required for this study in their regular inventory, which is a 6-inch ConFlat flange with ratings of 8 bar and 100 kV. Therefore, it is selected to be the one which will be mounted on the top of the pressurized ESP.

Next, the ESP body outer diameter needs to be adjusted to facilitate the welding between the ESP body and ConFlat flange. As shown in the Figure A4.1, ESP body outer diameter has to be short enough compared with the knife edges diameter of the ConFlat flange in order to create large enough space between the welding point and the knife edges. That way the welding process will not damage the knife edges, which are crucial to the gasket sealing under high pressure.

Knife edges diameter

ESP body outer diameter

Welding point

(a)

Electrical Feedthrough

Copper gasket

ESP body

(b)
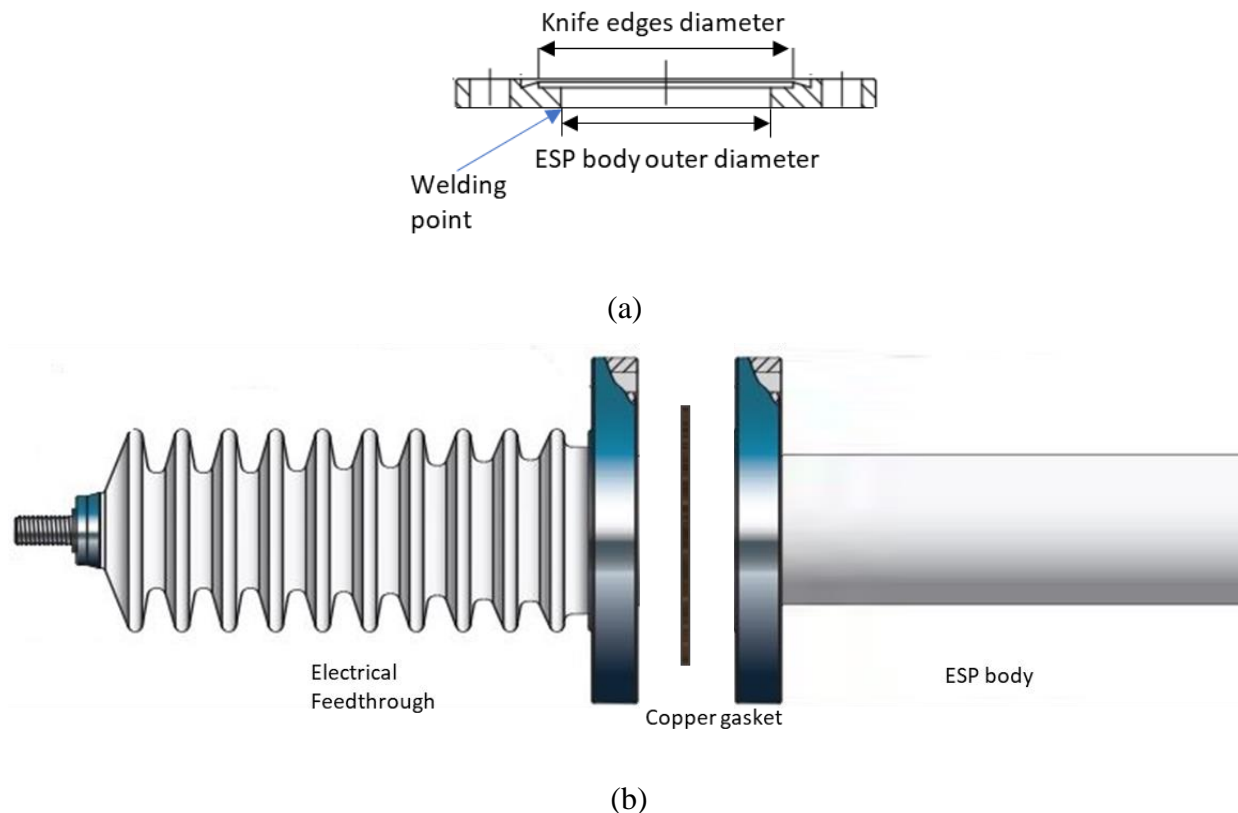
Figure A4.1 (a) The schematic of the welding point between ESP body and ConFlat flange; (b) the assembly schematic of electrical feedthrough flange, gasket and ESP body.

Therefore, a 2-ft Schedule 160 3-inch pipe (ASME/ANSI B36.10/19) is selected as the ESP body, whose inner diameter and thickness are 2.6 inch and 0.438 inch, respectively, and allowable pressure is around 400 bar. The thickness is selected so that it's large enough to cover the whole thread length of 1/8 NPT thread, which is used in safety valve, pressure gauge, and gas ports on the ESP body.

Since increasing current and voltage generally can increase the removal efficiency of pressurized ESP, the power supply is expected to offer as high as possible current and voltage as long as the budget allows. The high voltage supply is determined to be purchased from Spellman HV. It can provide voltage of up to 130 kV and current up to 9.2 mA. This is the one with the highest voltage and current ratings among the same model series. And according to the semi-empirical Deutsch-

Anderson equation, the removal efficiency of 10 nm particles can reach 90% using 9 mA and 54 kV under 10 bar, which is fairly good performance.

2. Insulation between wire and wall

At normal operation of ESP, the discharge electrode needs to be straight and tight and stay firmly at the center. Besides, it needs to be ensured that the wire is insulated from the bottom flange and the side wall of ESP. To keep the discharge wire straight and stable at the center of the ESP body, installing a ceramic rod at the lower end of the wire is an easy and feasible approach, which can also facilitate disassembly of the ESP and bottom ash cleaning. The discharge electrode, which is a piece of thin wire with diameter of 0.007 inch, was tied with a ceramic bar whose length is equal to the inner diameter of the ESP. This composite part was tied to the end of the conductive rod in the center of the electrical feedthrough flange. Thus the flange with the insulation bar hanging at the bottom can be mounted on the top of the ESP, and the insulation bar constricts the discharge electrode at the center line of the ESP. In this way, the discharge electrode is insulated from the ESP inner surface, which enables an environment for corona discharge.

3. Orifice at the outlet

Because the particle size distribution of fly ash needs to be measured at atmospheric pressure using a scanning mobility particle sizer (SMPS), the pressure of exhaust gas has to be reduced downstream of the combustor and upstream of the instrument by a certain pressure reducing unit. The pressure reducing unit is required to cause particle loss as little as possible. To compare the impacts in particle loss of different pressure reducing units, the particle size distributions of fly ash generated by a pressurized combustor under 3 bar were measured. The tested pressure reducers were an orifice (0.02 inch inner diameter) and a ball valve. The flow rate through the orifice was 8 lpm at 3 bar. The ball valve was tuned to maintain the same flow rate and pressure in the

combustor. The coal used was PRB coal and the feeding rate was kept constant while switching the pressure reducers. The measured particle size distributions showed that when the ball valve was used, the mode diameter was 44 nm, lower than the value (64 nm) when the orifice was used. Moreover, the peak concentrations when using the ball valve and the orifice were 2.1×10^6 #/cm^3 and 3.6×10^6 #/cm^3, respectively, indicating a much higher particle loss caused by the ball valve. This finding suggests that orifices with different diameters could be much better in terms of sampling particles under high pressure.

Appendix V: Computation codes for pressurized electrostatic precipitator design

1. Function for onset voltage of negative ESP

```
function y=onset_v(r0,r1,T,P)
%=======================================
% negative cylindrical ESP - onset voltage
%=======================================

%==============Input parameters===========
% r1                            % cross section radius      m
% r0                            % wire radius               m
% T                             % Temperature               K
% P                             % real pressure             Pa
%=======================================

%================Constants==============
P0=1.01325e5;                   % reference pressure        Pa

Ag=32.2e5;    % constant-1              V`m-1              (air)
Bg=8.46e4;    % constant-2              V`m-1/2            (air)

%=======================================
sigma=(25+273.15)*(P/P0)/T;
% relative density          #          (air; wrt 1 bar, 25 C)

%====Onset voltage under high pressure====
y=r0*log(r1/r0)*(Ag+Bg/(r0*sigma)^0.5)*sigma;% onset voltage  V
```

2. Function for number concentration collection efficiency of negative ESP

```
function y=eta_cal(r0,r1,h,I,T,P,Q0,dp)
%==============================================================
=======
% negative cylindrical ESP - number concentration collection
efficiency
%==============================================================
=======

%=================================Input
parameters=========================================

%------------------------ESP config---------------------
-----
% r0=0.000162;                          % wire radius
m
% r0=0.000162;
% r1=0.0254;                            % cross section radius
m
% r1=0.0254;
```

```
% h=0.254;                              % height
m
% h=0.254;                              % height
m
%--------------------------------Electrical condition--------------
-----
% I                                     % current
A
%--------------------------------Flow condition--------------------
-----
% Q0=0.00025;                           % flow rate at 1 bar
m3`s-1            (160 m3`h-1)
% Q0=160/3600;                          % flow rate at 1 bar
m3`s-1            (160 m3`h-1)
% T=273.15+25;                          % temperature
K
% T=273.15+300;                         % temperature
K
% P                                     % real pressure
Pa
%--------------------------------Particle property----------------
-----
% dp                                    % particle diameter
m


%=================================================================
==============================

%============================Empirical
factors======================
a1=1.78;                                % factor-1
#
a2=2.84;                                % factor-2
#

%==========================ESP
config============================
Ac=2*pi*r1*h;                           % collection area
m2
V_esp=pi*r1^2*h;                        % volume of ESP
m3

%==========================Constants=======================
=====
T0=298.15;                              % reference temp.
K
```

219

```
P0=1.01325e5;                                % reference pressure
Pa
mu=1.86e-5;                                  % viscosity
Pa`s                    (air)
dm=3.7e-10;                                  % collision dp
m                       (air)
NA=6.022e23;                                 % Avogadro const
#
k=1.38e-23;                                  % Boltzmann const
m2`kg`s-2`K-1
KE=9e9;                                      % const of
proportionality  N`m2`C-2
Mw_air=28.97;                                % molecular weight
g`mol-1
m_air=Mw_air/1000/NA;                        % mass of molecule
kg                      (air)
R=8.314;                                     % ideal gas constant
m3`Pa`K-1`mol-1

ci=(3*k*T/m_air)^0.5;                        % rms average thermal
speed of ions
e=1.6e-19;                                   % elementary charge
C
Zi=1.5e-4;                                   % mobility of ions
m2`V-1`s-1
K0=8.85e-12;                                 % free space
permittivity    F`m-1

%====================Voltage & charging
numbers====================
Vc=onset_v(r0,r1,T,P);                       % onset voltage
V
phi=(r1*log(r1/r0)/Vc)^2*I/h/2/pi/K0/Zi;% dimensionless current
#
phiI=phi/I*1e-6;
Ec=Vc/r0/log(r1/r0);                         % onset field strength
V`m-1
Ecr0=Ec*r0;
% V0=1.135^(P/1.01325e5-2.312)*(Vc+Ec*r0*((1+phi)^0.5-1-
log((1+(1+phi)^0.5)/2)))
                                             % corona voltage (at r0)
V
V0=(Vc+Ec*r0*((1+phi)^0.5-1-log((1+(1+phi)^0.5)/2)));
E0=V0/r0/log(r1/r0);                         % field strength (at r0)
V`m-1
E=E0*2*r0/(r1+r0);                           % field strength
(average)  V`m-1
```

```matlab
Ni=I/Ac/e/Zi/E;                          % ion concentration
#`m-3

Q=Q0*P0*T/P/T0;                          % real flow rate (in
ESP)    m3`s-1
t=V_esp/Q;                               % residence time
s

n_dif=dp.*(k*T/2/KE/e^2*log(1+pi*KE*dp*ci*e^2*Ni*t/2/k/T));
                                         % diffusion charging
number #
n_fie=(3*6.2/(6.2+2))*E*dp.^2/4/KE/e*(1/(1/pi/KE/e/Zi/Ni/t+1));
                                         % field charging number
#
n=a1.^(log(I)/log(20e-6)-P/1.01325e5)*n_dif+a2.^(log(I)/log(20e-
6)-P/1.01325e5)*n_fie;
                                         % total charging number
#
% n=a1.^(log(I*1e6)/log(20)-
P/1.01325e5)*n_dif+a2.^(log(I*1e6)/log(20)-P/1.01325e5)*n_fie;
% n=a1.^(I*P-20e-6*1.01325e5)*n_dif+a2.^(I*P-20e-
6*1.01325e5)*n_fie;

%========================Terminal
velocity========================
lambda=R*T/2^0.5/pi/dm^2/P/NA;           % mean free path
m                      (air)
Cc=1+lambda*(2.34+1.05*exp(-0.39.*dp/lambda))./dp;
                                         % Cunningham factor
#

Vte=n*e*E.*Cc/3/pi/mu./dp;               % terminal velocity
m/s

%======================Collection
efficiency======================
y=1-exp(-(Ac/Q*Vte)^0.5);

% fprintf('  P(bar)      \tT(C)      \tI(uA)    \tVc(kV)
\tV0(kV)  \tQ0(m3/s)  \tdp(nm)   \teta       \tphiI
\tEcr0(kV)\n');
%
fprintf('%8.0f\t%8.0f\t%8.0f\t%8.1f\t%8.1f\t%8.5f\t%8.0f\t%8.5f\
t%8.4f\t%8.1f\n', P/P0, T-273.15, I*1e6, Vc*1e-3, V0*1e-3, Q0,
dp*1e9, y, phiI, Ecr0*1e-3);
```

```matlab
fprintf('%8.0f\t%8.0f\t%8.0f\t%8.1f\t%8.1f\t%8.5f\t%8.3f\t%8.2f\
t%8.3f\t%8.5f\t%8.0f\t%8.5f\n', P/P0, T-273.15, I*1e6, Vc*1e-3,
V0*1e-3, Q0, r0*1e3, r1*1e2, h*1e2, h/t, dp*1e9, y);
```

3. Function for particle migration velocity of negative ESP

```matlab
function y=v_TE_plate(I,P,a1,a2,dp)
if P==1.01325e5
    Vc=8.2e3;
elseif P==1.01325e5*2
    Vc=1.28e4;
elseif P==1.01325e5*3
    Vc=1.63e4;
end

P=15;
T=598;

r0=0.3e-3;
L=80e-2;
H=40e-2;
W=20e-2;
w_w=10e-2;

s=W/2;
c=w_w/2;

s_c=s/c;

if s_c<=0.6
    d=4*s/pi;
elseif s_c>=2
    d=c/pi*exp(pi*s/2/c);
else
    d=c*0.335*exp(1.5264*s/c);
end

sigma=298*P/(298+T);
Ag=(38*0.82+29.1*0.06+26.2*0.12)*100000;
Bg=123000;

Ec=sigma*(Ag+Bg/(r0*sigma)^0.5);

Vc=r0*Ec*log(d/r0);
%===============================================
r0=0.0005;
% r0=0.323e-3/2;
```

222

```
r1=0.0254;
% r1=4.8e-2/2;
h=0.254;
Ac=2*pi*r1*h;
V_esp=pi*r1^2*h;
mu=1.86e-5;
dm=3.7e-10;
NA=6.022e23;
T=298.15;
T0=298.15;
P0=1.01325e5;
Q0=0.00025;

k=1.38e-23;

KE=9e9;
Mw_air=28.97;
m_air=Mw_air/1000/NA;
ci=(3*k*T/m_air)^0.5;

e=1.6e-19;
Zi=1.5e-4;
K0=8.85e-12;
phi=(r1*log(r1/r0)/Vc)^2*I/h/2/pi/K0/Zi;
V0=1.135^(P/1.01325e5-2.312)*Vc*(1+1/log(r1/r0)*((1+phi)^0.5-1-
log((1+(1+phi)^0.5)/2)));
E0=V0/r0/log(r1/r0);
% E=V0/(r1-r0);
E=E0*2*r0/(r1+r0);
Ni=I/Ac/e/Zi/E;

Q=Q0*P0*T/P/T0;
t=V_esp/Q;

n_dif=dp.*(k*T/2/KE/e^2*log(1+pi*KE*dp*ci*e^2*Ni*t/2/k/T));
n_fie=(3*6.2/(6.2+2))*E*dp.^2/4/KE/e*(1/(1/pi/KE/e/Zi/Ni/t+1));
n=a1.^(log(I)/log(20e-6)-P/1.01325e5)*n_dif+a2.^(log(I)/log(20e-
6)-P/1.01325e5)*n_fie;
% n=a1.^(log(I*1e6)/log(20)-
P/1.01325e5)*n_dif+a2.^(log(I*1e6)/log(20)-P/1.01325e5)*n_fie;
% n=a1.^(I*P-20e-6*1.01325e5)*n_dif+a2.^(I*P-20e-
6*1.01325e5)*n_fie;


R=8.314;
lambda=R*T/2^0.5/pi/dm^2/P/NA;
Cc=1+lambda*(2.34+1.05*exp(-0.39.*dp/lambda))./dp;
```

```matlab
y=n*e*E.*Cc/3/pi/mu./dp;
```

4. Code for predicting collection efficiency for ESPs

```matlab
% clc;
%---------------------------ESP config-----------------------
-----
r0_in=0.015/2;                              % wire radius
m                   (0.007" standard OD Stainless steel-wire)
r0=r0_in*0.0254;
% r0=0.000162;
r1_in=2.624/2;                              % cross section
radius      m                   (4.026" standard ID SS-40S pipe)
r1=r1_in*0.0254;
% r1=0.0254;
h_in=12*2;                                  % height
m                  (24"=2ft reasonable and standard length)
h=h_in*0.0254;
% h=0.254;
%-------------------------Electrical condition--------------
-----
I=1e-
6*[9,200,300,400,500];                                      %
current                     A
%-------------------------Flow condition-------------------
-----
Q0=0.00015*[1:1:3];          % flow rate at 1 bar        m3`s-1
T=273.15+[25,300];                          % temperature
K
% T=273.15+300;                            % temperature
K
% P=1.01325e5*15;                          % real
pressure              Pa
P=(1.01325e5)*[1:1:20];                                      %
real pressure             Pa
%-------------------------Particle property----------------
-----
dp=5e-9;                                 % particle diameter
m

fprintf('  P(bar)       \tT(C)       \tI(uA)    \tVc(kV)    \tV0(kV)
\tQ0(m3/s)   \tr0(mm)    \tr1(cm)     \th(cm)     \tvf(m/s)
\tdp(nm)    \teta\n');
eta=zeros(15);
eta(5)=eta_cal(r0,r1,h,I(1),T(2),P(10),Q0(1),dp);
```

Appendix VI: Curriculum vitae

Zhichao Li

z.li@wustl.edu
(+1) 314-520-8004
Brauer Hall, CB 1180, 1 Brookings Drive, St. Louis, Missouri, 63130, USA

EDUCATION

Department of Energy, Environmental & Chemical Engineering   09/2014-06/2019

Washington University in St. Louis, Missouri, USA

Doctor of Philosophy

- Key courses: Computational Fluid Dynamics, Mathematical Methods, Advanced Topics in Aerosols.

College of Environmental Sciences and Engineering   09/2010-07/2014

Peking University, Beijing, China

Bachelor of Engineering

- Key courses: Data Structure & Algorithm, Advanced Mathematics, Linear Algebra, Probability Theory & Statistics.

SKILLS

- **Programming Languages:** MATLAB, Python, C++&C, Fortran
- **Frameworks & tools & systems:** Qt (GUI), Git, Latex, Linux

PROFESSIONAL EXPERIENCE

Ph.D. Intern in Data Science   06/2018-08/2018

Air Products & Chemicals Inc., Allentown, Pennsylvania

TEACHING EXPERIENCE

Combustion Phenomena (E44.EECE.512.01, graduate course)   09/2016-12/2016

Instructed by Dr. Richard Axelbaum (Washington University)

Mass Transfer Operations (E44.EECE.304.01, undergraduate course)   01/2016-05/2016

Instructed by Dr. Janie Brennan (Washington University)

Aerosol Science and Technology (E44.EECE.504.01, graduate course)   09/2015-12/2015

Instructed by Dr. Pratim Biswas (Washington University)

PUBLICATIONS

- **Li, Z.**, Wang, Y., Lu, Y., & Biswas, P. (2019). Investigation of aerosol and gas emissions from a coal-fired power plant under various operating conditions. *Journal of the Air & Waste Management Association*, 69(1), 34-46.

- **Li, Z.**, Jing, H., & Biswas, P. (2016). Capture of submicrometer particles in a pressurized electrostatic precipitator. *Aerosol Science and Technology*, 50(10): 1115-1129.

- **Li, Z.**, & Biswas, P. Comparison of size distribution, charge fraction and electrostatic precipitation of fly ash from combustion of India, US and China coal. *In preparation*.

- **Li, Z.**, Wang, Y., & Biswas, P. Understanding the effects of flue gas aerosol pretreatment upstream amine-based CO_2 scrubber. *In preparation*.

- Wang, Z., **Li, Z.**, Ma, S., Zheng, S., & Biswas, P. Effects of pressure and coal type on characteristics of coal fly ash and submicrometer particle size distribution. *In preparation*.

- Dhanraj, I. A. D., **Li, Z.**, & Biswas, P. Aerosol formation and growth in amine-based CO_2 scrubber: experiments and numerical simulation. *In preparation*.

- Zhang, H., Sharma, G., Dhawan, S., Dhanraj, I. A. D., **Li, Z.**, & Biswas, P. Comparison and software development

for aerosol dynamic models: discrete, discrete-sectional, modal and moment model. *In preparation*.

- Reed, N., Zhang, Y., **Li, Z.**, Patel, S., Li, J., Wang, Z., Zheng, L., Kulkarni, P., & Biswas, P. Aerosol spark emission spectrometer (ASES) for the measurement of trace metals concentration in particulate emissions from the combustion of coal in a household heating and cooking stove. *In preparation.*

- Ray, J. R., Neil, C. W., Jung, H., **Li, Z.**, & Jun, Y. S. Redox chemistry of CeO_2 nanoparticles in aquatic systems containing Cr(VI)(aq) and Fe^{2+} ions. *Environmental Science: Nano*. Accepted.

CONFERENCE PRESENTATIONS

- **Li, Z.**, & Biswas, P. Comparison of charge fraction and electrostatic precipitation of fly ash from combustion of India, US and China coal. *The 10th International Aerosol Conference (IAC 2018)*, Saint Louis, Missouri, USA, 09/07/2018. **(Oral presentation)**

- Wang, Z.*, **Li, Z.**, Ma, S., Zheng, S., & Biswas, P. Effects of pressure and coal seams on the characteristics of coal fly ash and submicrometer particle size distribution. *The 10th International Aerosol Conference (IAC 2018)*, Saint Louis, Missouri, USA, 09/07/2018. **(Oral presentation; presenter marked with *)**

- Dhanraj, I. A. D.*, **Li, Z.**, & Biswas, P. Aerosol formation and growth in amine-based CO_2 scrubber: experiments and numerical simulation. *The 10th International Aerosol Conference (IAC 2018)*, Saint Louis, Missouri, USA, 09/04/2018. **(Oral presentation; presenter marked with *)**

- Reed, N.*, Zhang, Y., **Li, Z.**, Patel, S., Li, J., Wang, Z., Zheng, L., Kulkarni, P., & Biswas, P. Aerosol spark emission spectrometer (ASES) for the measurement of trace metals concentration in particulate emissions from the combustion of coal in a household heating and cooking stove. *The 10th International Aerosol Conference (IAC 2018)*, Saint Louis, Missouri, USA, 09/04/2018. **(Oral presentation; presenter marked with *)**

- Sharma, G.*, Dhawan, S., **Li, Z.**, Dhanraj, I. A. D., & Biswas, P. Comparison of different aerosol dynamics models based on accuracy and computational time. *The 10th International Aerosol Conference (IAC 2018)*, Saint Louis, Missouri, USA, 09/04/2018. **(Poster; presenter marked with *)**

- **Li, Z.**, Jing, H., & Biswas, P. Capture of submicrometer particles in a pressurized electrostatic precipitator. *XIV International Conference on Electrostatic Precipitation ICESP 2016*, Wroclaw, Poland, 09/22/2016. **(Oral presentation)**

AWARDS & HONORS

- **1st-place Winner of McDonnell Academy PhD-in-3D Competition** (Washington University)   04/2019
- **McDonnell International Scholar Academy Fellowship** (Washington University)   09/2014-06/2019
- **Top Talent Scholarship** (Peking University)   12/2013
- **Merit Student (2011-2012 Academic Year)** (Peking University)   12/2012
- **Top Talent Scholarship** (Peking University)   03/2012
- **Award for Academic Excellence (2010-2011 Academic Year)** (Peking University)   12/2011
- **Yihai Kerry Scholarship** (awarded by Yihai Kerry Group) (Peking University)   12/2011
- **1st-level Prize in 23rd National Chemistry Olympiad (Provincial Division)**   09/2009